
Optimization of the Front-End electronics of the $\overline{\text{P}}\text{ANDA}$ Barrel EMC

Inaugural-Dissertation
zur Erlangung des Doktorgrades der Naturwissenschaften (Dr. rer. nat.)
der Justus-Liebig-Universität Gießen
im Fachbereich 07
(Mathematik und Informatik, Physik, Geographie)

September 2016

vorgelegt von

Christoph Rosenbaum

aus Langenfeld / Rhld.

II. Physikalisches Institut
Justus-Liebig-Universität Gießen
Heinrich-Buff-Ring 16
35392 Gießen
Deutschland

Dekan: Prof. Dr. Bernhard Mühlherr
Prodekan: Prof. Dr. Kai-Thomas Brinkmann

Betreuer und 1. Gutachter: Prof. Dr. Kai-Thomas Brinkmann
2. Gutachter: Prof. Dr. Claudia Höhne
3. Prüfer: Prof. Dr. Horst Lenske
4. Prüfer: Prof. Dr. Alfred Müller

Tag der mündlichen Prüfung: 30. September 2016

Abstract

One major goal of the future FAIR¹ facility is the understanding of the structure of matter at a sub-nuclear level which is governed by a short range force, the strong interaction. The state-of-the-art $\bar{\text{P}}\text{ANDA}$ ² detector at FAIR will be used to study the strong interaction by investigating proton - antiproton interactions. The EMC³ of the target spectrometer with its expected excellent performance and efficiency for electromagnetic probes over a wide energy range from 10 MeV up to 15 GeV, will be one of the central components to achieve the physics goals. The Barrel part of the EMC will consist of more than 11,000 lead tungstate crystals operated at -25°C to achieve the requirements of the experiment.

Within the scope of this work, the performance of the most recent prototypes of the $\bar{\text{P}}\text{ANDA}$ Barrel EMC will be compared. The first large scale prototype PROTO60 was designed to test the performance of the improved tapered lead tungstate crystals. The PROTO60 which consists of 6×10 crystals was tested at various accelerator facilities over almost the complete envisaged energy range but missing the mid energy range. The results were fulfilling the requirements of the TDR of the $\bar{\text{P}}\text{ANDA}$ EMC in terms of energy, position and time resolution. Therefore, the resolution parameters were used as input parameters for the physics simulations of the research program of $\bar{\text{P}}\text{ANDA}$. Hence, the PROTO60 results represent a specification limit. However, complementary results of a beamtime time for the mid energy range will be presented in this work so as to additionally verify the previous results.

Despite the sufficient performance of the PROTO60, a second prototype PROTO120 has been constructed, in order to realize the final barrel geometry and to test the final

¹Facility for Antiproton and Ion Research (FAIR)

² $\bar{\text{P}}$ (Antiproton) ANnihilation at DArmstadt ($\bar{\text{P}}\text{ANDA}$)

³ElectroMagnetic Calorimeter (EMC)

front-end electronics. It represents a larger section of a barrel slice, containing the most tapered crystals and the close to final components for the \bar{P} ANDA EMC.

The emphasis of this work is the optimization of the Barrel EMC with respect to the front-end electronics. A significant improvement is out of reach because the essential parameters influencing the performance of the Barrel EMC like the quality of the envisaged lead tungstate crystals and the pre-amplifier have been improved significantly and reached its limits. However, the performance of the specially developed pre-amplifier of the Barrel EMC has not been verified under experimental conditions so far. Therefore, a beamtime test has been conducted with the PROTO120, which will be presented within this work. Furthermore, possibilities to optimize the performance will be discussed.

Another main goal of this work is the unique study of the impact of dead material in front of the PROTO60. The experiment with prototype detectors are performed under idealized conditions. But the material budget in front of the Barrel EMC is considered to have a significant influence on the performance for future operation within the \bar{P} ANDA detector. Therefore, the performance of the PROTO60 with a quartz plate in front has been measured. Results will be discussed within this work.

Zusammenfassung

Eines der großen Ziele der zukünftigen FAIR Anlage ist das Verständnis der Struktur von Materie im subatomaren Bereich. Dieser Bereich wird beherrscht von einer kurzreichweitigen Kraft, der starken Wechselwirkung. Der hochmoderne \bar{P} ANDA Detektor, welcher an der zukünftigen FAIR Anlage genutzt werden wird, wurde entwickelt um die starke Wechselwirkung mit Interaktion von Protonen und Antiprotonen zu untersuchen. Das Elektromagnetische Kalorimeter ist ein wichtiger Teil des Spektrometers, welches sich um den Interaktionspunkt herum befindet, mit einer erwarteten exzellenten Leistungsfähigkeit und Effizienz um elektromagnetische Teilchen über einen großen Energiebereich von 10 MeV bis zu 15 GeV nachzuweisen. Damit ist es ein essentieller Bestandteil um die zentralen Zielsetzungen des Physikprogramms von \bar{P} ANDA zu erreichen. Der Barrel Teil des EMC wird aus über 11.000 Bleiwolframatkristallen bestehen, welche bei einer Temperatur von -25°C betrieben werden, um den Anforderungen des Experiments gerecht zu werden.

Im Rahmen dieser Arbeit wird die Leistungsfähigkeit von den beiden neusten Prototypen des \bar{P} ANDA Barrel EMC verglichen. Der erste großformatige Prototyp PROTO60 wurde entwickelt, um die Leistungsfähigkeit der verbesserten Bleiwolframatkristalle zu testen. Der PROTO60 besteht aus 6×10 Kristallen und wurde an verschiedenen Beschleunigeranlagen über einen Großteil des vorgesehenen Energiebereichs getestet, wobei der Mittelenergiebereich ausgelassen wurde. Die Ergebnisse erfüllten die Anforderungen des TDR vom \bar{P} ANDA EMC was Energie-, Position- und Zeitauflösung angeht. Aufgrund dessen wurden die Auflösungsparameter als Eingangsgrößen für die Physiksimulationen des \bar{P} ANDA Forschungsprogramm verwendet. Deswegen werden die Ergebnisse des PROTO60 als Anforderungsbegrenzung für das Barrel EMC angesehen. In dieser Arbeit werden vervollständigte Ergebnisse eines Prototypentests im Mittelenergiebereich präsentiert um die vorherigen Ergebnisse zu

bestätigen.

Trotz der ausreichenden Leistungsfähigkeit des PROTO60, wurde ein zweiter Prototyp PROTO120 konstruiert, um die letztendliche Barrel Geometrie zu verwirklichen und die finale Front-End Elektronik zu testen. Dieser Prototyp repräsentiert einen größeren Teil von einem Barrel Stück mit den am meisten konisch zulaufenden Kristallen und den ausgewählten finalen Komponenten des \bar{P} ANDA EMC.

Der Schwerpunkt dieser Arbeit ist die Optimierung des Barrel EMC was die Front-End Elektronik anbelangt. Eine signifikante Verbesserung liegt außerhalb der Möglichkeit, da die entscheidenden Faktoren, welche die Leistungsfähigkeit des Barrel EMC beeinflussen, wie die Qualität der Bleiwolframatkristalle und die der Vorverstärker schon entscheidend verbessert wurden und an die Grenzen der Leistungsfähigkeit gebracht wurden. Nichtsdestotrotz muss die Leistungsfähigkeit des extra für das Barrel EMC entwickelten Vorverstärker noch unter experimentellen Bedingungen überprüft werden. Dafür wurde ein Test mit dem Prototypen an einer Beschleunigeranlage durchgeführt und die Ergebnisse werden in dieser Arbeit präsentiert. Des Weiteren werden Möglichkeiten zur Optimierung der Leistungsfähigkeit diskutiert.

Ein weiteres Ziel dieser Arbeit ist die einzigartige Untersuchung über den Einfluss von Material vor dem PROTO60. Die Experimente mit dem Prototypen wurden alle unter idealisierten Bedingungen durchgeführt. Allerdings wird erwartet, dass während der Operation im \bar{P} ANDA Detektor das Material von anderen Detektoren vor dem Barrel EMC einen entscheidenden Einfluss auf die Leistungsfähigkeit hat. Deswegen wurde die Leistungsfähigkeit des PROTO60 mit einer vorgestellten Quartzplatte untersucht. Die Ergebnisse werden in dieser Arbeit vorgestellt.

Contents

Abstract	I
Zusammenfassung	III
Contents	V
1 Introduction	1
1.1 \bar{P} ANDA Physics	3
1.1.1 Spectroscopy of QCD Bound States	5
1.1.2 Hadron structure experiments	10
1.1.3 Hadronic interaction experiments	11
1.2 \bar{P} ANDA Detetector	13
1.2.1 Target spectrometer	14
1.2.1.1 Target System	15
1.2.1.2 Tracking	16
1.2.1.3 Particle Identification	18
1.2.2 Forward spectrometer	23
1.2.2.1 Tracking	24
1.2.2.2 Particle identification	25
1.2.2.3 Shashlik Calorimeter	25
1.2.2.4 Muon Detector	26
1.2.3 Luminosity Detector	27
1.3 Electromagnetic Calorimeter	28
1.3.1 Interaction of Charged Particles with Matter	28
1.3.2 Interaction of Photons with Matter	33
1.3.3 Electromagnetic Shower	35

1.3.4	Requirements for the \bar{P} ANDA Electromagnetic Calorimeter	38
1.3.5	Scintillator material	39
1.3.6	Layout	41
1.3.7	Photo sensors	42
1.3.7.1	LAAPD	42
1.3.7.2	VPTT	47
1.3.8	Front End Electronics and Data Acquisition	48
1.3.8.1	ASIC	49
1.3.8.2	Low Noise and Low Power Charge Preamplifier	50
1.3.8.3	Data Acquisition	51
2	Beamtime test with PROTO60	53
2.1	PROTO60	53
2.1.1	Mechanics	53
2.1.2	Electronics	55
2.1.3	Readout and DAQ	57
2.2	Experimental setup in Bonn	65
2.2.1	ELSA	67
2.2.2	Beamtime procedure	76
2.3	Analysis	78
2.3.1	Energy calibration	78
2.3.2	Lineshapes	80
2.3.3	Linearity	81
2.3.4	Multiplicity	82
2.3.5	Energy resolution	82
2.3.6	Position resolution	86
2.4	Influence of dead material in front of the detector	94
2.4.1	Experimental setup	94
2.4.2	Experimental results	95
2.4.3	Simulation	97

3	Beamtime test with PROTO120	103
3.1	PROTO120	103
3.1.1	Mechanics	104
3.1.2	Electronics	105
3.1.3	Readout and DAQ	108
3.2	Experimental setup in Mainz	112
3.2.1	MAMI	113
3.2.2	Beamtime procedure	119
3.3	Electronic noise	120
3.4	Analysis	126
3.4.1	Calibration	126
3.4.1.1	APD calibration	127
3.4.1.2	Relative calibration	131
3.4.2	Energy resolution	133
3.4.2.1	Multiplicity	135
3.4.2.2	Summed traces	136
4	Discussion	139
4.1	CMS ECAL	142
4.2	PROTO60	145
4.2.1	Response of the PROTO60	145
4.2.2	Position resolution	147
4.3	PROTO120	148
4.4	Non-uniformity	150
4.5	Comparison PROTO60 and PROTO120	154
4.6	Influence of dead material in front of the Barrel EMC	157
4.7	Outlook	160
	Bibliography	161
	Glossary	169
	List of Figures	179

Contents

List of Tables	181
Acknowledgements	183
Erklärung	185

Chapter 1

Introduction

The upcoming international FAIR facility [1] at Darmstadt will be a unique accelerator and experimental facility for the frontier research and applied sciences with ions and antiprotons. It will be located at the site of the present GSI Helmholtzzentrum für Schwerionenforschung GmbH (GSI) as depicted in Fig. 1.1. The FAIR acceler-

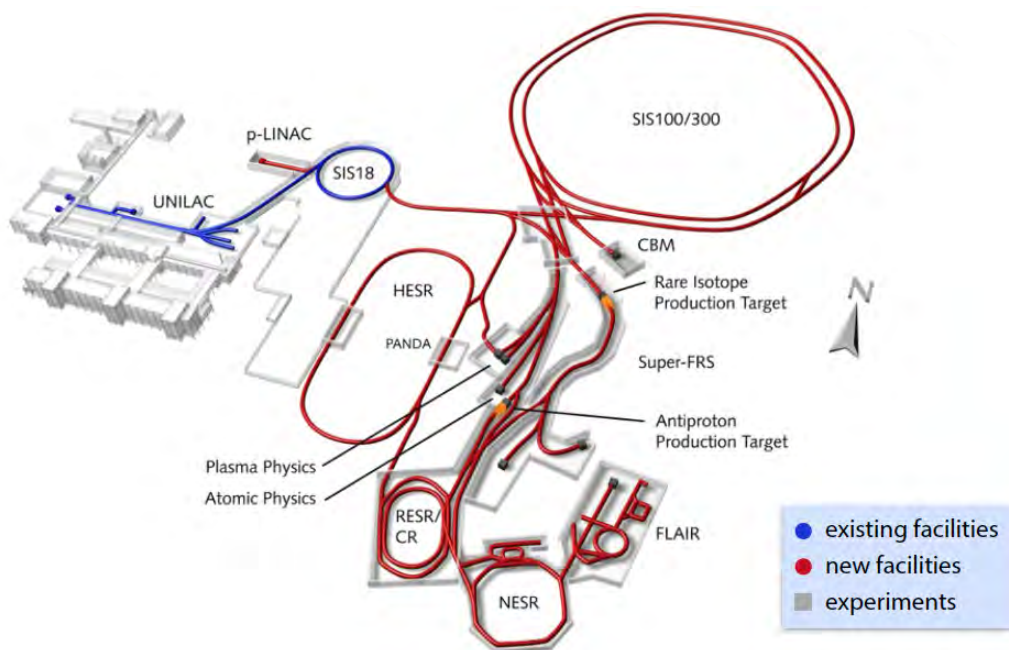


Figure 1.1: Planned FAIR facility (red) and the present GSI (blue).

ators will be capable of delivering high quality primary beams of protons and ions,

as well as secondary beams of antiprotons and stable and unstable nuclei to sundry experiments, dedicated to several topics in hadron and nuclear physics. The heart of the FAIR facility will be the **SchwerIonenSynchrotron 100 (SIS100)** with 1.1 km circumference and magnetic rigidities of 100 Tm, which is intended to accelerate the wide range of beam particles. In case of the protons, SIS100 will provide intense pulsed beams with intensities of 4×10^{13} protons per pulse at an energy of 29 GeV. Prior to the injection into the synchrotron, the presently existing GSI accelerators, **UNIversal Linear ACcelerator (UNILAC)** and the **Schwer-Ionen Synchrotron 18 (SIS18)**, will be used to pre-accelerate the ions while retaining the ability to provide beam for experiments at GSI. In addition, a new linear accelerator, the so-called **proton-LINear ACcelerator (p-LINAC)**, will be built which provides high intensity proton beams of 70 MeV for injection. FAIR has to ensure an efficient parallel operation of several experiments with different requirements. The four main pillars are:

- **Atomic Plasma Physics and Applications (APPA)**: plasma physics at high pressure and low temperature, atomic physics, applied research in material science and biology.
- **Compressed Baryonic Matter (CBM)**: investigation of the QCD phase diagram at high baryon density with nucleus-nucleus collisions.
- **Nuclear Structure Astrophysics and Reaction (NuSTAR)**: study of physics of atomic nuclei, new aspects of nuclear structure, nuclear astrophysics, fundamental interactions and symmetries using secondary beams of radioactive nuclei.
- **PANDA**: see dedicated chapter 1.1

For those experiments the SIS100 beam is converted into secondary beams and further enhanced by a system of cooling and storage rings. At present it is planned to have four subsequent rings: the **Collector Ring (CR)**, the **Recirculation Experimental Storage Ring (RESR)**, the **New Experimental Storage Ring (NESR)** and the **High Energy Storage Ring (HESR)**. The latter is most important for the $\bar{\text{P}}\text{ANDA}$ experiment and is shown schematically in Fig. 1.2. The HESR stores antiprotons produced at the antiproton production target made of nickel, iridium or copper and is able to

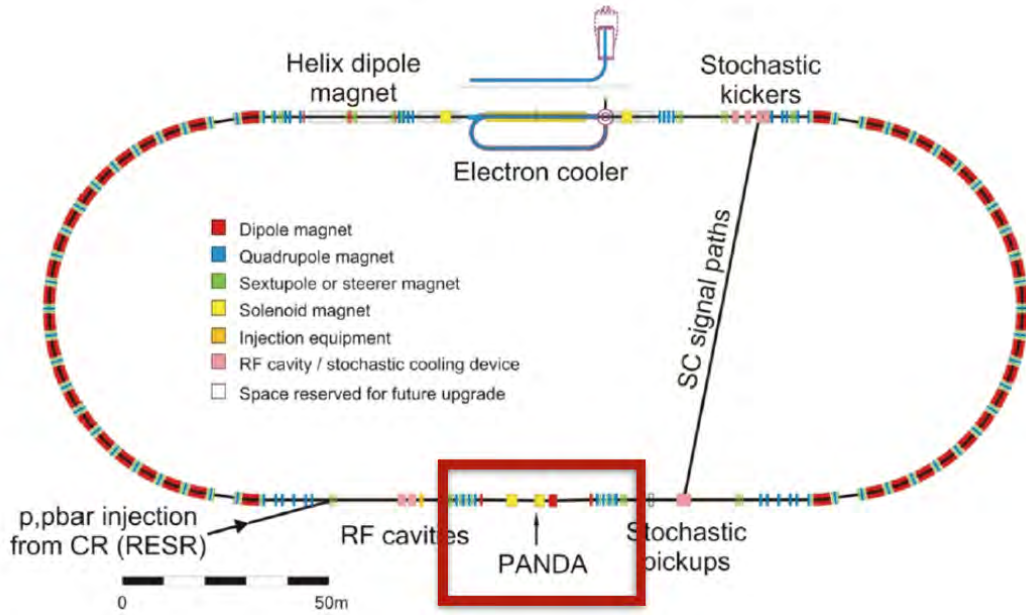


Figure 1.2: Schematic view of the HESR with indicated $\bar{\text{PANDA}}$ detector.

provide beam momenta in the range from $1.55 \text{ GeV}/c$ to $15 \text{ GeV}/c$. A system of both stochastic cooling as well as an electron cooler makes it possible to operate the HESR in two modes: the *high luminosity mode*, with a maximum luminosity of $\mathcal{L} = 2 \times 10^{32} \text{ cm}^{-2}\text{s}^{-1}$ and a beam momentum resolution of $\delta p/p < 10^{-4}$, and the *high resolution mode*, with an order of magnitude lower luminosity but better momentum resolution of $\delta p/p < 4 \times 10^{-5}$.

1.1 $\bar{\text{PANDA}}$ Physics

The HESR will provide antiproton beams of unprecedented intensity and quality enabling the $\bar{\text{PANDA}}$ experiment an unique tool to address fundamental questions like the investigation of the strong interaction and its corresponding fundamental theory, **Quantum ChromoDynamics (QCD)**, in the subnuclear regime. The theory is well understood and successful in describing phenomena at high energies and corresponding short distances ($< 10^{-15} \text{ m}$), where the strong coupling constant α_S and hence the basic interaction between quark and gluon, the force carrier of the strong interaction,

is small. In that case the interaction among quarks by gluon exchange can be treated in a good approximation by perturbation theory. Contrary to high energies, in the low energy regime and corresponding large interaction distances (\sim size of the nucleon), hadrons become the relevant degree of freedom and the application of perturbation theory is not allowed anymore, since the coupling constant increases strongly. The force among the quarks becomes so strong that they cannot be further separated which is related to the self-interaction of gluons. In this region effective theories have to be applied for calculations which are complicated and labour-intensive, but also experimental knowledge is limited. Since \bar{P} ANDA is a fixed-target experiment at a centre of mass energy between 2.2 GeV and 5.5 GeV, which is well in the non-perturbative region, it will provide access to the heavier strange and charm quarks and production of gluons as displayed in Fig. 1.3. The \bar{P} ANDA physics program is at the core

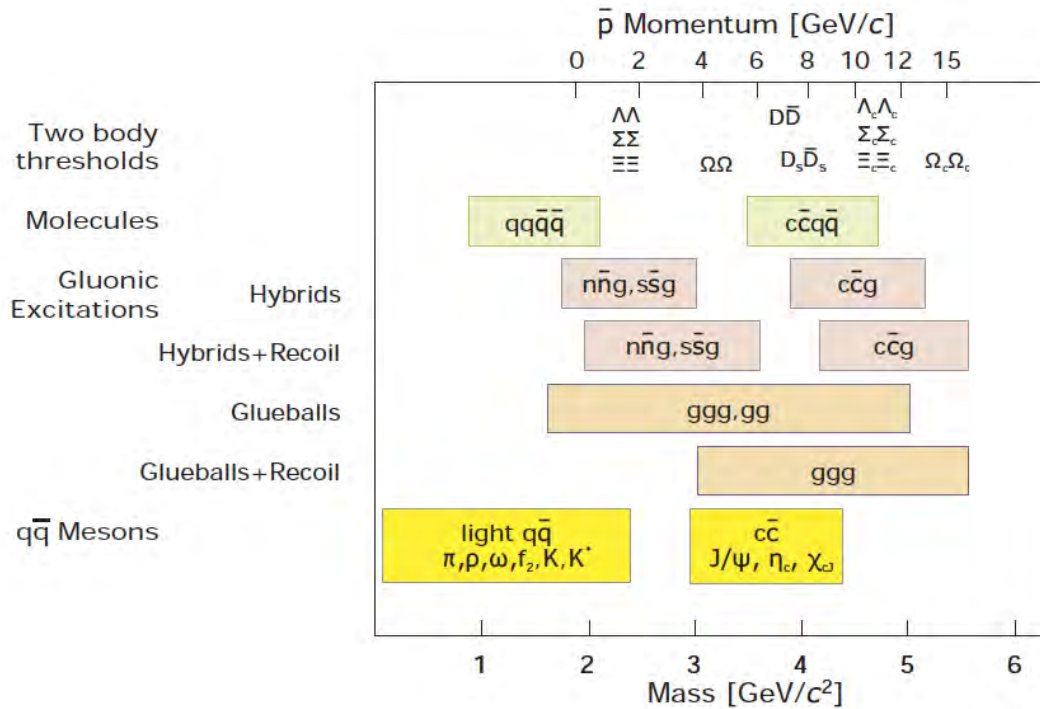


Figure 1.3: Invariant mass range accessible to \bar{P} ANDA with an antiproton beam [2]. The antiproton momenta for charmonium spectroscopy and other producible particles and resonances are indicated.

of hadron physics with its three superior topics: hadron spectroscopy, hadron struc-

ture and hadron interactions. These topics will be discussed in more detail in the following sections.

1.1.1 Spectroscopy of QCD Bound States

Charmonium spectroscopy

The charmonium, a system of a charm quark and a charm antiquark ($c\bar{c}$), gives a powerful tool to the fundamental understanding of the strong interaction in terms of QCD. In contrast to light quark (u, d, s) systems the coupling constant is rather small ($\alpha_S \approx 0.3$) and relativistic effects are manageable because of the relatively high mass of a charm quark ($m_c \approx 1.5 \text{ GeV}/c^2$). At the other extreme, the bottomonium system ($b\bar{b}$) would require too much technical advancement in terms of antiproton beams with presently unreachable high energies, resolution and intensity.

Despite the discovery of the J/Ψ , the vector state ($J^{PC} = 1^{--}$) of charmonium, in 1974 at **Stanford Linear Accelerator Center (SLAC)** and **Brookhaven National Laboratory (BNL)** [3] and the identification of many states in the charm region also at B-factories since then, there is huge lack by experimental precision data. Studies of charmonium via electron-positron-annihilations lead to a number of important discoveries but were restricted to the quantum numbers of the virtual photon $J^{PC} = 1^{--}$. All the other discovered states were produced by radiative transitions coming along with limited precision. In contrast to that, the $\bar{\text{P}}\text{ANDA}$ experiment can provide significant support, since antiproton-proton-annihilation must proceed via two or three gluons, and thus not only the vector states $J^{PC} = 1^{--}$ but even rare or exotic states can be directly formed with high abundance. The difference between production and formation experiments is schematically shown in Fig. 1.4. Another advantage comes about because of the cooling of the antiproton beam at the HESR which results in a high momentum resolution. Hence, the beam resolution can be translated directly into mass resolution which allows a scanning for even narrow resonances. Thus, with the $\bar{\text{P}}\text{ANDA}$ detector a direct and precise determination of the excitation curve is possible. On that account, charmonium spectroscopy at $\bar{\text{P}}\text{ANDA}$ can also provide an effective tool to compare between theoretical models. The charm system is illustrated

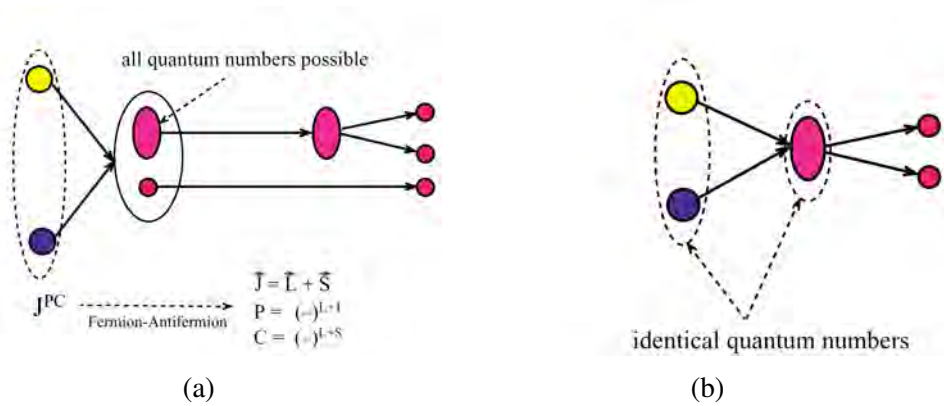


Figure 1.4: Schematic of production (a) and formation (b) experiments [4].

in Fig. 1.5 where experimental data and theoretical predictions are registered.

Open charm

The mostly unexplored region of charmonium states decaying into charmed mesons (open charm) and charmonium decays near the $D\bar{D}$ -threshold is accessible for \bar{P} ANDA as well. The possibility to precisely measure the width of such a state features the investigation of their nature which is presently fairly unclear for the D_s spectrum. For example, it would be possible to measure the width of the D_{sJ} (2317) in the order of 30 – 100 keV with a threshold scan [6] where only upper limits of a few MeV exist so far.

Exotic Excitations: Hybrids and glueballs

The existence of a new type of hadrons, gluonic excitations, is a fundamental feature of the QCD spectrum beside the naive quark model. There are two categories of gluonic excitations: *hybrids* and *glueballs*. Hybrids are bound states consisting of a quark and antiquark where the gluons themselves carry excitation degrees of freedom. Whereas glueballs are boundstates consisting purely of gluons. A promising feature of glueballs is that they can give an understanding for the creation of mass. Only a few percent of the proton mass is generated due to the Higgs mecha-

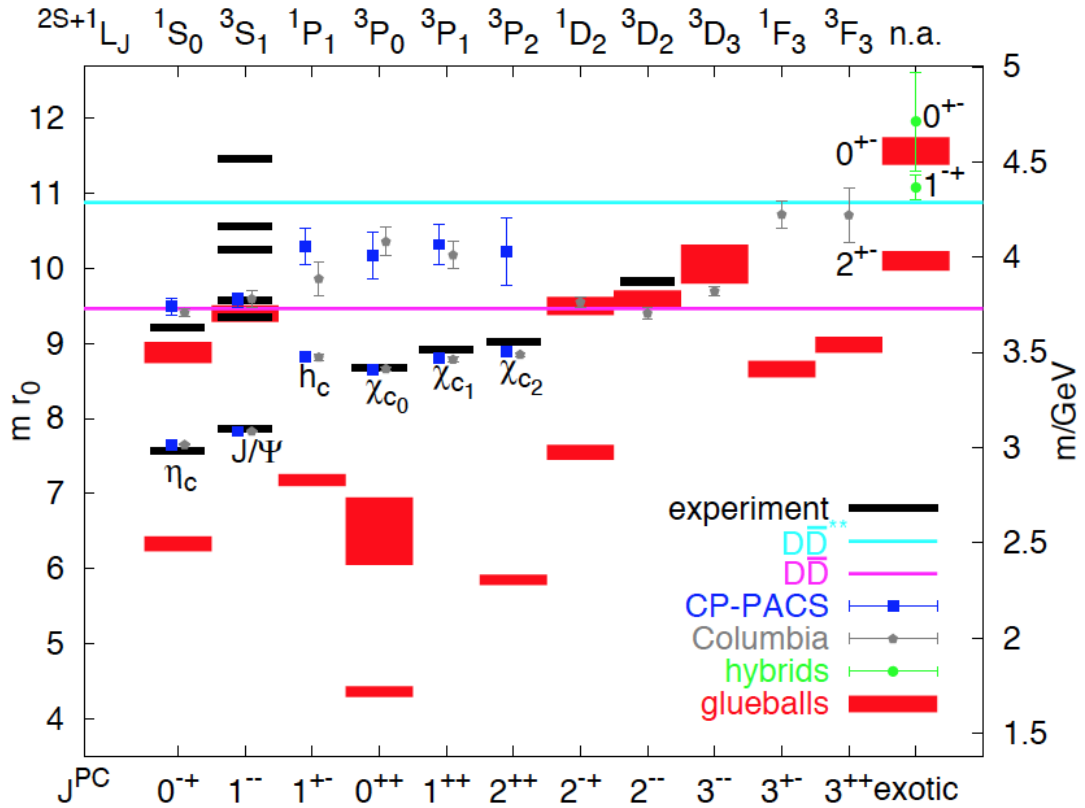


Figure 1.5: Level scheme of the charmonium system including states of glueballs and hybrids [5]. CP-PACS and Columbia data are obtained by lattice QCD calculations. The $D\bar{D}^*$ -threshold and $D^*\bar{D}$ -threshold are indicated.

nism, but most of it is created by the strong interaction. Glueballs gain their mass solely by the strong interaction and are therefore an unique approach to the mass creation by the strong interaction. Exotic gluonic excitations can be distinguished from normal mesons because they are allowed to have exotic quantum numbers (e.g. $J^{PC} = 0^{--}$, $J^{PC} = 1^{-+}$, $J^{PC} = 2^{+-}$) which are forbidden for mesons because the gluons carry additional degrees of freedom. Another differentiating factor is that the decay of glueballs has to be flavour-blind because of the absence of valence quarks. At LEAR/CERN it was demonstrated by experiments with proton-antiproton annihilation that candidates for glueballs can be produced. But for those candidates a non-ambiguous identification was not possible, because they mix with the multitude of mesons. A narrow state discovered at $1500 \text{ GeV}/c^2$ with a width of 112 MeV ,

$f_0(1500)$, is considered as the best candidate for the glueball ground state ($J^{PC} = 0^{++}$). The candidate is depicted in Fig. 1.6 but the interpretation as a glueball is somewhat difficult. It mixes with nearby light meson states leading in a non-flavour

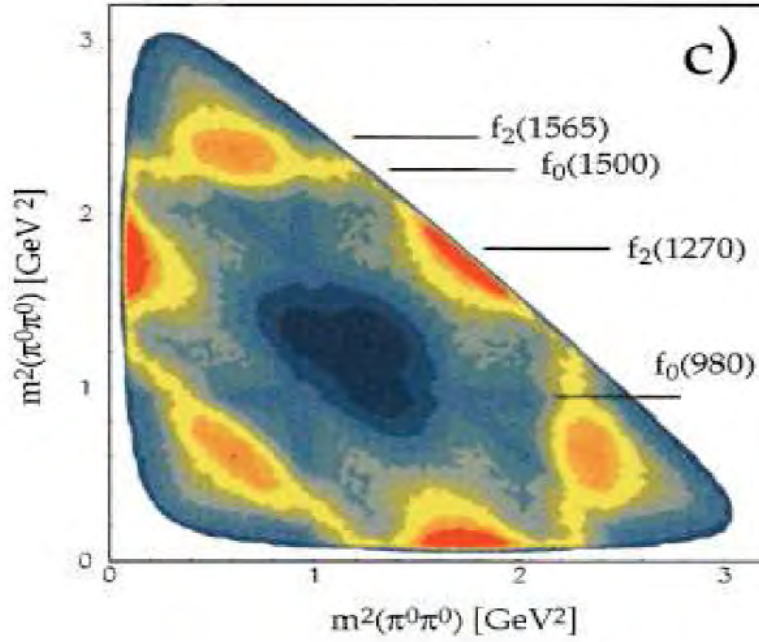


Figure 1.6: $\bar{p}p \rightarrow \pi_0\pi_0\pi_0$ Dalitz plot for the glueball candidate $f_0(1500)$ discovered in Crystal Barrel [7].

blind decay. However, until now the search for exotic excitations was mostly limited to the mass region. In the mass regime from $2 - 5 \text{ GeV}/c^2$, where calculations agree on exotic excitations with excluded mixing with charmonium states, $\bar{\text{P}}\text{ANDA}$ will be able to give an experimental identification. In principle, it will be possible to investigate also presently unknown heavier glueballs with masses around the $D\bar{D}$ -threshold, multiquarks or mesic excitations of $q\bar{q}$ -states. A candidate for the latter is the $X(3872)$ ($J^{PC} = 1^{++}$) with so far only an upper limit to the width and with a resolution in the order of a few MeV measured at B-factories. $\bar{\text{P}}\text{ANDA}$ simulations, depicted in Fig. 1.7, show that due to the sensitivity of $\bar{\text{P}}\text{ANDA}$ to the intrinsic line shape, the resolution of the width can be expected to be an order of magnitude better. The $\bar{\text{P}}\text{ANDA}$ EMC will be an important tool in the search for exotic excitations, whose benchmark channels are, e.g. for the charmonium hybrid state $\tilde{\eta}_{c1}$, decaying

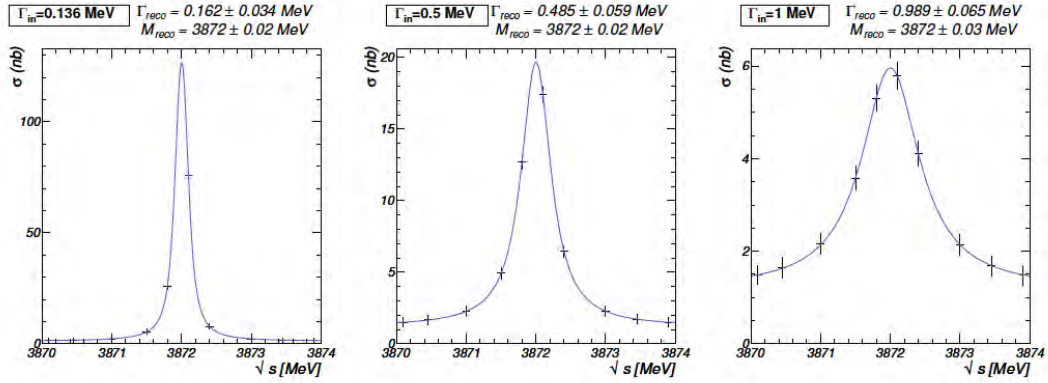


Figure 1.7: \bar{P} ANDA reconstruction of $X(3872)$ mass and width for various input widths (simulation) [8].

via lower lying charmonium states

$$\bar{p}p \rightarrow \tilde{\eta}_{c1}\eta \rightarrow \chi_{c1}\pi_0\pi_0\eta \quad (1.1)$$

or via open charm

$$\bar{p}p \rightarrow \tilde{\eta}_{c1}\eta \rightarrow D^0\bar{D}^{*0}\eta. \quad (1.2)$$

Only the EMC will be a suitable detector system in order to detect the numerous photons resulting from the neutral mesons in both decays.

Heavy baryons

The study and understanding of the excitation spectra of baryons is one of the major goals of non-perturbative QCD. The collected amount of data referring to the nucleon is sufficient, but the agreement with different theoretical quark model predictions is poor. Opposite to that, there is a very scarce data bank concerning strange and charmed baryons because the additional flavor content adds a degree of freedom. \bar{P} ANDA is able to fill the gap in the strange sector because the full Ξ^- - and Ω^- -spectra of baryon antibaryon pairs is accessible in the final state of inelastic antiproton-proton-annihilation. The cross sections for $\bar{p}p \rightarrow \Xi\bar{\Xi}$ in the order of $\approx \mu\text{b}$ and for $\bar{p}p \rightarrow \Omega\bar{\Omega}$

in the order of $\approx 0.03 - 0.1 \mu\text{b}$ [9] are rather large. In particular Ξ resonances can be produced in large abundance and with a narrower width than nucleon or Δ resonances which results in a promising discovery potential. In addition, the versatility of the $\bar{\text{P}}\text{ANDA}$ detector, like the almost 4π acceptance, sufficient resolution and precise **Particle IDentification** (PID) and tracking system, gives a unique tool to reconstruct the displayed decay vertices. Hence, $\bar{\text{P}}\text{ANDA}$ is a unique experiment in baryon spectroscopy beyond nucleon and Δ resonances.

1.1.2 Hadron structure experiments

The measurement of the form factors in the space-like region ($q^2 < 0$) and in the time-like region ($q^2 > 0$) yields a direct observation of the electromagnetic structure of the nucleon brought by the strong interaction. In the Breit frame, space-like electric G_E and magnetic G_M form factors are interpreted as the Fourier transform of the spatial charge and magnetization distribution. The time-like factor represents the frequency spectrum of the electromagnetic response of the nucleon. The space-like electromagnetic form factor is well explored, but in antiproton-proton-annihilations it is possible to measure the not explored time-like form factor above the kinematic threshold of $q^2 = 4m_p^2c^2$.

The proton electromagnetic form factor can be measured with lepton pair production. The main reaction for the cross-section measurement is $\bar{\text{p}}\text{p} \rightarrow e^+e^-/\mu^+\mu^-$ which are described by the **Generalized Parton Distributions** (GPDs) framework. For these reaction channels the EMC is essential in separating electrons and pions in the high momentum range where other PID subdetectors decrease in efficiency, since the main background channel is $\bar{\text{p}}\text{p} \rightarrow \pi^+\pi^-$. $\bar{\text{P}}\text{ANDA}$ will be able to measure the effective form factor up to $q^2 \sim 28 (\text{GeV}/c)^2$ with high precision. Furthermore, it will be possible to measure G_E and G_M individually as well as their ratio for which previous experiments have not collected a statistical sufficient data sample in this transferred momentum range. A transverse polarized proton target can give access to the relative phase of the proton time-like form factors. Even the proton form factors in the "unphysical region" $0 < q^2 < 4m_p^2c^2$ are possible to measure with $\bar{\text{p}}\text{p} \rightarrow e^+e^-\pi^0$.

Another possible study of electromagnetic interactions at $\bar{\text{P}}\text{ANDA}$ is the measurement

of **T**ransition **D**istribution **A**mplitudes (TDAs) with meson production in proton-antiproton-annihilation. In addition, recent studies allowed to describe hard exclusive antiproton-proton-annihilation processes like $\bar{p}p \rightarrow \gamma\gamma/\pi^0\gamma$ in terms of GPDs, which can be treated with handbag models at $\bar{\text{P}}\text{ANDA}$. For the measurement of these processes in dependence of the Mandelstam variables s and t , a good performance of the EMC is important as well.

$\bar{\text{P}}\text{ANDA}$ will also join the Drell-Yan-physics program with the evaluation of three of the most hunted **P**arton **D**istribution **F**unctions (PDFs) in a kinematical region where the valence contributions are expected to be dominant. With the Drell-Yan processes, where quark and antiquark annihilate to form a lepton pair via a virtual photon, the quark transverse momentum distribution as well as the spectral functions of quarks bound in nucleons can be accessed.

Further details concerning hadron structure experiment at $\bar{\text{P}}\text{ANDA}$ can be found in [10, 11].

1.1.3 Hadronic interaction experiments

Hadrons in matter

The in-medium properties of light quark mesons have been investigated both experimentally and theoretically in proton-, photon- or nucleus-nucleus collisions. The mass of the hadrons can be modified by the medium they are created in because of spontaneous chiral symmetry breaking. A chiral dynamic and partial restoration of chiral symmetry in a hadronic medium lead to the modification. Further, the in-medium widths of hadrons become larger, since more decay channels become available. $\bar{\text{P}}\text{ANDA}$ will be able to study a cold implantation of heavy quarks through antiproton-nucleus collisions with a unique antiproton energy of 3.5 – 4.5 GeV. This provides an insight into in-medium modifications of open-charm and charmonium states. In particular one expects a mass splitting between D and \bar{D} of about 100 MeV. Experimentally a cross section enhancement should be visible via sub-threshold production of charmed mesons. Additionally, a shift of the $D\bar{D}$ -threshold should result in a larger width going along with more decay channels.

Hypernuclear studies

A hypernucleus is a system where a nucleon of a nucleus is substituted by a baryon containing strange quarks, the so-called hyperon. Introducing strangeness into the nucleus adds a third dimension to the nuclear chart. A hyperon in a nucleus is able to access a large variety of nuclear states not available to protons or neutrons, since it is not affected by the Pauli exclusion principle. Thus, hyper-nuclei are an unique and useful tool to study the structure of nuclei. In addition, the properties of the nuclei can be investigated. In particular, level schemes and decay spectra of hypernuclear can give access to baryon-baryon interactions, weak decays, multi-strange atoms and exotic quark states. One has to notice that a dedicated configuration of the experimental setup of the $\overline{\text{P}}\text{ANDA}$ detector has to be used in order to measure the key channel $\bar{p}p \rightarrow \Xi^- \bar{\Xi}^+$ in the hypernuclear sector. Details can be found in [12].

1.2 $\bar{\text{P}}\text{ANDA}$ Detector

The $\bar{\text{P}}\text{ANDA}$ detector will be a multi-purpose detector able to detect a large variety of different particles enabling the manifold physics program described in the previous section. The state-of-the-art detector will perform precision measurements to analyze the final state particles produced by colliding an antiproton beam with different locally fixed targets. An advanced particle identification system consisting of charged particle tracking together with a high-resolution EMC offers the detection from charged leptons and mesons to neutral particles like photons and neutrons. In principle, the detector consists of two almost azimuthally symmetric units, the Target Spectrometer (TS) and the Forward Spectrometer (FS), achieving an almost full coverage of the solid angle. The layout of the $\bar{\text{P}}\text{ANDA}$ detector with all foreseen subdetector systems is depicted in Fig. 1.8. More detailed information on the subdetector systems are given in the following sections.

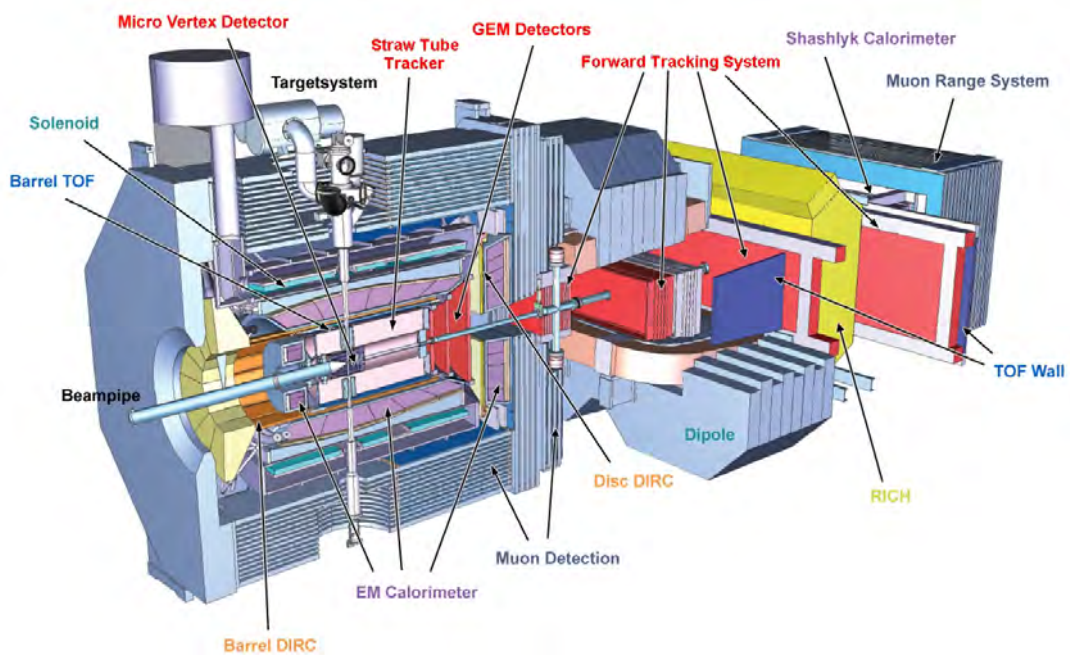


Figure 1.8: Layout of the $\bar{\text{P}}\text{ANDA}$ detector with indicated subdetector systems.

1.2.1 Target spectrometer

The target spectrometer, whose layout is depicted in Fig. 1.9, surrounds the interaction point and covers the detection of particles emitted from the interaction point with a larger polar angle than 10° and 5° for the horizontal and vertical direction, respectively. The operational area of the target spectrometer is permeated by a 2 T solenoidal magnetic field. However, most of the particles are kinematically boosted in forward direction with small polar angle and therefore not detected by the target spectrometer. But those particles are detected with the forward spectrometer, which will be described in Sec. 1.2.2

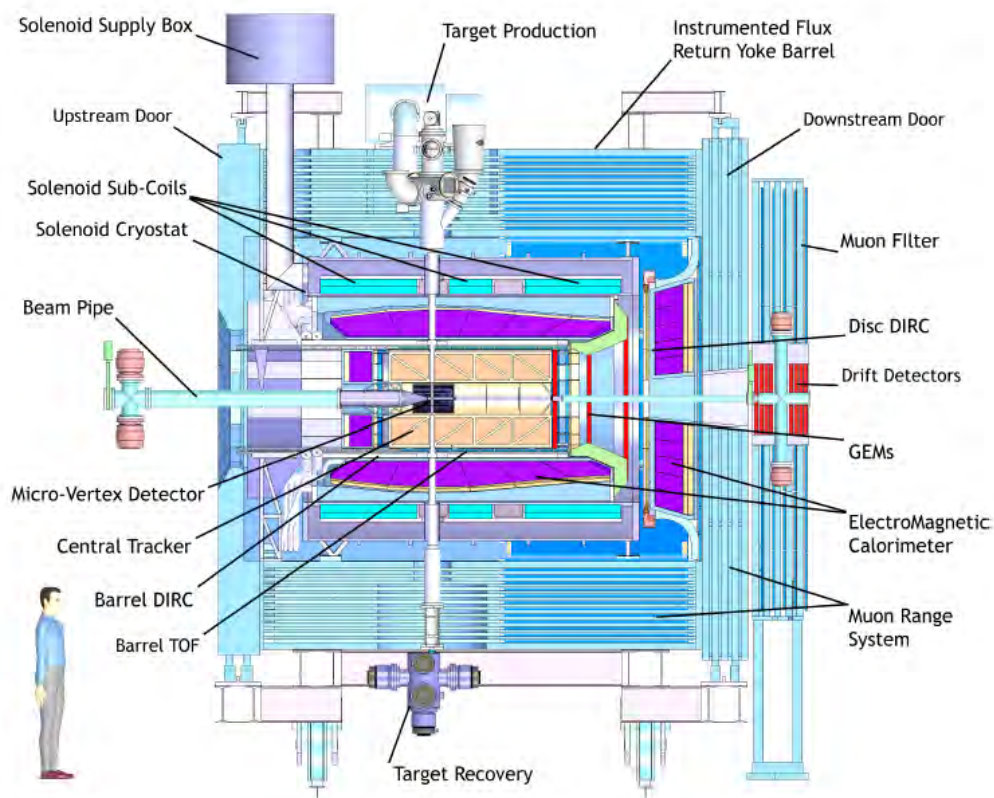


Figure 1.9: Layout of the target spectrometer with indicated subdetector systems.

1.2.1.1 Target System

\bar{P} ANDA is a fixed target experiment where antiprotons are collided on proton targets. The technical requirements for the internal target are manifold for the purpose of providing the experiment with a target accounting for the physics program. Two technical solutions, a *cluster jet target* and a *pellet target*, have been developed to complementary cover all requirements [13]. Both options consume only little space around the interaction point which is essential for the mechanical structure of the detector and further takes the solenoidal magnet into account. In addition, the target is required to not deteriorate the vacuum around the storage ring and to be minimum obtrusive to the conserved antiproton beam in order to maintain a high luminosity beam quality. \bar{P} ANDA aims to achieve luminosities up to $2 \cdot 10^{32} \text{ cm}^{-2}\text{s}^{-1}$ implying an effective target thickness of $3.8 \cdot 10^{15}$ hydrogen atoms per square centimeter.

Cluster Jet Target A supersonic cluster jet beam is produced by the expansion of a pre-cooled gas which is injected into the vacuum with a convergent-divergent nozzle. One major advantage of the cluster jet target is the possibility to place the target production outside the solenoid. Reason for that is the high mass of the condensed gas coming along with a negligible scattering of the beam particles on residual gas which enables high target densities even several meters away from the nozzle. A typical hydrogen cluster consists of $10^3 - 10^6$ molecules. Another advantage is a homogeneous target density distribution stable in time which prohibits high instantaneous event rates. A degradation of the stored beam is minimized by the possibility to modify the density during operation. Besides a proton H_2 and a neutron D_2 target, the cluster jet target is able to prepare cluster jets of heavier gases like O_2 , N_2 , Ne, Ar, Kr and Xe.

Pellet Target The pellet target consists of a stream of frozen hydrogen microspheres (pellets) traversing the antiproton beam vertically. The pellets are produced by injecting a liquid jet in a triple point chamber through a nozzle which disintegrates the jet into droplets that freeze out after being injected into vacuum. The facility to vary the pellet size has two main advantages. On the one hand it is easier to reach

high target densities. On the other hand the individual pellets can be tracked which allows the reconstruction of the interaction point. Then again, a disadvantage of the pellet option is a possible time structure of the target. Large thickness variations appear on time scales up to some ms for the pellets. This results in a time dependent luminosity and higher instantaneous event rates.

1.2.1.2 Tracking

The reconstruction of charged particle tracks in the target spectrometer is realized with a combination of the **Micro-Vertex-Detector (MVD)** located close to the interaction point surrounded by the **Straw Tube Tracker (STT)** and three **Gas Electron Multiplier (GEM)** disks placed in the forward direction.

MVD The innermost detector is designed to measure charged particle hit points as close as possible to the interaction point. It will provide vertex and momentum information with high precision in combination with the other tracking detectors. Its main duty is to reconstruct primary interactions vertices for the purpose of defining the initial reaction vertex. Thereby, the MVD serves as reference for the STT. But moreover, the detector is mandatory for secondary vertices to reconstruct short lived particles from weak decays of charmed and strange hadrons like D-mesons or hyperons. In order to facilitate the requirements, a vertex resolution better than $100 \mu\text{m}$ has to be achieved. The design, as depicted in Fig. 1.10, foresees four layer barrels surrounding the interaction point axially symmetric to the beam direction and six disks in the forward direction. The inner parts are equipped with so-called hybrid pixel detectors, whereas the outer parts consist of double-sided silicon strip detectors. Since the MVD will be the detector with the maximum flux of particles, it features a high rate capability and necessary radiation tolerance [14].

STT The **Straw Tube Tracker** [15], whose layout is shown in Fig. 1.11, is the central tracker of the $\bar{\text{P}}\text{ANDA}$ target spectrometer, consisting of 4636 individual straw tube modules. Each module is basically a drift chamber with cylindrical geometry. A module consists of an aluminized Mylar cylinder with 10 mm inner diameter, the

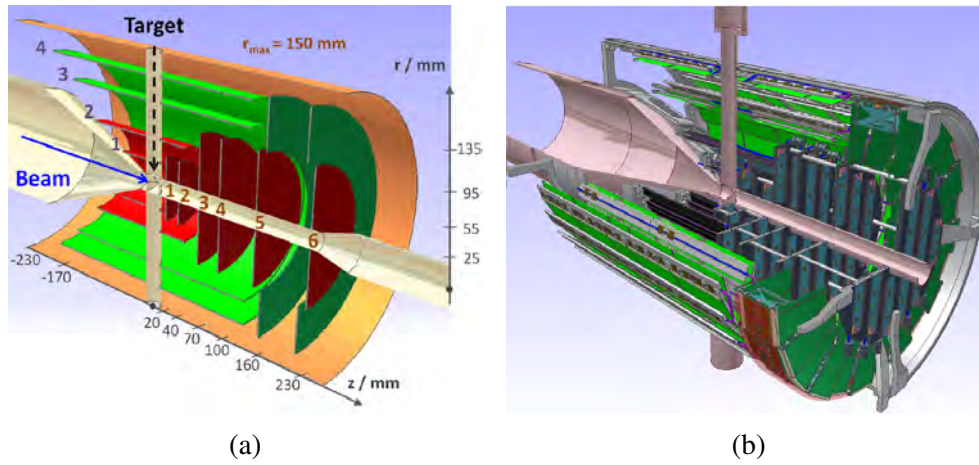


Figure 1.10: Basic MVD layout (a) with silicon hybrid detectors in red and double-sided silicon strip detectors in green and a CAD drawing (b).

cathode, and a $20 \mu\text{m}$ thick gold-plated tungsten-rhenium wire mounded in the cylinder axis, the anode. The tubes are filled with a gas mixture of over pressured Ar and 10% CO_2 , with the latter as quencher, allowing to operate the tube as a proportional counter. The charge collected in a tube defines the energy loss of a particle traversing the gas volume. In addition, the position along the wire can be determined by the signal delay. Since all tubes are stacked together in two half shells consisting of 27 layers, the position of a responding tube in the transverse plane of the STT relates to the particle position. Thereby, a position resolution better than $150 \mu\text{m}$ in the transverse plane can be achieved. The longitudinal coordinate is determined by 8 skewed layers positioned with a stereo angle of $\pm 2.9^\circ$ with respect to the other tubes. One can reach a longitudinal position resolution of about 3 mm. The STT covers a polar angle from 10° to 140° at a low average material budget of 1.23% of a radiation length X_0 . Polar angles between 3° and 20° are covered with the GEM detector which will be described in the next paragraph.

GEM The geometrical coverage of the STT will be complemented with three large-area planar gaseous micro-pattern detectors based on GEM foils as amplification stages. They will be positioned downstream from the interaction point in distances of 1.17 m, 1.53 m and 1.89 m with external radii increasing along the beam axis as

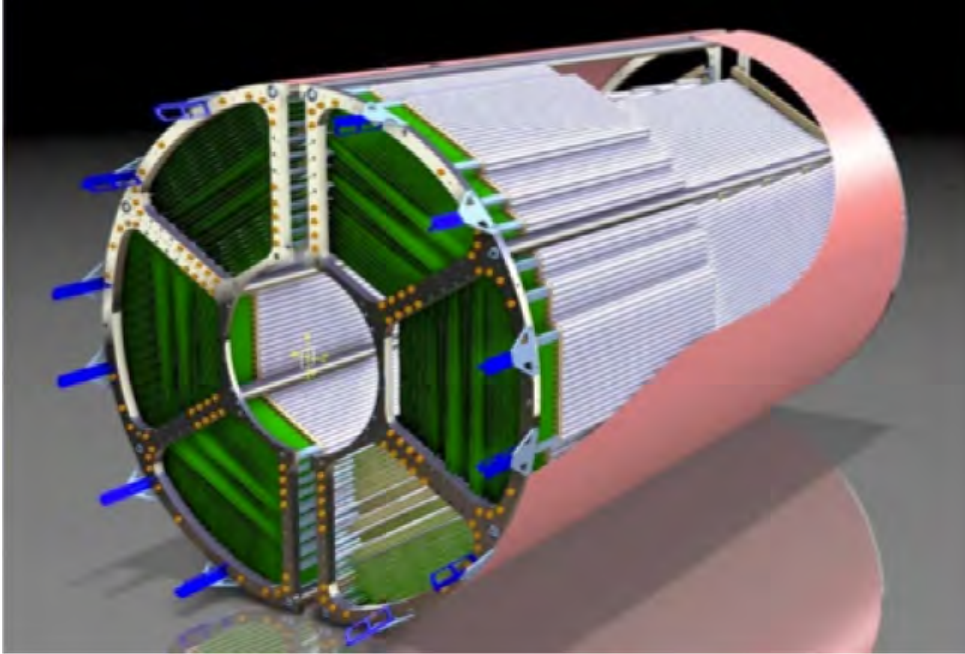


Figure 1.11: Layout of the STT detector [15].

depicted in Fig. 1.12a. The gas filled disks consist of a double-sided read-out pad plane for charge collection, two stacks with three actual GEM foils each, a cathode plane and a window foil per side (see Fig. 1.12b). Each disk will have four projections to resolve ambiguities of multiple hits on one plane which results in a position resolution better than $100 \mu\text{m}$. The advantage of a GEM detector is a more flexible geometry and a higher rate capability compared to conventional drift chambers.

1.2.1.3 Particle Identification

One substantial requirement for the $\bar{\text{P}}\text{ANDA}$ detector is the efficient identification of particles of different species in a large momentum range. For this reason $\bar{\text{P}}\text{ANDA}$ is making use of several dedicated PID systems and the target spectrometer in particular foresees a number of detectors aiming to provide the identification of particles. Particles with momenta above $1 \text{ GeV}/c$ are identified with a barrel and an end-cap disk type **D**etection of **I**nternally **R**eflected **C**herenkov **L**ight (DIRC) detector, slow particles in the target region with a **T**ime **O**f **F**light (TOF) system and muons by using

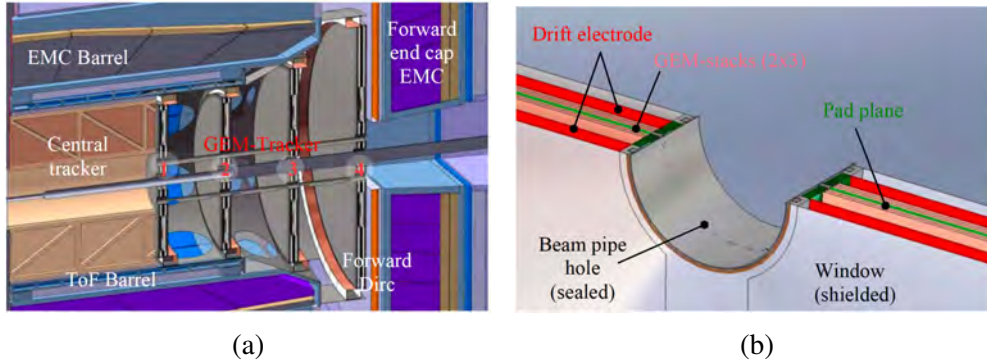


Figure 1.12: Position of the GEM disks downstream from the interaction point (a) and internal structure of a single disk (b) [16].

a **Muon Range System (MRS)**, combined with a **Ring Imaging Cherenkov Counter (RICH)** detector in the forward spectrometer for hadrons in forward direction.

DIRC detectors The barrel and the end-cap type DIRC detectors will provide most of the PID. The barrel DIRC features a 3σ pion Kaon (π/K) separation for the momentum range $0.5 - 3.5 \text{ GeV}/c$, whereas the end-cap disk DIRC offers a 3σ π/K separation for momentum up to $4 \text{ GeV}/c$. The barrel DIRC surrounds the beam at a distance of 48 cm and covers polar angles from 22° to 140° , while smaller angles between 5° and 22° are covered with the end-cap disk DIRC.

The basic principle of both detectors, which is based on the detection of Cherenkov light, is schematically shown in Fig. 1.13. Charged particles with velocity $\beta = v/c$ traversing a radiator with refractive index n emit Cherenkov photons on a cone with the half opening angle defined by

$$\cos \theta_C = \frac{1}{\beta n}. \quad (1.3)$$

The magnitude of Cherenkov angle θ_C is conserved during internal reflections of propagating photons through the radiator. The photons exit the radiator bars through optical focusing elements into an expansion volume which widens the initially small angular differences and images the photons on a photon detector array. The photon detector array measures the spatial coordinate and the arrival-time of photons.

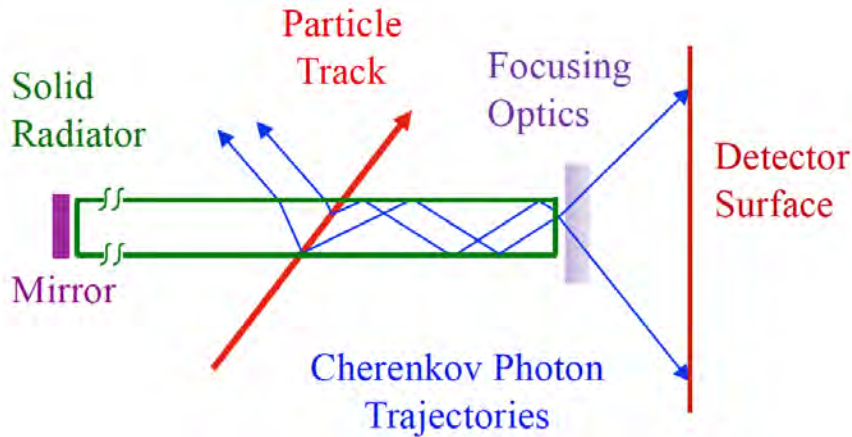


Figure 1.13: Basic principle of the detection based on Cherenkov light [17].

Hence, it defines the Cherenkov angle θ_C and the time of propagation of individual Cherenkov photons. According to Eq. 1.3 the Cherenkov angle is equivalent to the particle velocity. Thus, at known momentum the initial charged particle can be identified.

The design of the \bar{P} ANDA barrel DIRC, which is depicted in Fig. 1.14, is inspired by the BaBar-DIRC but with important improvements. A new lens system was developed for the focusing optics. It enables a better Cherenkov angle resolution which in the end amounts to about 8–9 mrad. In addition, a new compact array of microchannel plate **PhotoMultiplier Tubes (PMTs)** with up to $15 \cdot 10^3$ channels is considered as photon detector array. This array has to fulfill challenging requirements according to the experimental conditions. On the one hand, the photodetector array has to have a small expansion region and on the other hand the photon detectors themselves have to be fast, long living, high rate capable, operable in a magnetic field and minimum sensitive to the background.

Another advantage of the DIRC detectors has to be the moderate and uniform amount of material in front of the EMC. The EMC, which will be right next behind the barrel DIRC, is directly influenced by the radiator material since it adds substantially to the material budget before the EMC leading to conversion of photons. Both DIRC detectors use a radiator either in form of thin slabs in case of the barrel or a disc for the end-cap. In total 80 slabs of 1.7 cm thickness, 3.3 cm width and 250 cm length are foreseen for the barrel, while for the end-cap one octagonal disc of 2 cm thickness

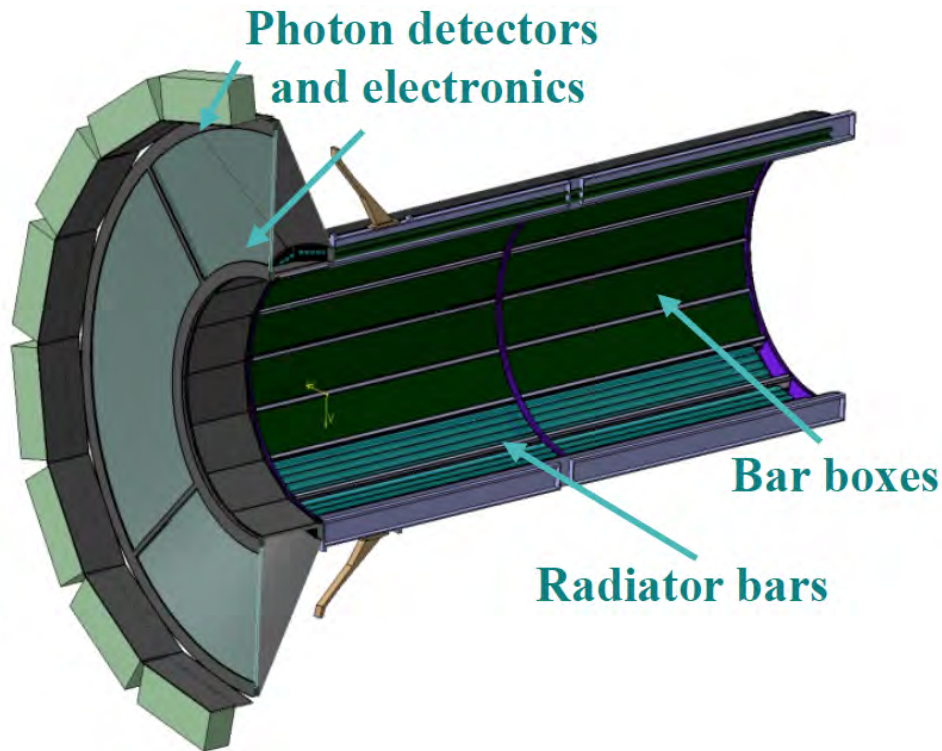


Figure 1.14: Layout of the Barrel DIRC.

and 2 m diameter is used. The chosen radiator material is fused silica which has the advantage of compactness due to higher photon yield, larger Cherenkov angles and lower threshold momentum compared to conventional gas-filled RICH detectors. But these advantages have to be counterbalanced with a higher photon absorption with a radiation length of $X_0 = 12.295$ cm. The influence of dead material, like fused silica, on the resolution and efficiency of the barrel EMC was investigated in a dedicated experiment with an EMC prototype and will be presented in chapter 2.4.

Time-of-flight system The \bar{P} ANDA TOF system [18] will consist of a barrel TOF detector, or a so-called **Scintillator Tile** (SciTil) Hodoscope, located in between the barrel DIRC and the EMC, and a TOF wall in forward direction. Its main purposes are the identification of slow charged particles with a momentum below 700 MeV/c complementing the DIRC detector, a precise determination of a timing signal for charged particles to prohibit event mixing and a relative time-of-flight measurement.

This will be achieved with a required time resolution of $\sigma < 100$ ps. Under these conditions a 3σ π/K separation as well as a 3σ kaon/proton (K/p) separation should be possible. Relating to the EMC, the SciTil hodoscope can be used to identify photon conversion in front of the EMC. Thereby, it is another requirement to use a minimum of material. In particular, it is foreseen to use less than 2% of a radiation length and less than 2 cm of space in radial direction. The hodoscope will be composed of 5760 plastic scintillator tiles with a size of $30 \times 30 \times 5$ mm³ read out with directly attached **Silicion PhotoMultipliers** (SiPMs).

EMC The EMC will be located next to the DIRC detectors and TOF system. It will consist of three parts: Barrel EMC, Forward and Backward Endcap, which are named with respect to the alignment in beam direction from the interaction point. The schematic layout is shown in Fig. 1.15. A detailed description can be found in Sec. 1.3.

Magnet All detectors within the target spectrometer are enclosed by a superconducting solenoid with an external iron return yoke [19]. It is designed to provide a homogenous 2 T magnetic field with field variations below 2% over a length of about 4 m and a diameter of about 1.9 m of a warm bore. A whole for the target feed pipe or the detector access are an additional requirement which compel the solenoid to be divided in three parts. In addition, the return yoke is used in combination with **Mini Drift Tubes** (MDTs) to detect muons. It enhances the quality of the magnetic field and serves as shielding for the outer world. The superconducting nature of the solenoid is enabled by a cryostat.

Muon Range System Muons are in the final state of many \bar{P} ANDA physic channels which requires an efficient muon detection system. It is foreseen to use a MRS [20] composed of a series of iron layer absorbers with interlaced layers of MDTs for muon detection. The target spectrometer features a split muon system divided into a barrel and a forward endcap. The active components of the barrel are interlaced with the iron layers of the solenoidal magnet with a granularity of 3 cm. In the forward

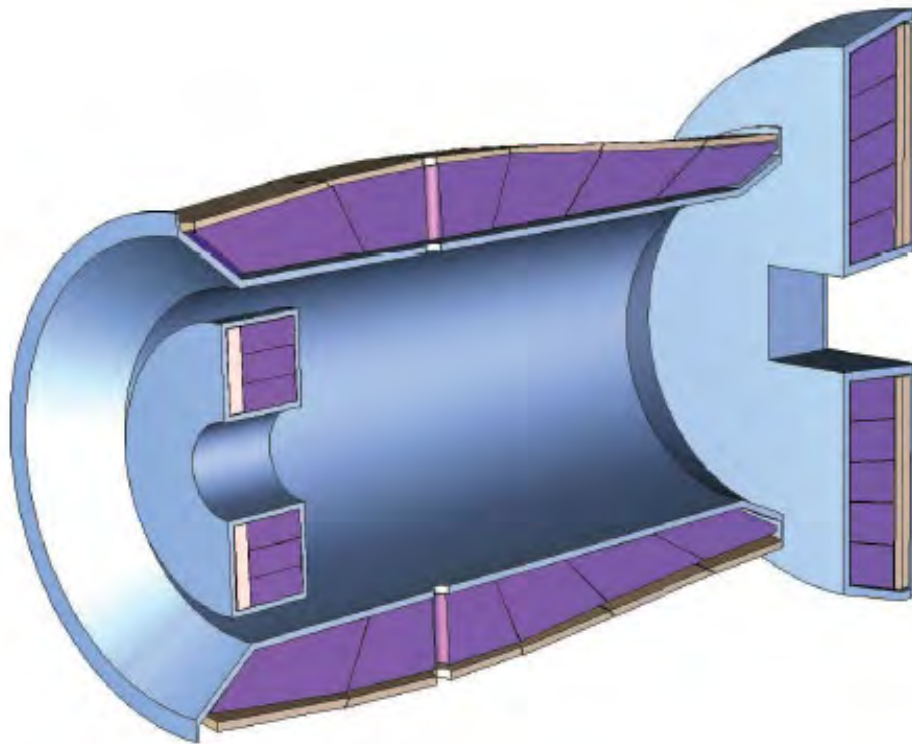


Figure 1.15: Layout of the EMC consisting of a backward endcap, Barrel calorimeter and forward endcap.

endcap, more material is needed because of higher momenta of the particles. In particular, five 6 cm thick iron layers in combination with corresponding detection layer are used. The absorber depth can be increased even further by an additional Muon Filter (MF) with similar mechanical design as the MRS-endcap.

1.2.2 Forward spectrometer

The forward spectrometer, depicted in Fig. 1.16, is designed to measure particles with polar angles below 5° vertically and 10° horizontally. A dipole magnet with a 2 Tm bending power will be the basis for analyzing high momentum particles. But the forward spectrometer will be used to measure both charged and neutral particles with a combination of a forward tracker, a calorimeter, muon detectors and PID detectors.

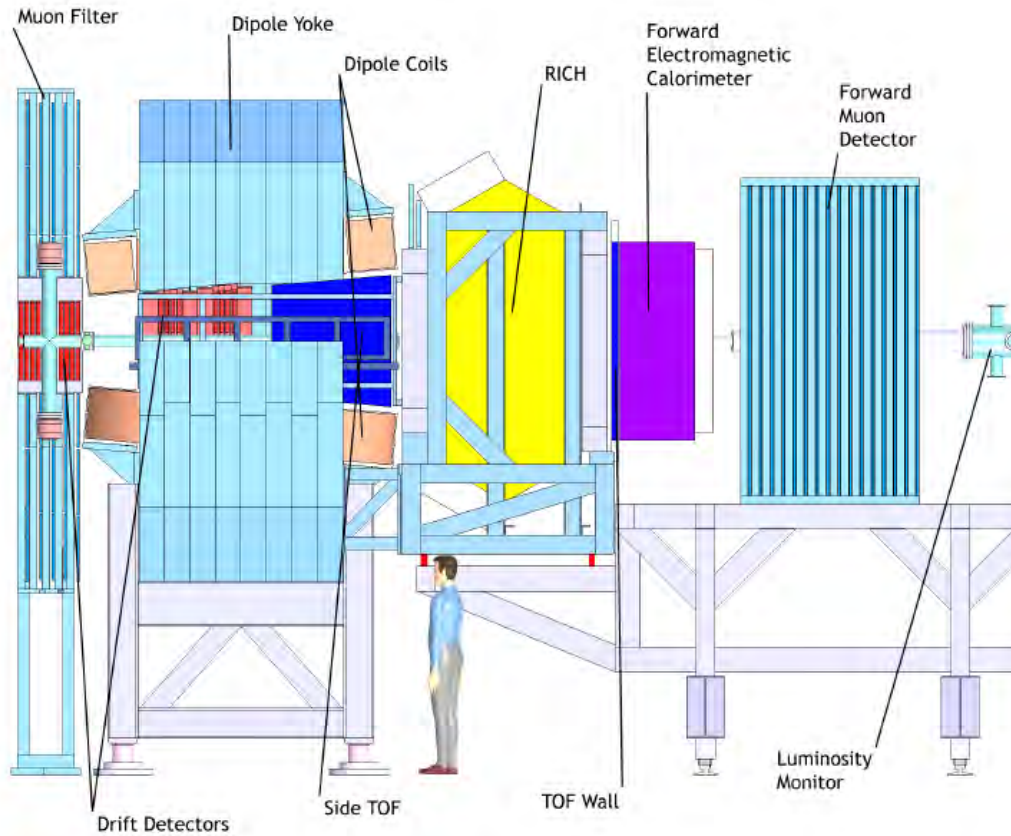


Figure 1.16: Layout of the forward spectrometer with indicated subdetector systems.

1.2.2.1 Tracking

Forward Tracker The so-called forward tracker features straw tubes with a planar arrangement. The tubes are used for momentum reconstruction of charged particles deflected by the magnetic field of the dipole magnet. Three pairs of planar tracking stations will be positioned respectively before, in the middle and after the dipole magnet. Each station will consist of four double-layer STT planes. Each detection layer will have a position resolution of 0.1 mm, resulting in a momentum resolution of the forward tracker better than 1%.

1.2.2.2 Particle identification

There are two dedicated detectors for particle identification in the forward spectrometer: a **Ring Imaging CHerenkov Counter (RICH)** detector and a **Time Of Flight (TOF)** wall.

RICH The detection principle of the RICH detector is based on the detection of Cherenkov light which was described for the DIRC detector in the target spectrometer. The RICH detector will consist of two radiators, silica aerogel and C_4F_{10} , with refraction indices of 1.0304 and 1.00137, respectively. It enables reliable separation of pions, kaons and protons in a wide momentum range between 2 GeV/c and 15 GeV/c. The light is focused on an array of PMTs with a system of mirrors.

TOF wall A TOF wall will be located 7 m downstream from the interaction point. It consists of plastic scintillator slabs which are read-out from both sides with PMTs. The expected time resolution of about 50 ps fulfills the requirements to use the TOF detector as a stop counter. A 3σ π/K separation as well as a 3σ K/p separation up to momenta of several GeV/c will be possible.

1.2.2.3 Shashlik Calorimeter

The forward calorimeter is foreseen as a Shashlyk-type calorimeter [21] which will be used to detect photons and electrons in the forward region covering the most forward angular range up to 5° in the vertical and 10° in the horizontal direction. The complete calorimeter will consist of 378 modules each consisting of a sandwich of 380 layers of lead absorber plates and 1.5 mm thick plastic scintillator tiles which corresponds to a total thickness of twenty radiation lengths. The light produced in a scintillator plate is matched to the range of highest sensitivity of the photo sensor cathode by wave length shifter. In addition, the module is composed of four optically isolated cells with a cross section of 5.5×5.5 cm² each. The design of such a Shashlyk-EMC module is depicted in Fig. 1.17. It is similar to operating Shashlyk calorimeters at other experiments. According to these, an energy resolution of $\frac{4\%}{\sqrt{E[\text{GeV}]}}$ in the GeV

range is feasible and hence required. Latest prototype tests have shown that a statistic term of $\frac{3.54\%}{\sqrt{E[\text{GeV}]}}$ can be achieved [22].

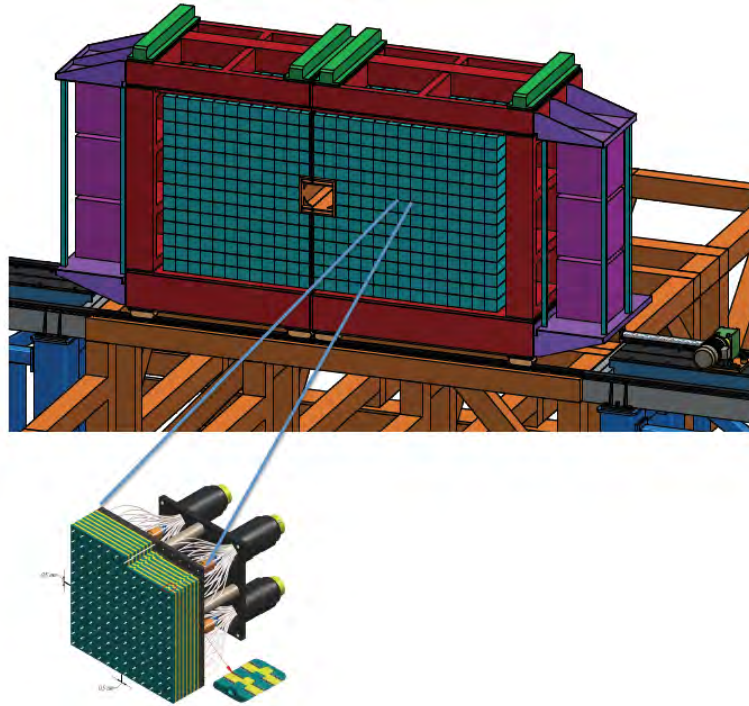


Figure 1.17: Layout of the $\bar{\text{P}}\text{ANDA}$ shashlyk EMC with a zoom on one detector module [21].

1.2.2.4 Muon Detector

A muon detector positioned 9 m downstream from the interaction point will be complementing the MRS of the target spectrometer. It is based on the the same principle and features a 6 cm thickness of the absorbing layers due to the high momenta of the particles. It can be used to distinguish between muons and pions and as a hadron calorimeter for stopped particles, but with a low resolution.

1.2.3 Luminosity Detector

The absolute luminosity at \bar{P} ANDA will be determined by measuring the elastic scattering of the antiproton beam with the protons of the target in the region of interference between the Coulomb and the nuclear contribution at a small scattering angle. For this purpose, a dedicated luminosity detector will be installed at the very end of the forward spectrometer. The layout is shown in Fig. 1.18. It will consist of four layers of **H**igh**V**oltage-**M**onolithic **A**ctive **P**ixel **S**ensor (HV-MAPS) with $80 \times 80 \mu\text{m}^2$ pixel size on a diamond wafer, placed in vacuum and separated up to 20 cm to the beam pipe.

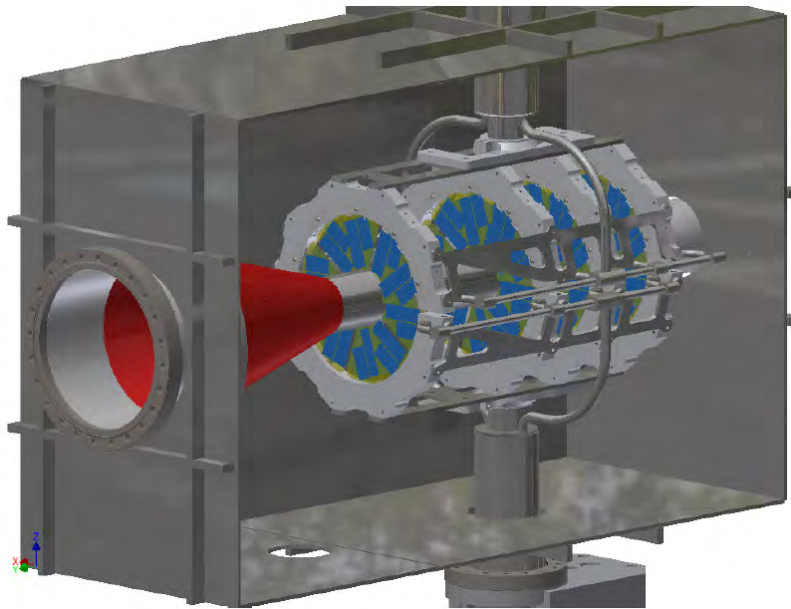


Figure 1.18: Design of the luminosity detector.

1.3 Electromagnetic Calorimeter

A calorimeter is one of the most crucial components of almost any experiment in high energy particle physics as well as in \bar{P} ANDA and it is essential for the detection of electromagnetic probes in various physics channels. Calorimeters exist in a wide variety and the choice of technology and detector parameters for the particular application is non-trivial. The requirements for the \bar{P} ANDA EMC and the technical solution will be described later in this chapter. First, the fundamental processes when a particle traverses matter will be discussed. In particular, an understanding of the detection of radiation and the measurement of its energy with an EMC will be given. The processes are split in two categories, interaction of charged particles and interaction of photons with matter, which will be discussed separately.

1.3.1 Interaction of Charged Particles with Matter

Charged particles change their energy and direction in matter. There are several processes contributing to these effects. All of them are based on the same phenomena which is the electromagnetic interaction with electrons and nuclei. The electromagnetic interaction is responsible for elastic and inelastic particle scattering, ionization and excitation of atoms and bremsstrahlung. Cherenkov and transition radiation are among those processes as well but result in a negligible energy loss and do not change the particles direction. On the contrary, ionization is the dominating process with the main contribution to the energy loss for heavy charged particles. For electrons and positrons bremsstrahlung comes into play as dominating process. The heavier the particle, the more crucial is the energy loss due to inelastic scattering. In such a hard collision a certain fraction of the kinetic energy is transferred causing an ionization. Thereby so-called δ electrons are produced. These are free electrons which are able to ionize further atoms. The energy loss by a heavy spinless particle can be determined by the Bethe-Bloch equation [23]. Considering a particle with atomic number Z , velocity $v = \beta c$ and kinetic energy ϵ , the energy loss is given by

$$-\left(\frac{dE}{dx}\right)_{\text{ion}} = K z^2 \frac{Z}{A} \frac{1}{\beta^2} \left(\frac{1}{2} \ln \frac{2m_e c^2 \beta^2 \gamma^2 \epsilon_{\text{max}}}{I^2} - \beta^2 - \frac{\delta}{2} \right), \quad (1.4)$$

with $K = 4\pi N_A r_e^2 m_e c^2 = 0.307075 \text{ MeV}/(\text{g}/\text{cm}^2)$, $\gamma = E/Mc^2$ and where I is the average ionization potential and δ a correction on the density-effect. In this notation z is the charge in units of the electron charge, A is the atomic mass and M the mass of the incoming particle, while r_e is the classical electron radius and m_e is the electrons mass. The parameter I is correlated with Z and in the order of eV, while the parameter δ can be considered as extension to the original Bethe-Bloch equation and gets dominant for very low and relativistic energies.

For different materials the ionization energy loss rate as function of the relativistic particle velocity is shown in Fig. 1.19. For low energies the various dependences

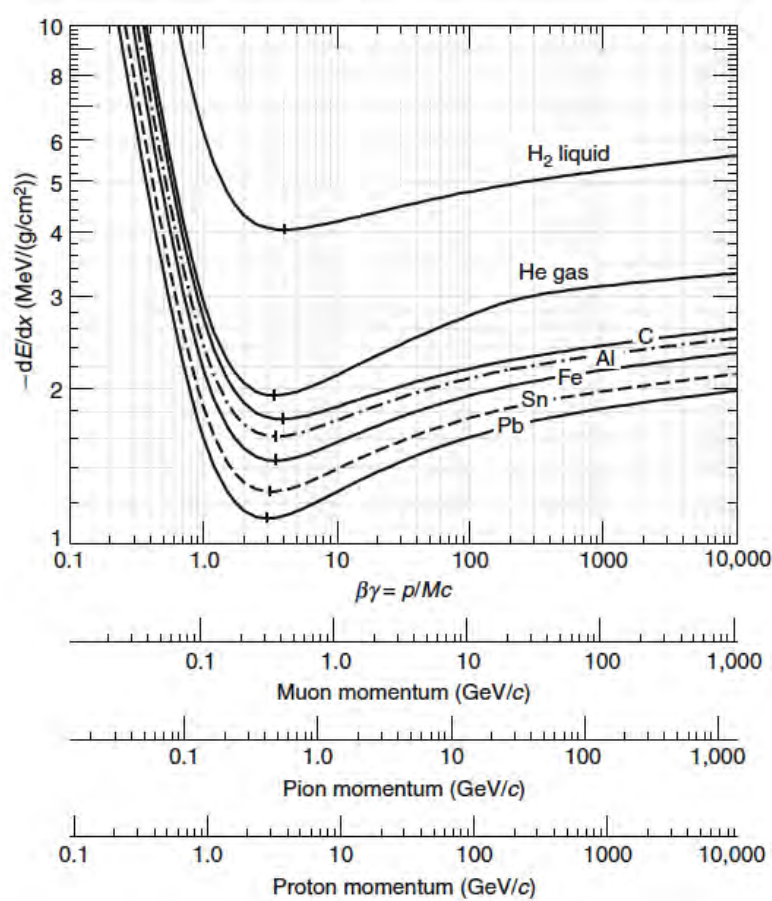


Figure 1.19: Ionization energy-loss rate in different materials [24].

have a common fast increase, as $1/\beta^2$. In the region around $\beta\gamma \approx 3$ the energy-loss rate has a wide minimum and increases slowly from there. Particles kinemati-

cally located near the minimum of the energy-loss rate are called **Minimum Ionizing Particles (MIPs)**. The ionization losses of MIPs are almost the same for most materials and within a range between $1 - 2 \text{ MeV}/(\text{g}/\text{cm}^2)$. This is the reason why usually large absorbers with high densities are mandatory to stop MIPs. A well-known example for MIPs are cosmic muons which penetrate a large amount of material.

As already mentioned, the emission of Bremsstrahlung gives a significant contribution to the energy loss for light charged particles like electrons and positrons. This process plays an important role in the development of an electromagnetic shower which will be discussed later. The contribution to the energy loss is only relevant for electrons and positrons because the cross section of bremsstrahlung is dependent on the mass, as $1/m^2$. The radiation emission energy loss of an electron or positrons with a mass m_e at an initial energy E_0 is given by

$$\frac{dE}{dx} = N E_0 \Phi_{\text{rad}}, \quad (1.5)$$

with

$$\Phi_{\text{rad}} = \begin{cases} 4Z^2 r_e^2 \alpha \left(\ln \frac{2E_0}{m_e c^2} - \frac{1}{3} - f(Z) \right) & \text{for } m_e c^2 \ll E_0 \ll 137 m_e c^2 Z^{-1/3} \\ 4Z^2 r_e^2 \alpha \left(\ln (183 Z^{-1/3}) + \frac{1}{18} - f(Z) \right) & \text{for } E_0 \gg 137 m_e c^2 Z^{-1/3} \end{cases} \quad (1.6)$$

where $\alpha = Z/137$, N is the number of atoms per cm^3 , Z is the atomic number of the material and $f(Z)$ is a correction function which takes into account the Coulomb interaction of the emitting electron in the field of the nucleus. Furthermore, Eq. 2.5 distinguishes two cases: no screening and a completely screened electric field of the nucleus by the surrounding bound electrons. In general, bremsstrahlung depends on the screening caused by atomic electrons because it occurs in the Coulomb field of the nucleus. But bremsstrahlung can also occur in the field of atomic electrons. In that case the term Z^2 in Eq. 2.5 has to be replaced by $Z(Z + 1)$.

The radiation length X_0 characterizes radiation losses and gives a more convenient

way to formulate Eq. 1.5. In terms of X_0 the equation can be expressed as

$$-\left(\frac{dE}{dx}\right)_{\text{rad}} = \frac{E}{X_0}. \quad (1.7)$$

Hence, the radiation length is defined as the mean pathlength in a layer of material after which the electron energy decreases to $1/e$ of its initial energy. It can be regarded as the natural unit of absorber thickness. Values of X_0 dependent on the material can be calculated by solving Eq. 1.7. In a common approximation [25] the radiation length is given by

$$X_0 = \frac{716.4 \text{ g/cm}^2 A}{Z(Z+1) \ln(287/\sqrt{Z})}, \quad (1.8)$$

which was found to be accurate within 2.5% for almost every material.

Most scintillator materials are mixtures or compounds for which the radiation length can be approximated by

$$X_0 = \frac{1}{\sum \rho_i X_0^i}, \quad (1.9)$$

where ρ_i is the mass fraction of the i^{th} component with its radiation length X_0^i .

A comparison of the specific radiation losses, $-(dE/dx)_{\text{rad}}$, and the ionization losses, $-(dE/dx)_{\text{ion}}$, respectively Eq. 1.7 and Eq. 1.4, reveals that at high energies the linear rise of the radiative loss dominates the logarithmic rise of the ionization loss. For absorbers with high atomic number Z the effect sticks out even more, since it contributes quadratically to specific radiation losses. The energy at which specific radiation losses and ionization losses are equal is called critical energy E_c . For solids and liquids the critical energy for electrons can be approximated [23] and is given by

$$E_c = \frac{610 \text{ MeV}}{Z + 1.24}. \quad (1.10)$$

The Cherenkov effect causes additional energy losses in a radiator via emission of coherent Cherenkov light. The effect was already discussed for a radiator such as

fused silica in the $\overline{\text{PANDA-DIRC}}$ detector (see paragraph 1.2.1.3). The effect is not negligible for the lead tungstate, PbWO_4 (PWO-II) crystals which are used in the $\overline{\text{PANDA EMC}}$. The detected energy information of a PWO-II crystal shows a small fraction originated from Cherenkov radiation. If a particle with charge $z \cdot e$ irradiates a medium, the number of photons emitted per distance can be calculated by

$$\frac{dN}{dx} = 2\pi z^2 \alpha^2 \sin^2 \theta_c \int_{\lambda_1}^{\lambda_2} \frac{1}{\lambda^2} d\lambda, \quad (1.11)$$

where the Cherenkov angle θ_c is defined by Eq. 1.3. The evaluation of the integral over the range of sensitivity of a typical **Avalanche Photo Diode** (APD) used in the $\overline{\text{PANDA EMC}}$ leads to

$$\left. \frac{dN}{dx} \right|_{350 \text{ nm}}^{850 \text{ nm}} = 771 \cdot z^2 \sin^2 \theta_c \frac{\text{photons}}{\text{cm}}. \quad (1.12)$$

Hence, in case of PWO-II, a rather small number of only a few hundred of photons per cm originate from Cherenkov radiation. This corresponds to approximately a fifth of the overall light output at $+18^\circ\text{C}$ for a MIP in PWO-II.

Furthermore, the energy loss due to elastic scattering on nuclei is negligible low as well. In that case, the mass of the absorber atom is much higher than the mass of the incoming particle which results in low momenta transfer. The contribution becomes only relevant at very low velocities $\beta < 10^{-3}$ and is important for the detection of neutrons.

Above all, a nuclear reaction can occur, if a particle is able to overcome the Coulomb barrier. However, the cross section for a nuclear reaction is generally small compared to electromagnetic cross sections. Therefore, the mean free pathlength of the nuclear reaction Λ_{NR} , which is defined as the distance after which the number of particles is reduced by $1/e$ because of nuclear reactions, is larger than the electromagnetic radiation length X_0 . For this reason, electromagnetic processes are dominant.

1.3.2 Interaction of Photons with Matter

Photons interacting with electrons or nuclei change significantly their energy and direction in contrast to charged particles. A photon beam is attenuated exponentially according to

$$I = I_0 \cdot e^{-\mu x} , \quad (1.13)$$

where I_0 is the primary intensity, x the thickness of the material and μ the mass attenuation coefficient. The latter is defined by

$$\mu = \frac{N_A \cdot \rho}{A} \cdot \sigma , \quad (1.14)$$

where N_A is Avogadro's number, ρ the density of the material, A the mass number and σ , defined by

$$\sigma = \sigma_{Photo} + Z \cdot \sigma_{Compton} + \sigma_{Pair} , \quad (1.15)$$

is the sum of the cross-section fragments coming from the main processes of a photon interacting with matter: Photoeffect, Comptoneffect and Pair-production. These processes are now discussed briefly.

- **Photoelectric effect:**

The photoelectric effect describes the complete absorption of an incident photon by an inner-shell electron. The electron receives the photon energy and is then ejected as a so-called photoelectron. A photoelectric effect on free electrons is prohibited due to energy and momentum conservation. The energy of the photoelectron and the electron's binding energy E_B equal the energy of the incident photon E_γ . Hence, the photoelectric effect provides information about the energy of the photon directly. The total photoabsorption cross-section is rather complicated because of the need to transfer the appropriate recoil momentum and different atomic shell effects. For energies above the K-edge it is

proportional to

$$\sigma_{Photo} \propto \frac{Z^5}{E_\gamma^{7/2}}. \quad (1.16)$$

- **Compton effect:**

In case of $E_\gamma \gg E_B$ the photon scatters inelastic on a quasi-free atomic electron. The inelastic scattering of photons in matter results in a decrease in photon energy. Following energy and momentum conservation, part of the energy is transferred to the scattering electron E_e . The electron recoils and is ejected from its atom. The rest of the energy is then taken by the scattered photon. This photon has a lower energy E'_γ , which is dependent on the scattering angle θ . The energy E'_γ is determined by the following formula:

$$E'_\gamma = \frac{E_\gamma}{1 + \epsilon \cos \Theta}, \quad (1.17)$$

where $\epsilon = \frac{E_\gamma}{m_e c^2}$.

Further, the total Compton cross section can be calculated by integration of the Klein-Nishima formula. The general dependence for $E_\gamma \gg m_e c^2$ follows

$$\sigma_{Compton} \propto Z \cdot E_\gamma^{-1}. \quad (1.18)$$

Beside Compton scattering there are two other similar processes, namely Thompson (free electron case: $E_\gamma \ll m_e c^2$) and Rayleigh or coherent scattering ($E_\gamma \ll E_B$). They are both elastic processes but not resulting in a reduced photon energy. Nevertheless, they change the direction of the incident photon. But they can mostly be neglected for high energies.

- **Pair production:**

If the incident photon energy is larger than $2m_e c^2$, it is possible to produce an electron positron pair. Due to energy and momentum conservation a recoil partner is required which can be any massive charge. Nonetheless, pair production can also occur in the field of atomic electrons. In the region $m_e c^2 \ll E_\gamma \ll 137m_e c^2 Z^{-1/3}$ screening effects are excluded and the pair production

cross section has the dependence

$$\sigma_{Pair} \propto Z^2 \cdot \ln E_\gamma . \quad (1.19)$$

In case of complete screening, $E_\gamma \gg 137m_e c^2 Z^{-1/3}$, the nucleus and atomic electrons have to be taken into account. Then the cross section for pair production amounts to

$$\sigma_{Pair} = 4\alpha r_e^2 Z^2 \left(\frac{7}{9} \ln \frac{183}{Z^{1/3}} - \frac{1}{54} \right) . \quad (1.20)$$

The mean free path length Λ_{pair} a photon can travel before undergoing conversion is equal to

$$\Lambda_{pair} = \frac{9}{7} \cdot X_0 \quad (1.21)$$

Notable is that the number of photons is almost bisected with a factor $1/e^{7/9}$ after an absorber thickness of one radiation length X_0 .

The influence of the described processes on the mass attenuation coefficient μ/ρ of lead tungstate as a function of the photon energy is shown in Fig. 1.20.

1.3.3 Electromagnetic Shower

The understanding and reconstruction of electromagnetic showers is a crucial part in calorimeter physics. At sufficiently high energies a electromagnetic shower is initiated by an electron or photon. The underlying main processes bremsstrahlung and electron-positron pair production, respectively for electrons and photons, have been discussed in the previous section. These processes result in the development of an electromagnetic cascade in matter going along with an increasing number of particles which is called an electromagnetic shower.

First, a photon impinging the detector material with a sufficient energy more than a few MeV, produces an electron positron pair. If the energy of the electrons and positrons does not exceed the critical energy E_c , they both lose energy due to ioni-

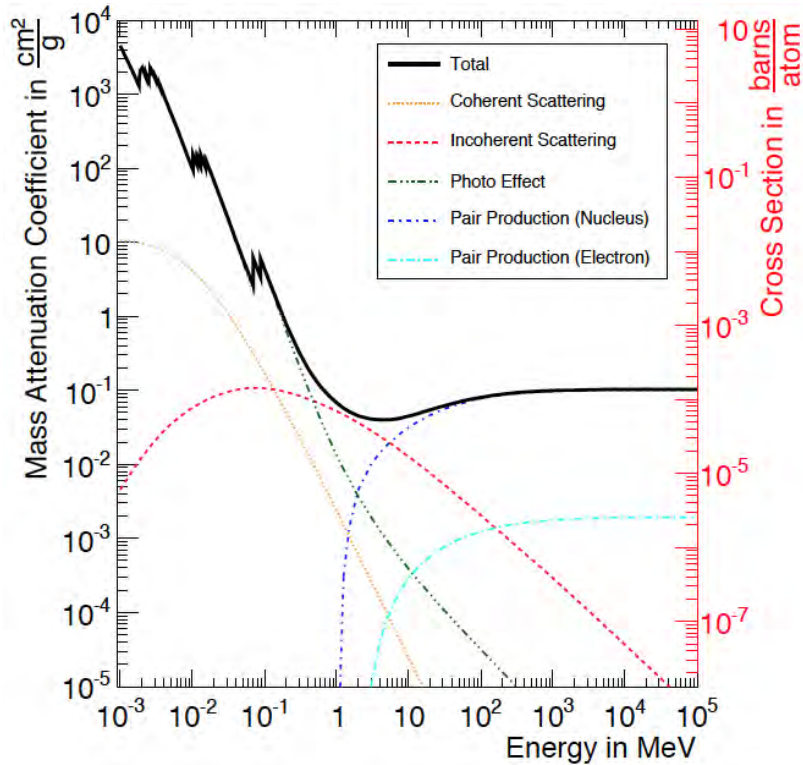


Figure 1.20: Mass attenuation coefficient of lead tungstate as a function of the photon energy [26, 27]. Shown are the contributions from the main interactions of photons with matter and the resulting total mass attenuation coefficient.

sation of the material. Hence, they radiate bremsstrahlung and thereby produce new high energetic photons. In secondary reactions these photons again produce electron positron pairs. This leads to the development of a cascade of electromagnetic reactions. The shower development continues until the energy of the leptons decreases to the critical energy E_c or the secondary photon energy is insufficient for pair production.

A natural measure for the electromagnetic shower development is the radiation length X_0 . Reason is that the two main processes leading to a shower are characterized by X_0 . Since the radiation length was defined to eliminate material-dependences, the shower development can be considered approximately material-independent. In general, one distinguishes a longitudinal electromagnetic shower development in di-

rection of the primary particle and a lateral or transversal development. Both are described separately. In the longitudinal case the development is characterized by the parameters $y = E/E_c$ and $t = x/X_0$, the energy-deposition rate and the penetration depth in an absorber, respectively. The longitudinal center of gravity of the shower energy profile t_{cg} and its peak maximum t_{max} are summarized in Tab. 1.1 for photons and electrons. Figure 1.22a shows the typical longitudinal expansion of an

	Incident photon	Incident electron
t_{max}/X_0	$1.01 \cdot (\ln y - 0.5)$	$1.01 \cdot (\ln y - 1)$
t_{cg}/X_0	$t_{max} + 1.7$	$t_{max} + 1.4$

Table 1.1: Parameters for a longitudinal shower development [28].

electromagnetic shower in a thallium doped caesium iodide (CsI(Tl)) crystal caused by photons. The shower profile has a pronounced tail to larger values of t . The lateral width of the electromagnetic shower is caused by the angular distribution of the particles produced by bremsstrahlung, which is very narrow, and the multiple scattering of electrons and positrons. The mean transverse deflection can be described in units of the Molière radius R_M of the absorber material

$$R_M = \frac{21 \text{ MeV}}{E_C} X_0 [\text{g/cm}^2] . \quad (1.22)$$

About 95% of the total shower energy is contained in a cylinder with radius

$$R (95\%) = 2R_M \quad (1.23)$$

centered around the shower axis. The lateral expansion of an electromagnetic shower in CsI(Tl), as depicted in Fig. 1.21b, shows an exponential decrease. This dependence has an impact on the energy response of a common electromagnetic calorimeter which is segmented laterally. On the one hand the segmentation enables the determination of the impact position of an impinging particle, but on the other hand it risks lateral energy leakage. A width of a single segment of one Molière radius was found to be a good compromise.

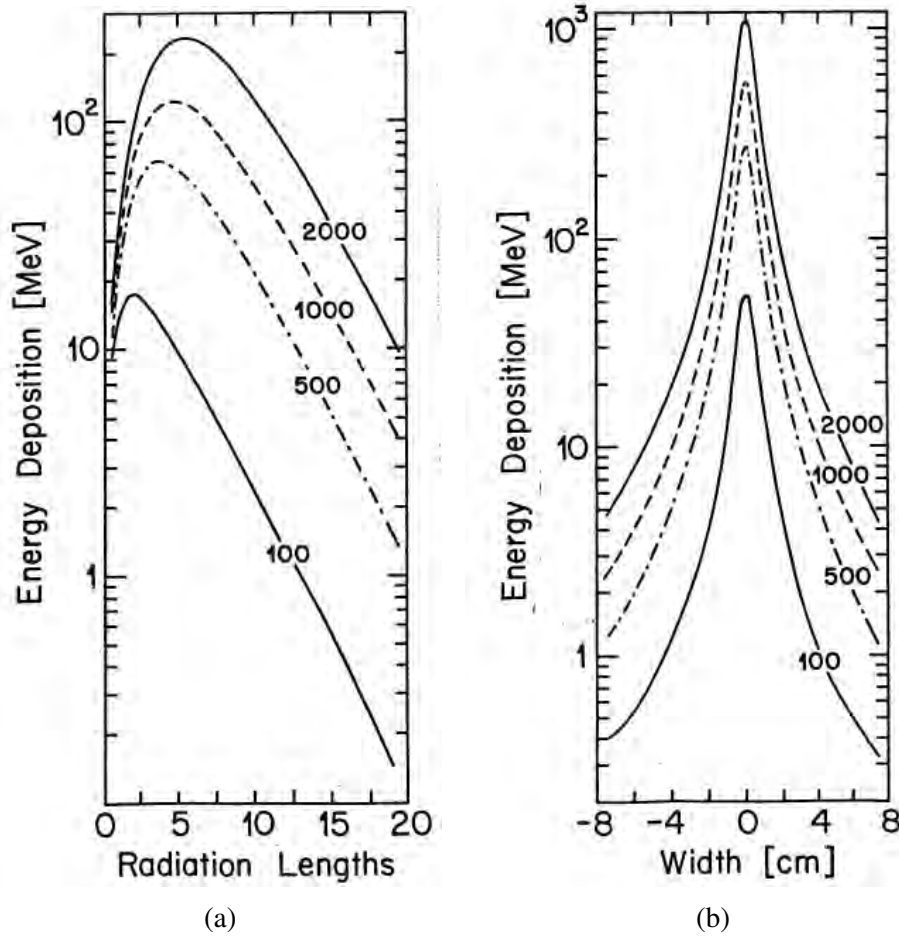


Figure 1.21: Shower energy profile caused by photons with various energies in CsI(Tl) as a function of the radiation length (a) and the lateral shower width (b) [29].

1.3.4 Requirements for the $\bar{\text{P}}\text{ANDA}$ Electromagnetic Calorimeter

The manifold physics program of the $\bar{\text{P}}\text{ANDA}$ experiment involves various requirements for the EMC. The basic function of the calorimeter is the efficient detection of electromagnetic probes by measuring the deposited energy and the direction via the point of impact. Almost the full solid angle has to be covered and the response has to be precise over a large energy range from 10 MeV up to 15 GeV. Further constraints are coming along with the limited size of the superconducting solenoid.

Hence, the EMC has to have a compact design and to be operable within a magnetic field. In addition, a fast response is essential due to a required high count rate capability coping with an annihilation rate of 10^7 Hz. Since the $\bar{\text{P}}\text{ANDA}$ Data AcQuisition (DAQ) system is foreseen to be triggerless, a time resolution σ_t below 1 ns is necessary. Long time operation demands a radiation hard detector to ensure a minimum of performance loss. Selected requirements for the EMC based on a luminosity of $2 \cdot 10^{32} \text{ cm}^{-2}\text{s}^{-1}$ are summarized in Tab. 1.2.

General properties	Required performance value		
energy resolution σ_E/E	$\leq 1\% \oplus \frac{\leq 2\%}{\sqrt{E/\text{GeV}}}$		
energy threshold (photons)	10 MeV		
energy threshold (singel crystal) E_{xtl}	3 MeV		
RMS noise (energy equivalent)	1 MeV		
angular coverage in % of 4π	99%		
Subdetector specific requirements	backward	barrel	forward
	$\geq 140^\circ$	$\geq 22^\circ$	$\geq 5^\circ$
energy range maximum	0.7 GeV	7.3 GeV	14.6 GeV
spatial resolution σ_θ	0.5°	0.3°	0.1°
maximum signal load f_γ	100 kHz		500 kHz
shaping time t_s	400 ns		100 ns
maximum annual dose	10 Gy		125 Gy

Table 1.2: Requirements for the $\bar{\text{P}}\text{ANDA}$ EMC. All values are with respect to the $\bar{\text{P}}\text{ANDA}$ EMC Technical Design Report (TDR) [30].

1.3.5 Scintillator material

The chosen lead tungstate, PbWO_4 (PWO) scintillation crystals for the $\bar{\text{P}}\text{ANDA}$ EMC meet the requirement to be a compact, extremely fast and radiation hard scintillator. Lead tungstate is a high Z material coming along with a short radiation length X_0 and a small Molière radius R_M . These properties allow for a compact design of the calorimeter. The crystal structure is of tetragonal symmetry and it has a negative birefringent nature. The emission spectrum of the scintillation light is Gaussian-like with

a most probable wavelength of $\lambda_{\text{mean}} = 420$ nm and a **F**ull **W**idth at **H**alf **M**aximum (FWHM) of 40 nm.

PWO has become the dominant material in high-energy physics over the past decades. It has been optimized and produced in large scale, especially for the electromagnetic calorimeter of the **C**ompact **M**uon **S**oleniod (CMS) experiment at the **L**arge **H**adron **C**ollider (LHC). But **R**esearch & **D**evelopment (R&D) efforts were made for the $\bar{\text{P}}$ ANDA EMC to improve the scintillation material even further. These efforts lead to the development of a new generation of quality, called PWO-II. One major disadvantage of the first crystal generation for $\bar{\text{P}}$ ANDA applications would be the relatively low light yield compared to other scintillator materials. The R&D program improved the scintillation efficiency for application in a lower photon energy regime. Because the doping elements have different distribution coefficients, they are introduced in different stages during the growing process to avoid an imbalanced concentration within the crystal. The improvements are related to reducing the defect concentrations, lowering the doping concentrations and changing operation temperature to $T = -25^\circ\text{C}$. The light yield is enhanced by a reduction of the concentration of rare earth La and Y, which causes shallow traps and reduce the luminescence yield, resulting in a reduction of defects in the crystal structure. The reduction can be achieved by an improved control of stoichiometry during the growing process. Altogether this leads to an increase of scintillation light in the order of 80% compared to the quality of the CMS crystals [30] and a sufficient radiation hardness. Nevertheless, an additional enhancement of the light yield is gained by cooling down the scintillation crystals to a temperature of $T = -25^\circ\text{C}$. At the reduced temperature thermal quenching effects influence the light emission such that the light yield can be improved by another factor of approximately 4 compared to room temperature. This improvement is crucial for low energies in order to improve the Poisson statistics and hence the relative energy resolution. Then again, the drawback of the reduced temperature is a rise of the scintillation light's emission decay constant τ_{decay} . At room temperature a short $\tau_{\text{decay}} = 6$ ns enables a fast collection of the scintillation light which makes it capable of high count rates. Despite the slower collection at the reduced temperature, it is still possible to collect 97% of the scintillation light within a time gate of 100 ns. Table 1.3 summarizes selected properties of PWO and PWO-II.

Parameter	Value		Unit
	PWO	PWO-II	
Effective atomic number Z_{eff}	75.6		
Density ρ	8.28		g/cm^3
Radiation length X_0	0.89		cm
Molière radius R_M	2.00		cm
Decay constant τ_{decay}	6.0		ns
Scintillation wavelength λ_{max}	420.0		ns
Index of refraction at λ_{max}	2.24/2.17		
Relative Light Yield (LY) to NaI	0.3* 0.8†	0.6* 2.5†	% (LY NaI)
dLY/dT	-3.00*		%/°C
Energy loss dE/dx (MIP)	10.2		MeV/cm
Critical energy E_c	9.64/9.31*		MeV
Nuclear interaction length λ_A	20.27		cm

Table 1.3: Properties of lead tungstate. [30] (*: at room temperature; †: at a temperature of -25°C ; *: respectively electron and positron)

1.3.6 Layout

As depicted in Fig. 1.15, the $\bar{\text{P}}\text{ANDA}$ EMC consists of a Barrel EMC, a **B**ackward **E**nd **C**ap (BEC) and a **F**orward **E**nd **C**ap (FEC). The EMC will be assembled in total out of 15552 PWO-II crystals which are divided into 11360 crystals in the Barrel EMC, 3864 crystals in the FEC and 592 crystals in the BEC. In the FEC the crystals are of type EC, featuring a tapered parallelepipedal shape, which has a polar angle equivalent of 1° . Compared to the polar angle equivalent of 4° for the other crystal types, the granularity and the hit occupancy of a single crystal is increased for the FEC. These characteristics are accounting for the kinematics of a fixed-target experiment. The Barrel EMC consists of 16 similar slices, as depicted in Fig. 1.22, each consisting of 710 crystals subdivided into super modules. All crystals of a slice are tilted by the same polar and azimuthal angle of 4° with respect to the target in order to decrease material between the crystals. For this reason, 11 different crystal types are needed featuring tapered parallelepipedal shape with individual dimensions. In addition, there are two longitudinally mirror-inverted designs for each type, which are labeled L and R. A schematic drawing of the crystal geometry is depicted in Fig. 1.23.

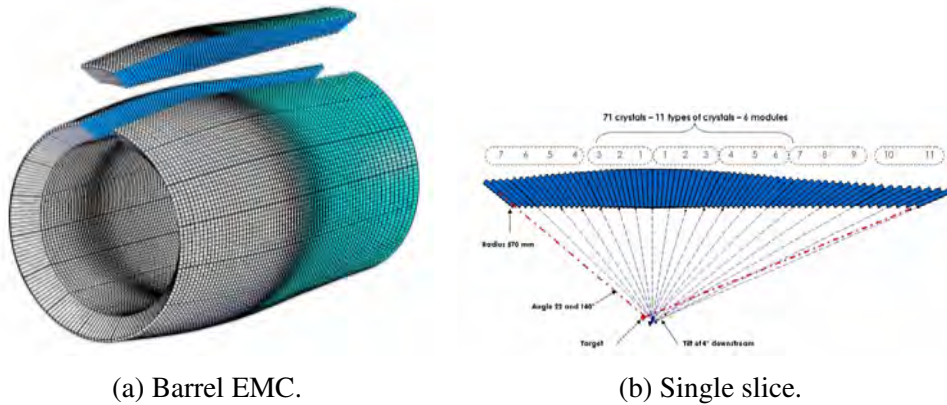


Figure 1.22: Arrangement of the crystals in the Barrel EMC.

The values for the side lengths of the different crystal types are listed in Tab. 1.4. The length is the same for all crystals and amounts to 200 mm.

1.3.7 Photo sensors

The main requirement for the photo sensors is the operation within a magnetic field of ~ 2 T. Thus, it is not possible to read out the crystals with conventional PMTs. In addition, the sensors should have an internal gain. Because of the relatively low LY of PWO-II, the sensors are required to amplify the primary signal. Another requirement is the radiation hardness down to the operation temperature of -25°C . Two kinds of photo sensors are envisaged for parts with expected relatively low and high rates, respectively. The **L**arge **A**valanche **P**hoto **D**iodes (LAAPDs) and **V**acuum **P**hoto **T**etrodes (VPTTs) are discussed in the following paragraphs.

1.3.7.1 LAAPD

The above-mentioned LAAPDs are foreseen to read out the crystals in the Barrel part and the BEC of the EMC because of their insensitivity to a magnetic field and their compact design. The APDs used at CMS were the basis for the LAAPDs used at $\bar{\text{P}}\text{ANDA}$. This type of APD has been developed and adapted to PWO in a common

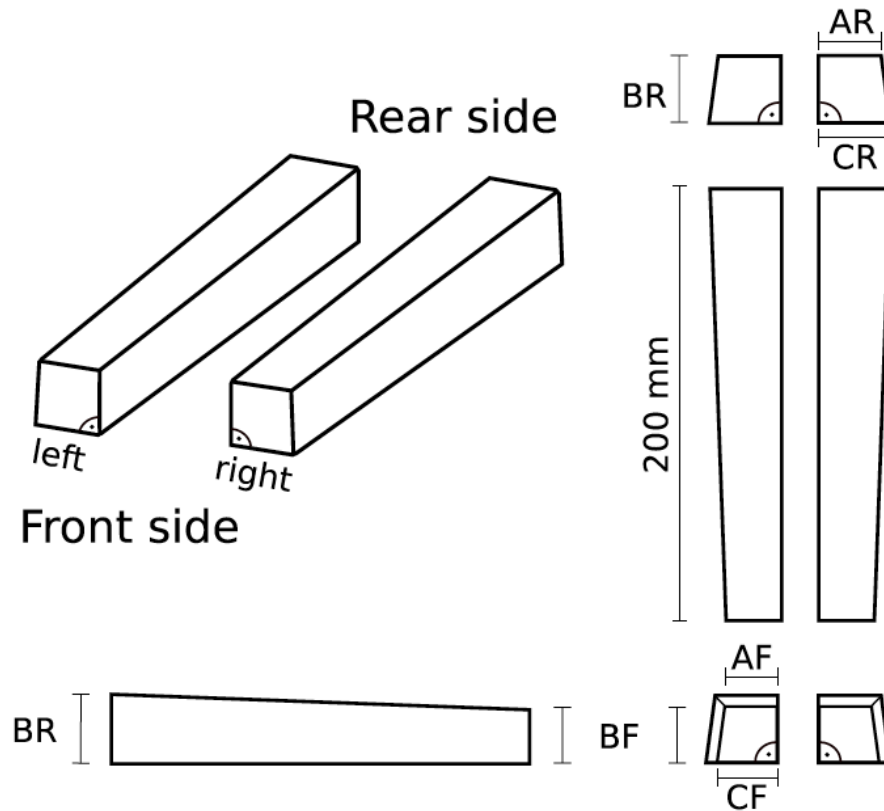


Figure 1.23: Schematic drawing of the crystal geometry with the definition of the geometry parameters. The individual dimensions of the parameters are given in Tab. 1.4.

effort of the CMS collaboration and the manufacturer *Hamamatsu Photonics*. It has the following advantages:

- 200 μm thickness
- thin conversion layer
- high **Quantum Efficiency (QE)** in the wavelength range of PWO ($\sim 80\%$)
- insensitive to magnetic field
- low cost for mass production

For $\bar{\text{P}}\text{ANDA}$ the original size of $5 \times 5 \text{ mm}^2$ has been enlarged to a surface of 1 cm^2 .

Type	Volume cm ³	AF	BF	CF	AR	BR	CR
				mm			
1	126.86	21.21	21.28	21.27	29.04	28.75	29.12
2	126.56	21.18	21.28	21.39	28.78	28.75	29.07
3	125.79	21.17	21.28	21.51	28.36	28.75	28.81
4	120.85	21.17	21.28	21.60	27.90	27.22	28.45
5	119.69	21.17	21.28	21.69	27.35	27.22	28.01
6	118.35	21.19	21.28	21.78	26.72	27.22	27.47
7	112.90	21.22	21.28	21.86	26.23	25.47	26.99
8	111.75	21.23	21.28	21.91	25.70	25.47	26.51
9	110.52	21.23	21.28	21.95	25.14	25.47	26.00
10	107.01	21.25	21.28	22.00	24.70	24.42	25.56
11	106.25	21.25	21.28	22.02	24.35	24.42	25.23
EC	126.88	24.38	24.38	24.38	26.00	26.00	26.00
EC-R	118.58	24.35	24.35	24.35	24.35	24.35	24.35

Table 1.4: Definition of the geometrical parameters of the PWO-II crystals. Listed are the values of the trapezoidal rear face AR, BR and CR and of the front face AD, BF and CF.

Generally, the internal structure of a LAAPD is based on a p-n-junction operated on reverse bias voltage which is a distinctive feature. Compared to conventional Si-photodiodes, the LAAPDs are operated at significantly higher voltages coming along with a large electric field strength at the p-n-junction. Hence, LAAPDs are able to create an avalanche of secondary ionizations. The amount of secondary charge is proportional to the primary charge. Thus, depending on the bias voltage, an effective charge multiplication, the LAAPD gain M , up to a factor in the order of several hundred can be achieved. The described internal charge carrier multiplication via avalanche is a statistical process. Its relative width σ of a signal from n photoelectrons is given by

$$\sigma = \sqrt{\frac{F}{n}}. \quad (1.24)$$

Hence, the statistical fluctuations are characterized by the excess noise factor F , which in general itself depends on the gain. The excess noise factor can be calcu-

lated by [31]

$$F = kM + (1 - k) \left(2 - \frac{1}{M} \right), \quad (1.25)$$

with the carrier ionization ratio k . According to the producer Hamamatsu [32], the latter formula can be approximated by an empirical formula:

$$F = M^x. \quad (1.26)$$

Here, the exponent x represents the excess noise index.

In order to characterize the front-end electronics, the influence of the excess noise on the total energy resolution has to be investigated. In general, the width of a photo peak with a Gaussian shape is described by

$$\sigma_E = \sqrt{(Fn)^2 + \sigma_{\text{pre}}^2}, \quad (1.27)$$

where the noise of the preamplifier σ_{pre} is included. Then, the total energy resolution can be described by

$$\frac{\sigma_E}{E} = \sqrt{\frac{F}{n}} = \sqrt{\frac{F}{LY \cdot E}}. \quad (1.28)$$

Since the excess noise and the photon current increase with the gain, there is a optimum signal to noise ratio at certain gain value. The method to find the optimal gain is depicted in Fig. 1.24.

The general structure of a LAAPD with its distinctive reverse structure is depicted in Fig. 1.25. First, the light traverses the impassive protective Si_3N_4 layer, which reduces loss of light due to reflections, and then the more positively doped p^{++} -anode. After that the light is converted into electron-hole pairs in the thin p^+ layer. The charge carrier multiplication via avalanche takes place in the directly neighboring p-n-junction. After that the electrons drift through the n^{++} substrate to the n^{++} -doped cathode.

In addition to the structure of the LAAPD, there are more R&D improvements. It

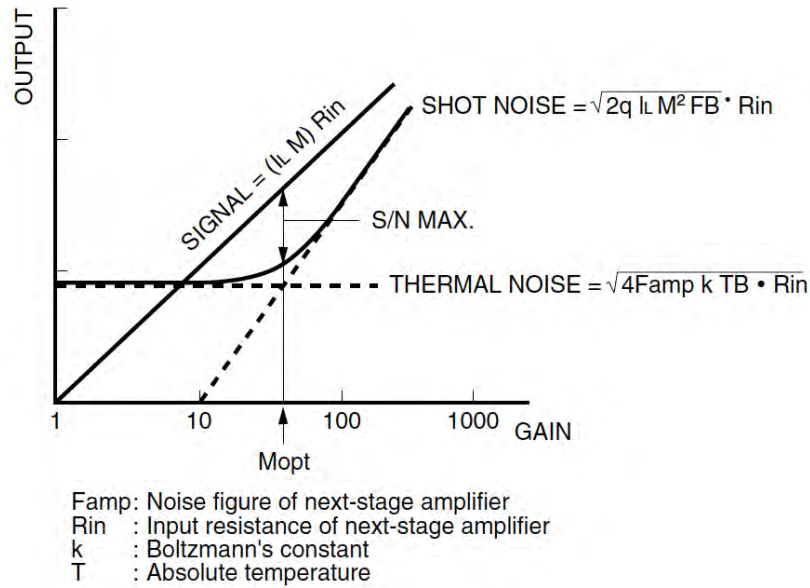


Figure 1.24: Method to find the optimal gain for an APD [32].

has already been mentioned that the active area was enhanced from 0.25 cm^2 to 1 cm^2 which lead to the name **Large Area APD**. This R&D step accounts for the low envisaged energy threshold which requires to collect as much scintillation light as possible. A single quadratic LAAPD is used in the first prototype of the Barrel EMC, the PROTO60. In a next step a rectangular version with edge lengths of $0.7 \text{ cm} \times 1.4 \text{ cm}$ but same active area was developed. This type is integrated in the most recent prototype PROTO120 and is envisaged to be used in the $\bar{\text{P}}\text{ANDA EMC}$. The rectangular shapes allows to fit two LAAPDs on one crystal which doubles the amount of collected scintillation light and should improve the achievable energy resolution, especially at low energies. Another advantage of two LAAPDs is the rejection of fake events caused by neutrons. It was observed at the CMS experiment that there is a non-zero probability for a neutron crossing the APD volume and creating an unusually high energy signal due to spallation. Comparing the signals of both sensors enables the rejection of those events. The thin conversion layer prevents another effect, the so-called **Nuclear Counter Effect (NCE)**, which can affect the energy resolution. It occurs if a charged particle creates electron-hole pairs in the silicon layer of the LAAPD ($\sim 100 \text{ e/h}$ pairs per μm) in addition to the signal caused by the scintillation light. Charge produced in the large drift region is negligible compared to the

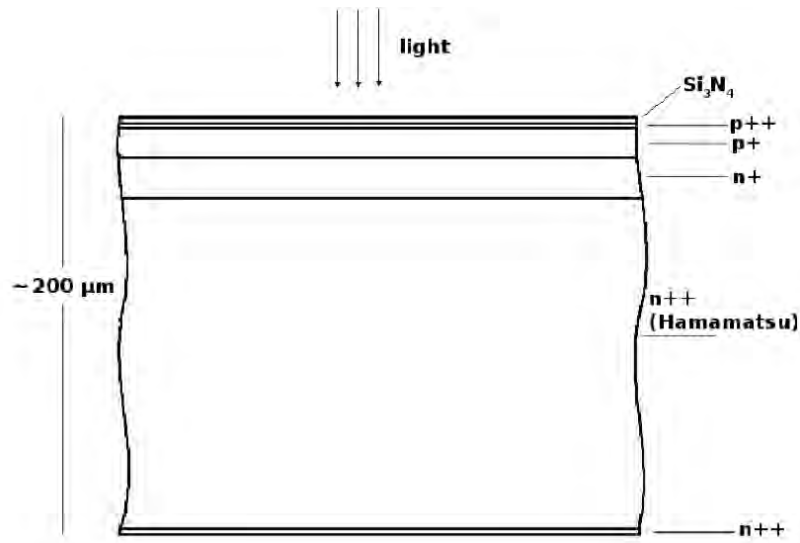


Figure 1.25: Layout of the structure of an APD with its various layers of doped silicon [33].

charge produced by scintillation light because it is not multiplied.

1.3.7.2 VPTT

A certain amount of crystals within the FEC with a low polar angle, where high rates up to 500 kHz are expected, will be read out by VPTTs. Reason is the fast response of VPTTs compared to LAAPDs. In principle, the functionality of a VPTT can be compared with a conventional PMT. It can be described as a two stage photomultiplier with a different number of dynodes. A schematic layout of a VPTT is depicted in Fig. 1.26. A VPTT consists of an evacuated cylindrical glass tube with a photo cathode on one end face. The photo cathode, a photo sensitive bialkali coating, converts visible photons into electrons via the photoelectric effect. The electrons are accelerated to a mesh dynode where amplification takes place. Then they are further accelerated to a metal grid anode and afterwards to another dynode where even further amplification takes place. The produced secondary electrons will subsequently be accelerated backwards to the anode where they are collected. A VPTT achieves a nominal signal amplification of ~ 20 which is significantly lower compared to a conventional PMT. But then VPTTs can be operated in a strong magnetic field where

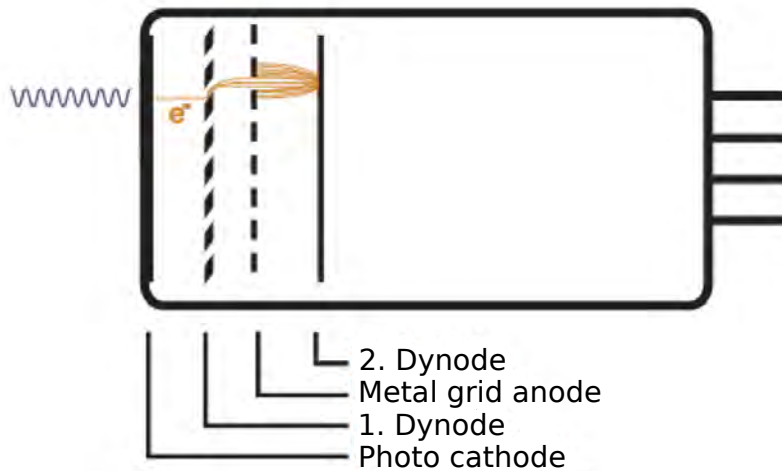


Figure 1.26: Schematic layout of a VPTT.

one nevertheless has to accept a degradation of a VPTT gain up to 45% for a magnetic field of 1.2 T depending on the alignment of the sensor relative to the magnetic streamlines.

1.3.8 Front End Electronics and Data Acquisition

The front end readout electronics has to fulfill several requirements to achieve the envisaged performance of the $\bar{\text{P}}\text{ANDA}$ EMC. The energy range from the low single crystal threshold of 1 MeV up to the maximum expected energy deposition in a single crystal of 12 GeV has to be covered resulting in a dynamic range of 12,000. In addition, the limited space within the EMC cooling compartment should be used efficiently. On that account, the preamplifier should be as close as possible to the crystal sensors which features a decreasing probability of pick up noise. Furthermore, a low power consumption of the preamplifiers is essential to guarantee a homogenous cooling along the crystal. Two different concepts were developed for the two envisaged photo sensors. On the one hand the ASIC for **P**ANDA **F**ront-end **E**lectronics (APFEL) Application Specific Integrated Circuit (ASIC) was developed as a preamplifier for the Barrel part and on the other hand the **L**ow **N**oise and **L**ow **P**ower charge Preamplifier (LNP-P) for the FEC. Both concepts will be described in the following

sections.

1.3.8.1 ASIC

Each crystal within the Barrel EMC is equipped with two LAAPDs which are read out simultaneously by one ASIC, the so-called APFEL [34]. An APFEL ASIC has two equivalent channels per chip. Each readout channel consists of a charge sensitive preamplifier, a third order semi-Gaussian shaper stage and a differential output driver. The schematic layout of this kind of ASIC is displayed in Fig. 1.27 and a picture can be seen in Fig. 1.28. Preamplifier and shaper use state of the art 350 nm

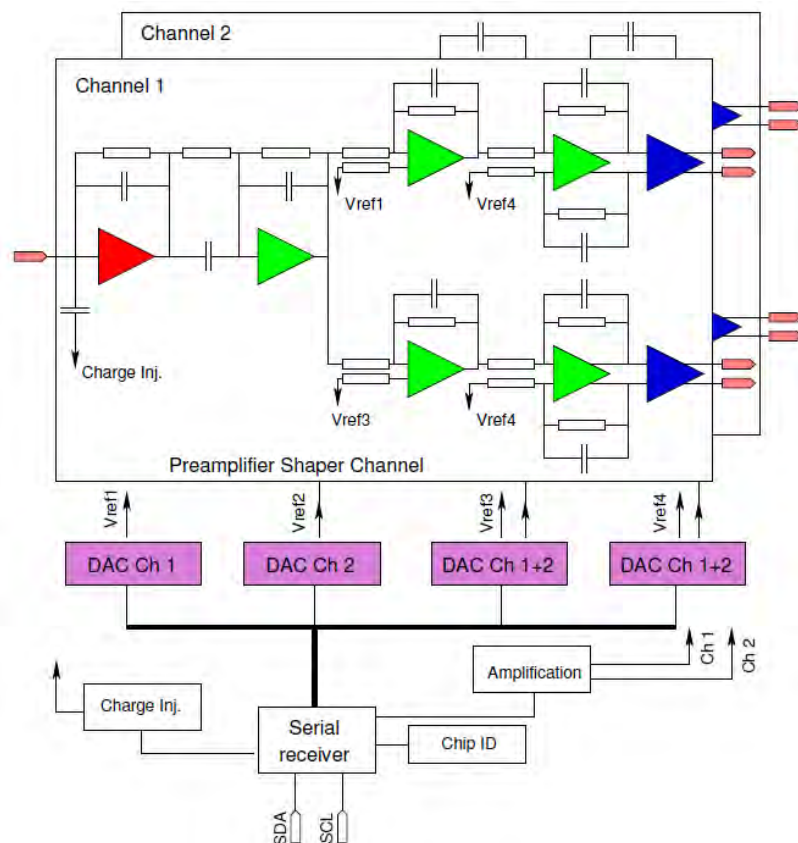


Figure 1.27: Schematic layout of the APFEL. Marked are the charge sensitive preamplifier (red), the third order shaper stage (green) and the differential output driver (blue).

Complementary **Metal-Oxide-Semiconductor** (CMOS) technology operated at 3.3 V single core voltage. The complete readout electronics fit on $3.4 \times 3.5 \text{ mm}^2$. The input of one LAAPD is split by the APFEL which provides two outputs with different amplifications to cover the dynamic range. Their relative gain can be programmed to a factor of 16 or 32. The design features to be more sensitive to low energies in the high gain branch while it is still possible to observe the complete energy range with the low gain branch. A maximum input charge of 8 pC results in a digital dynamic range of $> 10,000$. At GSI an **Equivalent Noise Charge** (ENC) of $(4125 \pm 67) e^-$ was measured at $T = -25^\circ\text{C}$ while $4500 e^-$ were required. Furthermore, the APFEL is able to handle the required event rates of 350 kHz and the power consumption is less than the required 60 mW per ASIC. The digital part of the APFEL features a serial interface on the chip for autocalibration to detect the right DC voltages for a given temperature. The output DC voltage is dependent on the temperature resulting in a change of operating points of the amplifier. The dependency was measured and amounts to 25 mV/K. Hence, with fixed voltage references a temperature shift would lead to a decreasing dynamic range of 2%/K. This is solved with an adjustable voltage reference. In addition, an optional charge injection as a test pulser is possible, the DAC setting can be read and written and each chip has an ID for single chip and bus communication.

1.3.8.2 Low Noise and Low Power Charge Preamplifier

The photo sensors in the FEC, both LAAPDs and VPTTs, will be read out with variations of the LNP-P developed at Basel University [35]. Here, there is only one preamplifier channel per photo sensor. Further, an additional shaper board is needed to guarantee high rate capability together with the currently developed **Sampling Analogue to Digital Converter** (SADC). A former version of this preamplifier is used in the Barrel EMC prototype PROTO60. A LNP-P is based on **Junction Field Effect Transistor** (J-FET) technology where the input charge is linearly converted into a positive output voltage. The power consumption of a single LNP-P is in the range of 45 mW up to 90 mW depending on the event rate and energy of the photons.

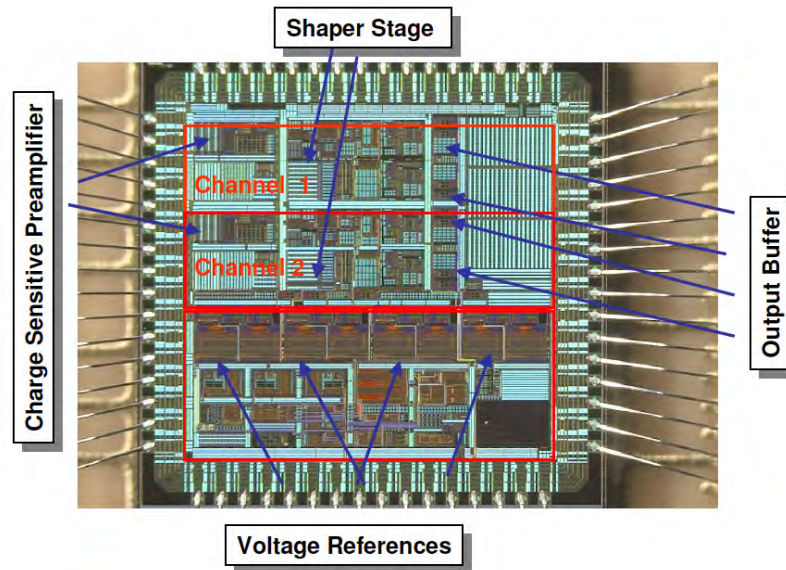


Figure 1.28: Picture of the APFEL 1.4 ASIC.

1.3.8.3 Data Acquisition

The schematic layout of the \bar{P} ANDA EMC DAQ is depicted in Fig 1.29. The pre-amplified and shaped signals from the photo sensors are routed from the cold volume to a digitizer module for digitization. The digitizer module consists of an SADC and an on-board **F**ield **P**rogrammable **G**ate **A**rray (FPGA) for feature extraction and hit building. The online pulse data processing is performed in two stages. First, pulses are identified by monitoring the continuously digitized signal baseline. In case of a pulse, a time stamp is set to the maximum. Additionally, possible pile-up is indicated. In the second stage, the precise time and pulse height are determined. This hit data is then transmitted via optical links to the data concentrator. The task of the data concentrator is the EMC event building which includes time ordering, pile-up recovery and synchronization and communication of the SADC clock information with the global time distribution system and slow control information. A processed event is then send to the compute node. Here, the information of the other sub-detector systems is connected with the EMC information and the online physics event reconstruction takes place. Flexible software trigger conditions are set to store events to hard disk. The conditions are not tuned to specific reaction channels like for most

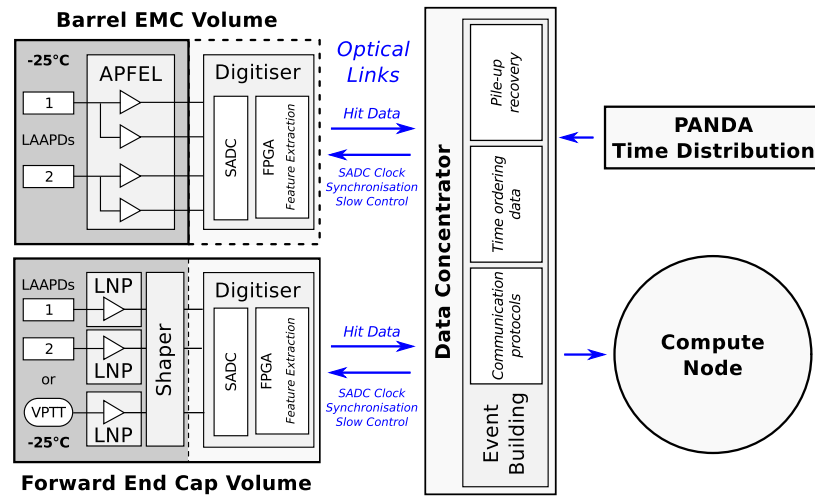


Figure 1.29: Schematic layout of the \bar{P} ANDA EMC DAQ [27].

hardware triggers. Thus, most channels and possible rare reactions are not suppressed at \bar{P} ANDA. The amount of collected data is only limited by the dead time of the individual sub-detector systems and the buffer size of the compute node.

Chapter 2

Beamtime test with PROTO60

2.1 PROTO60

The PROTO60 is the first real-size prototype of the \bar{P} ANDA Barrel EMC. The geometry is arranged to resemble a subsection of a barrel slice, as schematically shown in Fig. 2.1. It consists of 60 geometry type-6 L & R shaped PWO-II crystals arranged in 10 columns and 6 rows. The difference to a barrel slice is that only maximum 4 rows of the same type are grouped together. The reason is a simplification of the carbon alveoli holding structure in case of the PROTO60. In addition, a crystal is read out with only one LAAPD. As in the Barrel the crystals are operated at a temperature of -25°C . Mechanics, electronics, readout and DAQ of the PROTO60 are described in the following sections in more detail.

2.1.1 Mechanics

A single PWO-II¹ crystal is wrapped with enhanced specular reflector film (VM2000) which is a mirror-like multilayer polymer foil with a reflection coefficient of 0.994 at 440 nm and a thickness of $65\ \mu\text{m}$ [36]. The foil is supported by Mylar film. Four crystals are grouped together as a package of two right and two left type crystals. Thin carbon sheets are placed between the crystals to avoid optical crosstalk and to

¹PWO-II: lead tungstate crystal of improved quality (see Chapter 1.3.5)

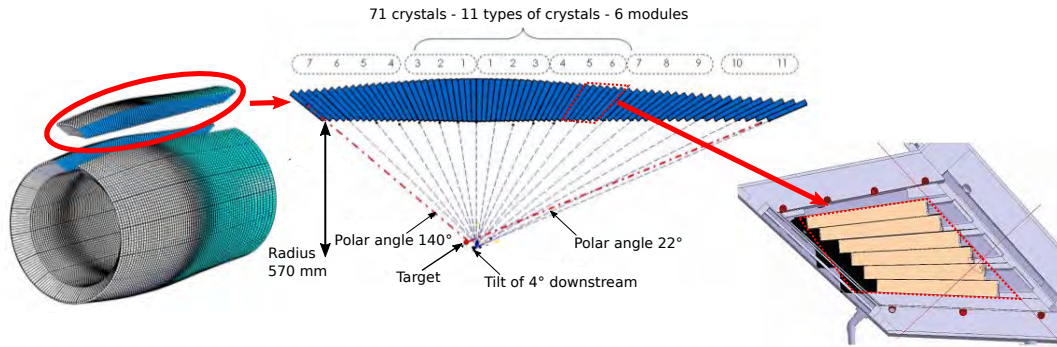
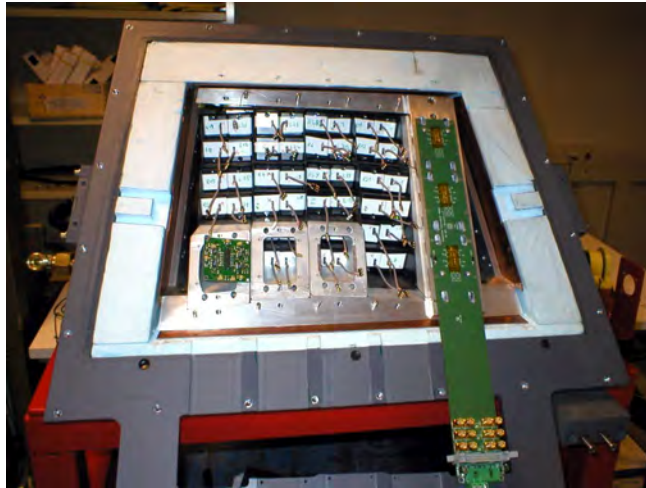


Figure 2.1: Schematic view of the Barrel EMC. The PROTO60 represents a subsection of a Barrel slice. It contains type 6 PWO-II crystals.

assure homogeneity of the dead material. The subunit is placed into a carbon alveole with a wall thickness of $200 \mu\text{m}$. The distance between the crystals adds up to 0.68 mm including mechanical tolerances. Aluminum inserts are glued to the alveole to ensure mechanical stability of the detector since they have to carry the weight of all 60 crystals with a weight of $\sim 1 \text{ kg}$ each. In addition, the inserts integrate the cooling system, electronics and a monitoring system. All the 15 inserts are mounted to the backplane of the prototype housing. In the end the complete matrix is placed in a copper clad aluminum box surrounded by a PVC housing. For cooling purposes of the matrix meandering copper pipes are attached to the inner side of the box. The pipes are filled with a mixture of water and ethanol. The fluid is circulated by a chiller which achieves the required thermal power of 80 W . To prevent ice formation, the inside of the PROTO60 is rinsed with overpressured dry nitrogen. In addition, the housing is sealed with silicium and the empty space of the housing is filled with insulating styrene foam to ensure a stable operation at -25°C . Furthermore, 13 temperature sensors are installed within the PROTO60. The monitoring of the temperature is necessary because the light yield and the LAAPD gain are temperature dependent. During long term tests it turned out that the temperature variation stays below $\pm 0.05^\circ\text{C}$. The entrance window in front of the matrix is built differently since it has the purpose to provide thermal shielding with minimum attenuation of incoming particles. Hence, it consists of two thin aluminum plates with an evacuated gap in between.



(a) Four grouped crystals which are each wrapped with VM2000 and equipped with one LAAPD.



(b) Open back view of PROTO60.

Figure 2.2: Photographs taken during assembly of PROTO60.

2.1.2 Electronics

Each crystal is equipped with a single quadratic 1 cm^2 LAAPD² with technical details given in Tab. 2.1. In order to minimize the light loss due to transition between materials with different refractive index, the LAAPD is optically coupled to the crystal with silicon grease³. The LAAPD is stabilized by a black plastic capsule. The high voltage settings for the LAAPDs were once adjusted using a stabilized light pulser

²Hamamatsu S8664-1010SPL

³Baysilone M300000, Bayer

and the energy deposition of cosmic radiation. The procedure was necessary since the manufacturer provides only the individual voltages for a gain of 50 at room temperature. The utilized gain at -25°C is defined to a value of 150. In a next step the small

Parameter	Specification
effective area	100 mm ²
spectral response range	320 – 1000 nm
QE at 420 nm	70%
capacitance	270 pF
maximum gain	~ 500
operating voltage (at gain 150)	$\sim 350\text{ V}$
typ. dark current	10 nA

Table 2.1: Properties of LAAPDs used in PROTO60 [37].

charge pulse from a LAAPD has to be converted into a voltage signal suitable for digitization. In case of the PROTO60, the LAAPD signal is amplified by a SP883b Quad LNP-P type preamplifier, designed and built at Basel University by W. Erni (compare Chapter 1.3.8.2) [35], which is attached to the insert. Each circuit board houses 4 preamplifiers. The preamplifiers are connected to the LAAPD by 25 mm long twisted pair wires. The circuit boards are kept in the cold volume in order to reduce electronic noise and to minimize the length of the wires. On that account, the LNP-P has been adapted to this circumstance by having a low power consumption and power dissipation, respectively. This ensures the required low cooling power and a small temperature gradient within the crystal. The preamplified signals are guided from the cold to warm volume with one readout backplane per two columns, supplying three preamplifiers and connected photosensors, via narrow slits. In the warm volume coaxial connectors provide a routing of signals to a DAQ system.

For later analysis it is crucial to ensure a low electronic noise because it is necessary to obtain a low energy threshold in the order of a few MeV. Therefore, the dynamic range and the noise of the PROTO60 preamp will be estimated in the following paragraph.

The PROTO60 preamplifier generates an ENC of $1250 e_{\text{RMS}}^-$ at -25°C at the detector input. It was measured that the ENC combined with a LAAPD at a gain of

Gain	Preamp noise / MeV	Max. single crystal energy / GeV
50	1.06	15.58
100	0.53	7.79
150	0.35	5.19
200	0.27	3.9

Table 2.2: Estimated dynamic range and noise of the PROTO60.

50 amounts in total to $1700 e_{\text{RMS}}^-$ at -25°C . The LNP-P amplification is given in [35] as 0.5 V/pC . The light yield of a type 6 crystal was measured with a 2 inch bialkali photo cathode photomultiplier tube covering the whole crystal endface and with an QE of 20 %. The value can be converted to PROTO60 conditions. The light yield increases from 18.7 phe/MeV at 18°C to 67.32 phe/MeV at -25°C . Comparing the spectral distribution of scintillation light and QE of the photomultiplier tube and the LAAPD gives a factor of 3.5 increased LAAPD QE compared to the photomultiplier tube [33]. Since a LAAPD covers only $\sim 13.6 \%$ of the full endface, the number of photoelectrons inside a LAAPD can be approximated to 32.04 phe/MeV at -25°C . The resulting estimated dynamic range and noise of the preamp according to the LAAPD gain are given in Tab. 2.2.

2.1.3 Readout and DAQ

DAQ

This subsection will describe the signal processing from the primary signal of the photo sensor to the digitization. The scintillation light from the PWO-II crystal is converted to a charge pulse by the LAAPD and afterwards amplified by a LNP-P. The LNP-P signals are routed to SIS 3302 SADCs modules (8 channels each) [38] by coaxial cables. The sampling frequency was set to 50 MHz, accounting for one sample every 20 ns. The trace length amounted to 250 samples, corresponding to a time window of $5\mu\text{s}$. A scheme of the test experiment DAQ is shown in Fig. 2.3. The corresponding electronic modules are listed in Tab. 2.3.

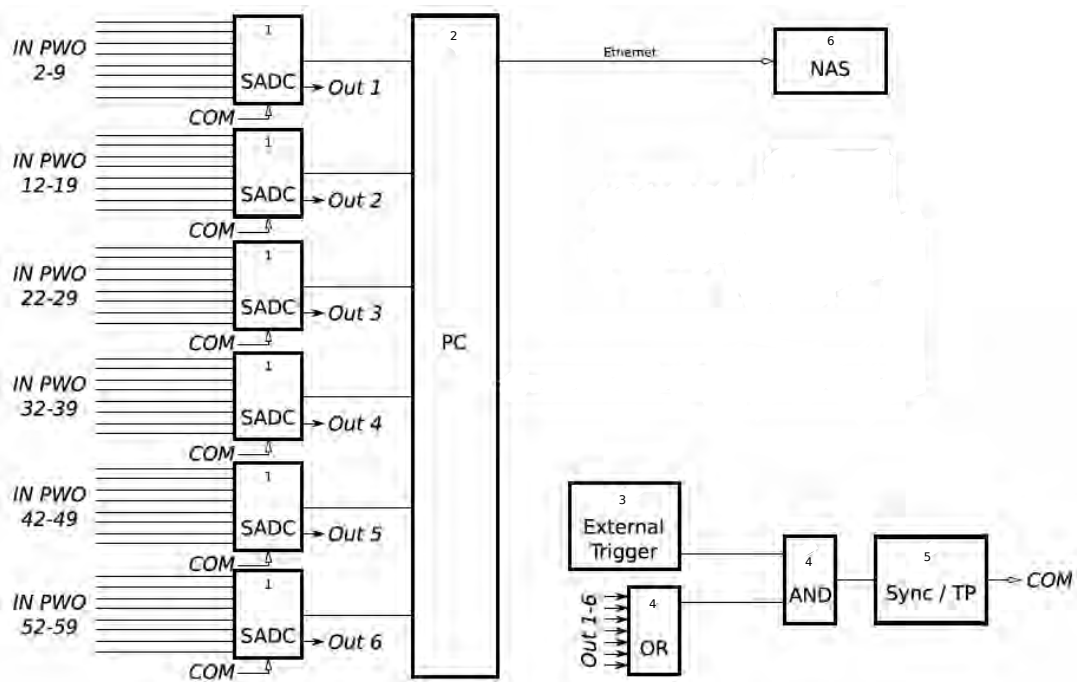


Figure 2.3: Schematic of the PROTO60 readout.

Module number	Function	Type	Standard / connection
1	SADC	Struck SIS 3302 SADC	VME
2	PC	VME CPU with Tundra-II chipset	
3	External trigger	Discriminated plastic scintillator paddle signal	NIM
4	AND or OR	LeCroy Module 622 Quad Coincidence	NIM
5	Sync / TP	Customized synchronisation module incl. test pulser	VME
6	NAS	QNAP TS-659 Pro+ NAS	TCP/IP

Table 2.3: Electronics modules of the PROTO60 test setup.

The SADCs are continuously taking samples of each preamplified LAAPD pulse. A trace is stored in case of a trigger signal. The 250 samples taken before a trigger signal are sent via Versa Module Eurocard (VME) bus to the Central Processing Unit (CPU) where the trace is further processed. The trigger signal is a coincidence of a logical OR of the responding tagger channels and a logical OR of all channels of PROTO60. Software was used to set a threshold for each channel individually. In order to prevent additional trigger signals before the previous event is processed completely, a test pulser integrated in the customized synchronization module generates a supplementary trigger.

Feature extraction

As a final step in the readout chain the raw SADC traces will be used to extract energy and time information. In the \bar{P} ANDA Barrel EMC the digitized signals from the Analogue to Digital Converters (ADCs) will be processed by FPGAs. For this purpose feature extraction algorithms have to be on the one hand simple enough to allow an implementation in the FPGA and on the other hand fast and robust. Different algorithms have been studied for application in the \bar{P} ANDA EMC in [39, 40]. These algorithms have to be tested on experimental data and are therefore the basis for the following analysis. In purpose of the test beam data, the algorithms are implemented via software since the SADC data is stored and analyzed offline. The algorithms are briefly explained in the following, showing the deduction of energy and time information. Examples for each feature extraction step are shown in Fig. 2.4. The offline analysis is performed with the ROOT/CERN framework which is an object oriented program and library for large scale data analysis based on C++ developed especially for particle physics [41]. As a first step, the raw LNP-P signal (Fig. 2.4a) is shaped with the so called Moving Window Deconvolution algorithm (MWD). The preamplifier signal has a decay time in the order of $\sim 25\mu s$, which is shaped to a much shorter pulse resulting in a reduced pile-up probability for signals arriving in a fast sequence. The used algorithm is defined such by

$$x_{MWD} = x(n) - x(n - M) + \frac{\ln 2}{\tau} \sum_{i=n-M}^{n-1} x(i), \quad (2.1)$$

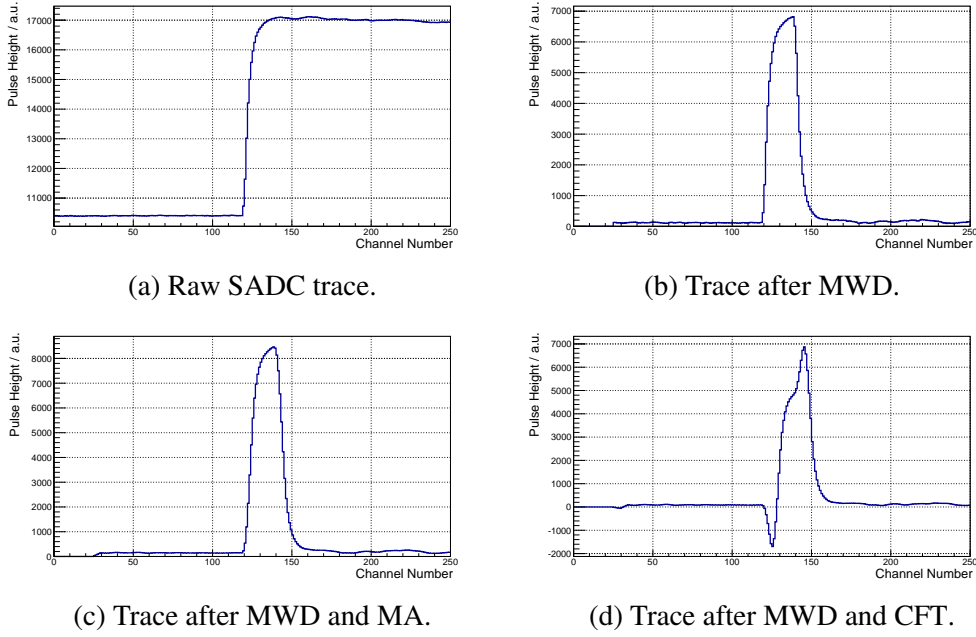


Figure 2.4: SADC traces of a random crystal after indicated feature extraction steps.

that the pulse height $x(n)$ of a sample n and a previous sample $n - M$ is subtracted and the **Moving Average** algorithm (MA) of the samples in between is added. Since the parameter M defines the final length of the output pulse, it has to be matched to the rise time of the raw signal. The parameter τ corresponds to the decay constant of the raw LNP-P signal. After optimization the parameter M was set to 400 ns and the parameter τ to 25 ns as a compromise between energy and time response. A variation of the parameter M is shown in Fig. 2.5 where a physical reasonable local minimum could be found for $M = 400$ and the parameter $L = 80$, which represents the smoothing length for the MA filter. The obtained trace as depicted in Fig. 2.4b is then further processed for the purpose of energy and time extraction. In case of the energy extraction a MA filter is applied to the MWD shaped trace. The MA filter is shown in Eq. 2.2,

$$x_{MA}(n) = \sum_{i=n-L}^{n-1} x_{MWD}(i), \quad (2.2)$$

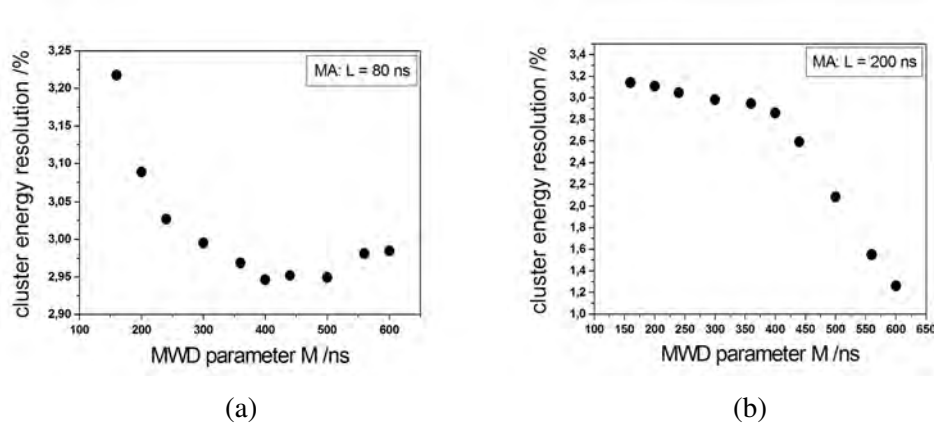
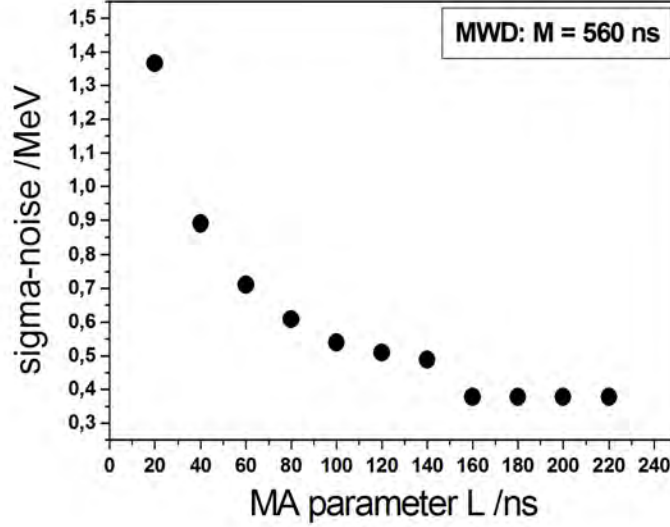


Figure 2.5: Cluster energy as a function of the MWD parameter M for two different MA parameter L

where the parameter L represents the smoothing length responsible to reduce the noise level. The optimization progress of the pulse shape in Fig. 2.4c cannot be seen by eye, but signal fluctuations are suppressed. Nevertheless, this can exemplarily be seen in Fig. 2.6 by plotting the difference of sigma and noise against the parameter L . Similarly behavior was observed for various MWD settings. In the end, the parameter L was set to 80 ns. Furthermore, the significance of the MA filter algorithm increases for low signal heights resulting in an improved energy resolution. The influence of the parameters M and L on the signal shape can be seen in Fig. 2.7.

Finally, the deposited energy in a crystal is proportional to the signal amplitude. The signal amplitude is simply obtained by subtracting the pulse maximum and the baseline (see Fig. 2.8). The baseline is deduced as the average of the first 1200 ns of a trace. Energy in terms of eV is deduced after a calibration. The noise level was obtained by studying noisy traces as depicted in Fig. 2.9. Here, noise is defined as the **Root Mean Square (RMS)** of the baseline. In case of this beamtime the noise was at a level of $\sigma_{\text{noise}} = 0.62$ MeV. Therefore, a crystal threshold of around $3 \cdot \sigma_{\text{noise}} = 1.85$ MeV should be considered. The threshold was further optimized with regard to an optimal relative energy resolution. A so-called threshold scan, where the threshold is varied and the relative energy resolution is obtained, is depicted in Fig. 3.29. The threshold scan identifies for the presented three tagger energies an inflection point at 1.6 MeV. The same behavior was investigated for the other tagger

Figure 2.6: Signal fluctuations for various MA parameter L .

energies. Therefore for this beamtime a summation threshold of 1.6 MeV was set in the analysis.

For extracting the time information, the MA filter is replaced by a **C**onstant **F**raction **T**iming algorithm (CFT) filter. The CFT filter treats the pulse like a conventional analogue **C**onstant **F**raction **D**iscriminator (CFD). The MWD shaped signal is delayed by a parameter D and subtracted by it with a parameter R scaled amplitude. The corresponding algorithm can be found in Eq. 2.3 and the obtained trace can be seen in Fig. 2.4d.

$$x_{CFT}(n) = x_{MWD}(n - D) - R \cdot x_{MWD}(n) \quad (2.3)$$

In order to obtain the timing information a certain number of points are extrapolated with a linear function to determine the zero crossing. Since the obtained traces show an unexpected behavior with a bump in the peak (compare Fig. 2.4d), the time information by the CFT algorithm was considered not reliable.

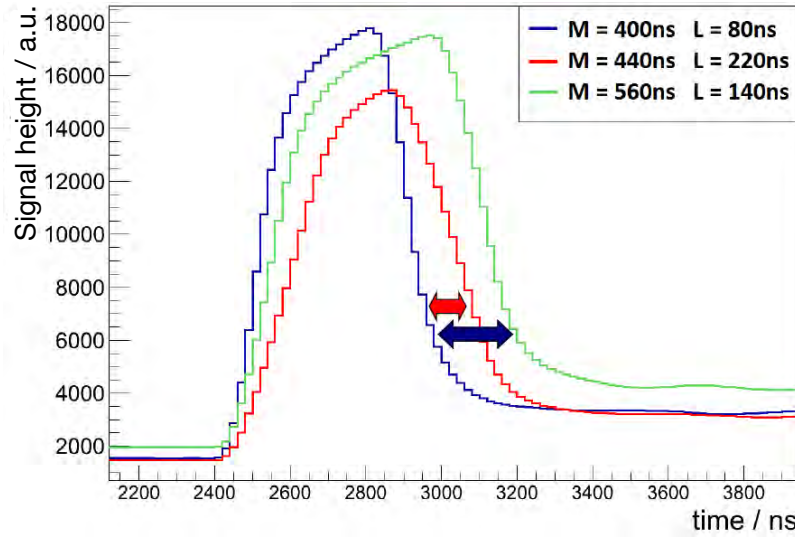


Figure 2.7: Signal shapes after MWD processing for different values of M and L .

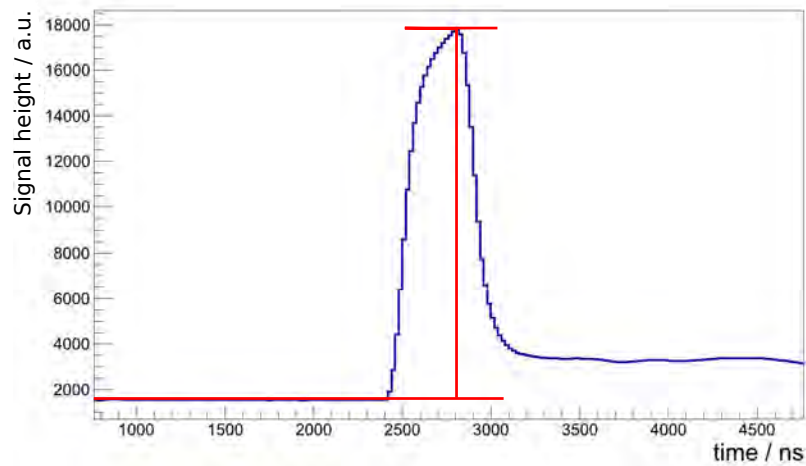


Figure 2.8: Signal shape after MWD and MA with indicated energy extraction (maximum-baseline).

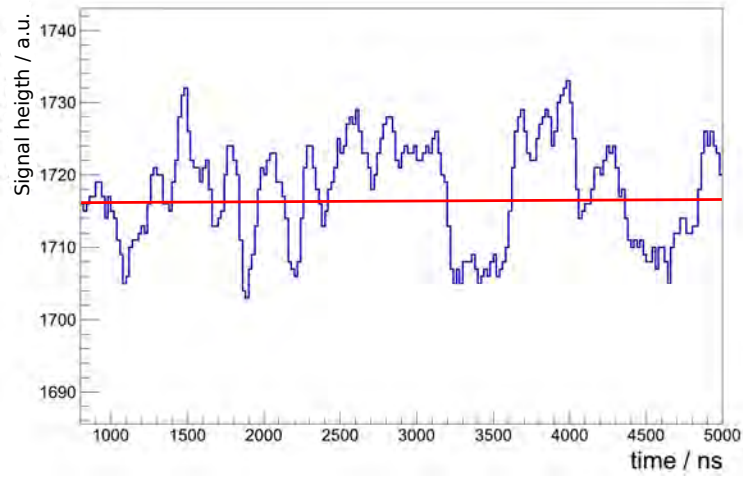


Figure 2.9: Noise event with indicated baseline.

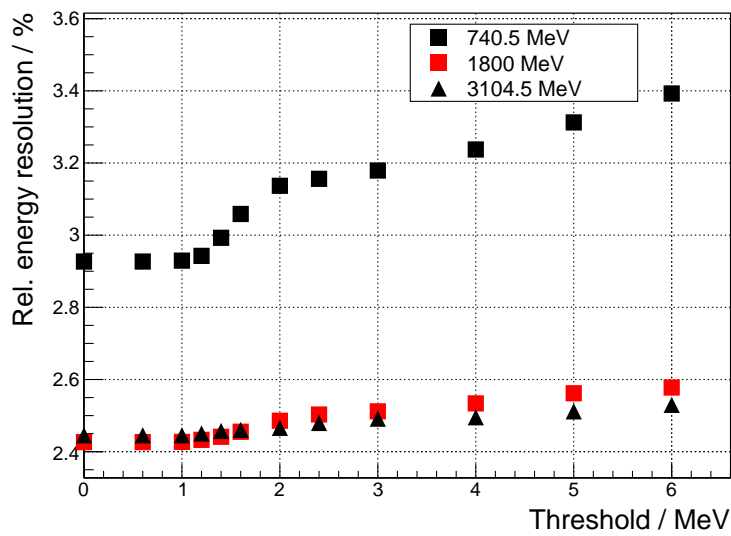


Figure 2.10: Threshold scan for different tagger energies.

2.2 Experimental setup in Bonn

The performance of the PROTO60 has been tested at various accelerator facilities. Beamtimes at **MA**inzer **MI**krotron (MAMI) with photons in an energy range from 50 – 1500 MeV and at **Conseil Européen pour la Recherche Nucléaire** (CERN)-**Super Proton Synchrotron** (SPS) exploiting the 15 GeV/c positron beam showed a sufficient resolution and efficiency fulfilling the requirements stated in the TDR of the $\bar{\text{P}}\text{ANDA}$ EMC [30]. Detailed results of the beamtimes can be found in [40]. Nonetheless, the medium energy range was not covered in these tests. Therefore, a PROTO60 test measurement was performed at the **EL**ektronen **St**retcher **An**lage (ELSA)-Facility in the Rheinische-Friedrich-Wilhelms-Universität in Bonn as a basis for the final design of the $\bar{\text{P}}\text{ANDA}$ Barrel EMC. The beamtime test was carried out at the CBELSA/TAPS experimental area with the exact location depicted in Fig. 2.11. The PROTO60 setup including DAQ, power supply, nitrogen and a vacuum pump was placed downstream of the location of the Crystal-Barrel and **Two Arms Photon Spectrometer** (TAPS) detector. The setup of the PROTO60, relative to the beam, is shown in Fig. 2.12, whereas it was possible to move the prototype in horizontal and vertical direction perpendicular to the beam with a positioning table, the so called x-y-table. The x-y-table is operated by stepper motors monitored by four digital measuring slides. The positioning accuracy is in the order of 0.1 mm. The absolute positioning with respect to the beam direction was conducted with a laser leading to position markers on front and back side of the PROTO60 housing. The markers reflect the vertical symmetry axis of the crystal matrix and divide it horizontally into 3 crystal rows each. In order to identify charged particles, a Veto detector was placed in front of the PROTO60. Charged particles can be created within the Coulomb field of any nucleus on the trajectory of the photons by pair production. The Veto consists of a plastic detector wrapped with reflector material and shrinking tube and is read out with a PMT. The threshold of the plastic detector was set just above the noise level.

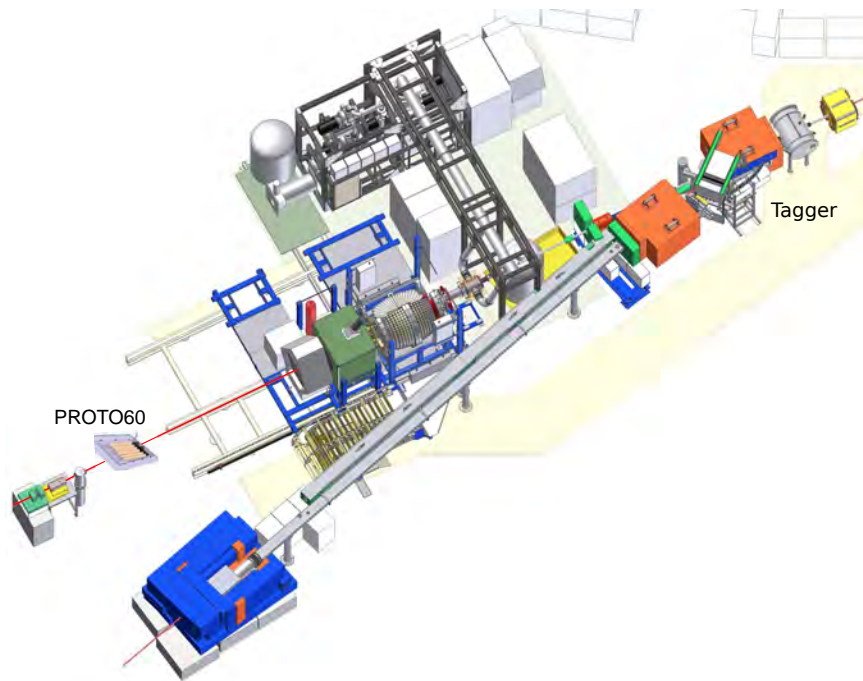


Figure 2.11: CBELSA/TAPS area where the positions of the PROTO60 and the tagger are marked.

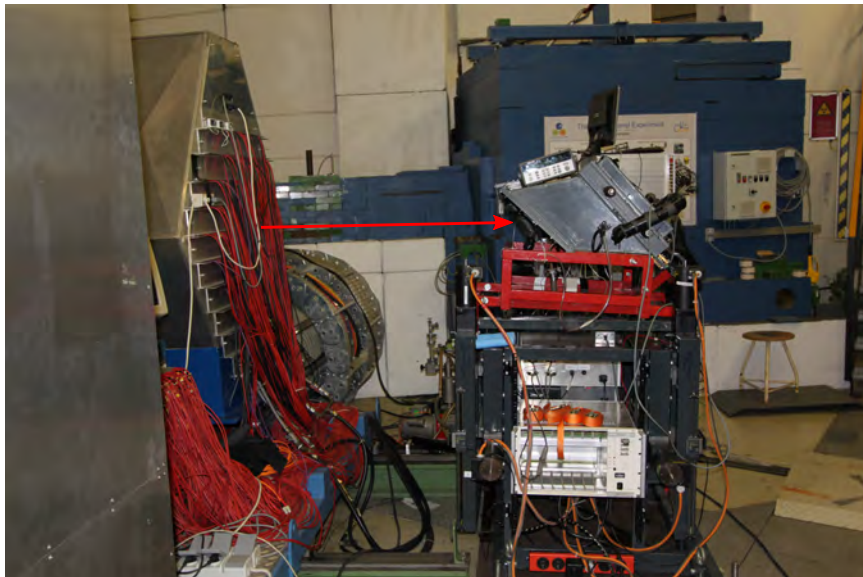


Figure 2.12: Photograph of the PROTO60 setup in Bonn with indicated photon beam.

2.2.1 ELSA

Accelerator

The ELSA-facility [42], shown in Fig. 2.13, is a three stage electron stretcher accelerator consisting of a linear accelerator, a booster synchrotron and a stretcher ring. The facility is able to provide two electron sources which are accelerated to a maximum energy of 3.5 GeV. The first electron source emits unpolarized electrons from a 48 keV thermal source, while the second source produces longitudinally polarized electrons via photoemission induced by a circularly polarized laser beam incident on a GaAs-like crystal. The electrons are injected into two kinds of **LINear ACcelerator**s (LINACs). LINAC1 provides unpolarized electrons whereas LINAC2 provides linearly polarized electrons. The two LINACs pre-accelerate the electrons up to 20 MeV or 26 MeV, respectively. In a next step the electrons are accelerated to an energy up to 1.6 GeV in a booster synchrotron. After that the electrons are injected as bunches into the stretcher ring with a frequency of 50 MHz. The stretcher ring can be operated in three different modes, depending on the requirements of the respective experiment: The *stretcher mode* delivers a quasi-continuous beam by slowly extracting the electrons to the experimental area without further acceleration. In the *post-accelerator mode* the electron bunches are accumulated, stretched and accelerated to a maximum energy of 3.5 GeV. During the PROTO60 test measurement ELSA was operated in this mode. The third mode, the so-called *storage mode*, keeps the electron beam in the stretcher ring with a constant energy and high beam current to study synchrotron radiation.

Photon beam

The aim of the PROTO60 test is the investigation of the response of the PROTO60 to photons. For this, photons within the energy range of interest have to be produced from the primary electron beam. The photon beam for the CBELSA/TAPS experimental area, where the PROTO60 test setup is located, is produced via bremsstrahlung of electrons. Electrons passing through matter lose energy by three processes: ionization, radiation of bremsstrahlung and Møller scattering. The relative strength of these

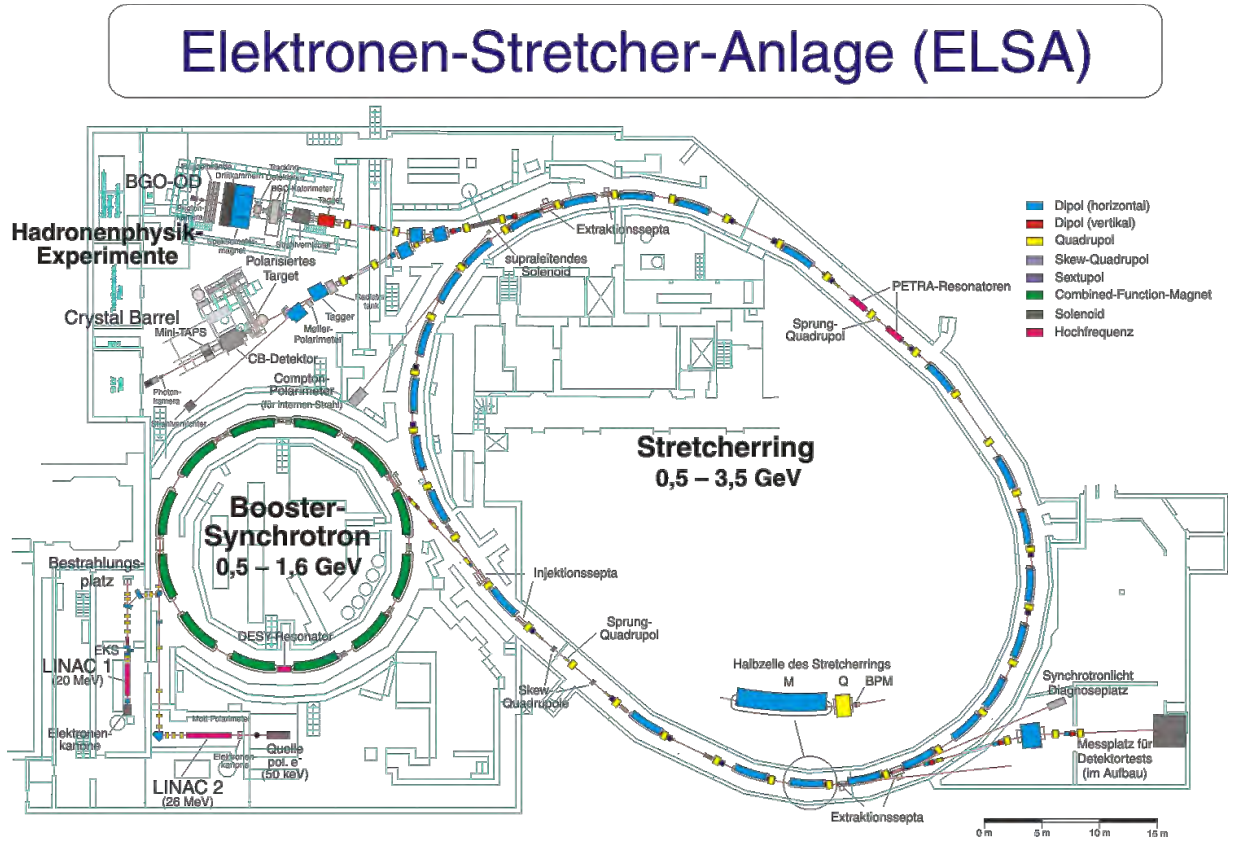


Figure 2.13: Floor plan of the ELSA-facility [42].

contributions as functions of the incoming electron energy is depicted in Fig. 2.14. Møller scattering is generally a low contribution to the energy loss of electrons. In the low energy regime ionization is the leading contribution, while bremsstrahlung dominates above 10 MeV in case of Pb. These two processes are equal at the critical energy, E_c which can be approximated by [43]

$$E_c = \frac{800 \text{ MeV}}{Z + 1.2}, \quad (2.4)$$

for each radiator material. The primary electrons with the energy E_0 are collided with a radiator, either a copper foil or a diamond. The approximation in Eq. 2.4 leads to critical energies of $E_c \approx 26.5 \text{ MeV}$ for copper and $E_c \approx 111 \text{ MeV}$ for diamond (carbon). These values are well below the primary electron beam energy and

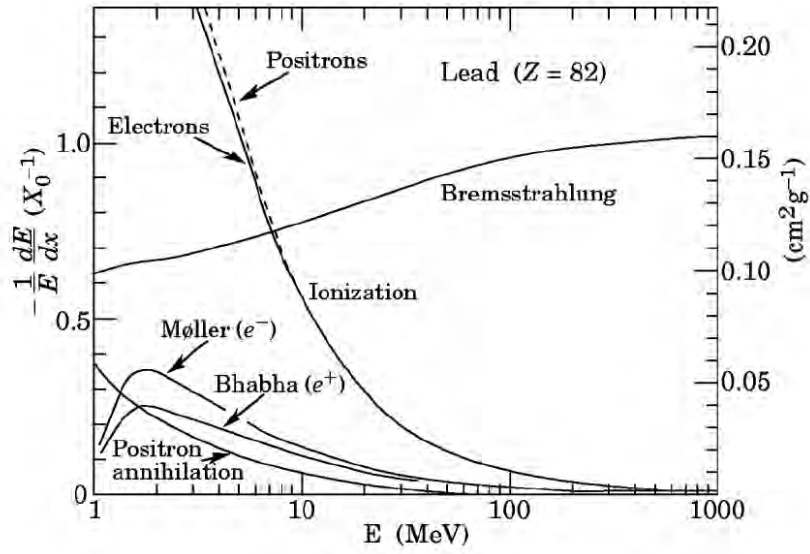


Figure 2.14: Fractional energy loss per radiation length in lead as a function of the incoming electron energy. At typical ELSA energies bremsstrahlung clearly dominates. [24]

therefore bremsstrahlung is the relevant process. Thus, the primary electrons interact via Coulomb interaction with the nuclei of the radiator. Inside the electric field of the nucleus the electron produces a real photon according to the bremsstrahlung process shown in Eq. 2.5.



The maximum energy of the produced photons is given by the energy loss of the primary electrons after the bremsstrahlung process

$$E_\gamma = E_0 - E_{e^-}^{\text{after}} \quad (2.6)$$

with the measured electron energy after the bremsstrahlung process $E_{e^-}^{\text{after}}$. The energy distribution can be described by the expression

$$N_\gamma \sim \frac{1}{E_\gamma} \quad (2.7)$$

for energies in the region $0 < E_\gamma \leq 0.8 \frac{h \cdot f}{E_{max}}$. The average half-angle of the emitted photons defined by

$$\sqrt{\langle \Theta^2 \rangle} = \frac{1}{\gamma} = \frac{m_e c^2}{E} \quad (2.8)$$

is less than 0.5 mrad at typical ELSA energies. Therefore, the photon beam is collimated quite well since it points into the direction of the electron beam. In case of this beamtime the collimator had a diameter of 4 mm. The beam profile was measured with a photon camera during the beam test several meters away from the target. The diameter of the photon beam was 5 mm.

Tagger

The tagging system determines the energy of the photons produced via bremsstrahlung of the incoming electrons. The tagger, a magnetic electron spectrometer, consists of a horizontally deflecting magnet operated at maximum current of 1500 A, which corresponds to a maximum magnetic field of 2 T, and 96 overlapping plastic scintillator bars read out with PMTs. A Computer-Aided Design (CAD) drawing of the Tagger is shown in Fig. 2.15.

The energy-momentum conservation for each event is given by Eq. 2.6 and holds true since the energy of the incoming electrons E_0 is known with high precision ($\frac{\Delta E}{E} = 0.09\%$ at 3.5 GeV) and the momentum transfer to the radiator nuclei is considered negligible. Therefore, the energy of the generated photon equals the energy loss of the electron and it requires to obtain the remaining energy of the electron to determine the energy of the corresponding photon. For relativistic electrons the energy is approximately equal to the momentum and thus the energy of the deflected electron can be calculated by

$$E_{e^-} = p_{e^-} \cdot c = B \cdot r \cdot c \cdot e \quad \text{for} \quad p_{e^-} \gg m_{e^-} \quad (2.9)$$

with magnetic field B and bending radius r of the electron track. Since the cross section for bremsstrahlung is relatively small, most of the electrons do not interact

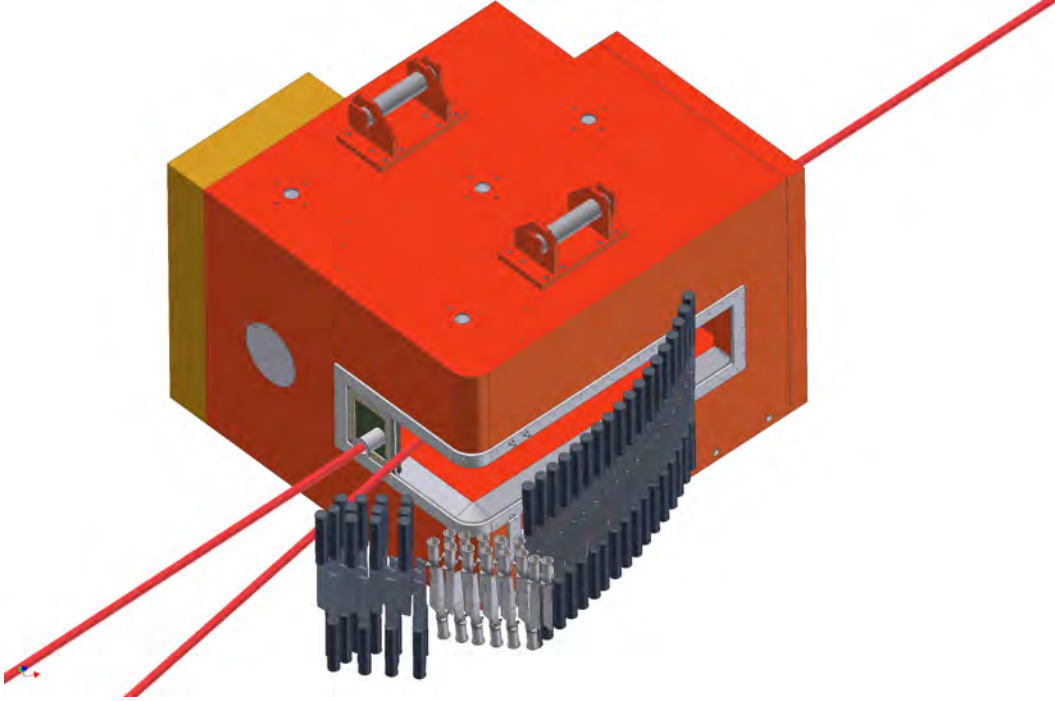


Figure 2.15: CAD model of the tagger magnet and the 96 scintillator bars [44].

according to the bremsstrahlung process. These electrons are discriminated via their energy E_0 and deflected into the electron beam dump. Finally, the energy of the generated photon can be calculated with the following equation:

$$E_\gamma = E_{e^-}^{\text{accelerator}} - E_{e^-}^{\text{measured}} \quad (2.10)$$

with the known initial energy of the electron $E_{e^-}^{\text{accelerator}}$. The deflected electrons are detected by the 96 plastic scintillator bars in the focal plane of the magnet which cover the range between 18% and 96% of the electron-beam energy as depicted in Fig. 2.16. The scintillator bars are read out by two photomultipliers each whose signals are processed by **T**ime-to-**D**igital **C**onverters (TDCs) and **C**harge(**Q**)-to-**D**igital **C**onverters (QDCs) and counted by scalars. The energy resolution for the tagger bars shown in Fig. 2.17b varies between 14% for low energy photons and 0.3% for the highest energies due to their size.

In order to improve the energy resolution for low energy photons the tagging system was upgraded with a upstream fiber detector consisting of 480 scintillating fibers

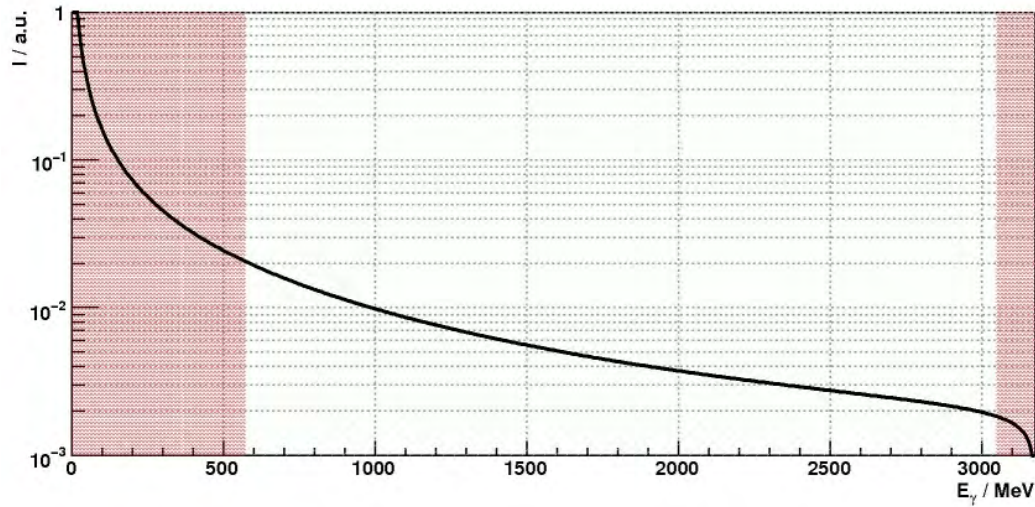


Figure 2.16: Energy coverage of the tagger for an incident electron energy of 3.2 GeV (shaded energy regions are not tagged) [45].

grouped within 30 overlapping modules. The fibers are read out by multi-anode photomultipliers in sets of 16, whose signals are processed by multi-hit TDCs and counted by scalars. The energy resolution for the tagger fibers varies from 3.9% for low energy photons to 0.07% for the highest energies (see Fig. 2.17a).

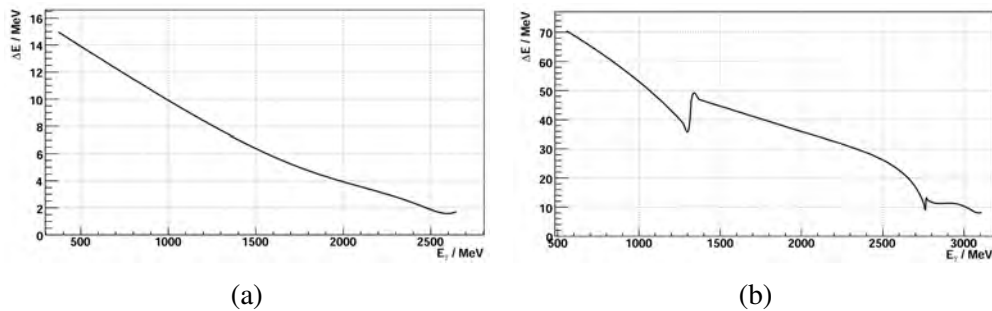


Figure 2.17: Intrinsic tagger energy resolution for the tagger fibers (a) and tagger-bars (b) [45].

During the commissioning of the detector setup the tagger was calibrated. With the energy calibration shown in Fig. 2.18 it is possible to derive the real photon energy from the tagger bar or fiber hit by a deflected electron. Moreover, this data is fitted with a polynomial in order to obtain a calibration function. A certain fraction of the

bars and fibers was not directly accessible for calibration. Those were calibrated by extrapolating the existing data with the help of a **GEometry ANd Tracking Version 4** (Geant4) simulation. The final energy calibration in MeV is then given by the following polynomials:

$$\begin{aligned}
 E_{\gamma}^{bars(1-34)} = E_0 & \\
 & \cdot (0.981551858 \\
 & - 2.677455348 \cdot 10^{-3} \cdot x \\
 & + 5.948036477 \cdot 10^{-5} \cdot x^2 \\
 & - 8.104094833 \cdot 10^{-6} \cdot x^3 \\
 & + 2.842305724 \cdot 10^{-7} \cdot x^4 \\
 & - 3.286101393 \cdot 10^{-9} \cdot x^5) \tag{2.11}
 \end{aligned}$$

$$\begin{aligned}
 E_{\gamma}^{bars(35-81)} = E_0 & \\
 & \cdot (0.074848493 \\
 & + 0.070512336 \cdot x \\
 & - 2.230723412 \cdot 10^{-3} \cdot x^2 \\
 & + 3.22108407 \cdot 10^{-5} \cdot x^3 \\
 & - 2.380053524 \cdot 10^{-7} \cdot x^4 \\
 & + 6.866668345 \cdot 10^{-10} \cdot x^5) \tag{2.12}
 \end{aligned}$$

$$\begin{aligned}
 E_{\gamma}^{bars(82-96)} = E_0 & \\
 & \cdot (-1.199255027 \\
 & + 0.050839352 \cdot x \\
 & - 3.804562119 \cdot 10^{-3} \cdot x^2) \tag{2.13}
 \end{aligned}$$

$$\begin{aligned}
 E_{\gamma}^{fibers} = & E_0 \\
 & \cdot (0.834852997 \\
 & - 4.972545291 \cdot 10^{-4} \cdot x \\
 & + 7.807181044 \cdot 10^{-7} \cdot x^2 \\
 & - 1.451094725 \cdot 10^{-8} \cdot x^3 \\
 & + 4.391997834 \cdot 10^{-11} \cdot x^4 \\
 & - 5.392772359 \cdot 10^{-14} \cdot x^5)
 \end{aligned} \tag{2.14}$$

where x is the tagger bar and fiber index, respectively. For the beamtime test with the

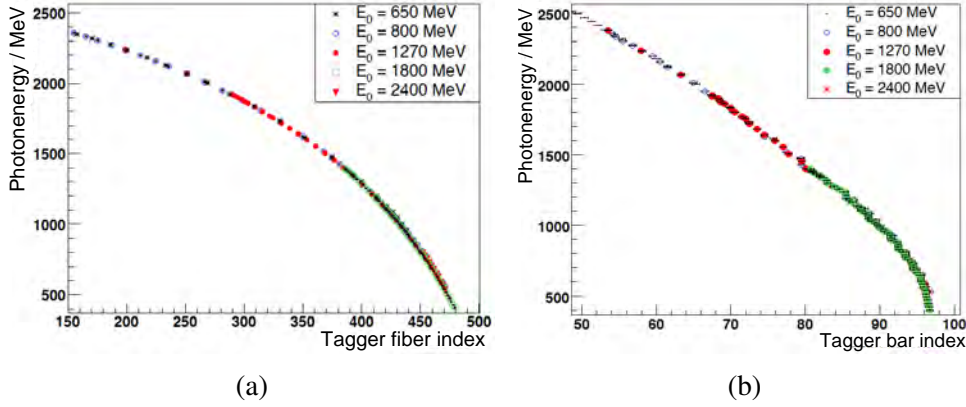


Figure 2.18: Energy calibration for the tagger fibers (a) and tagger bars (b) for different beam energies [45].

PROTO60 two different tagger configurations were chosen. The first configuration was a logical OR of 8 single bars (see Fig. 2.19a). An energy cut on the peaks in the spectrum gives 8 energy channels. The other configuration was a logical OR of all bars in either a low, medium and high energy region. In this case an energy cut on single bins was applied giving various numbers of energy channels. Due to the fact that the energy resolution of the tagged photons is energy dependent, both energy cuts were chosen according to the absolute energy resolution shown in Fig. 2.20.

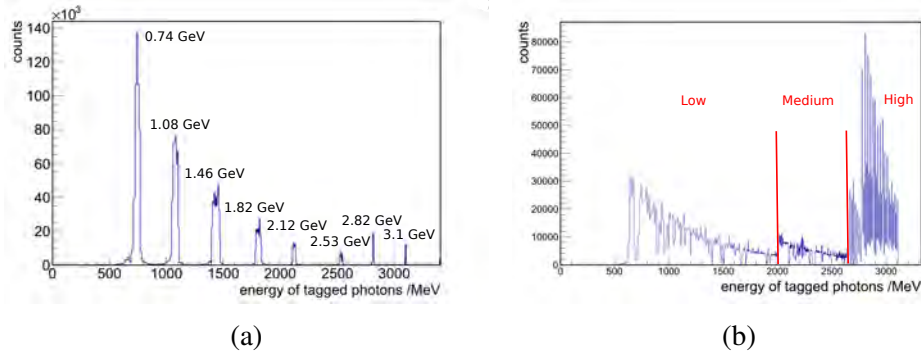


Figure 2.19: Tagger configuration with a logical OR of 8 single bars (a) and of all bars one region (b). Variable binning has been applied.

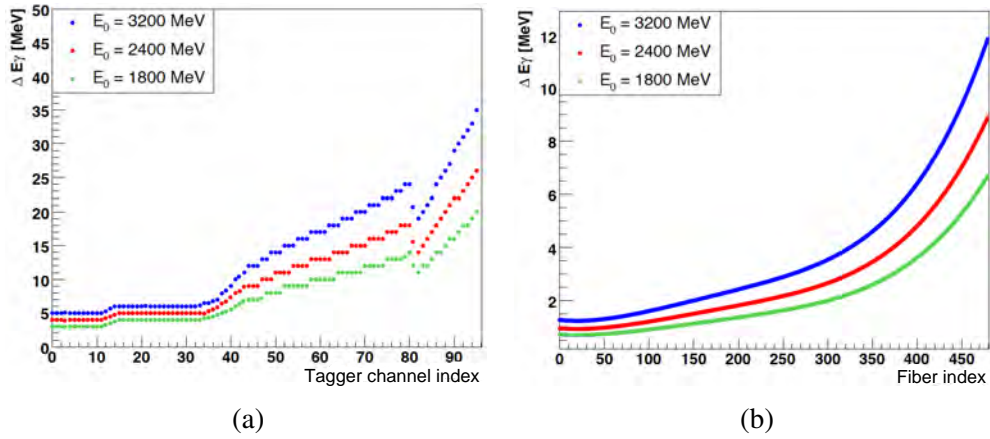


Figure 2.20: Absolute energy resolution for two neighboring tagger bars (a) and the tagger fibers (b) [45].

2.2.2 Beamtime procedure

The performed program in the 2013 beamtime at ELSA is described in this paragraph. Fig. 2.21 shows a schematic crystal map of the PROTO60 with indicated 3x3 and 6x6 crystal matrices, respectively. Altogether twenty runs were performed with different

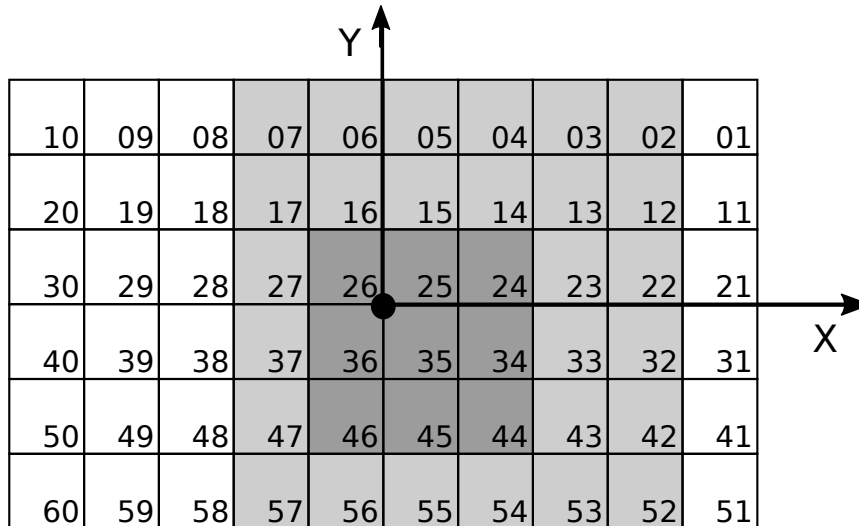


Figure 2.21: Schematic crystal map of the PROTO60. Indicated are the crystal numbers and a 3x3 and 6x6 crystal matrix. The PROTO60 coordinate system is indicated with a x- and y-axis with its origins marked.

experimental setups, point of impact and tagger configurations. All the runs are listed in Tab. 2.4. The corresponding point of impact positions are shown schematically in Fig. 2.22. The aim of the beamtime was to study the detector resolution in this energy region and additionally the effect on the performance for different point of impact positions. Furthermore, the influence of dead material in front of the detector was studied. For the calibration of the detector cosmic radiation was measured afterwards in Gießen with the same detector settings. This measurement could not be performed in Bonn due to an unavailable time slot during the beam time. A sufficient amount of cosmic radiation data can only be collected over at least a few days.

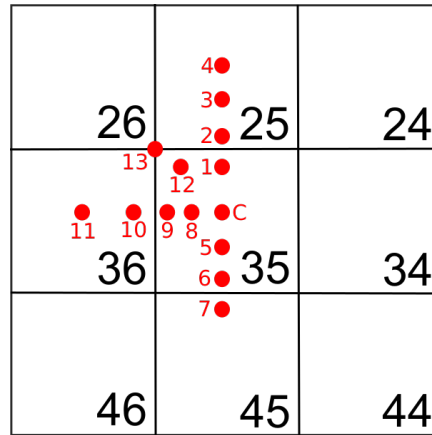


Figure 2.22: 3×3 matrix out of the PROTO60 with marked beam positions and crystal numbers.

Run number	Tagger	Beam position / configuration	Number of Vetos
1	8 energies	center of crystal 35	1
2	low region	center of crystal 35	1
3	high region	center of crystal 35	1
4	medium region	center of crystal 35	1
5	high region	center of crystal 35 + Quartz	2
6	8 energies	center of crystal 35 + Quartz	2
7	lowest range of the 8 energies	center of crystal 35 + Quartz	2
8	8 energies	Pos. 1 (11/-3.5)	1
9	8 energies	Pos. 2 (11/1.5)	1
10	8 energies	Pos. 3 (11/6.5)	1
11	8 energies	Pos. 4 (11/11.5)	1
12	8 energies	Pos. 5 (11/-13.5)	1
13	8 energies	Pos. 6 (11/-18.5)	1
14	8 energies	Pos. 7 (11/-23.5)	1
15	8 energies	Pos. 8 (6/-8.5)	1
16	8 energies	Pos. 9 (1/-8.5)	1
17	8 energies	Pos. 10 (-4/-8.5)	1
18	8 energies	Pos. 11 (-9/-8.5)	1
19	8 energies	Pos. 12 (-4/-4)	1
20	8 energies	Pos. 13 (0/0)	1

Table 2.4: Beam positions for the beamtime.

2.3 Analysis

2.3.1 Energy calibration

The deposited energy of a particle impinging the crystal matrix is distributed over several crystals. Therefore, the response of the detector modules has to be aligned. Furthermore, the pulse height signal in terms of voltage needs to be converted into energy. In principle one has to distinguish between two iterative steps, a relative and absolute calibration, composed to an energy calibration. In a relative calibration, the signal caused by a certain energy deposition is normalized to a reference crystal. In order to test the performance of a prototype detector, an energy resolution obtained with a relative calibration is sufficient. In an absolute calibration, the summed energy of the detector is calibrated to the real deposited energy. The composed energy calibration is then given by

$$E_{cal} = C_{abs} \cdot \sum_i S_i(t) \cdot c_i \cdot E_{i/uncal} \quad (2.15)$$

with the uncalibrated pulse height signal $E_{i/uncal}$, a relative calibration factor c_i and an absolute calibration factor C_{abs} . The factor $S_i(t)$ takes into account signal loss due to radiation damage. For beamtimes short in time and a reasonably low radiation dose the factor $S_i(t)$ can be assumed as constant.

There are different possibilities to calibrate a detector with respect to the described general procedure. In the beamtime at ELSA in Bonn the PROTO60 was calibrated via cosmic radiation. Interesting events for the calibration are exclusively generated by traversing cosmic muons. A coincidence of the top and bottom crystal row was chosen as trigger condition. In this case an interpenetration of the complete detector is guaranteed. Furthermore this trigger condition is in favor of background suppression. Additionally, only events where all six crystals of one column produce a signal above a threshold were taken into account. This threshold has to be well above the noise threshold, in the present case at 10 MeV. In this way obtained line shapes can be fitted with a Landau distribution without fit-range restrictions as depicted in Fig. 2.23. For a relative calibration, muon signals of each crystal are divided by the response

of a reference crystal. A relative calibration factor F , which aligns all cosmic peak positions Δ_p to the value X , can be obtained by

$$F = \frac{X}{\Delta_p - \text{ped}_p}. \quad (2.16)$$

In order to obtain an absolute energy calibration the new peak position has to be set to the corresponding energy. Therefore, an energy has to be assigned to the value F . Cosmic muons are assumed to be MIPs and deposit $10.2 \text{ MeV} \cdot \text{cm}^{-1}$ inside lead tungstate [24]. Further, one can assume that the energy deposition is almost constant. The average vertical path length through a horizontally aligned type 6 crystal is 24.032 mm, which corresponds to a deposition of 24.513 MeV [33]. The simulation model of the PROTO60 for the simulation of cosmic muons will be described in Sec. 2.4.3. This method has one major uncertainty which is the impact of the Non-Uniformity (NUF) in light collection.

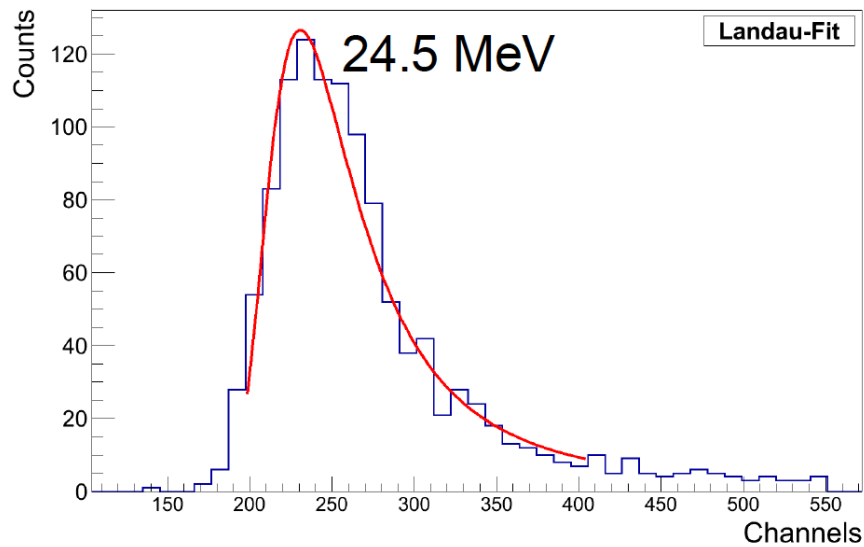


Figure 2.23: Deposited energy spectrum of cosmic radiation in crystal 35 after the column cut. The most probable value Δ_p is obtained with a Landau-fit.

2.3.2 Lineshapes

In order to reconstruct the energy deposition in the detector, the contribution from each crystal in a crystal matrix needs to be added. Before adding a summation threshold is applied. Due to the common readout of all detector modules, responding crystals are selected by applying a signal threshold to minimize the contribution of pure noise. In particular, the energy deposition for low energy photons, which distribute their energy only over a few modules, can be faked by noise. Fig. 2.24 shows the lineshapes of run1 for a summed matrix of 6x6 crystals with a summation threshold of 1.6 MeV. The line shape for the reconstructed energy is asymmetric due to

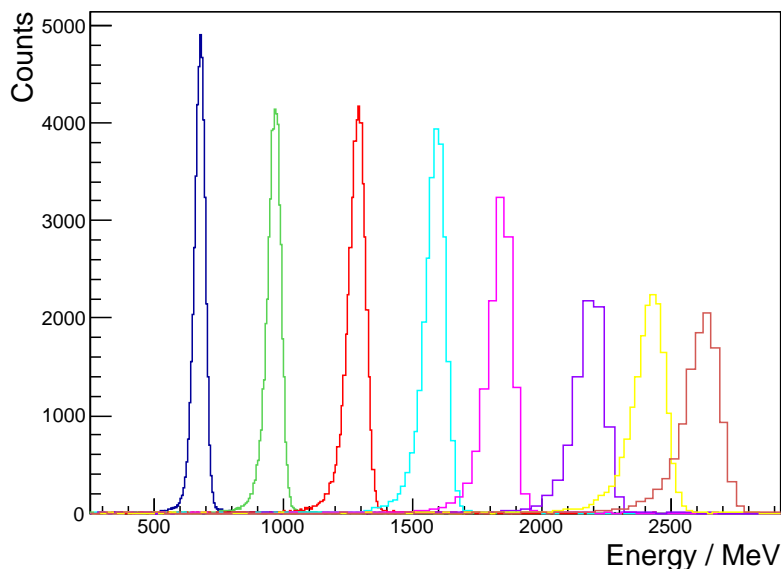


Figure 2.24: Summed lineshapes for a matrix of 6×6 crystals with a summation threshold of 1.6 MeV for the 8 tagger energies (run1). Various binning for the different tagger energies is applied.

energy leakage out of the detector and absorption within dead material which leads to an incomplete energy deposition within the active volume. A skewed Gaussian distribution describes the distribution of the total energy deposit of monoenergetic photons interacting in a detector very well. The so-called “Novosibirsk function” is

a commonly used function (example can be seen in Fig. 2.25). It is defined by

$$f(x) = Ae^{-\frac{1}{2}\left(\frac{\ln^2(1+\Lambda\tau(x-\mu_{max}))}{\tau^2} + \tau^2\right)} \quad (2.17)$$

where

$$\Lambda = \frac{\sinh(\tau\sqrt{\ln 4})}{\sqrt{\ln 4}\tilde{\sigma}} \quad (2.18)$$

is parametrized by the asymmetry τ , width $\tilde{\sigma} \equiv \frac{\text{FWHM}}{2\sqrt{\ln 4}}$ and mode μ_{max} which is the value that is most likely to be observed in a measurement [46].

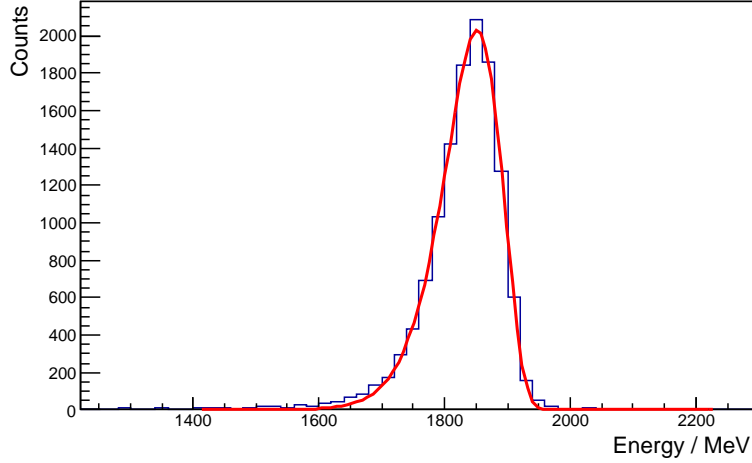


Figure 2.25: Summed lineshape for a matrix of 6×6 crystals with a summation threshold 1.6 MeV for one tagger energy (run1) and fitted Novosibirsk function.

2.3.3 Linearity

For a reliable energy measurement a linear response is necessary. There are various reasons for a nonlinear response like saturating preamplifier, inhomogeneities in the crystal material or the nonlinear light collection. In order to verify a linear response, the reconstructed energy is plotted versus the incident beam energy. A linear response

could be verified for this beam test and an example is shown in Fig. 2.26.

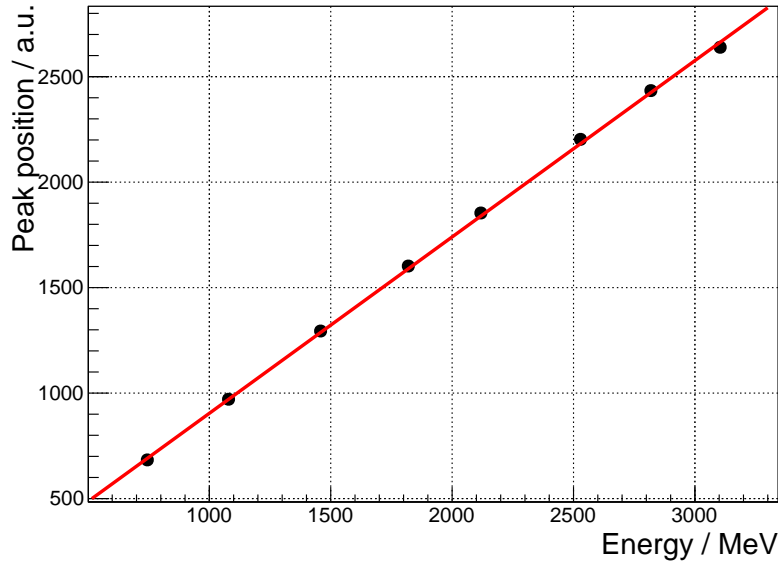


Figure 2.26: Reconstructed energy vs. beam energy for the 8 tagger energies (run1).

2.3.4 Multiplicity

The multiplicity is defined as the number of crystals for one event which create a signal above the software threshold. It depends on the beam energy, the value of the threshold and matters to statistical fluctuations. The mean value is obtained by fitting a Gaussian to the distribution of all events. The multiplicity as a function of the 8 tagger energies can be seen in Fig. 2.27 for different threshold values.

2.3.5 Energy resolution

Stochastic processes play an important role in the read-out of a scintillating detector interacting with a photon. The light creation process inside the scintillator, the light conversion process in the photomultiplier and the electronic noise from the electronics cause statistical fluctuations. Furthermore, leakage of light causes fluctuations in

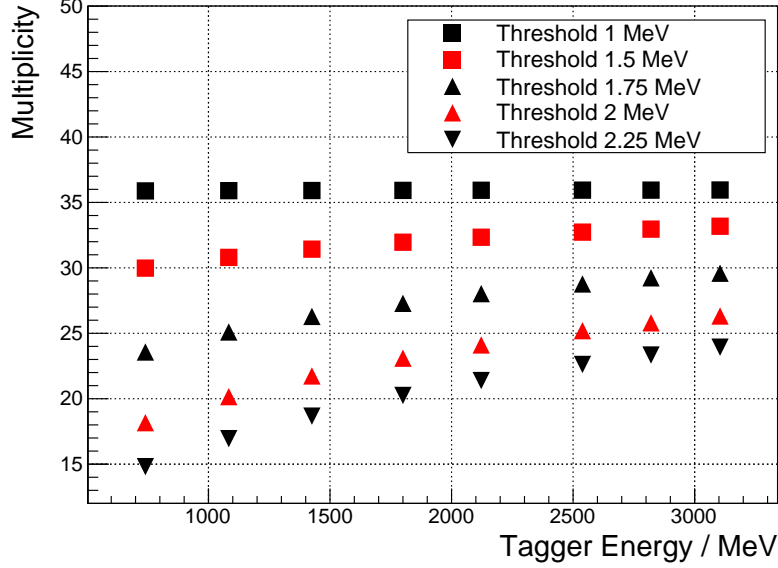


Figure 2.27: Multiplicity as a function of the beam energy for various thresholds.

deposited energy. All these contributions can not be determined precisely. An estimate of the contributions can be determined by measuring the total fluctuations in the signal under various conditions. Three contributions are commonly included for describing the energy resolution of calorimeters.

The *Poisson statistics* of the light collection process is one contribution. The variance of such a distribution is $\sigma^2(N) = N$, where N is the number of photoelectrons in the photomultiplier. This number is proportional to the deposited energy and described by the relation $N = \beta E$. The constant factor β is dependent on the material, light transport and quantum efficiency of the sensor. The energy determination has the following uncertainty [47]:

$$\sigma_P(E) = \frac{1}{\beta} = \sqrt{\frac{E}{\beta}} \quad (2.19)$$

Since PWO has not a high light yield, the contribution from Poisson statistics to the relative resolution σ/E is rather large. Therefore, good wrapping of the crystals with a specular reflective foil is essential to secure high efficiency in collecting the created light.

Another contribution comes from *electronic noise*. This contribution is independent of the deposited energy. Therefore the contribution is

$$\sigma_N = b \quad (2.20)$$

where b is the RMS noise.

The last contribution comes from *crystal properties* and *leakage of energy*. Examples for this contribution are NUF of the produced light inside the crystal, radiation damage and temperature gradients. Leakage depends on the overall volume in lateral and longitudinal dimensions. But even part of the shower is scattered backwards and remains undetected. These effects are linear proportional to the energy because they are proportional to the signal strength:

$$\sigma_C(E) = c \cdot E \quad (2.21)$$

If variables are uncorrelated and the underlying distributions are convoluted, then the variances add as:

$$\sigma_{1+2}^2 = \sigma_1^2 + \sigma_2^2 \quad (2.22)$$

Thus, the variance of the energy resolution has the form

$$\sigma_E = \sigma_P(E)^2 + \sigma_N^2 + \sigma_C(E)^2 = a^2 E + b^2 + c^2 E^2 \quad (2.23)$$

where $a^2 = 1/\beta$.

The required response of the \bar{P} ANDA EMC is shown in Tab. 1.2. They correspond to the values $a = 2500$ photoelectrons per GeV, $b = 1$ MeV and $c = 0.01$.

Obtained energy resolution

To obtain the energy resolution of the PROTO60 the summed lineshapes for different beam energies are fitted with a Novosibirsk function (see Eq. 2.17). The fitted lineshapes for the 8 tagger energies are depicted in Fig. 2.28. The energy resolution is

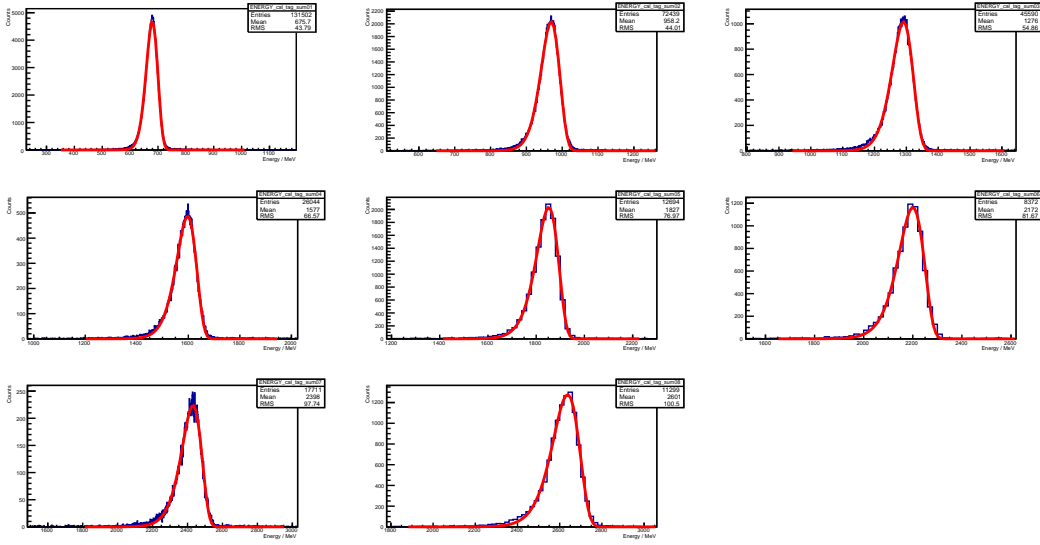


Figure 2.28: Lineshapes for the 8 tagger energies and a matrix of 6×6 crystals with a summation threshold 1.6 MeV (data from run1). Fitted is a Novosibirsk function with reference to Eq. 2.17. Note that the single histograms are zoomed in.

then defined by

$$\frac{\sigma_E}{E} = \frac{\tilde{\sigma}}{\mu_{max}}. \quad (2.24)$$

The energy resolution for the PROTO60 for a matrix of 6×6 crystals with the beam impinging the center of the central crystal of the matrix is shown in Fig. 2.29. The data is fitted with the function in Eq. 2.23. The following parametrization of the relative energy resolution could be obtained:

$$\frac{\sigma}{E} = \frac{1.43\%}{E/\text{GeV}} \oplus \frac{0.01\%}{\sqrt{E/\text{GeV}}} \oplus 2.37\%. \quad (2.25)$$

An energy resolution of 2.8% at 1 GeV could be achieved at this beamtest in Bonn. The energy resolution of the 6×6 matrix is compared with a matrix of 3×3 crystals in Fig. 2.30 in order to study the containment of energy distribution in the first and second ring. The energy resolution for a 3×3 matrix is inferior to a 6×6 matrix. At 1 GeV the energy resolution for a 3×3 matrix is 3.1%. The energy resolution seems

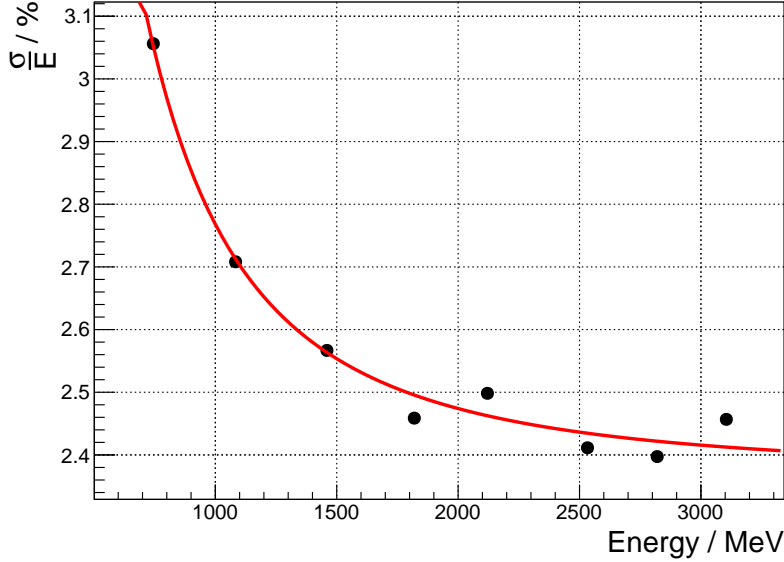


Figure 2.29: Energy resolution for a matrix of 6×6 crystals with a summation threshold 1.6 MeV and data from run1. Fit function with reference to Eq. 2.25.

to be strongly dependent on the number of rings. Additionally, the energy resolution for different shaping parameter values of M and L are compared (see Fig. 2.31). Finally, the energy resolutions for the two tagger configurations are compared in Fig. 2.32. Here, the energy resolution obtained for energies below around 1.5 GeV are similar, but differ significantly at energies above 2 GeV depending on the tagging version.

2.3.6 Position resolution

The basic algorithm for determining the position of a photon hitting the $\bar{\text{P}}\text{ANDA}$ calorimeter is similar to the one used in the **B** and **B-bar** (BaBar) experiment. The method is investigated by B.B. Brabson et al. in [48]. The procedure starts with finding a cluster of hits from crystals with a signal above a threshold. After that a bump splitting procedure is applied since it is possible that a cluster can be the result of more than one photon striking the calorimeter (i.e. two overlapping clusters). In the experiment at ELSA one could expect only single photon events, due to the relatively

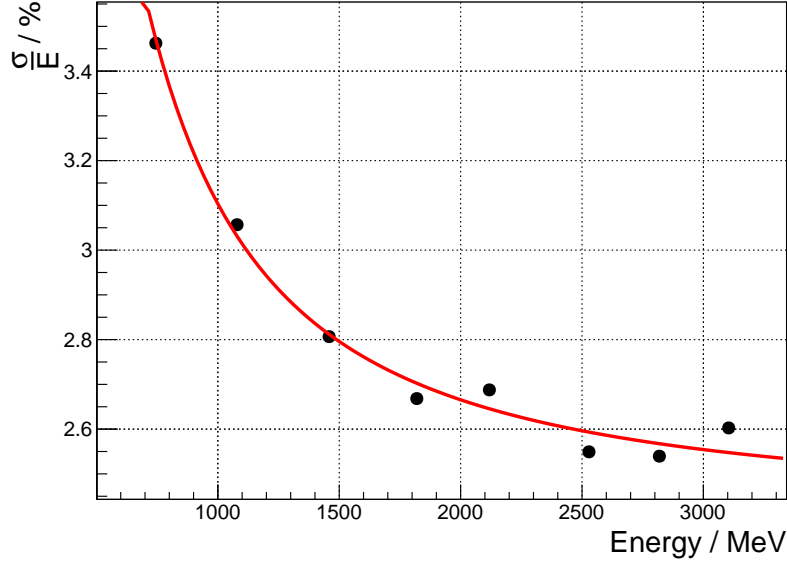


Figure 2.30: Energy resolution for a matrix of 3×3 crystals. Data from run1 with a summation threshold of 1.6 MeV.

low intensity of the beam. Further information about the cluster finding procedure is given by Ferguson [49] and about the bump splitting in the \bar{P} ANDA EMC technical design report [30].

A photon is completely described with a four-vector. For the four-vector not only energy information but also the momentum component is needed. The spatial resolution is basically given by the granularity of the detector ($\sigma_{x/y} = 1/\sqrt{12}$). It can be improved significantly below the size of the individual modules with many different methods. All methods use the observed division of energy among the crystals to estimate the impact position (x_{pos}, y_{pos}) depending on the Molière radius R_M of the individual modules. In case of the PROTO60 with crystals of a diameter comparable to R_M , most of the energy is deposited in the central crystal, but some of the energy escapes from the central crystal. Due to the narrow distribution in transverse dimensions, for an improved position resolution an extra weight is associated to the energies that are deposited in the outer crystals. This method is described in the next paragraph. The method is also applied for positions when the beam was not directed

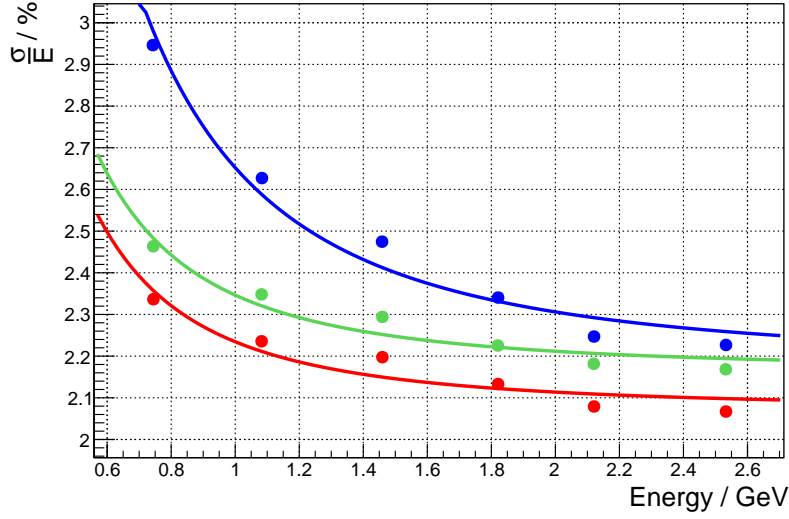


Figure 2.31: Energy resolution for the shaping parameters $M = 440$ ns, $L = 220$ ns (red) compared with $M = 560$ ns, $L = 140$ ns (green) and with $M = 400$ ns, $L = 80$ ns (blue). Data from run1 with a summation threshold of 1.6 MeV.

at the center of a crystal. These positions were shown in Fig. 2.22.

Impact position for the weighted mean

Various algorithm developed by Brabson [48] have been considered to determine the impact position (x_{pos}, y_{pos}) of a photon initiating an electromagnetic shower within the PWO-II array. Each of these methods is based on the weighted mean

$$x_c = \frac{\sum_J^N w_J(E_J) \cdot x_J}{\sum_J^N w_J(E_J)}. \quad (2.26)$$

Here, x_c is the calculated x-position of where the photon hits the detector. The same formula holds for the y-position. The sum is carried out over all the crystals within an array. The weight, $w_J(E_J)$, is a function of the energy of the Jth crystal. In this

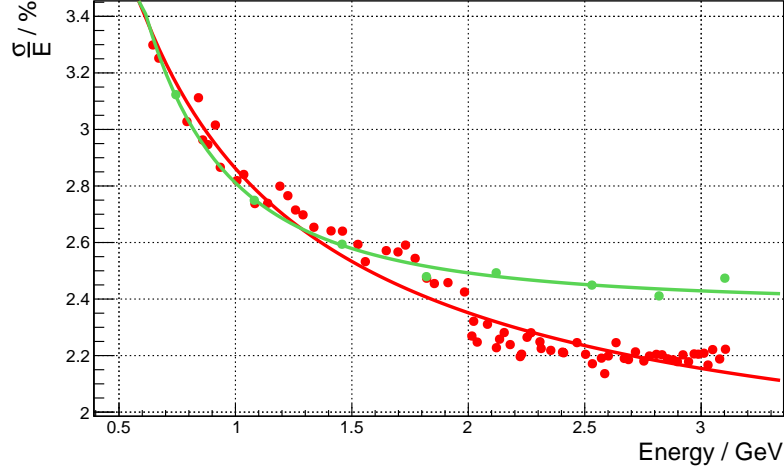


Figure 2.32: Energy resolution for a matrix of 6×6 crystals with tagger configuration "three regions" (red) compared with "8 energies" (green). Data from run1 with a summation threshold of 1.6 MeV.

thesis only the well established logarithmic weighting function

$$w_J(E_J) = \text{Max} \left\{ 0, a_0 + \ln \frac{E_J}{E_{tot}} \right\}, \quad (2.27)$$

is considered where E_{tot} is the total energy in all crystals and a_0 an energy dependent factor. The PANDA EMC technical design report states that a_0 varies from 2.1 for low energies to 3.6 for high energies [30].

Results on the position resolution

For the analysis of the beamtime test in Bonn the energy dependent factor $a_0 = 4.4$ was chosen. The factor was optimized for the energy range. A still gaussian distribution was required at low energies. The reconstructed impact positions with a logarithmic weighting function (see Eq. 2.27) for run1 are shown in Fig. 2.33 for 8 different photon energies. The beamspot has been reconstructed in Fig. 2.34. The actual beamsize of $\sigma \approx 5$ mm has been measured with a photcamera. The position resolution is obtained by fitting a Gaussian to the distribution of the reconstructed

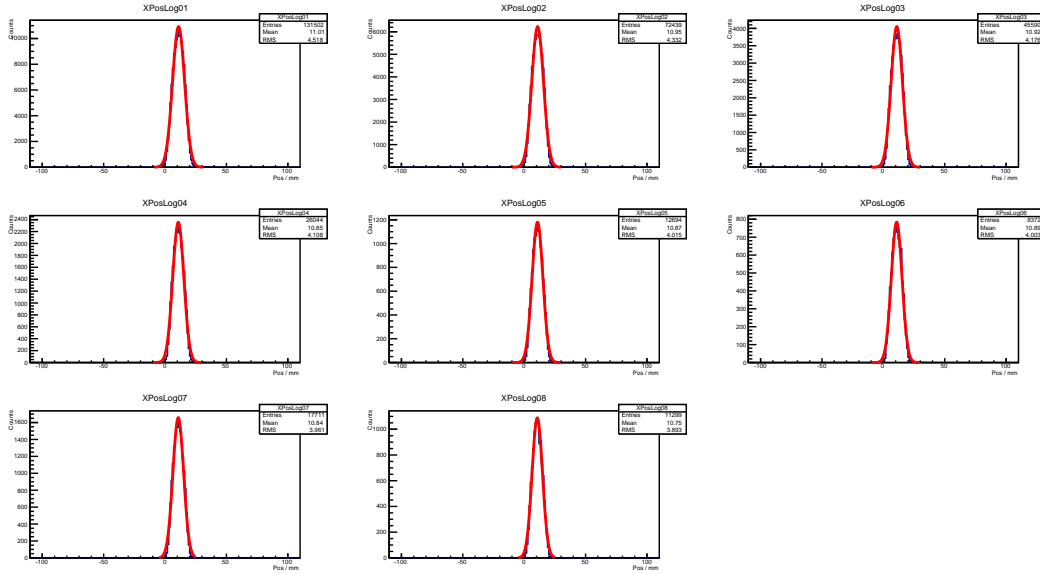


Figure 2.33: Reconstructed impact position in x-direction with a logarithmic weighting function for run1.

impact position. Then, the resolution is given by the standard deviation of the Gaussian. One example can be seen in Fig. 2.35. The position resolution for impinging the center of the crystal surface (run1) for x- and y-direction is depicted in Fig. 2.36. For an energy of 1 GeV a position resolution of 4.8 mm in x-direction and 4.1 mm in y-direction was obtained.

The method was applied as well for positions when the beam was not directed at the center of a crystal surface. In particular, the obtained position resolutions for the beam moved vertically (see Fig. 2.37) and horizontally (see Fig. 2.38). Additionally, the position resolution for the beam aimed at center of four crystals is shown in Fig. 2.39. The obtained position resolutions are shown in Tab. 2.5.

Position	Resolution x in mm	Resolution y in mm
2	4.8	3.2
9	3.8	4.2
13	3.9	3.4

Table 2.5: Position resolution for various impact positions at 1 GeV.

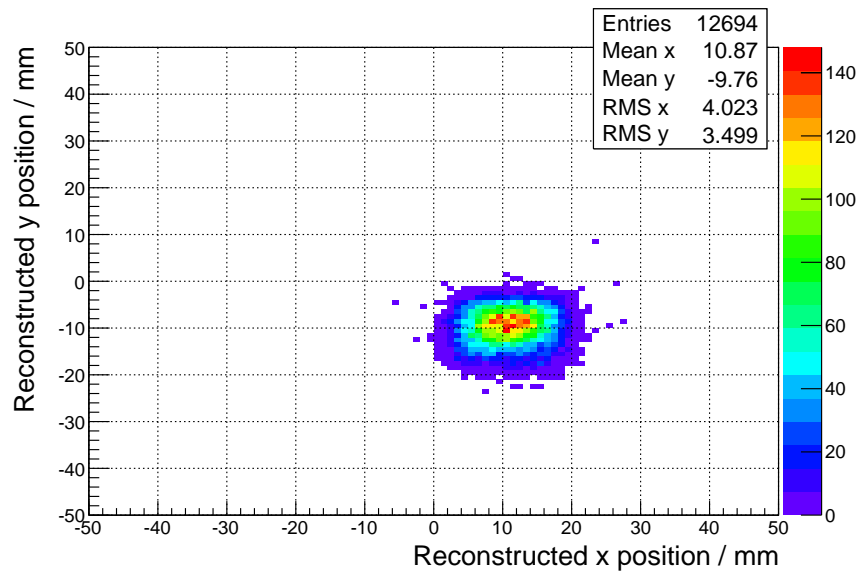


Figure 2.34: Reconstructed beamspot with a logarithmic weighting function for run1.

For a beam energy of 1 GeV the position resolution improves in all cases compared to the beam aimed in the center of the crystal. For higher photon energies the fluctuations in position resolution get very strong since statistics of collected events is very low. It is obvious that in all cases except Position 9 the position resolution in y-direction is significantly better.

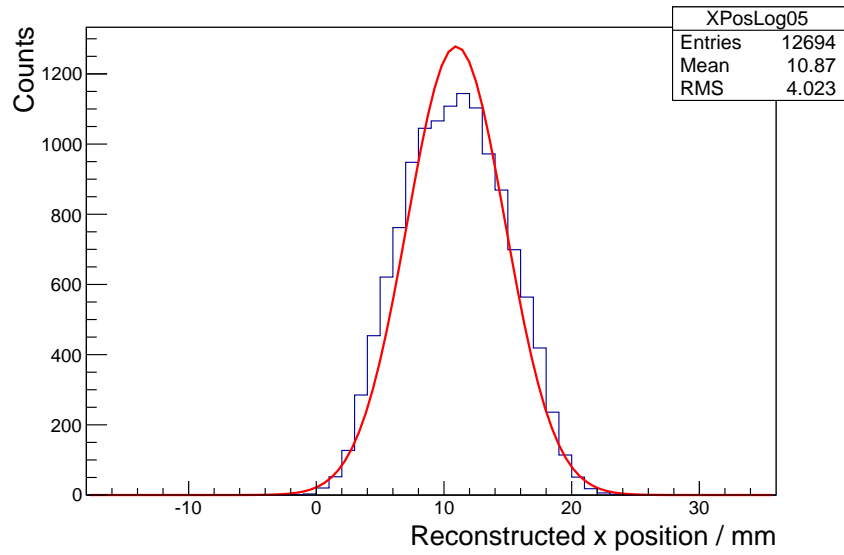


Figure 2.35: Reconstructed impact position in x-direction with a logarithmic weighting function for run1 for one energy. Fitted with a Gaussian.

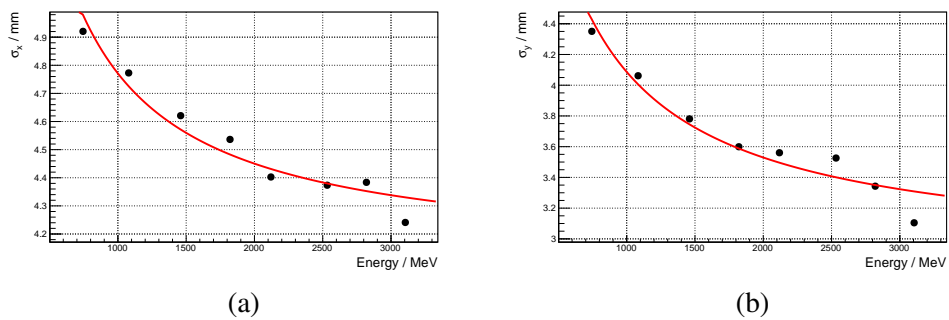
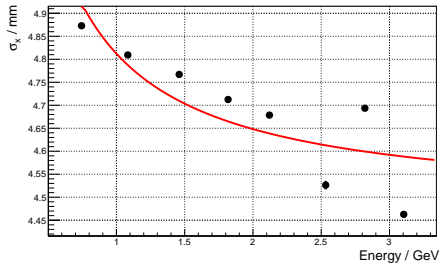
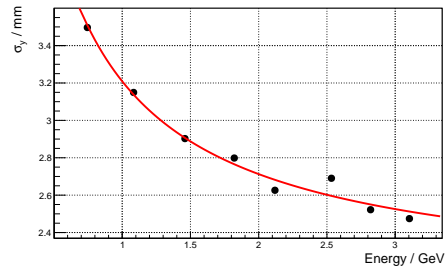


Figure 2.36: Position resolution for run1 in x-direction (a) y-direction (b).

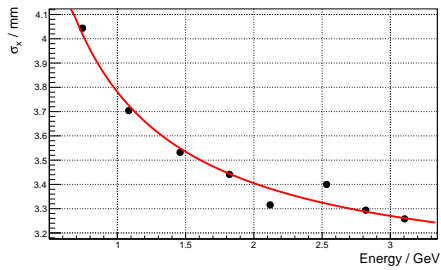


(a)

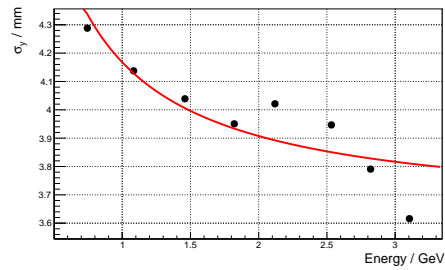


(b)

Figure 2.37: Position resolution for run9 (corresponding to position 2) in x-direction (a) y-direction (b).

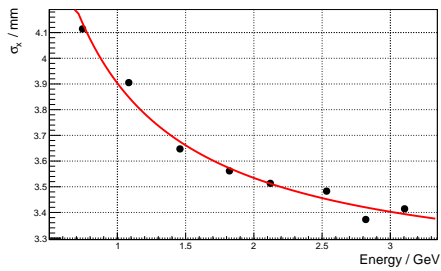


(a)

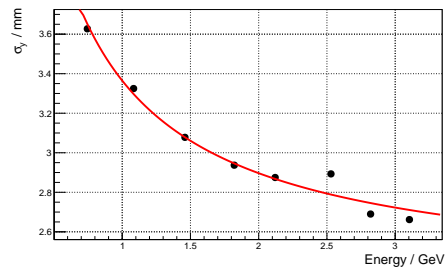


(b)

Figure 2.38: Position resolution for run16 (corresponding to position 9) in x-direction (a) y-direction (b).



(a)



(b)

Figure 2.39: Position resolution for run20 (corresponding to position 13) in x-direction (a) y-direction (b).

2.4 Influence of dead material in front of the detector

2.4.1 Experimental setup

A key aspect of the beamtime test at ELSA in Bonn was to study the influence of dead material in front of the detector. The modified setup is shown in Fig. 2.40. A

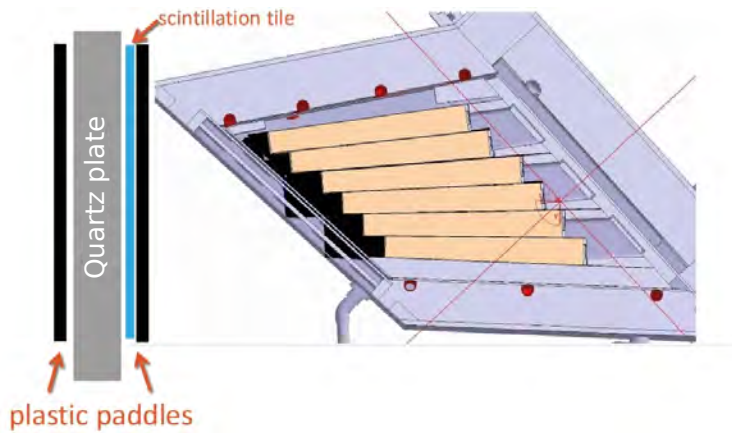


Figure 2.40: Setup to test the influence of dead material in front of the detector.

quartz (SiO_2) plate represents the dead material. The quartz plate has a thickness of 1.5 cm and the properties of quartz are listed in Tab. 2.6. Two plastic paddles

Radiation length X_0	12.3 cm
Density	$2.2 \frac{\text{g}}{\text{cm}^3}$
dE/dx	$1.699 \frac{\text{MeV}}{\text{g}\cdot\text{cm}^2}$

Table 2.6: Properties of quartz.

in front and behind the quartz plate are installed as Vetos to discriminate between electrons/positrons and photons. The first paddle measures conversion caused in air between the radiator and the detector while the second one detects additional conversion within the passive material. The complete setup is not identical to the final $\bar{\text{PANDA}}$ detector but considers the main contribution of the Barrel Dirc. The distance

between the crystals of the PROTO60 and the vacuum insulation panel is larger than the distance between the DIRC detector, represented by the quartz plate, and the the Barrel EMC crystals. Thus, the quartz plate was mounted directly on the second plastic paddle.

2.4.2 Experimental results

The energy and position resolution with the quartz plate in front were obtained like described in the previous chapters. The energy resolution shown in Fig. 2.41 is comparable to the resolution without the quartz plate (2.75% at 1 GeV). In contrast, the

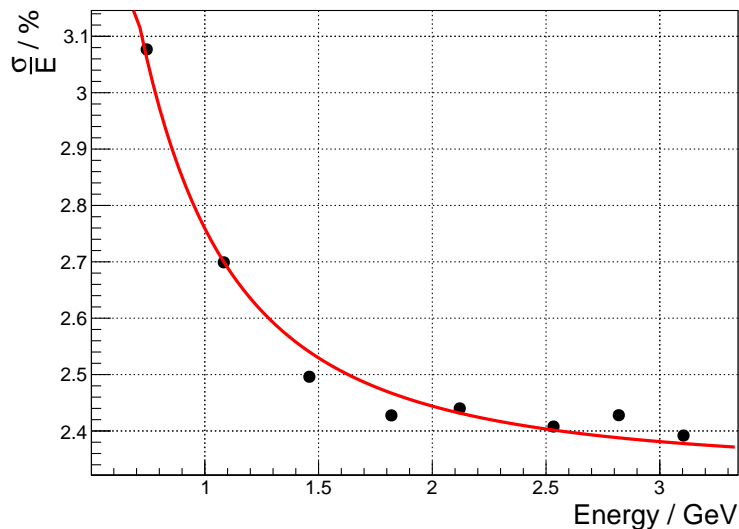


Figure 2.41: Energy resolution for a 6×6 crystal matrix with a quartz plate in front and a summation threshold of 1.85 MeV.

position resolution, depicted in Fig. 2.42, deteriorates. Due to conversion within the quartz plate, the energy resolution is composed of a photon and an electron resolution. The second Veto is used to discriminate photon from electron events due to conversion. In case of a photon event both plastic paddles do not generate a trigger. If there are electron events which are produced within the quartz plate, the plastic paddle before the quartz plate generates no trigger, but the plastic paddle after the quartz plate generates a trigger.

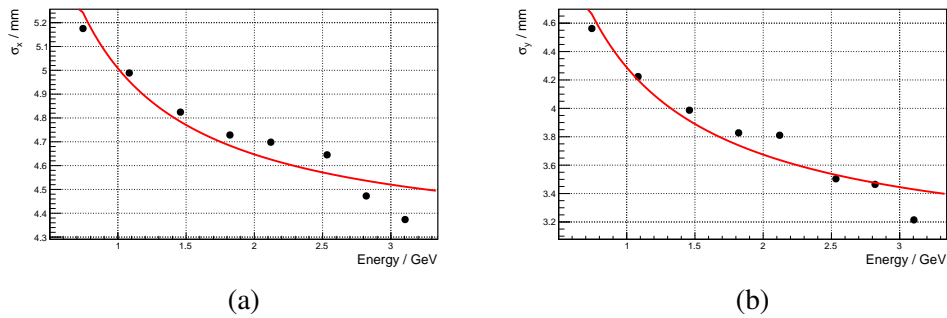


Figure 2.42: Position resolution for run6 (with quartz plate) in x-direction (a) y-direction (b).

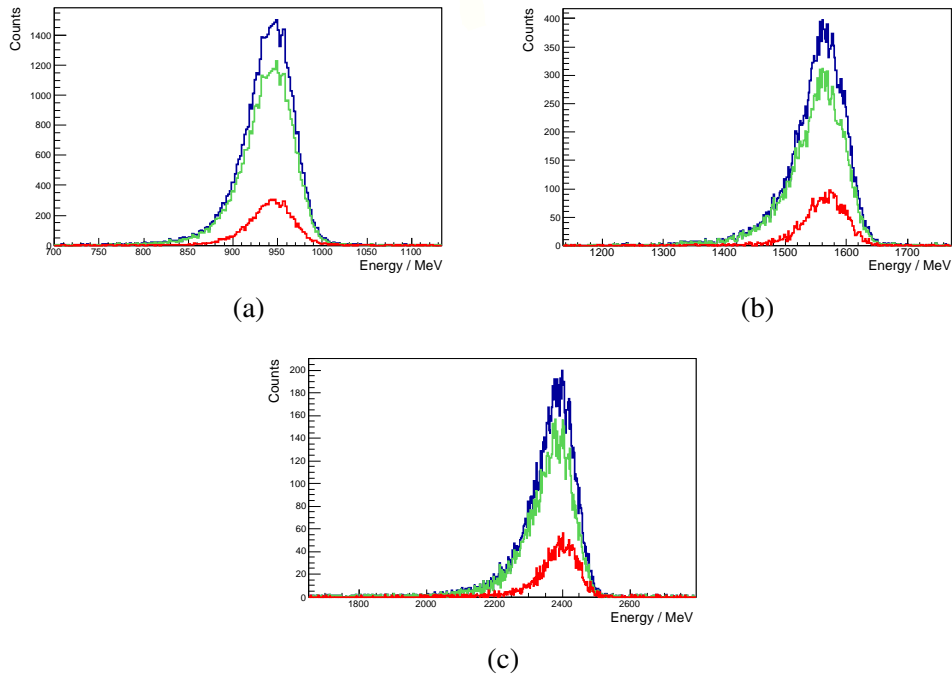


Figure 2.43: Lineshapes of a summed 6×6 crystal matrix with a quartz plate in front and a summation threshold of 1.85 MeV. Electrons in green, photons in red and both together in blue.

The separated lineshapes and energy resolutions are shown in Fig. 2.43 and in Fig. 2.44, respectively.

The energy resolution for electrons from conversion events is significantly better. The

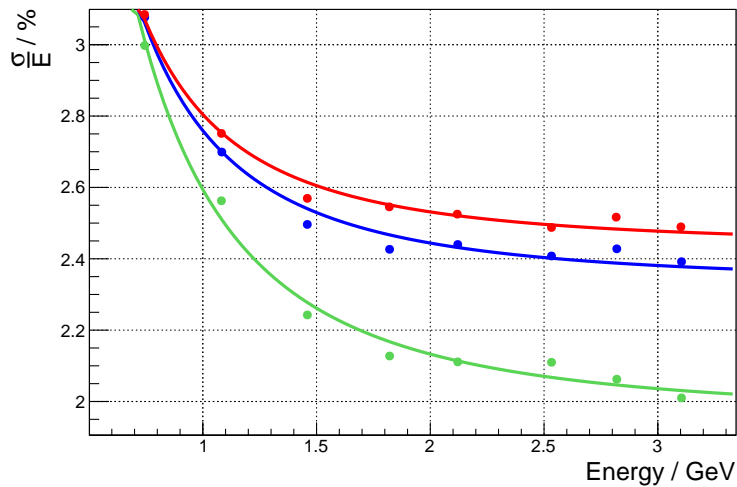


Figure 2.44: Energy resolutions for a 6×6 crystal matrix with a quartz plate in front and a summation threshold of 1.85 MeV. Electrons in green, photons in red and both together in blue.

same was explored for a 3×3 matrix (see Fig. 2.45), but only for energies above 1 GeV the effect was observed. Furthermore, the position resolutions were determined and are shown for electrons in Fig. 2.46 and for photons in Fig. 2.47. Here, deteriorations could be observed as well.

2.4.3 Simulation

In order to investigate and understand the data of the experiment with the quartz plate in more detail, a simulation with the toolkit Geant4 was carried out. Generally, the aim of reproducing the experimental data via a simulation is to get a confident understanding of the results. The Geant4 toolkit makes it possible to simulate the passage of particles through matter with Monte Carlo Methods. The methods are based on random sampling with respect to the probability of the physical interaction. Included are optical, hadronic and electromagnetic processes described by experimental data, parametrization and theory. Additionally, a set of particles, elements and materials is included.

To achieve a high consistency of simulated results with the experiment, all instru-

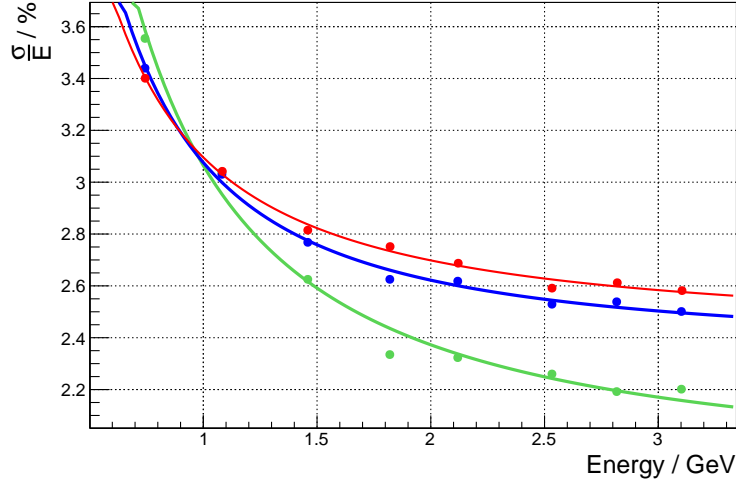


Figure 2.45: Energy resolutions for a 3×3 crystal matrix with a quartz plate in front and a summation threshold of 1.85 MeV. Electrons in green, photons in red and both together in blue.

mental details of the experiment have to be reproduced as accurately as possible. The parameters used for the simulation will be described in the following. The geometry of the PROTO60 is manually derived from CAD drawings. The G4Trap class was used to create a crystal type6 geometry with respect to the PANDA EMC TDR [30]. The composition of PWO-II is of $1 \times Pb$ (lead), $1 \times W$ (tungsten) and $4 \times O$ (Oxygen) with their individual molar masses and its total density of 8.28 g/cm^3 . The crystal is wrapped with a $264 \mu\text{m}$ thick layer of carbon with a density of 2 g/cm^3 which represents the reflector material and alveole. In order to mimic real experimental conditions, the complete setup is placed inside a large volume filled with air. This simulates the air between the end of an accelerator and the detector where high energetic photons traversing the air and undergo pair production. The components of Air are Nitrogen (70%) and Oxygen (30%) with a density of 1.29 mg/cm^3 .

The non-uniform light collection within a tapered crystal has an impact on the detector characteristics and has to be implemented into the simulation. NUF is caused by the interplay of absorption and focussing effect. The influence on the amount of scintillation light reaching the readout end face is shown in Fig. 4.6. It is possible to simulate the scintillation process with Geant4, but only with extensive comput-

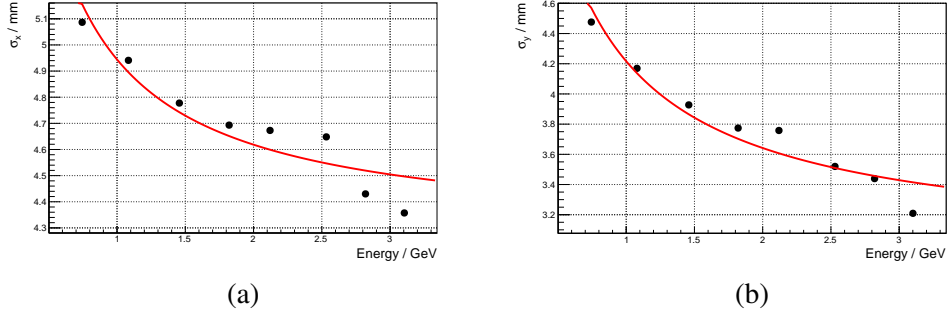


Figure 2.46: Position resolution for run6 (with quartz plate and discriminated electrons) in x-direction (a) y-direction (b).

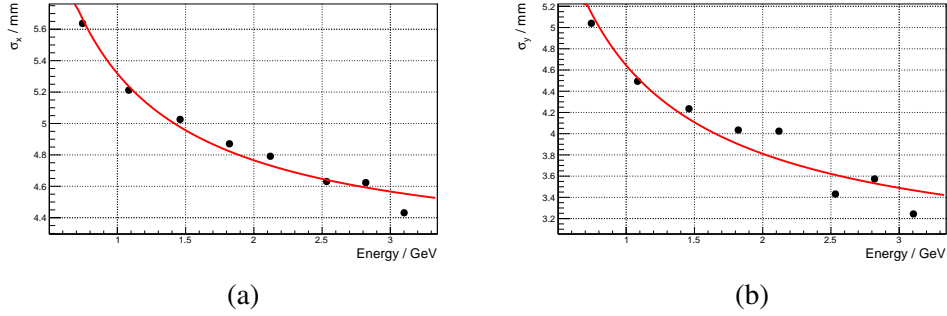


Figure 2.47: Position resolution for run6 (with quartz plate and discriminated photons) in x-direction (a) y-direction (b).

ing time. However, birefringent material, like lead tungstate, is not supported by the software. Furthermore, for a realistic crystal macro defects have to be considered within the simulation. All these properties are included in the so called PROTO60-NUF-model. It is based on an experimental program where the light collection for all $\bar{\text{P}}\text{ANDA}$ crystals was investigated. At **K**ernfysisch **V**ersneller **I**nstituut-Center for **A**dvanced **R**adiation **T**echnology (KVI-CART) Groningen, the Netherlands, a proton beam was used to scan a type 6 crystal perpendicularly to the crystal axis with respect to the light collection. Like in the PROTO60 the crystal was equipped with one LAAPD and VM2000 reflector foil. A signal increase of $\sim 23\%$ between the two ends of a crystal has been measured (see Fig. 2.49). The NUF can be fitted with

$$LY_n(d) = 0.00046 \cdot d^2 + 0.00244 \cdot d + 0.99339 \quad (2.28)$$

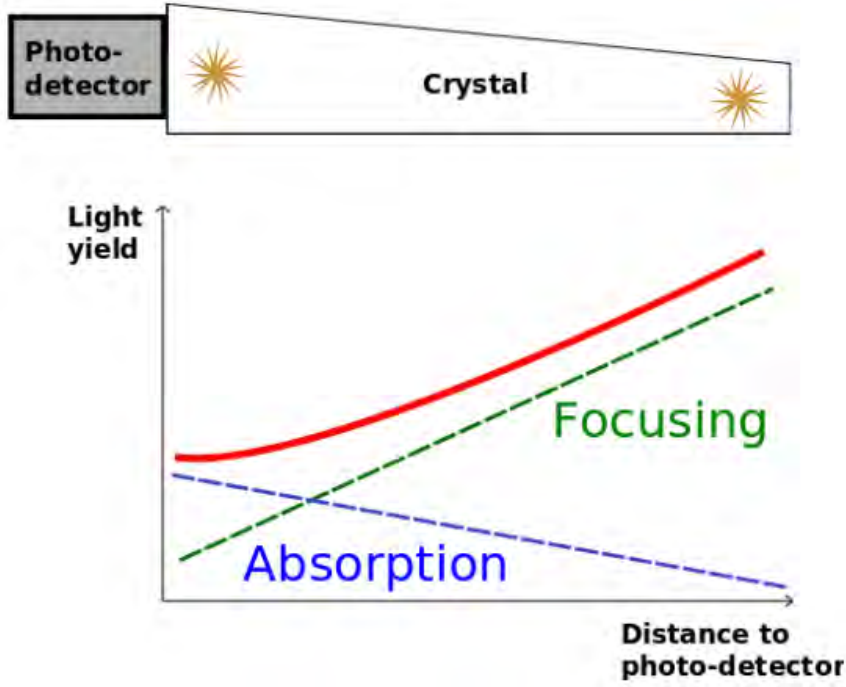


Figure 2.48: Schematic light collection in case of NUF.

where the distance d between front end and sensor is given in cm. This function can be used to weight the deposited energy within the simulation. Since a simulated event is divided into a number of interaction steps, each local energy deposition $E_{\text{step}}(z)$ has to be weighted with formula 2.28 depending on the crystal length. The total weighted deposited energy E_{crystal}^* can be obtained by summing up the weighted deposited energy for each step E_{step}^* :

$$E_{\text{crystal}}^* = \sum E_{\text{step}}^* = \sum E_{\text{step}}(z) \cdot LY_n(z) \quad (2.29)$$

Finally, the number of photoelectrons can be calculated by

$$N_{\text{phe}} = E_{\text{crystal}}^* \cdot \frac{32.04 \text{ phe/MeV}}{LY_n(20 \text{ cm})}. \quad (2.30)$$

In a next step to a real detector response, the PROTO60-NUF-model is extended to a so called PROTO60-NUF-NOISE-model which takes into account the excess noise of the photo detector and the electronic noise of the preamplifier. Photon statistics

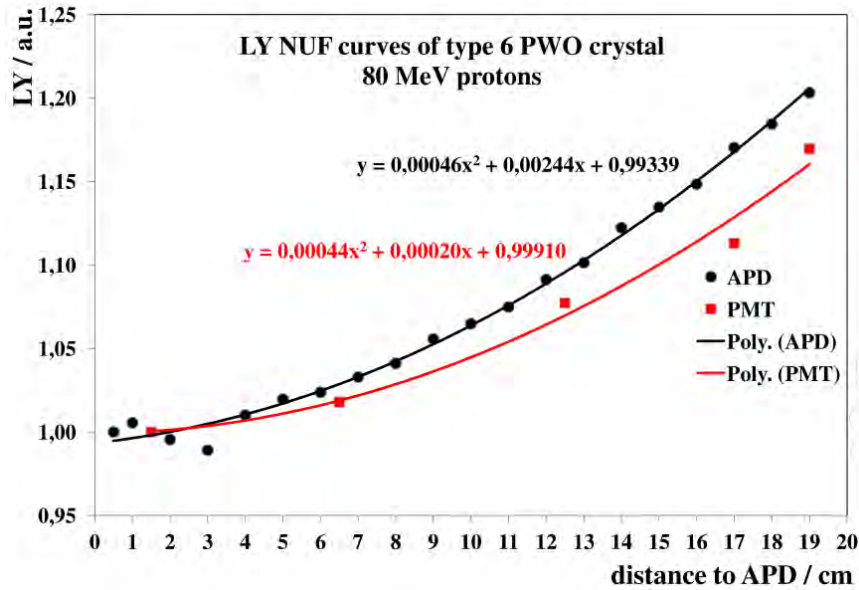


Figure 2.49: Measurement of NUF of a type 6 crystal at KVI-CART [33].

are implemented by weighting the number of photoelectrons with a Gaussian distribution. A LAAPD excess noise factor of 2.72, corresponding to a gain in the order of 150, was applied and preamplifier noise of $\sigma_{\text{pre}} = 0.25$ MeV deposited energy was set.

Simulated experiment

The previously described settings were used to simulate the response of the PROTO60 for a 3 GeV photon and positron beam impinging the central crystal, respectively. The summed lineshapes for a crystal matrix impinged by a photon and a positron beam, respectively, are shown in Fig. 2.50. The mode of the positron line shape is shifted to higher deposited energy and the FWHM is significantly narrower compared to the photon lineshape confirming the better resolution observed experimentally.

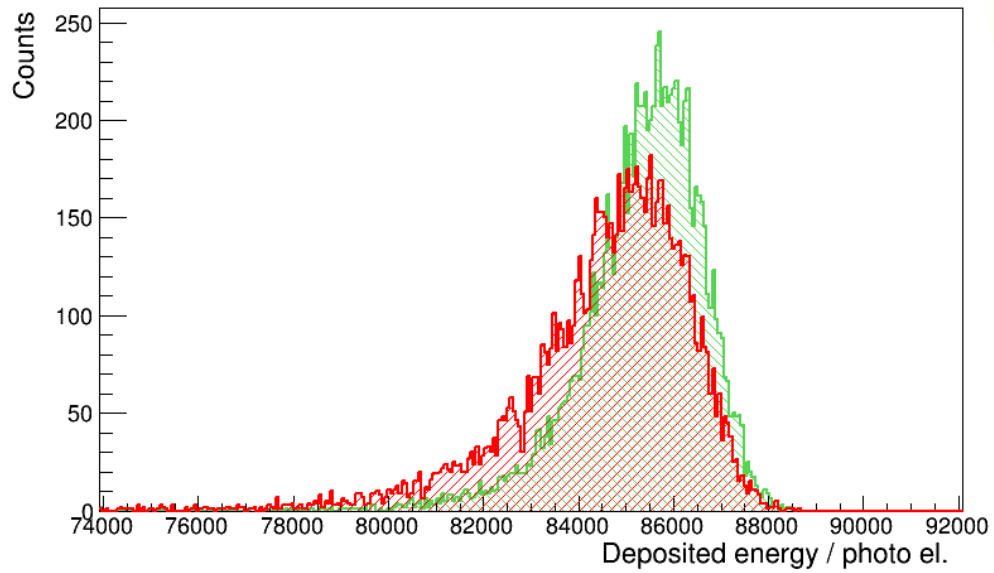


Figure 2.50: Summed lineshapes for a 3 GeV photon and positron beam impinging the central crystal of a crystal matrix. Positrons in green and photons in red.

Chapter 3

Beamtime test with PROTO120

The response of the first generation of prototypes, the PROTO60, has been tested at various accelerator facilities over the complete envisaged energy range. A test with the complementing energy range was presented in the last chapter. A sufficient resolution and efficiency was achieved for all the PROTO60 tests which satisfied the requirements stated in the TDR of the \bar{P} ANDA EMC [30]. Nevertheless, among other things, the readout concept used in the PROTO60 differs from the foreseen concept for the Barrel EMC. In particular, the envisaged pre-amplifier for the Barrel, the so-called APFEL ASIC, is integrated for the first time in a new generation of prototype, the PROTO120. The main issues which were investigated in the beamtime test presented in this chapter are a performance test of the new pre-amplifier and the response of the new prototype in general.

3.1 PROTO120

The most recent real-size prototype of the \bar{P} ANDA Barrel EMC, PROTO120, represents a larger section of a Barrel slice, as schematically shown in Fig. 3.1. It contains the most tapered crystals and the close to final mechanical components and electronics. In total 120 PWO-II crystals are divided into three blocks containing 40 L & R shaped crystals of type 1, 2 and 3, respectively, which are arranged in 10 columns and 4 rows. The readout is performed with two 1 cm^2 rectangular LAAPDs, which

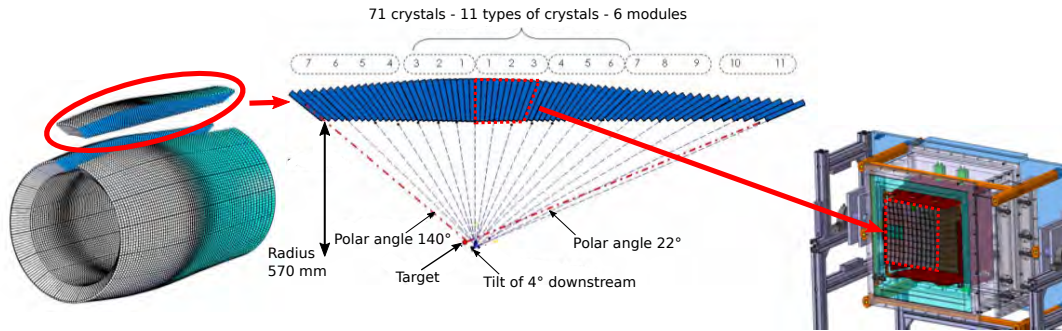


Figure 3.1: Schematic view of the Barrel EMC. The PROTO120 represents a subsection of a Barrel slice. It contains 40 PWO-II crystals respectively of type 1, 2 and 3.

are read out separately via the custom made APFEL-ASIC. Mechanics, readout electronics and DAQ are described in more detail in the following sections.

3.1.1 Mechanics

The lateral sides of each PWO-II crystal are wrapped with $63.5 \mu\text{m}$ VM2000s and placed into a carbon alveole with a wall thickness of $200 \mu\text{m}$. Hence, accounting for an additional gap for mechanical tolerances, the average distance between two crystals amounts to approximately $680 \mu\text{m}$. 40 crystals fit in one alveole and each alveole holds 20 right and 20 left type crystals of geometry type 1, 2 and 3, respectively. The mechanical stability and attachment on the support plate of the detector are ensured by glueing aluminum inserts into the alveole on the rear side of the crystals after inserting the latter. The crystal is finally fixed by a reflective front stopper which will be adapted to allow the insertion of the fiber bundles for monitoring. Intermediated plates with varying geometry are fixated on the inserts for further stability and the attachment to the support plate. In addition, an intermediated plate features a planar surface allowing to mount each matrix to a Super Module Plate. In order to cool down the matrices to $T = -25^\circ\text{C}$ a cooling plate with meandering copper pipes is attached to the Super Module plates. Fixing foos serve as distance holder between cold and warm volume. They are fixated on one side at the Super Module

Plate and on the other side at the Support Beam. The Support Beam is basically a thick aluminum plate. The emerging gap is filled with stone wool to insulate the cold and warm volume. A PVC box is mounted on the Support Beam where the electronics is placed. For further cooling purposes, meandering copper pipes are attached to the sides around the three crystal matrices. Meandering copper pipes are attached to the sides. The pipes are floated with a mixture of water and ethanol and the fluid is circulated by a chiller. Matrices and cooling sides are surrounded by insulation foam to ensure stable operation at the envisaged operation temperature. The temperature is monitored by several flat temperature sensors which are placed between the VM2000 and the wall of the alveole. A PVC box is mounted to the Support Beam and houses the crystal matrix and cooling system. The box is sealed with silicon to stabilize the operating temperature even further. The interspace of the PVC crystal box is rinsed with dry air or N_2 to prevent ice formation or condensation of water. The entrance window consists of an evacuated micro porous thermal insulating panel¹ with excellent insulating properties. It serves the purpose to attenuate incoming particles very little while providing thermal shielding. The central crystal of the first column of the type 1 alveole is the only crystal aligned approximately perpendicular to the entrance window. Like all other crystals, the crystal is facing to the central point of the Barrel which is tilted 4° downstream compared to the target according to the barrel layout. Hence, all other crystals show an relative angle to the entrance window of the prototype. This has to be considered for test measurements with straight beams. A vertical and horizontal cross-section through the crystal arrangement is depicted in Fig. 3.2.

3.1.2 Electronics

The crystals are equipped with two rectangular 1 cm^2 LAAPDs² with technical details given in Tab. 3.1. The LAAPDs are optically coupled to the crystal with a silicon glue³ [50]. Both LAAPDs are covered by a black plastic capsule. The individual high voltage settings for a gain of 150 at $T = -25^\circ\text{C}$ are provided by the APD Lab at GSI. The LAAPDs are sorted and grouped in pairs according to their operating voltage.

¹Va-Q-Tec

²Hamamatsu

³DOW CORNING 3145 RTV

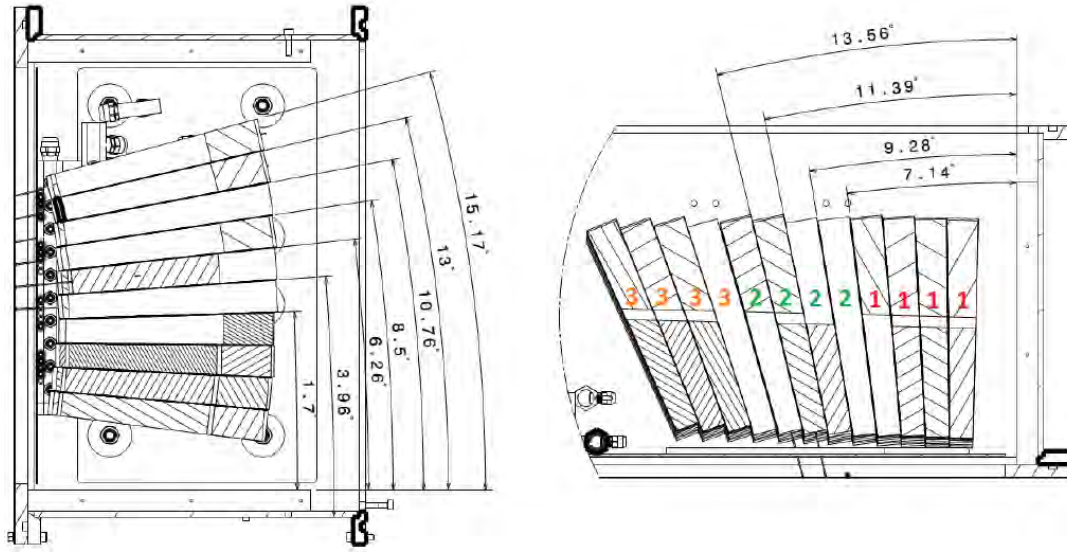


Figure 3.2: Vertical (left) and horizontal (right) cross-section through the crystal arrangement. The vertical direction is shown at the position of the sixth crystal column and in horizontal direction at the position of the fifth crystal row relative to the left upper corner relative to the left upper corner of the entrance window in Fig. 3.1. The angles are measured relative to the entrance window.

The mean of the two voltages is then applied to the LAAPD pair since only one high voltage supply channel is available per pair. The weak charge pulse of a LAAPD is converted into a voltage signal and amplified by the custom made APFEL 1.4 ASIC. Both LAAPDs are read out simultaneously by one APFEL chip. The signal processing of the APFEL ASIC is depicted in Fig. 3.3. The APFEL chip is mounted on a small PC-board which is attached to the insert. Hence, the APFEL chip is kept in the cold volume which features a reduced electronic noise. The chip has been adapted to this circumstance by having a low power consumption and power dissipation, respectively. On that account, a small temperature gradient within the crystal can be provided. The preamplifier is connected to a backplane Printed Circuit Board (PCB) via a double-layer flex cable which guides the pre-amplified signal from the cold volume to the warm volume. The flex cables are optimized for a minimal noise pick-up. In addition, they supply the high voltage for the LAAPDs and the low voltage and slow control information of the ASIC. The current version of the backplane

Parameter	Condition	Specification	Unit
effective area		100	mm ²
spectral response range		320 – 1000	nm
QE	at 420 nm	70	%
capacitance	at gain 50	230 – 270	pF
operating voltage	at gain 100	365 – 445	V
typ. dark current	at gain 100	30	nA

Table 3.1: Properties of LAAPDs used in PROTO120.

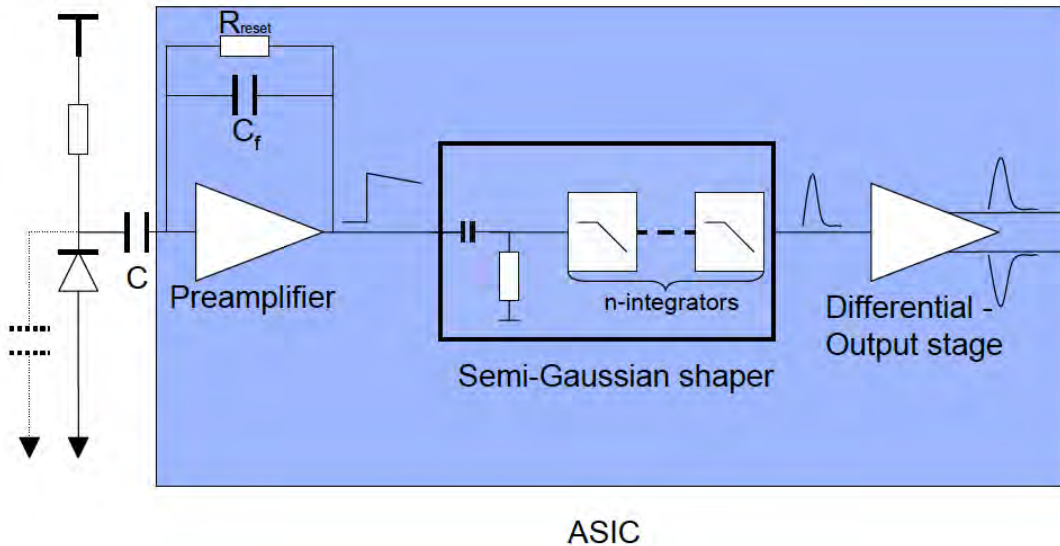


Figure 3.3: Schematic of the APD readout with the APFEL ASIC with indicated signal processing [51].

PCB is designed for the communication with four ASICs. It is responsible for signal routing and the power supply for low and high voltage. Two backplane PCBs are connected with flat cables to Driver PCB Buffer Boards which provide signal routing to a DAQ system. In addition, a Slow Control Hub is connected to the Buffer Boards for controlling and monitoring the conditions within the prototype. A schematic of the PROTO120 electronics is depicted in Fig. 3.4 and a picture of a test setup with indicated readout electronics is shown in Fig. 3.5.

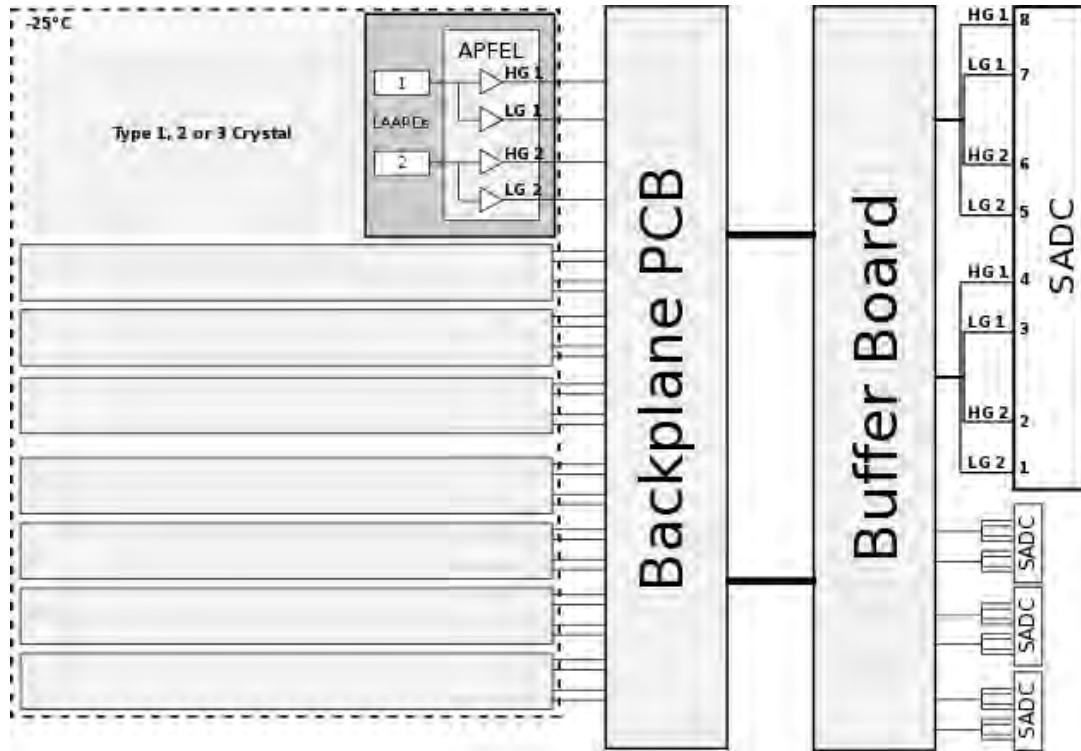


Figure 3.4: Schematic of the PROTO120 electronics.

3.1.3 Readout and DAQ

DAQ

The primary scintillation light from the crystals is converted into a charge pulse by the LAAPDs and afterwards amplified, digitized and shaped by an APFEL ASIC. The differential signals are routed to SIS 3302 SADC modules (8 channels each)[38] by specially shielded Ethernet over Coax cables. Each cable is transporting the information of the high and low gain of the two APDs of one crystal. The sampling frequency was set to 50 MHz, accounting for one sample every 20 ns. The trace length amounted to 500 samples, corresponding to a time window of 10 μ s. A scheme of the test experiment DAQ is shown in Fig. 3.6. The corresponding electronic modules are listed in Tab. 3.2. The SADCs are continuously taking samples of each preamplified low and high gain LAAPD pulse. A trace is stored in case of a trigger signal. The 500 samples taken before a trigger signal are sent via VME bus to the CPU where

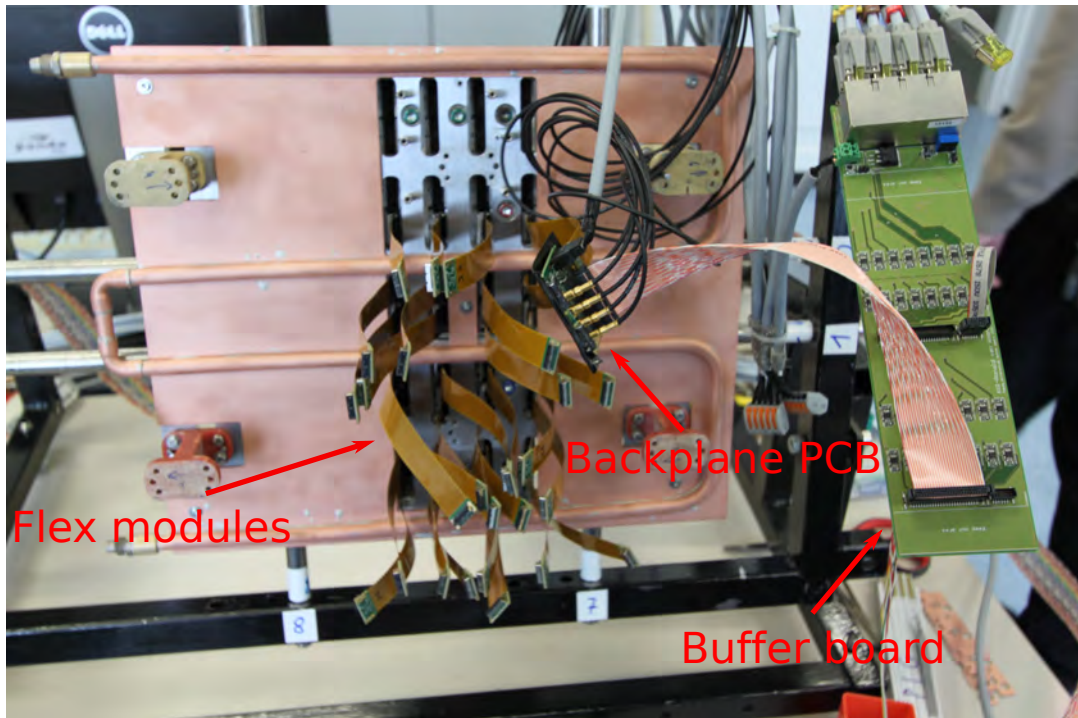


Figure 3.5: Picture of a PROTO120 test setup with indicated readout electronics.

the trace is further processed. The trigger signal is a coincidence of a logical OR of the tagger and a logical OR of all channels of PROTO120. Software was used to set an internal leading-edge threshold of the SADC for each channel individually. The time information of the tagger is recorded with a TDC which is not shown in Fig. 3.6. The information of the tagger channels is converted into the Nuclear Instrumentation Module (NIM) standard, delayed and used as a stop-signal for the TDC. The start-signal is the coincidence signal of tagger and detector. The TDC is configured to a range of 140 ns and a resolution of 8 bit, resulting in a relative tagger time resolution of about 550 ps. The time spectra of the tagger channels are recorded in order to identify and reduce events with random coincidences offline.

Feature extraction

The final step in the readout chain is the extraction of energy and time information from the raw SADC trace. As already mentioned in the PROTO60 chapter, different

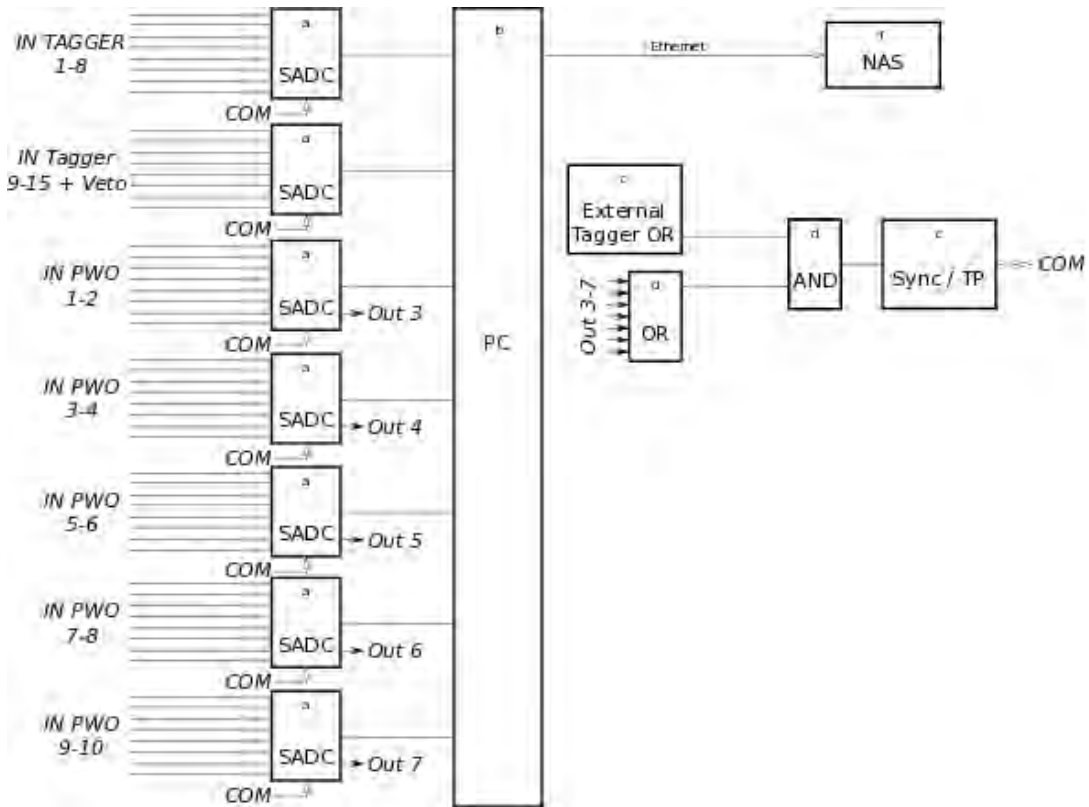


Figure 3.6: Schematic of the PROTO120 readout.

feature extraction algorithms with strict requirements, like being fast and robust, have been studied for application in the \bar{P} ANDA EMC in [39, 40]. These algorithms have to be tested on experimental data and are therefore the basis for the following analysis. In purpose of the test beam data, the algorithm is implemented via software since the SADC data is stored and analyzed offline. The algorithms are briefly explained in the following, showing the deduction of energy and time information. The offline analysis is performed with ROOT/CERN framework which is an object oriented program and library for large scale data analysis based on C++ developed especially for particle physics [41].

Since the raw signals of the LAAPDs are shaped by the APFEL ASIC, it remains to deduce the energy information. The deposited energy in a crystal is proportional to the signal amplitude. In a basic approach, the signal amplitude is obtained by subtracting the baseline and the pulse minimum. A typical trace with indicated en-

Module	Function	Type	Standard / connection
a	SADC	Struck SIS 3302 SADC	VME
b	PC	VME CPU with Tundra-II chipset	
c	External trigger	Discriminated plastic scintillator paddle signal	NIM
d	AND or OR	LeCroy Module 622 Quad Coincidence	NIM
e	Sync / TP	Customized synchronisation module incl. test pulser	VME
f	NAS	QNAP TS-659 Pro+ NAS	TCP/IP

Table 3.2: Electronics modules of the PROTO120 test setup.

ergy deduction is depicted in Fig. 3.7. Furthermore, the bin of the pulse minimum is defined as the coarse time information.

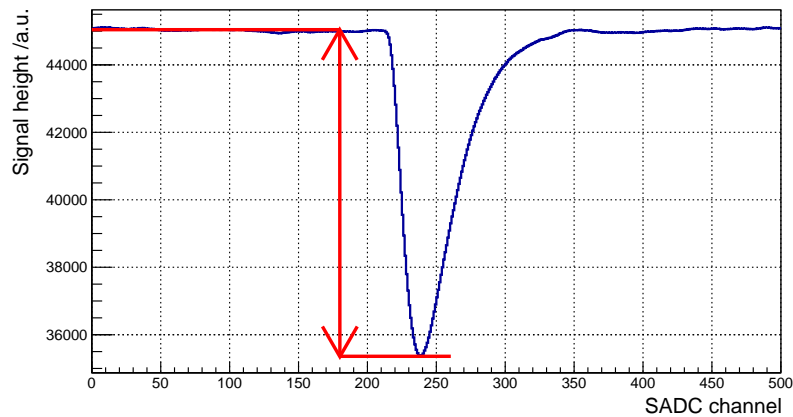


Figure 3.7: Signal shape after shaping of the APFEL with indicated energy extraction (baseline-minimum).

3.2 Experimental setup in Mainz

A first test measurement with the PROTO120 was performed at the MAMI-facility of the Johann Gutenberg University in Mainz, Germany, in 2015. The test setup was located in the A2 experimental hall in the Institut für Kernphysik. The exact location is depicted in Fig. 3.8. The PROTO120 setup including DAQ, power supply and

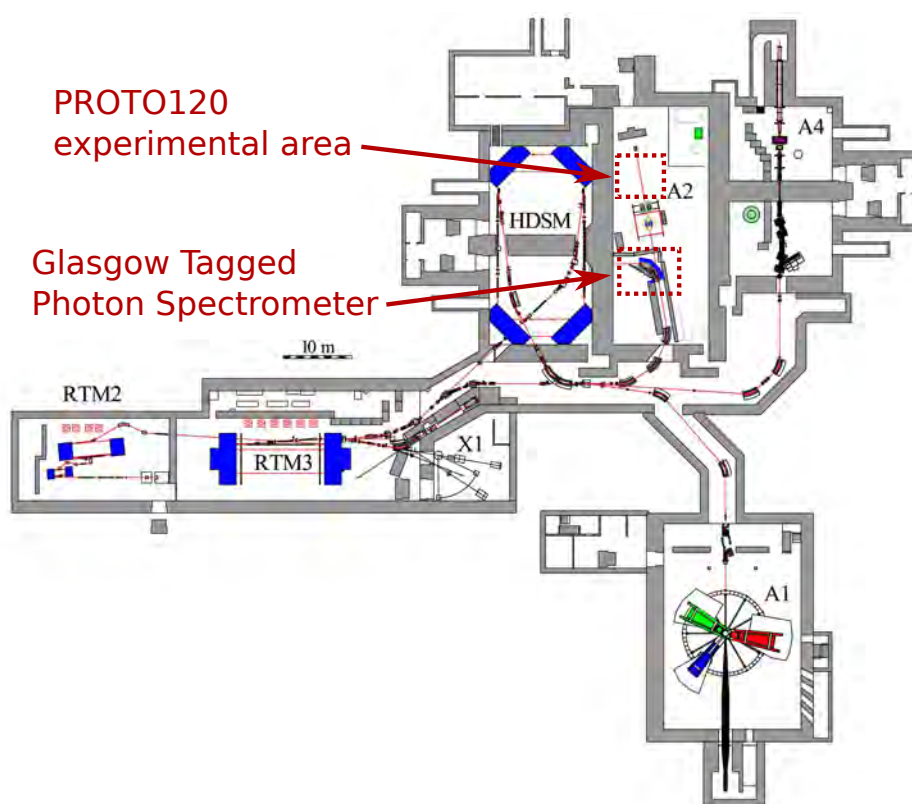


Figure 3.8: Site plan of the MAMI accelerator facility [52]. The positions of the PROTO120 and the Glasgow Tagger are marked.

a chiller was placed downstream to the local Crystal Ball detector. Pictures of the PROTO120 setup are shown in Fig. 3.9.

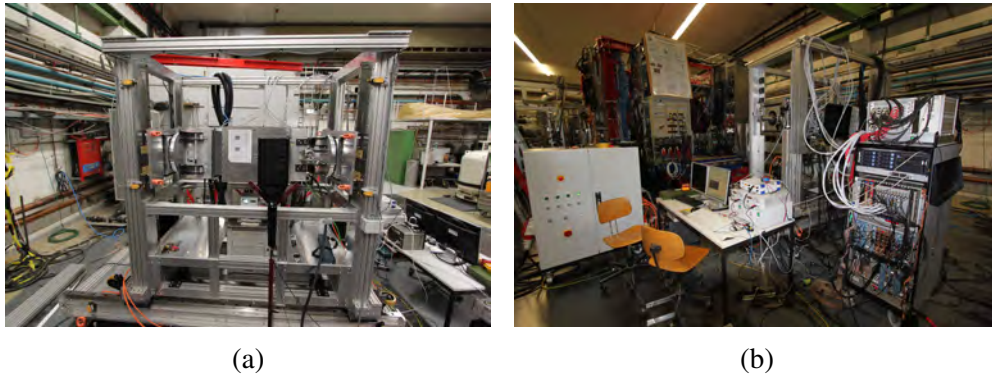


Figure 3.9: Pictures of the PROTO120 test setup in the A2 hall at MAMI. Front view (a) and side view (b) with respect to the beam direction.

The PROTO120 was placed in a x-y-table, a positioning table, whereby it was possible to move the prototype in horizontal and vertical direction perpendicular to the beam. The table is operated by stepper motors with a positioning accuracy below 0.1 mm which are monitored by digital measuring slides. In addition, it was possible to rotate the prototype around its horizontal symmetry axis mechanically. This allowed an alignment of the vertical symmetry axis of the crystal matrix with the beam axis. Thus, the beam was impinging the crystal surface perpendicular. The projected positions of the crystals on the front side of the PROTO120 were calculated with a CAD drawing of the prototype and position markers were fixed on the prototype. Then, the absolute positioning with respect to the beam direction was conducted with a laser leading to the position markers. In order to identify charged particles, a Veto detector was placed in front of the PROTO120, which can be seen in Fig. 3.9a. Charged particles can be created within the Coulomb field of any nucleus on the trajectory of the photons by pair production. The Veto consists of a thin plastic detector wrapped with reflector material and shrinking tube and is read out with a PMT. The threshold of the plastic detector was set just above the noise level.

3.2.1 MAMI

At the MAMI-facility, a tagged photon beam is provided in combination of the MAMI electron accelerator [53] and the Glasgow Tagged Photon Spectrometer [54].

Both will be discussed in the following.

Accelerator

The basis of the MAMI accelerator are an injector LINAC and a cascade of three **R**ace **T**rack **M**icrotrons (RTMs), which are providing an electron beam of $100 \mu\text{A}$ up to an energy of 855 MeV. The facility was upgraded in 2006 by adding a fourth stage, the **H**armonic **D**ouble **S**ided **M**icrtron (HDSM), providing a beam energy up to 1.5 GeV.

At first, an electron source, a thermionic DC-gun, supplies 100 keV electrons to the LINAC. The LINAC again supplies electrons with an energy of 3.97 MeV to the RTMs. The electrons are accelerated stepwise by each RTM with energies according to Tab. 3.3. The three RTMs have a similar functionality and the same basic setup

Parameter	Unit	Injector LINAC	RTM 1	RTM 2	RTM 3	HDSM
injection energy E_{inj}	[MeV]	-	3.97	14.86	180	855
extraction energy E_{ext}	[MeV]	3.97	14.86	180	855	1500
magnetic field	[T]	-	0.103	0.555	1.284	1.53 – 0.95
number of turns	-	-	18	51	19	43
energy gain ΔE per turn	[MeV]	-	0.60	3.24	7.50	16.58 – 13.66
LINAC length	[m]	4.93	0.80	3.55	8.87	8.6 and 10.1
RF-system frequency	[GHz]	2.4495	2.4495	2.4495	2.4495	4.8890 2.4495
beam energy spread (1σ)	[keV]	1.2	1.2	2.8	13.0	110.0

Table 3.3: General MAMI parameters [53].

which is depicted in Fig. 3.10. In principle, an electron beam injected into a RTM is recirculated several times through the RTM while the energy is increased in each cycle. The electron beam passes the **R**adio **F**requency (RF)-cavities with a frequency of about 2.45 GHz. This results in an energy gain of ΔE for the electrons which is

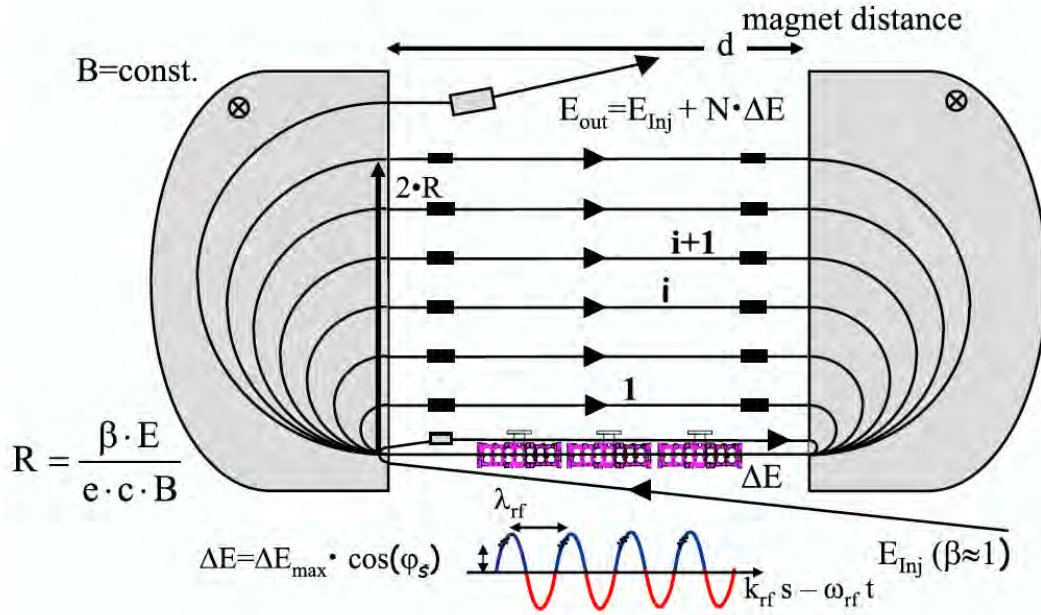


Figure 3.10: Basic setup of a RTM [53].

in the order of a few MeV. Two dipole magnets provide each a constant magnetic field. Both magnets have the purpose to deflect the electron beam by approximately 180° back to the RTM. The bending radius R of an electron beam with a velocity $\beta = v/c \approx 1$ increases linear with the beam energy because of the constant magnetic field and amounts to

$$R = \frac{\beta \cdot E}{e \cdot c \cdot B}. \quad (3.1)$$

Furthermore, it has to be ensured that the electrons stay within the same phase of the alternating voltage in the linear section. Hence, the difference in time between each cycle has to match an integer multiple of the period of the accelerator frequency. In addition, the RTM features an automatic phase correction which enables a rather small spread in energy of the electron beam. If a beam particle has a larger or lower energy than the energy of their corresponding cycle, the path in the bending sections will be larger or smaller, respectively. Thus, the beam particle arrives respectively later or earlier in the linear section. Due to the fact that the electrons enter the high frequency with a different phase, the beam particle is under-accelerated or

over-accelerated, respectively, in the next cycle. This results in an energy correction. Finally, after a fixed amount of cycles N , the beam is extracted by a so-called kicker magnet with an energy of

$$E_{\text{ext}} = E_{\text{inj}} + N \cdot \Delta E . \quad (3.2)$$

The MAMI-facility was upgraded in 2006 with the HDSM which is now the last section of the MAMI accelerator structure. The working principle is similar to the RTMs. The electron beam is accelerated stepwise to the final energy of up to 1.5 GeV by two LINACs operated at 2.45 GHz and 4.9 GHz. The beam is bended by four dipole magnets each time by $\sim 90^\circ$. It takes 43 turns within the HDSM before the beam is being extracted to the experimental areas. The scheme of the HDSM including LINAC-, bending- and focussing sections is depicted in Fig. 3.11. One has to note that the HDSM was not used for the experiment presented in this thesis.

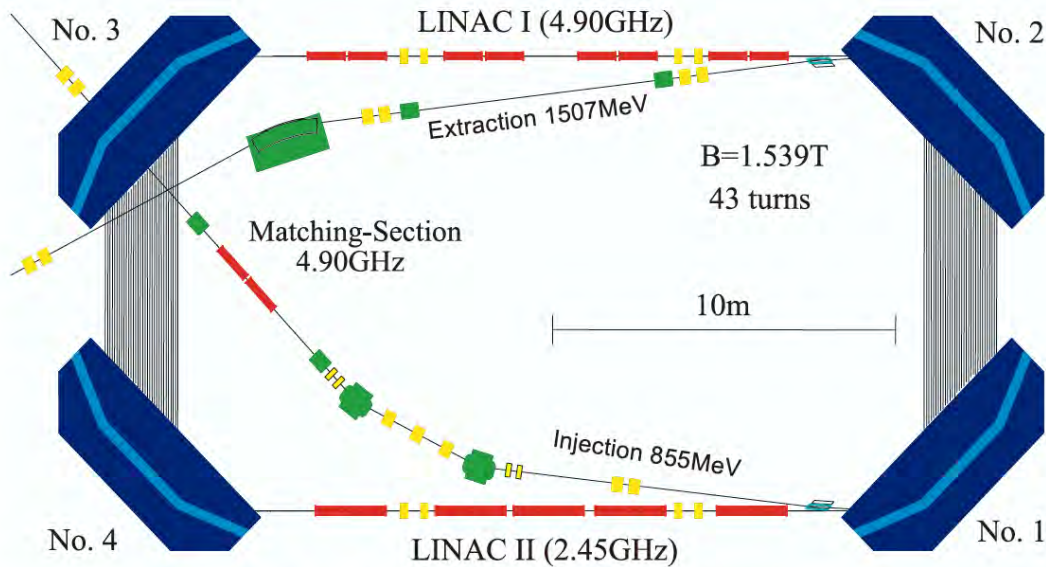


Figure 3.11: Scheme of the HDSM of MAMI C [53]. The beam is accelerated to the maximum facility energy of 1.5 GeV by two LINACs and bended by four dipole magnets.

The Glasgow Photon Tagging Spectrometer

The beamtime test with the PROTO120 has the goal to investigate the response of the prototype to photons in the low energy regime. At the MAMI facility, the electron beam is converted into a continuous and collimated photon beam by a tagging system. Electrons with a known initial energy E_0 impinge a radiator made of either copper or diamond. Hence, the photons are produced within the Coulomb field of the nuclei of the radiator via bremsstrahlung. The remaining momentum of the electrons is measured with the Glasgow Photon Tagging Spectrometer whose basic scheme is depicted in Fig. 3.12. The electrons are bended towards a focal plane by the magnetic

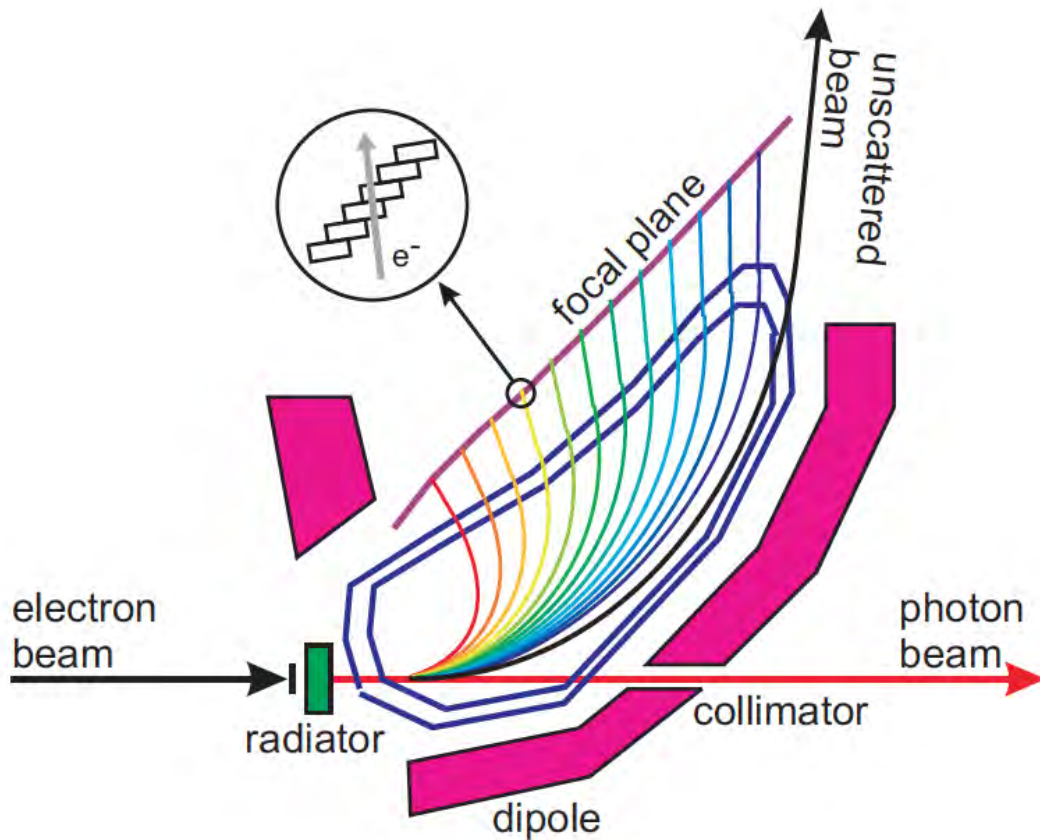


Figure 3.12: Basic Scheme of the Glasgow Photon Tagging Spectrometer [55].

field of a dipole magnet with a flux of $B = 1.8$ T due to the Lorentz force. The focal plane consists of 353 overlapping plastic detectors, each 24 mm wide and 2 mm

thick, read out via PMTs. The point of impact in the focal plane gives the remaining momentum of the electron which amounts to

$$p_e = R \cdot q \cdot B , \quad (3.3)$$

with the known curvature R . Then, the photon energy E_γ can be calculated with the initial beam energy E_0 and the energy of the deflected electron E_e by

$$E_\gamma = E_0 - E_e . \quad (3.4)$$

Almost monoenergetic photons can be selected out of the bremsstrahlung spectrum via a coincidence between the individual channels of the tagging system, which are digitized by a TDC, and a detector, the PROTO120 in case of the presented beamtime. The width of the tagged photons is given by the energy resolution of the tagger and amounts to be below 3 MeV depending on the energy. A set of collimators is placed 2.5 m downstream of the radiator (compare to Fig. 3.13). In case of the presented beamtime a collimator with a diameter of 1.5 mm ensures a small opening angle of 0.0172° of the photon beam. Geometrical considerations lead to an upper limit for the diameter of the impinging beam on the PROTO120 of 9.3 mm.

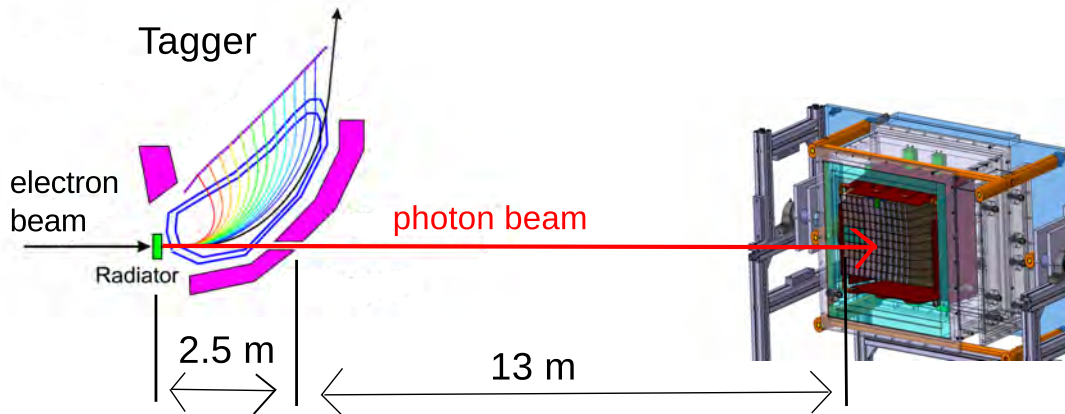


Figure 3.13: Schematic setup of the PROTO120 at MAMI.

3.2.2 Beamtime procedure

For the beamtime test in April 2015 at MAMI only the matrix of 40 PWO-II crystals of type 2 was integrated in the PROTO120. Out of these, a matrix of 4×4 crystals corresponding to 64 channels were read out with SADCs. The readout channels were limited due to the available readout electronics at that moment. A 883.2 MeV electron beam was provided by the MAMI accelerator which was converted into a photon beam by a copper radiator. 16 photon energy channels of the tagging system were selected via software, summarized in Tab. 3.4, for the beamtime test. A schematic crys-

TDC channel	Photon energy [MeV]
1	766.76 ± 1.70
2	743.92 ± 1.72
3	681.17 ± 2.04
4	641.73 ± 2.12
5	599.91 ± 2.26
6	462.34 ± 2.64
7	438.13 ± 2.65
8	406.30 ± 2.72
9	376.65 ± 2.75
10	238.40 ± 2.78
11	191.58 ± 2.84
12	159.78 ± 2.86
13	128.20 ± 2.86
14	104.08 ± 2.83
15	80.12 ± 2.79
16	56.36 ± 2.74

Table 3.4: Selected Tagger channels at the beamtime.

tal map of the read out matrix of the PROTO120 is depicted in Fig. 3.14. Indicated is a 3×3 matrix within the complete matrix and the impact positions for the main runs are marked with red dots. The performed program comprised different runs:

- calibration run for each crystal (~ 20 minutes)
- long run in the center of the 4×4 matrix (~ 3 hours)
- long run in the center of the 3×3 matrix (~ 3 hours)

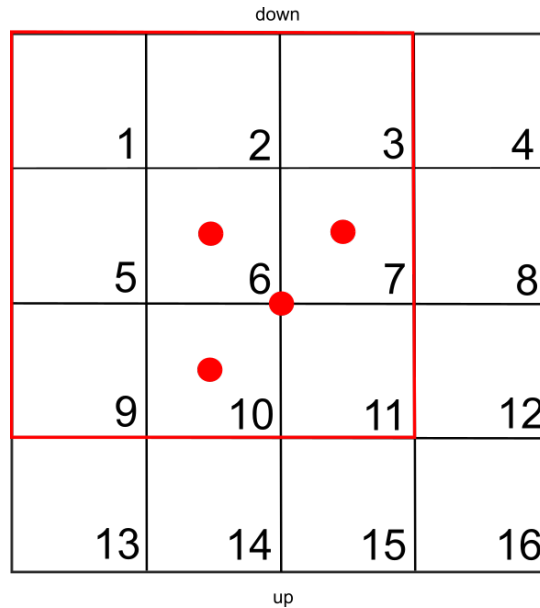


Figure 3.14: Schematic crystal map of the read out matrix of the PROTO120. Indicated is a 3×3 matrix within the complete matrix and the impact positions for the main runs are marked with red dots.

- long runs in crystals 7 and 10 (~ 2 hours)

For the calibration of the detector cosmic radiation was measured right after the beam time for a couple of days. Data was taken with muons traversing the crystal matrix vertically and horizontally.

3.3 Electronic noise

The beamtest presented in the previous section has the task to test the front-end electronics, in particular for the first time the APFEL ASIC, under real experimental conditions. The main criterion to judge the foreseen front-end electronics is the electronic noise. Therefore, the electronic noise during the beamtime will be discussed in this chapter with a focus on the APFEL ASIC. For the \bar{P} ANDA EMC it is crucial to detect low energetic photons which requires a low electronic noise. A high electronic noise would superimpose with the signals from low energetic photons. Hence, those

photons would be indistinguishable from the noise.

The requirements for the APFEL ASIC foresee an ENC of less than $13000 e^-$ at a detector capacitance of 300 pF. The main noise source of the preamplifier, basically designed like a folded cascade, as depicted in Fig. 3.15, is a current change at the input transistor. Generally, the noise depends on the current and the transistor area.

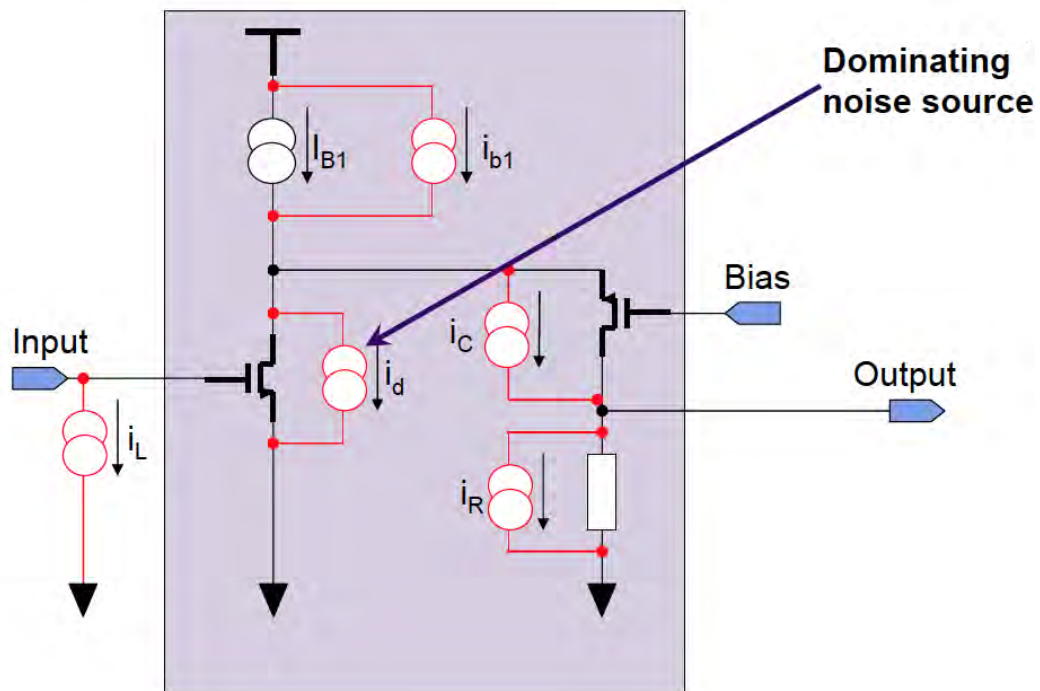


Figure 3.15: Schematic design of the charge sensitive preamplifier as a folded cascode. The main noise source is indicated [51].

Other noise sources are listed in Tab. 3.5. In addition, the signal to noise ratio is dependent on the shaping time which is a design value. The shaping time was set as a compromise between power consumption, the transistor area and the shaping time itself to 250 ns. Measurements in the laboratory at GSI with the APFEL ASIC have shown a sufficiently low noise level. Details can be found in [34]. Nevertheless, the functionality has to be verified under experimental conditions. A typical SADC trace without a signal from the beamtime is depicted in Fig. 3.16. First, the baseline is determined as the mean of the signal heights of the first 130 SADC channels. Then, the noise is defined as the RMS of the baseline. The distribution of the noise for all

Noise source	Dependency
Shot noise (due to I_L)	$i_L^2 = 2q \cdot I_L$
Thermal noise	$I_t^2 = \frac{8}{3} \cdot k_B \cdot T \cdot g_m$
$1/f$ noise	$i_f^2 \sim \frac{I_D}{L^2 \cdot f}$

Table 3.5: Noise sources with leakage current I_L , transconductance g_m , frequency f and gate length L .

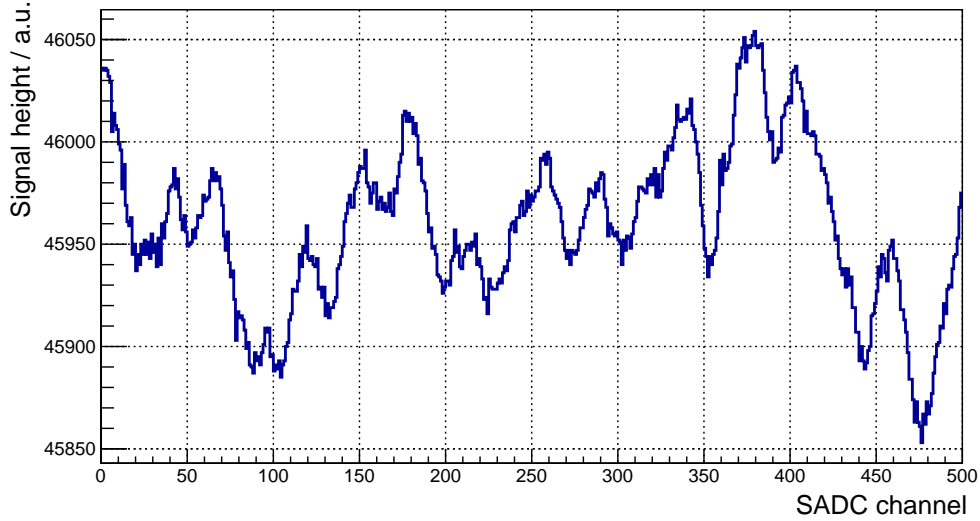


Figure 3.16: SADC trace without a signal.

events is depicted in Fig. 3.17 and Fig. 3.18 for the high gain branch and low gain branch, respectively. A not correlated noise would have a Gaussian shape. But in that case, the noise distributions show a tail to higher energies. This indicates a correlated noise. The mean, the standard deviation, the corresponding electronic noise level and the summation threshold determined by

$$\sigma_{\text{thr}} = \mu + 3 \cdot \sigma, \quad (3.5)$$

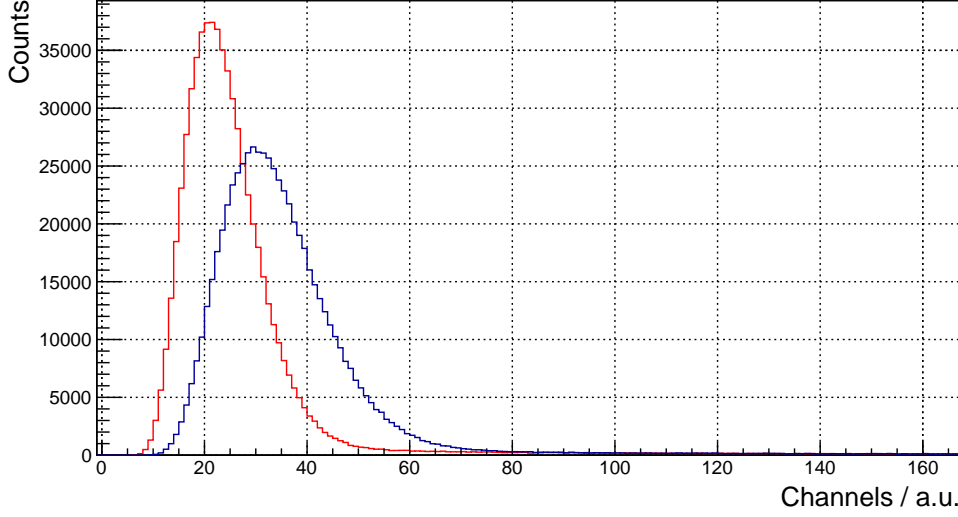


Figure 3.17: Distribution of the RMS of the baseline for all events with the beam in the central crystal 6 for the high gain branch of one LAAPD (blue) and for summed traces (red).

are depicted in Tab. 3.6. Here, the energies in MeV are determined by an absolute cosmic calibration which gives a calibration factor of

$$c_{\text{abs}} = 43.5 \frac{\text{ch}}{\text{MeV}}. \quad (3.6)$$

Details about the cosmic calibration can be found in [22]. The summation threshold

Noise	μ [channels]	σ [channels]	σ_{noise}	σ_{thr} [MeV]
HG1 RMS	31.50	10.15	0.72	
HG1 "Noise"	61.39	18.10		2.7
HG add "Noise"	43.53	12.04		1.8

Table 3.6: Determination of the summation threshold and noise level.

is not determined by RMS distribution but by a distribution which is generated by subtracting the maximum signal height within the baseline with the baseline value. This method takes into account strong fluctuations of the baseline. The distribution of this kind of "pseudo-noise" for the run with the beam impinging the central crystal 6

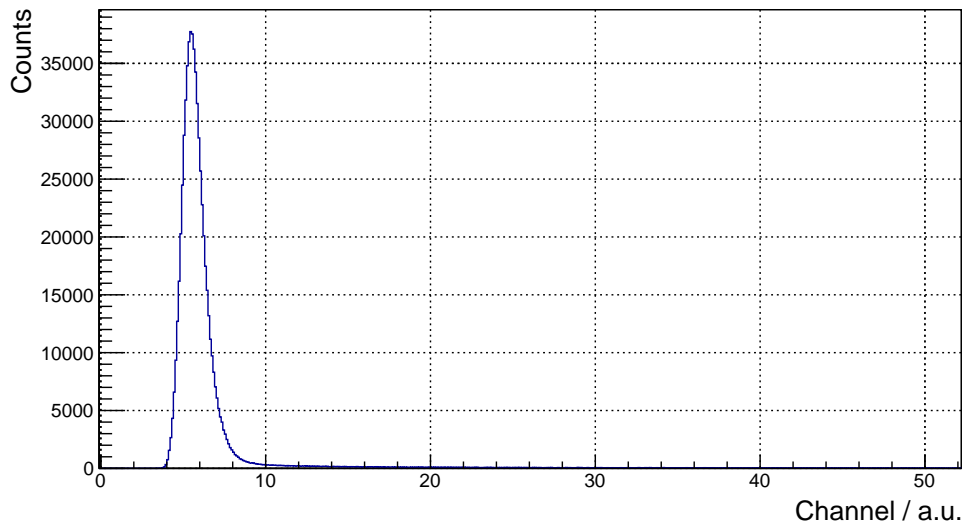


Figure 3.18: Distribution of the RMS of the baseline for all events with the beam in the central crystal 6 for the low gain branch.

is shown in Fig. 3.19. The determined summation threshold is listed in Tab. 3.6. In a next step the noise level was investigated for a different feature extraction method. In this method the original traces of the two LAAPDs are added bin by bin and the sum is divided by two before being feature extracted. The new added trace is treated in the known manner (see Fig. 3.7). The distribution of the RMS, the "noise" distribution and the summation threshold and noise level for the added traces are depicted in Fig. 3.17, Fig. 3.19 and Tab. 3.6, respectively. It is evident that the noise level and the summation threshold can be significantly improved by a different feature extraction method.

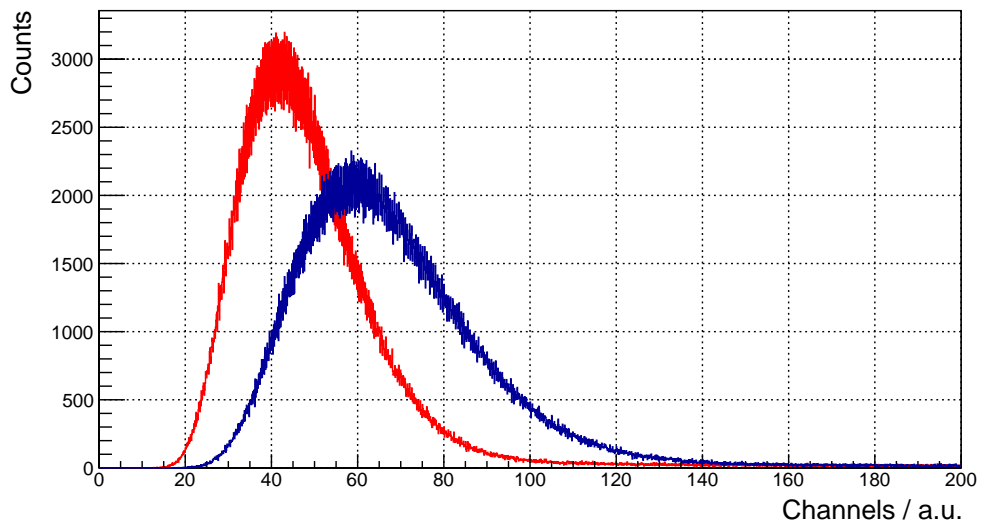


Figure 3.19: Distribution which is generated by subtracting the maximum signal height within the baseline with the baseline value with the beam in the central crystal 6 for the high gain branch of one LAAPD (blue) and for summed traces (red).

3.4 Analysis

3.4.1 Calibration

The basic calibration procedure for the analysis is depicted in Fig. 3.20. First, for

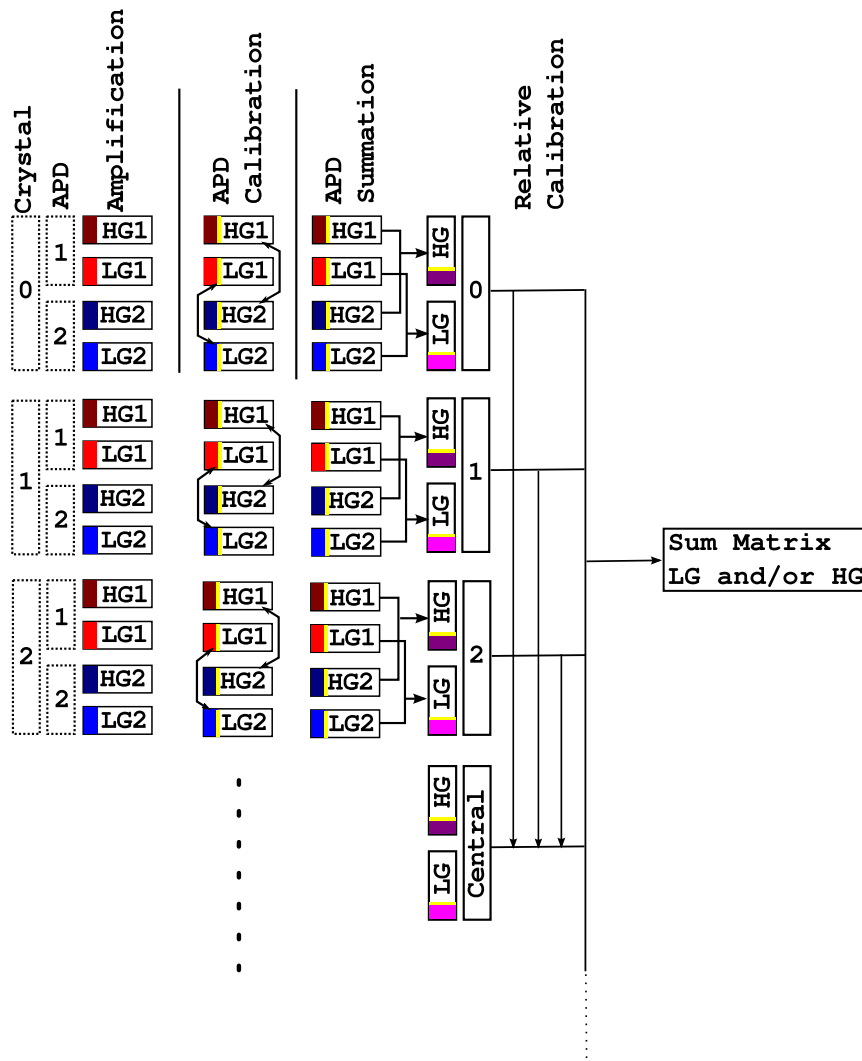


Figure 3.20: Schematic of the calibration procedure of the beamtime data for analysis purposes.

each crystal the two APD signals, which are decomposed in high gain and low gain, are calibrated before being summed. Since the deposited energy of a particle is dis-

tributed over several crystals, the response of the crystals is aligned with a relative calibration. A relative calibration is sufficient in order to obtain the energy resolution. Hence, an absolute calibration will not be presented here.

3.4.1.1 APD calibration

The linearity of the two APDs of the central crystal of the 3×3 matrix (crystal 6) is exemplarily shown in Fig. 3.21 and in Fig. 3.22 for the high gain branch and low gain branch, respectively. Plotted are the signal amplitudes in the respective branch of both APDs against each other. The slope of the straight line is used as scaling factor for the APD calibration of this crystal.

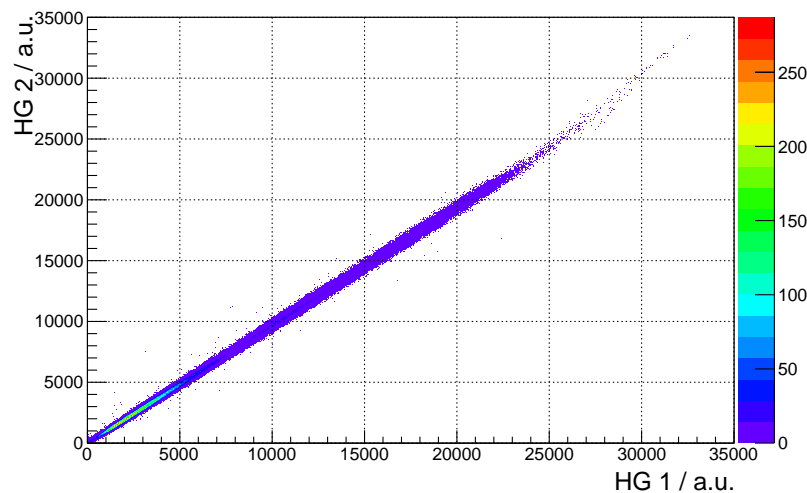


Figure 3.21: APD linearity of the central crystal for the high gain branch. Plotted are the signal amplitudes of both APDs. The slope is used for the APD calibration.

Nonetheless, not every APD pair showed a linear correlation. For example, in the high gain branch of crystal 1 a kink at approximately 5000 channels was observed. The correlation between both APDs of crystal 1 is shown in Fig. 3.23 for the high gain. Contrary to this observation, in the low gain branch a similar behavior was not investigated. Here, as depicted in Fig. 3.24, a linear correlation stuck out for the complete range. This indicates a wrong programming of the ASIC of crystal 1 or a

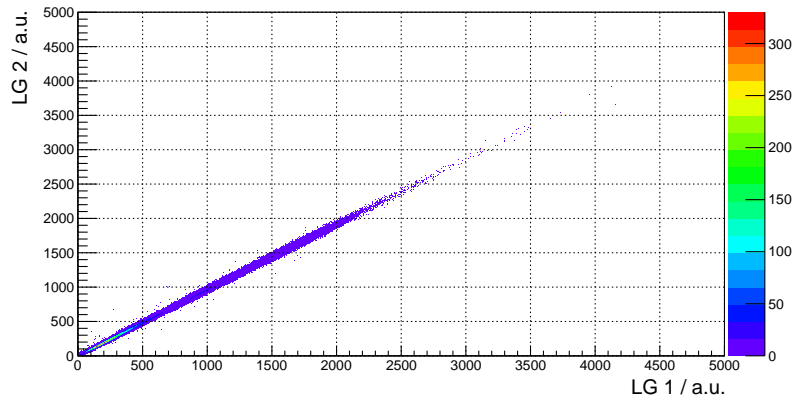


Figure 3.22: APD linearity of the central crystal for the low gain branch. Plotted are the signal amplitudes of both APDs. The slope is used for the APD calibration.

too high gain of the APD. In that case, only the linear part until the kink was used as the scaling factor for the APD calibration of this crystal.

The distribution of all APD calibration scaling factors is depicted in Fig. 3.25. In the ideal case both APDs convert the same amount of light which would correspond to a slope of 1. The observed relatively broad distribution can have various reasons. For example, the matching of the APDs can be wrong in a few cases. The APDs are matched according to their individual bias voltage for the envisaged gain. A wrong bias voltage would result in a gain difference of the APDs. But another reason could be a difference in light collection between the two APDs. Simulations with Geant4 are showing indications which support this reason. Investigations are still ongoing because such a behavior is not expected on statistical average.

In addition, the intrinsic ASIC amplification was obtained with the signal amplitudes of both gain branches. The distribution of the ratio of the signal amplitudes of the high gain branch and the signal amplitudes of the low gain branch is depicted in Fig. 3.26 and leads to an amplification of ~ 11 which is lower than the design value of the ASIC to be 16. But since the amplification is constant, the discrepancy has no influence on the analysis.

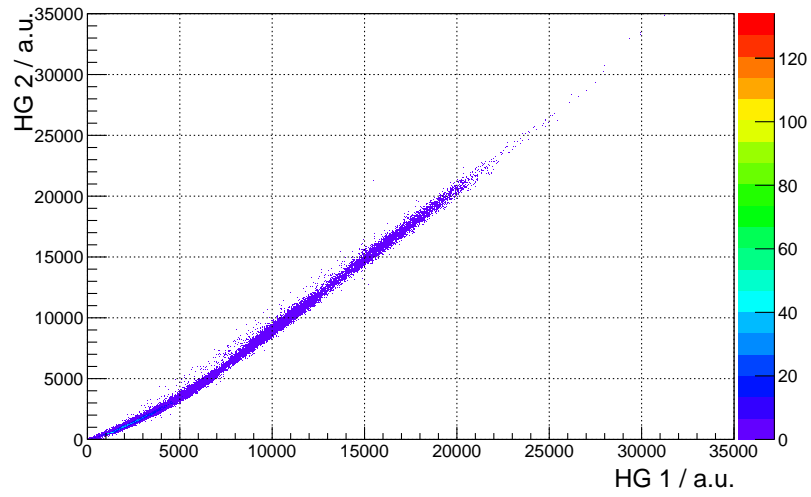


Figure 3.23: APD linearity of crystal1 for the high gain branch. Plotted are the signal amplitudes of both APDs. The slope is used for the APD calibration.

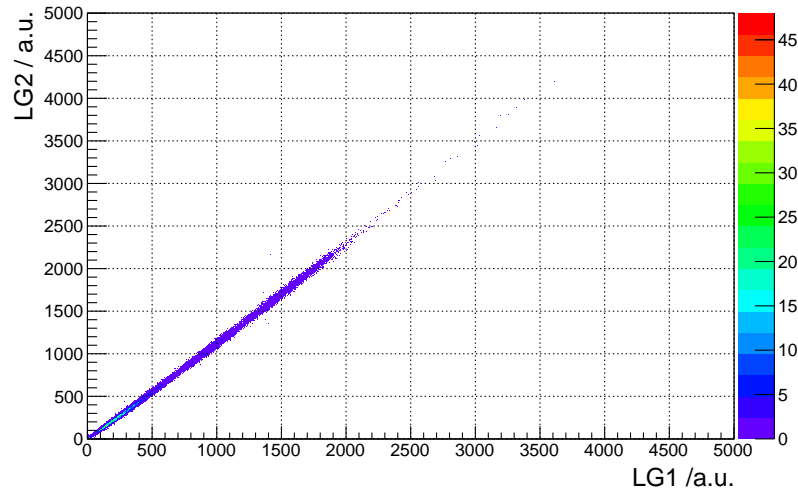


Figure 3.24: APD linearity of crystal1 for the low gain branch. Plotted are the signal amplitudes of both APDs. The slope is used for the APD calibration.

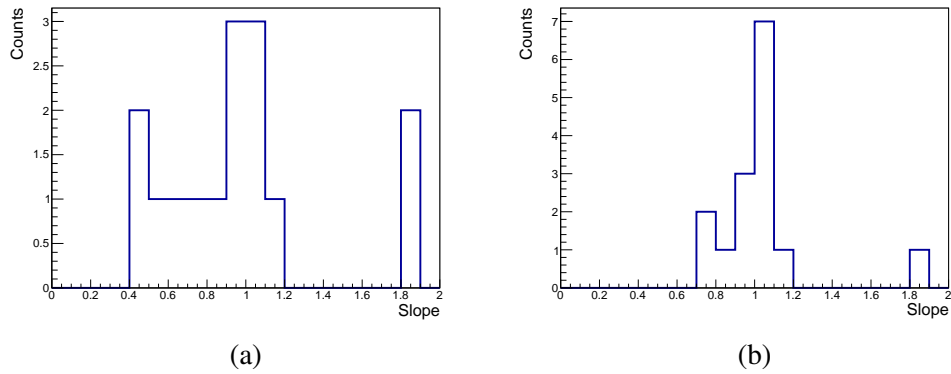


Figure 3.25: Distribution of the slopes of the APD correlation for all crystals. (a) shows the distribution for the high gain branch and (b) for the low gain branch. The slopes are used as a scaling factor for the APD calibration.

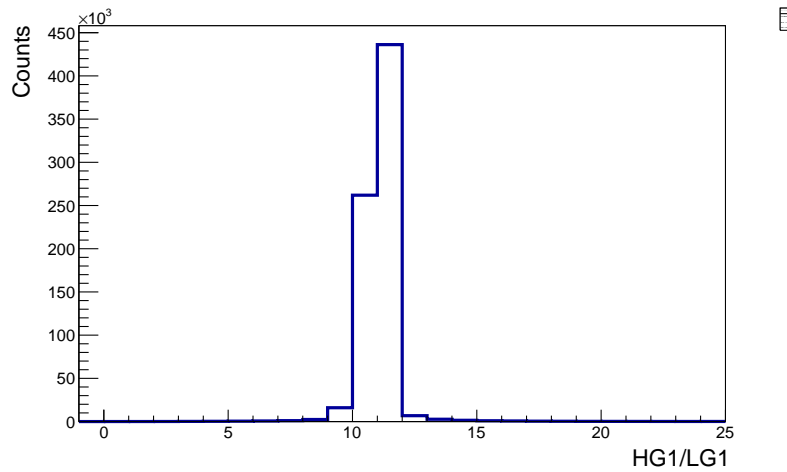


Figure 3.26: Intrinsic ASIC amplification. Plotted is the distribution of the ratio of the signal amplitudes of the high gain branch and low gain branch.

3.4.1.2 Relative calibration

The granularity of the crystal matrix results in an energy deposition of an impinging photon over more than one crystal. Hence, a relative calibration necessitates because energy contributions from several detectors have to be added. Therefore, functions are created that map the read-out from identical events for all detector elements onto a representative reference read-out. One detector element could be enough to calibrate the rest of the matrix. The only condition would be that the output is linear in energy. But there is a spectrum of possible outputs given that the read-out is statistical. This distribution is called response which is described by a skewed Gaussian distribution, the so-called Novosibirsk function (see Eq. 2.17). The response of the central crystal of the 3×3 matrix for selected tagger channels is depicted in Fig. 3.27. Finally, the

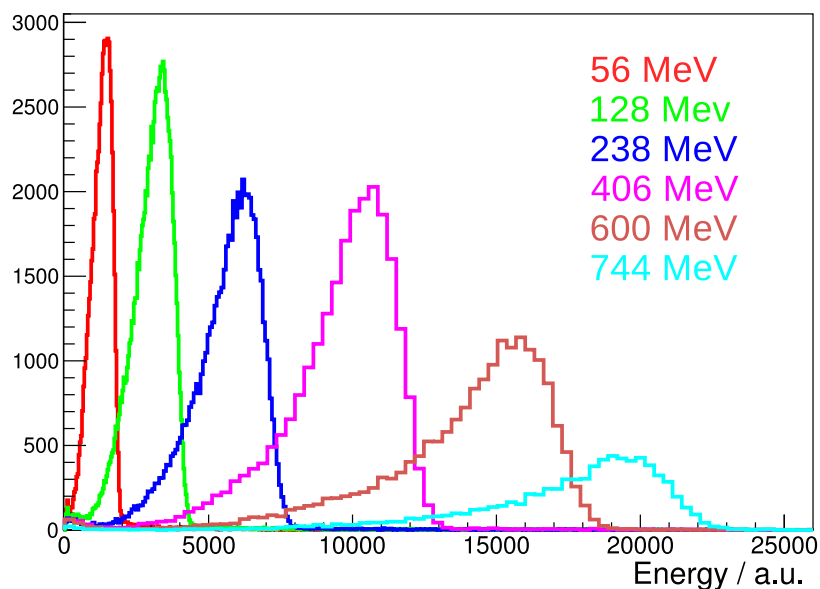


Figure 3.27: Tagged lineshapes for the central crystal 6. Variable binning is applied.

location of the response, the mode of the Novosibirsk function, is used as calibration point. This is done not only for the central crystal but also for the runs with the beam impinging the other crystals. Then, the central crystal 6 is used as reference crystal and the mode of its tagged response is plotted against the mode of the tagged response of the other crystals. The relative calibration is exemplarily shown for crystal 2 in Fig. 3.28. The correlation between the central crystal and crystal 2 is linear. Hence,

the fitted slope can be used for the relative calibration.

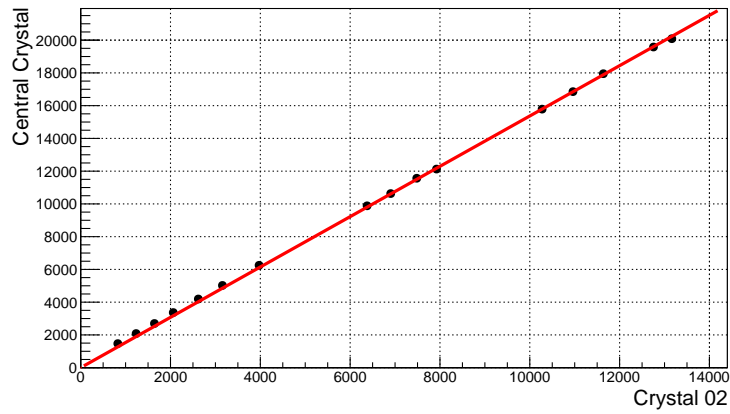


Figure 3.28: Relative calibration of crystal 2. The data points correspond to a tagger channel and plotted are the modes of the detector responses which were fitted with a Novosibirsk function.

3.4.2 Energy resolution

After the relative calibration of the detector elements, the responses of all crystals within the 3×3 matrix are added. But only contributions above the summation threshold of 2.7 MeV are included in the summation. Reason is the common gate read out of the PROTO120 modules, because of which a certain amount of channels assimilated only the noise contribution. Especially the case of impinging photons with low energies has to be considered. Their energy would be distributed over a few modules only. By adding up the signal of all modules of the matrix the resolution would be deteriorated. Therefore, a summation threshold has to be set. The influence of the threshold on the energy resolution was investigated in Fig. 3.29. There is no

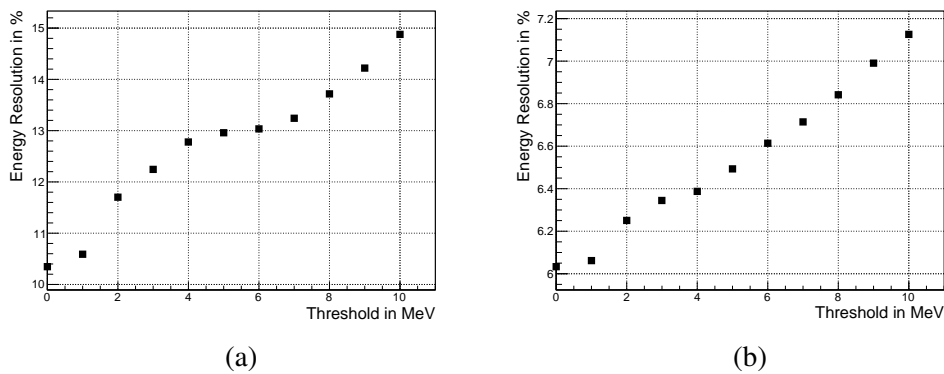


Figure 3.29: Energy resolution as a function of the applied threshold for a 56 MeV (a) and 192 MeV (b) photon beam.

evidence for an expected influence of a threshold within the investigated range. For lower energies (see Fig. 3.29a) a minimum was expected, but the noise seems to be dominant. Nevertheless, at the value $3 \cdot \sigma_{\text{noise}} = 2.7$ MeV there is a inflection point. Therefore, for the energy sum, this threshold value will be used unless otherwise specified. In addition, a cut on the tagged time distribution of the central crystal was applied. The time cut will also be used unless otherwise specified.

The gain in resolution by taking into account the neighboring crystals can be seen in Fig. 3.30. Here, the lineshapes of the central crystal and the summed 3×3 matrix are compared for one tagger channel.

All the summed and tagged lineshapes of the 3×3 matrix for the run in the central

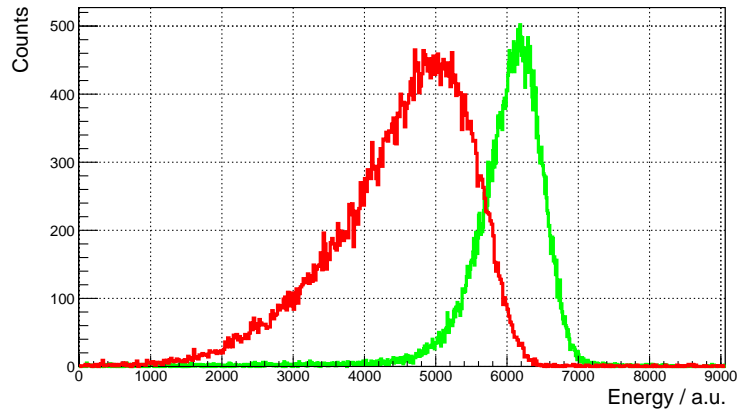


Figure 3.30: Lineshapes of the 3×3 matrix (green) and the central crystal (red) for the beam in the central crystal 6. A tagger energy of 192 MeV is selected.

crystal 6 of this matrix are depicted in Fig. 3.31 for selected tagger channels.

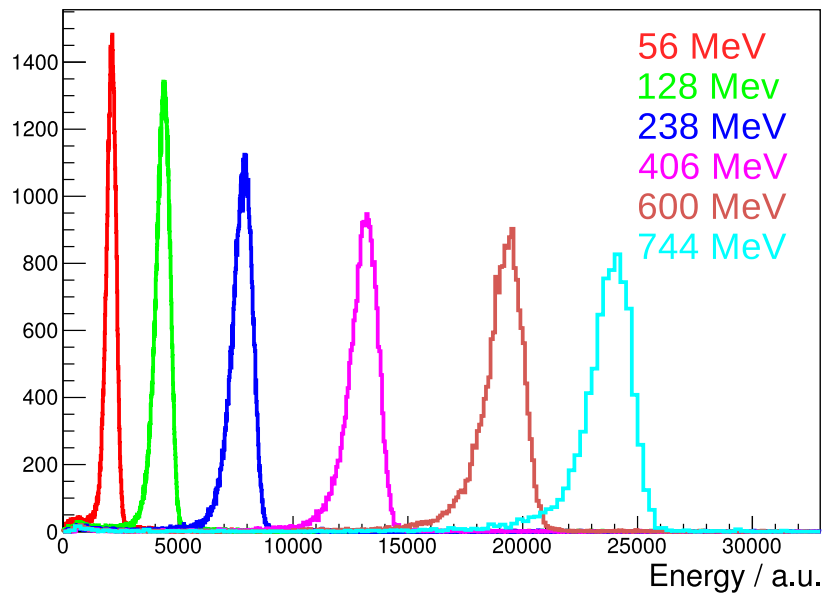


Figure 3.31: Summed and tagged lineshapes of the 3×3 matrix for the beam in the central crystal 6. Variable binning is applied. Only selected tagger channels.

Finally, the summed and tagged lineshapes are fitted with a Novosibirsk function (see Eq. 2.17) and the energy resolution σ_E/E is obtained. The energy resolution for the

beam impinging the center of the 3×3 matrix is depicted in Fig. 3.32. The following

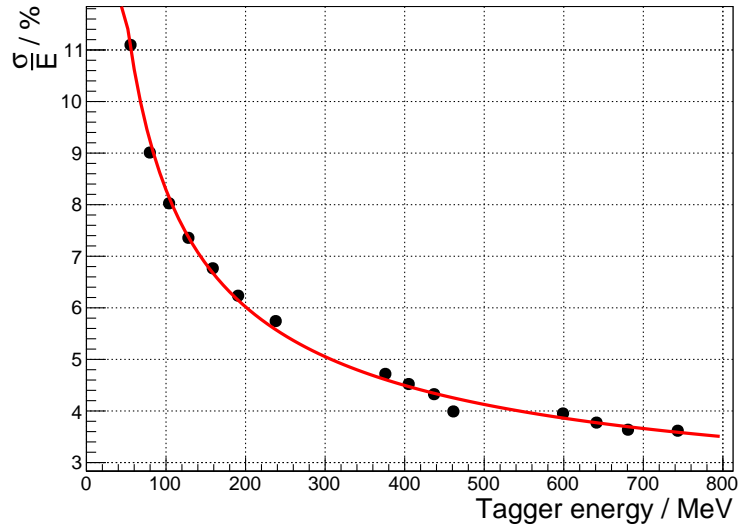


Figure 3.32: Energy resolution of the 3×3 matrix for the beam in the central crystal 6.

parametrization of the energy resolution could be obtained:

$$\frac{\sigma}{E} = \frac{0.16\%}{E/\text{GeV}} \oplus \frac{2.46\%}{\sqrt{E/\text{GeV}}} \oplus 2.32\% . \quad (3.7)$$

3.4.2.1 Multiplicity

The multiplicity is a quantity which gives the number of crystals which create a signal above the threshold. It is dependent on the photon energy, the threshold and it is affected by statistical fluctuations. The multiplicity as a function of the tagger energy is investigated in Fig. 3.33. Here, the mean value of the multiplicity was determined by a Gaussian distribution fit of the tagged multiplicity distribution. Exemplarily shown for different tagger energies is also the multiplicity as a function of the threshold in Fig. 3.34.

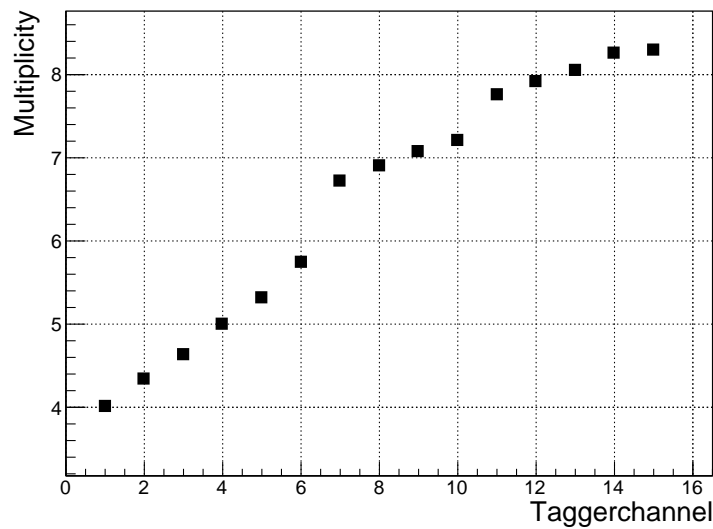


Figure 3.33: Multiplicity as a function of the taggerenergy.

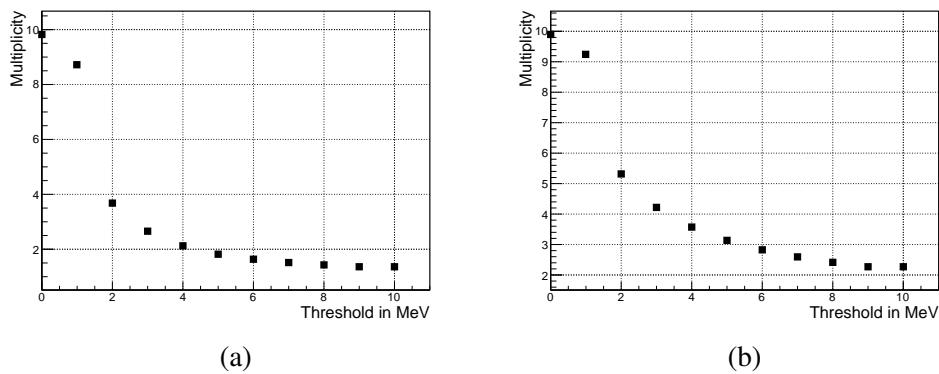


Figure 3.34: Multiplicity for various threshold values. (a) 56 MeV and (b) 192 MeV photon energy, respectively.

At the chosen summation threshold an inflection point can be observed.

3.4.2.2 Summed traces

It has been shown that the noise level can be reduced by summing up the traces before the feature extraction. The obtained energy resolution with this method is depicted

in Fig. 3.35. Here, a new relative calibration was performed. Further, a summation

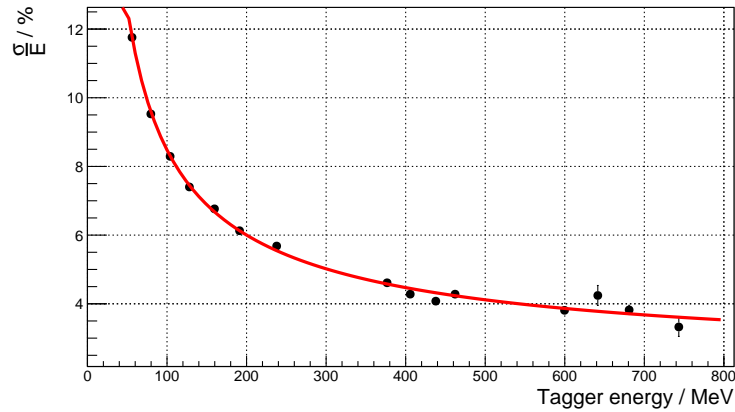


Figure 3.35: Energy resolution of the 3×3 matrix for the beam in the central crystal 6. The traces of both LAAPDs were added before the feature extraction

threshold of 2.4 MeV, which was obtained via threshold scan, was applied. This method shows a worse resolution for low energies and comparable results for higher energies.

In addition, the summed lineshapes have been compared with the lineshapes of one LAAPD which can be seen in Fig. 3.36. There is no indication for an improvement by adding the information of both LAAPDs.

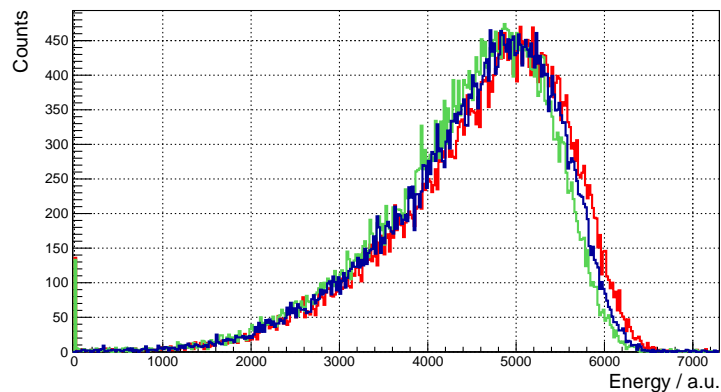


Figure 3.36: Comparison of the summed lineshapes of the 3×3 matrix for the beam in the central crystal 6 with the information of the summed traces and one LAAPD.

Chapter 4

Discussion

The main goal of this work is the optimization of the \bar{P} ANDA Barrel EMC with respect to the front-end electronics. In the past, the essential parameters influencing the performance of the Barrel EMC like the quality of the envisaged lead tungstate crystals have been improved significantly and put to the utmost. In addition, the performance of the preamplifier has reached its limits. On the other hand, studies have shown that straight crystals which are read-out with PMTs would accomplish a better performance. However, this configuration would not be usable in the geometry and environment of the \bar{P} ANDA experiment. Therefore, a significant further improvement of the performance of the Barrel EMC is out of reach. But the optimization of the Barrel EMC is still ongoing with prototype tests and results will be discussed within this chapter.

Two different prototypes for the \bar{P} ANDA Barrel EMC were presented within the scope of this work. The first prototype, the PROTO60, was designed to test the performance of an array of improved PWO-II crystals with an APD readout at a temperature of -25°C . The array consists of 60 type 6 crystals each read out with a single quadratic 1 cm^2 APD. The most recent prototype, the PROTO120, was developed to test the performance of a close to final design of the \bar{P} ANDA Barrel EMC with mechanical components, cooling and readout electronics as envisaged for the final Barrel layout. It consists of 120 crystals of the most tapered geometries, read out with two rectangular 1 cm^2 LAAPDs and the specially developed APFEL ASIC

as preamplifier and shaper.

Two dedicated chapter will reflect the results from beamtime tests for each prototype. On the one hand, Sec. 4.2 will focus on the reached performance of the PROTO60, while Sec. 4.3 covers the achieved present status of the PROTO120. For a better understanding of the performance of the prototypes, the predecessor of the $\bar{\text{P}}\text{ANDA}$ EMC, the CMS Electromagnetic CALorimeter (ECAL), will be discussed before the two prototypes in Sec. 4.1. In the end, Sec. 4.6 will discuss the unique results of a study of the impact of dead material in front of the PROTO60.

In all sections, the emphasis is put on the obtained energy resolution and the energy threshold in order to judge the front-end electronics. In that comparison, the results obtained for the PROTO60 represent sort of a specification limit, since the resolution parameters obtained in previous experiments with the prototype are used as reference for the detailed physics simulations of the research program of $\bar{\text{P}}\text{ANDA}$. The energy resolution is a crucial parameter for the $\bar{\text{P}}\text{ANDA}$ Barrel EMC because it has a strong impact on the accuracy of the invariant mass determination, like for example for J/Ψ states. In addition, the energy resolution influences the determination of the E/p ratio of electrons and positrons. The limit of the constant term of the energy resolution, which is the resolution limit at high energies, is determined by the separation of electrons and positrons from pions via their E/p ratio. Therefore, the constant term of the barrel EMC should be comparable to the momentum resolution of the tracking detectors in order to prevent a deterioration of the E/p ratio. Hence, the envisaged constant term for the $\bar{\text{P}}\text{ANDA}$ EMC should be close to 1%. Furthermore, a sufficient energy resolution is needed to identify light mesons like π^0 and η which contribute significantly to the background. It was shown that a reconstructed width of the mass of less than $8 \text{ MeV}/c^2$ and $30 \text{ MeV}/c^2$ for the π^0 and η , respectively, is desirable for a good identification. This leads to a required statistical term of 2% for the barrel EMC [30].

On the other hand, the energy threshold is important for the reconstruction of low energetic photons. Low energetic photons are a major contribution to many background channels at $\bar{\text{P}}\text{ANDA}$. Furthermore, for example in the charmonium physics program, many interesting channels have a significantly lower production ratio than the expected background contribution. Therefore, it is important to detect all photons

in order to reject the background events efficiently. Then again, the energy threshold is limited by the electronic noise of a single channel and the distribution of the deposited energy at low energies. The TDR of the EMC [30] states a reasonable compromise of 10 MeV as an energy threshold of the photon energy. In addition, simulations with an energy threshold of 10 MeV have shown that only 1% of the π^0 -mesons cannot be reconstructed. Whereas for an energy threshold of 30 MeV already 10% cannot be reconstructed. The detection threshold of 10 MeV translates directly to a single crystal threshold of ≤ 3 MeV. An incoming 10 MeV photon or electron deposits its energy in the worst and most unlikely case in between four modules with a single energy deposition of 2.5 MeV. Thus, a single crystal threshold of 3 MeV has to be guaranteed.

In conclusion, the calorimeter is essential for most of the physics channels and in particular for the invariant mass determination, but the efficiency of the calorimeter to detect all photons is considered more crucial than a perfect energy resolution. Hence, a good energy resolution for the invariant mass is desirable, but the focus is put on a low noise level for the detection of all photons.

The two beamtime tests investigated the response to tagged photons for an energy range up to about 800 MeV and up to 3.5 GeV at the MAMI facility in Mainz and at the ELSA facility in Bonn, in case of the PROTO120 and PROTO60, respectively. These energies correspond to the envisaged low and mid energy range of the $\bar{\text{P}}\text{ANDA}$ EMC. Hence, they cover the most relevant energies for the $\bar{\text{P}}\text{ANDA}$ Barrel EMC as confirmed in a simulation which is depicted in Fig. 4.1 [30]. It shows the simulated photon energy distribution for an antiproton energy of 15 GeV performed with a **Dual Parton Model (DPM)** based event generator. In general, the highest photon energies have to be handled by the forward spectrometer while the maximum photon energy decreases significantly for larger angles. It is evident that in the case of the Barrel EMC, which covers angles between 22° and 140° , the beamtime test energy range up to 3.5 GeV is fully sufficient.

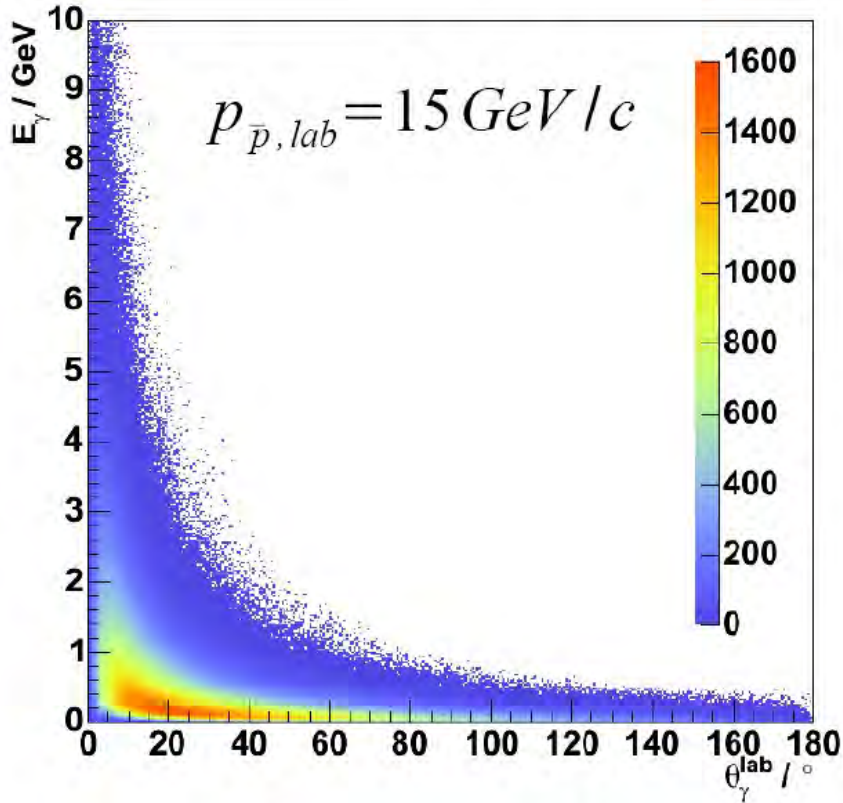


Figure 4.1: Simulated photon energy distribution vs. the laboratory angle for an antiproton energy of 15 GeV [30]. The Barrel EMC covers angles between 22° and 140° .

4.1 CMS ECAL

The design concept of the $\bar{\text{P}}\text{ANDA}$ EMC contained many features of the predecessor, the CMS ECAL. Hence, both calorimeters are considered to be comparable. The inherent difference of the CMS ECAL and the $\bar{\text{P}}\text{ANDA}$ EMC is the much larger energy regime of CMS compared to $\bar{\text{P}}\text{ANDA}$. Because of the high energetic electromagnetic probes at CMS, the lead tungstate crystals are $3.3 X_0$ longer in order to provide more stopping power for a better containment of the shower. In addition, the geometry of the CMS ECAL is bigger and therefore the geometry of the CMS crystals is less tapered due to the larger distance to the interaction point and beam axis. CMS accomplished a linearized light collection by roughing one of the crystal surfaces.

Furthermore, the crystals are operated at room temperature. The application of the design concept with a prototype test obtained the following parametrization of the relative energy resolution [56]:

$$\left(\frac{\sigma}{E}\right)_{\text{CMS}} = \frac{12\%}{E/\text{GeV}} \oplus \frac{2.8\%}{\sqrt{E/\text{GeV}}} \oplus 0.3\%. \quad (4.1)$$

The latter parametrization was achieved at beamtime tests with an electron beam impinging on the central crystal of a matrix of 3×3 crystals. The stochastic term of the energy resolution parametrization of CMS is significantly high because the CMS crystals are not optimized to be sensitive to low energetic photons. Moreover, the crystals are operated at room temperature which results in a significantly lower light yield compared to the crystals operated at a temperature of -25°C at $\bar{\text{P}}\text{ANDA}$. But like the electronic noise term, which is not optimized as well, both are not relevant for the high energies at CMS. The resolution limit at high energies is dominated by the constant term which turned out to be sufficiently low at the beamtime tests. The main contribution to the constant term is the longitudinal non-uniformity of light collection which had been optimized by a linearized light collection.

However, it has to be considered that the performance in Eq. 4.1 has been studied thoroughly at beamtime tests in an ideal environment. The impact of the magnetic field, radiation damage and the material in front of the ECAL while operated in the CMS detector do not merge into the latter performance. But the relative photon energy resolution has also been measured during operation of the complete CMS detector at the CERN LHC. Data of proton-proton collisions at the center-of-mass energy of 8 TeV was used for this analysis. The single-photon energy resolution in $Z \rightarrow e^+e^-$ events is depicted in Fig. 4.2 where the electron showers are reconstructed as photons. The resolution is shown in bins of the pseudorapidity η which is measured with respect to the interaction vertex from which the shower originates. In addition, the resolution depicted in Fig. 4.2 is analyzed by different R_9 variables. The R_9 variable is defined as the energy sum of the 3×3 crystals centered on the most energetic crystal in the supercluster divided by the energy of a supercluster. Hence, a low value of R_9 corresponds to photons converted before the ECAL, while higher values correspond to unconverted photons. The resolution for showers with a $R_9 \geq$

0.94 and a $R_9 < 0.94$ are shown in Fig. 4.2a and Fig. 4.2b, respectively. In contrast

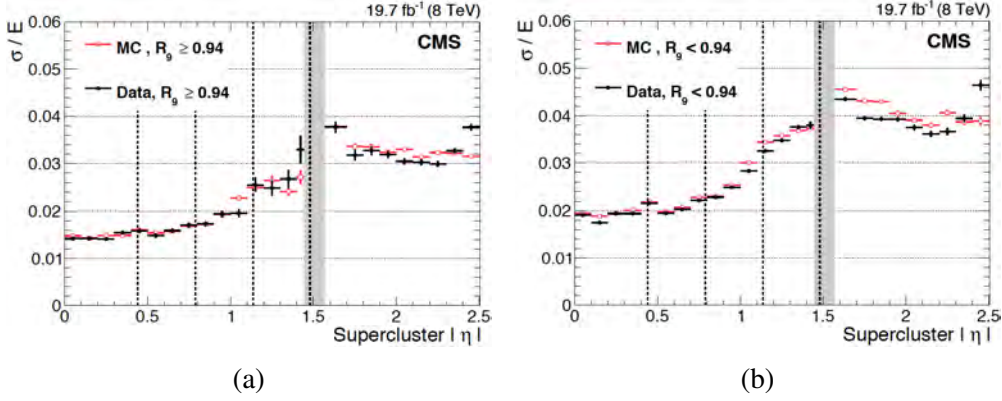


Figure 4.2: Relative photon energy resolution measured in small bins of absolute supercluster pseudorapidity in $Z \rightarrow e^+e^-$ events, for data (solid black circles) and simulated events (open squares), where the electrons are reconstructed as photons. The resolution is shown for (a) showers with $R_9 \geq 0.94$ and (b) $R_9 < 0.94$. The vertical dashed lines mark the module boundaries in the barrel, and the vertical grey band indicates the range of $|\eta|$, around the barrel/endcap transition, removed from the fiducial region [57].

to the beamtime test, the run data at such high energies shows a resolution from 1.5% up to 4% depending on the pseudorapidity. It is evident from Eq. 4.1 that a much lower irreducible constant term of only 0.3% could be achieved at the beamtime test. In general, the constant term is affected by energy leakage, single-channel response uniformity and stability which could explain the discrepancy [58]. This observation is significant, but cannot be translated directly to the $\overline{\text{PANDA}}$ EMC because of the much higher beam energy. Nevertheless, it indicates the influence of the experimental environment on the energy resolution.

In addition, CMS observed an effect on the single channel noise during run time. The single channel noise has been measured on the pre-samples of the laser events taken during standard monitoring sequences in 2011 and 2012. The evolution of the single channel noise, depicted in Fig. 4.3, shows an increasing noise level in run time and deterioration of about 10 MeV [59].

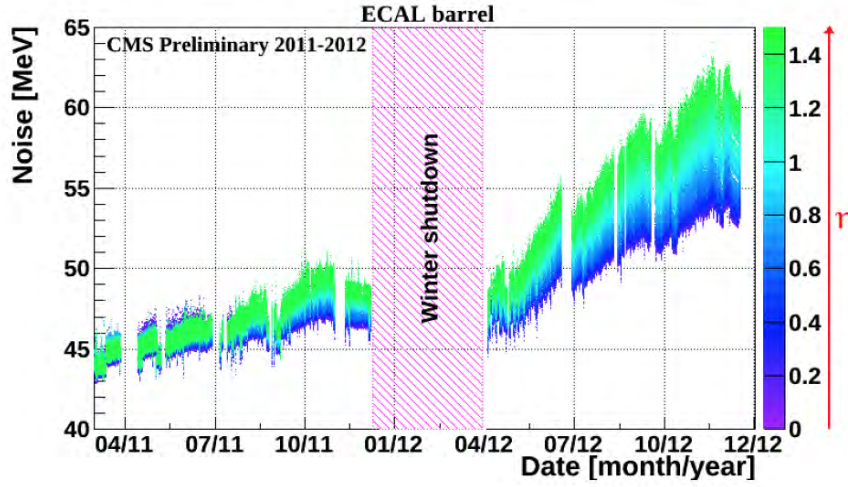


Figure 4.3: Single channel noise measured on the pre-samples of the laser events taken during standard monitoring [59].

4.2 PROTO60

4.2.1 Response of the PROTO60

The response of the PROTO60 was already investigated for almost the complete envisaged energy range of the \bar{P} ANDA experiment. The low energy regime has been covered with several experiments at the MAMI-facility in Mainz with tagged photons. Whereas the highest energies were covered with a positron beam at CERN. One goal of this work was to confirm the expected results for the response measured at experiments at Mainz and give complementary results for the mid energy range. Therefore, the response was explored with a tagged photon beam in the energy range from 0.5 – 3.5 GeV at the ELSA-facility in Bonn. The following parametrization of the relative energy resolution could be obtained for a 6×6 matrix:

$$\left(\frac{\sigma}{E}\right)_{\text{PROTO60, Bonn}} = \frac{1.43\%}{E/\text{GeV}} \oplus \frac{0.01\%}{\sqrt{E/\text{GeV}}} \oplus 2.37\% . \quad (4.2)$$

The results at Bonn are comparable to those at Mainz at an overlapping photon energy of 1 GeV. The energy resolution at 1 GeV and the summation threshold explored at

both facilities are depicted in Tab. 4.1. In addition, the EMC TDR value for the energy

	Energy resolution @ 1 GeV	Threshold
ELSA @ Bonn	2.8%	1.6 MeV
MAMI @ Mainz	2.4%	0.85 MeV
EMC TDR	2.2%	

Table 4.1: Comparison of selected results of the beamtime in Bonn with an older beamtime in Mainz and the TDR of the \bar{P} ANDA EMC.

resolution at 1 GeV is given. In general, to achieve the envisaged physics program, it is stated in the TDR that the parametrization of the energy resolution has to be better than

$$\left(\frac{\sigma}{E}\right)_{\text{TDR}} = \frac{2\%}{\sqrt{E/\text{GeV}}} \oplus 1\%. \quad (4.3)$$

Both experiments revealed a resolution worse than the EMC TDR requirement. While the resolution of the PROTO60 obtained at experiments at Mainz is only slightly worse, the deviation is more significant for the experiment at Bonn. The difference in resolution can be explained with the size of the beam spot. Earlier beam tests at the MAMI-facility have shown that the resolution is dependent on the position in the beam line and thereby on the size of the beam spot [26]. The beam spot at MAMI is much more narrow than the beam spot at ELSA. In addition, the intrinsic resolution of the tagger is significantly better at MAMI.

Generally, the energy resolution for the PROTO60 in Bonn is slightly worse not only at 1 GeV but also at low energies and energies above 1 GeV. Concerning the low energies, it was expected that the use of two LAAPDs per crystal will improve the resolution significantly. The photo statistics term should be reduced up to a factor of $\sqrt{2}$ by doubling the collected scintillation light. Therefore, two LAAPDs have been implemented in the next prototype PROTO120. Looking at higher incident energies, where the response is influenced by the constant term, there is room for improvement. The constant term is rather large compared to the CMS ECAL. In reference to the CMS ECAL, a possible improvement of the constant could be reached by linearizing the light collection. This possibility has been studied and will be discussed

in further detail in a dedicated chapter (see Sec. 4.4). Additionally, the constant term is affected by inaccuracies of the relative calibration. In case of the PROTO60, a cosmic calibration had turned out to be most reliable. A comparison of a cosmic muon calibration and an impinging muon beam calibration could be performed during a beamtime test at CERN. It revealed a difference in the energy deposition of 1.6% for a cosmic simulation with the PROTO60-NUF-NOISE model [33]. However, since the simulation has to include the correct non-uniformity in light collection for the crystals, a certain error has to be considered.

4.2.2 Position resolution

The resolution of the reconstructed position is strongly dependent on the incident photon energies. The obtained resolutions at the beamtime test in Bonn vary from 3.9 mm up to 4.8 mm at 1 GeV depending on the position of the beam. This is in a good agreement with results from an earlier beamtime test in Mainz which are shown in Fig. 4.4. However, both resolutions are not corrected for the spot size of the photon

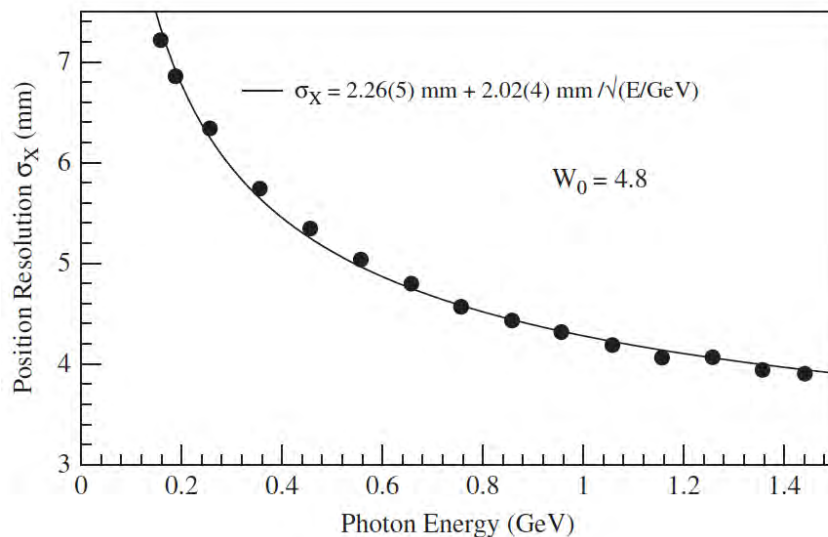


Figure 4.4: The resolution of the reconstructed position as a function of the incident photon energy measured at MAMI [40].

beam. It has to be considered that

$$\sigma_x = \sigma_{\text{Beam}} \otimes \sigma_{\text{Detector}} . \quad (4.4)$$

Therefore, at the highest energies the obtained resolutions seem to reflect the dimensions of the photon beam. Hence, these resolutions are not the limit which will be achievable for the Barrel EMC. Better resolutions of the reconstructed position in the order of $\sigma_{x,y} \approx 1.1$ mm have been obtained at a beamtime test of the PROTO60 together with prototype tracking detectors of the $\bar{\text{P}}\text{ANDA}$ MVD [27].

4.3 PROTO120

Despite the fact, that the first generation of prototype, the PROTO60, had achieved a sufficient performance which almost satisfied the requirements of the $\bar{\text{P}}\text{ANDA}$ EMC TDR, a new generation prototype, the PROTO120, had been constructed. The inherent difference is the read-out electronics. In particular, the specially developed APFEL ASIC preamplifier whose performance test was the principal task of the beamtime test with the PROTO120 presented within this work. The main requirement of the preamplifier deduces from the $\bar{\text{P}}\text{ANDA}$ physics program which relies on the detection of low energetic photons. Therefore, the read-out electronics is required to feature a low electronic noise level. A sufficiently low noise level had been stated by the developers at GSI in Darmstadt which had to be verified under real experimental conditions in a beamtime test with a prototype detector. Such a test has been performed with the PROTO120 at the MAMI-facility in Mainz. The obtained relative energy resolution of a 3×3 crystal array can be parametrized by

$$\left(\frac{\sigma}{E}\right)_{\text{PROTO120}} = \frac{0.16\%}{E/\text{GeV}} \oplus \frac{2.46\%}{\sqrt{E/\text{GeV}}} \oplus 2.32\% , \quad (4.5)$$

where the first component estimates a rather low electronic noise contribution, the second a sufficient stochastic term and the third a rather large constant term.

The electronic noise level of the beamtime test and the intrinsic photon equivalent

noise equivalent of the ASIC are calculated explicitly and compared in the following in order to judge the performance of the ASIC. Here, the electronic noise is defined as the standard deviation of a trace without the presence of a signal. In order to guarantee that, the baseline of each event was used to calculate the standard deviation. The obtained maxima of the distribution leads to an electronic noise level of $\sigma_{\text{noise}} = 31.5 \text{ ch} = 0.72 \text{ MeV}$.

The intrinsic photon equivalent noise equivalent of the ASIC can be calculated by the following formula:

$$\sigma_{\text{noise,ASIC}} = \frac{\text{Dynamic Range} \cdot \text{Noise} \cdot \text{Amplification}}{\text{Maximal Input Charge}} . \quad (4.6)$$

At the beamtime test, the ASIC saturated at around 24000 channels in the high gain branch which corresponds to a dynamic range of approximately 745 MeV. The ASIC amplification during the beamtime test deviated from the design value of 16 and amounted to 11. The large discrepancy is not understood until now. However, it has no influence on the analysis because it is constant. The noise of the ASIC had been measured at the laboratory at GSI for a maximal input charge of 8 pC and amounted to 0.74 fC. Finally, the photon equivalent noise level of the ASIC amounts to $\sigma_{\text{noise,ASIC}} = 0.76 \text{ MeV}$.

Hence, the noise level of the high gain branch is comparable to the intrinsic noise level of the ASIC. This indicates that the shielding and grounding concept of the PROTO120 is more than sufficient to reduce the influence of pick-up noise. Therefore, the ASIC can be regarded as the limiting factor of the noise level.

The electronic noise can be translated directly to the summation threshold of a single crystal. The summation threshold corresponds to the level where most of the noise contribution is rejected. The noise distribution is expected to be Gaussian. Therefore, more than 99.7% of the events are within a $3 \cdot \sigma$ -range. This range is usually set as the summation threshold. For the beamtime test a summation threshold of 2.7 MeV has been set to reject the noise contribution.

The summation threshold is below the single crystal threshold of 3 MeV which allows a cluster reconstruction threshold of 10 MeV required by the TDR. However, the summation threshold does not imply a sufficient low signal to noise ratio for photons below 3 MeV. In addition, the noise distribution showed a tail to higher energies.

The discrepancy to an expected Gaussian shape indicates a correlated noise. In order to get rid of the high noise level, a different feature extraction method had been tested. Adding the original traces of the two LAAPDs before the feature extraction steps, showed a significantly lower noise level. Nevertheless, the high energy tail did not vanish and the relative energy resolution obtained by this method did not show an improvement.

However, the trigger-less readout of the final Barrel EMC has to be considered. On the one hand, a single crystal threshold of 2.7 MeV would avoid a trigger of single channels which is caused by misidentified electronic noise events. On the other hand, the threshold makes it impossible to recover small pulses which are rejected below the threshold. Alternatives to the independent triggering are currently being discussed. A cluster trigger readout would feature the recovery of channels within the cluster which are below the threshold. Then again, the readout of a cluster would challenge the data processing. Therefore, the reduction of the threshold is considered as well. This method would enable the recovery of small pulses but would go along with an increased count rate of the detector which is limited by the rate capability of the electronics.

Furthermore, it should be accounted for the observed increasing noise level at CMS (see Sec. 4.1). A similar behavior at \bar{P} ANDA would foil the goals of the physics program.

4.4 Non-uniformity

The energy response of an electromagnetic calorimeter can be influenced by inhomogeneities. Studies with the \bar{P} ANDA crystals have shown that the light yield output is increasing with the level of tapering. The distribution of the light yield for the varying degree of tapering of the crystals is depicted in Fig. 4.5. The scintillation light produced in the front part of a non-tapered crystal is absorbed and thereby reduced compared to the light produced in the rear part. Responsible for the varying intrinsic absorption is the different path length. Therefore, a natural non-uniformity is introduced in longitudinal direction. In contrast, the tapering introduces a focussing

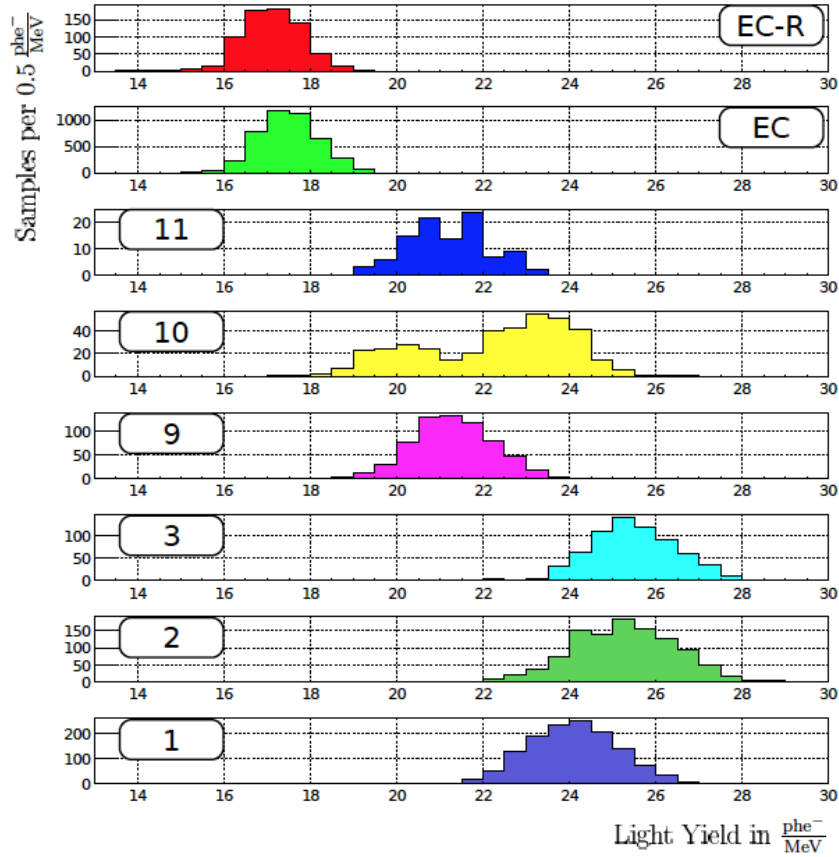


Figure 4.5: Distribution of the light yield for the varying tapered crystals. The light yield is measured relatively to a reference crystal by ACCOS [60] at CERN and calibrated to absolute values at JLU Gießen [26].

effect. The scintillation light produced in the front part is enhanced when focused to the rear part of the crystal due to the tapering [61]. The combination of both effects, focussing and absorption, results in a non-uniformity curve where the light produced in the front part of the crystal increases up to 50% for the most tapered crystals [27]. The interplay of the two effects and the resulting non-uniformity curve is illustrated in Fig. 4.6. Additionally, the nonlinear light collection becomes relevant for an electromagnetic shower within a staggered matrix. The average distribution of the energy deposition is not symmetric for the neighboring crystals with respect to the central crystal because of the staggered geometry. As an example, a schematic of an electromagnetic shower within the PROTO60 is depicted in Fig. 4.7. The event-wise variation of the position of the showers center of gravity is responsible for the

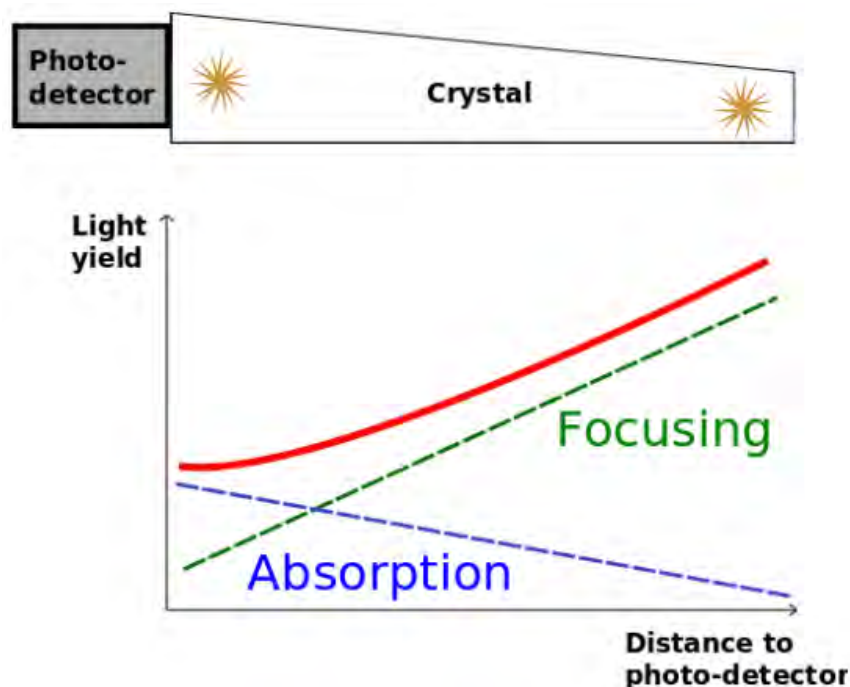


Figure 4.6: Focusing effect and absorption effect which are contributing to the light collection non-uniformity in tapered PWO-II crystals. Concept from [62].

deterioration of the energy resolution by the non-uniformity in light collection. The number of collected scintillation photons per deposited energy is larger for forward shifted crystals where the energy deposition is located closer to the photo sensors compared to the backward shifted crystals.

The CMS ECAL collaboration has studied several methods to reduce the non-uniformity and thereby to improve the energy response [63, 64]. At the rather larger energies of the electromagnetic probes detected by the CMS ECAL, the non-uniformity causes a deterioration of the constant term of the energy resolution. For energies above a few hundred MeV the shower dimensions and its fluctuations increase which amplifies the smearing of the energy response by the non-uniformity. On the other hand, the impact of photon statistics and electronic noise on the energy resolution is significantly reduced at higher energies. In order to meet the requirement of low constant term which is dominant at higher energies, the CMS ECAL collaboration decided to linearize the light collection. The most tapered side face of the crystals has been depolished whereby the light yield detected by the APD is equalized. The

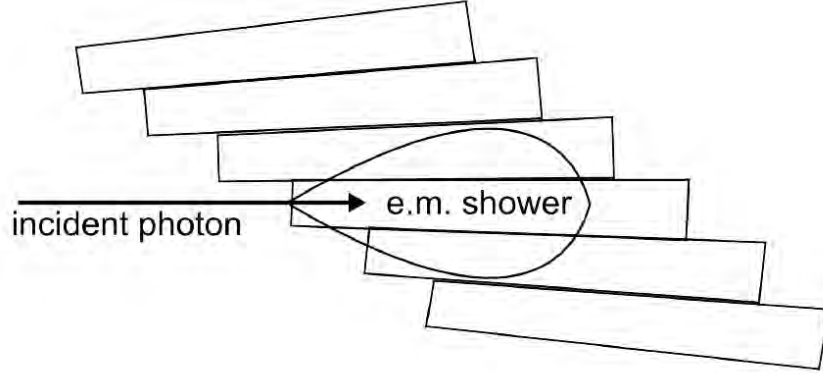


Figure 4.7: Schematic of an electromagnetic shower within the PROTO60. [33].

linearization of the light collection showed satisfactory results for the constant term of the energy resolution (see Eq. 4.1).

However, the $\bar{\text{P}}\text{ANDA}$ EMC is foreseen to detect much lower energetic electromagnetic probes. While the low energetic threshold is of more than 200 MeV at CMS [65], it is only 10 MeV at $\bar{\text{P}}\text{ANDA}$. Therefore, the photon statistics has to be considered as a crucial parameter at $\bar{\text{P}}\text{ANDA}$. A linearization of the light collection by depolishing reduces the light yield and is expected to deteriorate the resolution for energies below 100 MeV. Nonetheless, for $\bar{\text{P}}\text{ANDA}$ it is an optimization problem to balance the compensation of the non-uniformity and a deteriorated resolution for low energies while the resolution improves for increasing energies. Therefore, a sub-matrix within the PROTO120 has been equipped with crystals where one side is depolished. Detailed studies can be found in [22]. The relative energy resolution for a 3×3 linearized crystal array can be parametrized by

$$\left(\frac{\sigma}{E}\right)_{\text{Depolished}} = \frac{0.27\%}{E/\text{GeV}} \oplus \frac{2.30\%}{\sqrt{E/\text{GeV}}} \oplus 0.50\% . \quad (4.7)$$

This result will be discussed in comparison with a polished crystal matrix within the PROTO120 and results from PROTO60 in the following section.

4.5 Comparison PROTO60 and PROTO120

The results from the first prototype of the Barrel EMC, the PROTO60, are considered as performance limit for the envisaged preamplifier of the $\bar{\text{P}}\text{ANDA}$ Barrel EMC, the APFEL ASIC. The parametrization of the relative energy resolution of the PROTO60 for the energy range from 50 MeV up to 15 GeV can be described by [33]

$$\left(\frac{\sigma}{E}\right)_{\text{PROTO60, 1 MeV}} = \frac{0.25\%}{E/\text{GeV}} \oplus \frac{1.86\%}{\sqrt{E/\text{GeV}}} \oplus 1.46\% . \quad (4.8)$$

The latter parametrization was obtained for all 60 crystals of the PROTO60 and a summation threshold of 1 MeV. Therefore, the results of the PROTO120 cannot be compared directly, since only a 3×3 crystal array with an higher noise level has been measured so far. In order to be able to compare the performance of both detectors, the data of a beamtime test with the PROTO60 at MAMI in 2011 has been re-analyzed. The new analysis considered only a 3×3 crystal array and a summation threshold of 2.8 MeV while the other details of the analysis are identical to [33]. The new analysis results in the following parametrization of relative energy resolution:

$$\left(\frac{\sigma}{E}\right)_{\text{PROTO60, 2.8 MeV}} = \frac{0.32\%}{E/\text{GeV}} \oplus \frac{2.11\%}{\sqrt{E/\text{GeV}}} \oplus 1.6\% . \quad (4.9)$$

In addition, the obtained relative energy resolution of the re-analyzed PROTO60 data is depicted together with the relative energy resolution of the PROTO120 in Fig. 4.8. The relative energy resolutions of both prototypes with the same threshold show rather comparable results for the lower energies but a discrepancy of about 0.5% – 1% for increasing energies. Nevertheless, a significantly better energy resolution can be achieved with a 1 MeV threshold because of the lower experimental noise level of the PROTO60. The two prototypes can be compared even better by investigating the performance of the PROTO60 with a SADC readout. Details about a beamtime test and the corresponding analysis can be found [40]. The obtained relative energy resolution for a 3×3 crystal array and a 2 MeV summation threshold is parameterized

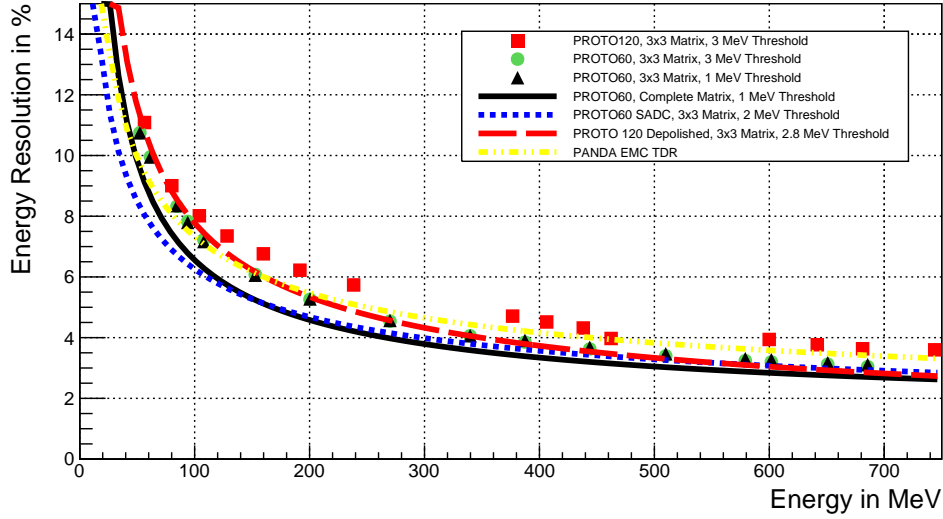


Figure 4.8: Comparison of the relative energy resolution of the PROTO60 and PROTO120. In both cases, the resolution is obtained for a 3×3 crystal array and a summation threshold of 3 MeV.

by

$$\left(\frac{\sigma}{E}\right)_{\text{PROTO60, SADC}} = \frac{1.70\%}{\sqrt{E/\text{GeV}}} \oplus 0.88\% . \quad (4.10)$$

The electronic noise term is below 10^{-4} and therefore neglected. It is evident that the resolution of the PROTO 60 with a SADC readout is superior to the resolution obtained with the PROTO120. This indicates a limitation of the achievable performance due to the intrinsic noise level of the APFEL ASIC.

In summary, the electronic noise term of the parametrization of the energy resolution is comparable for the PROTO60 and PROTO120 with the same threshold, significantly better for a reduction of the threshold of PROTO60 to 1 MeV and is negligible small for a SADC readout of the PROTO60.

The stochastic term was considered to improve for the two APD readout of the PROTO120 compared with the single APD readout of the PROTO60 by a factor up to $\sqrt{2}$. However, the stochastic term improved only non-significant. This has been verified by analyzing PROTO120 data with information from one APD and both APDs.

Considering the constant term, the requirements of the \bar{P} ANDA EMC TDR can only be fulfilled with the depolished crystals.

In conclusion, despite the fact that the preamplifier has reached its performance limits, there is still room for improvement. The linearization of the light collection results in a significant improvement for the energy resolution at higher energies. But since a linearization has not been considered initially, the results have to be confirmed at lower energies and also for a larger crystal matrix.

Additionally, there are other parameters which still can be optimized to improve the energy resolution at higher energies. The relative calibration of the detectors has a significant uncertainty which results in lateral inhomogeneities and influences the achievable energy resolution. The influence of the relative calibration is discussed in [22]. The calibration with data from the interaction of cosmic muons seems to be advantageous compared to a calibration with data from an in-beam calibration which was used for this work. But it has to be considered that the alignment of the photon beam has not been adjusted for the outer crystals during the calibration runs of the in-beam data. The alignment of the photon beam has a strong impact on the response of a single crystal. On the other hand, cosmic calibration can only be used as a pre-calibration for the final \bar{P} ANDA EMC. The envisaged final calibration uses the reconstruction of the invariant mass of photon pairs from neutral pions or eta mesons. At lower energies, there is the possibility to improve the energy resolution with different feature extractions. The method used for this work is a simple peak sensing feature extraction. The influence of different methods on the energy resolution has been studied with the depolished crystal matrix [22]. One method obtains the energy information by fitting the signal traces. This method provides an improved energy resolution for energies above 100 MeV and is expected to be even better for larger cluster sizes. The improvement results from the averaging of trace fluctuations and noise contributions for low energetic signals in the outer crystals. Another feature extraction method integrates the signal over a limited region around the extremum. Since this method provides similar results like the peak sensing feature extraction, the fitting method can be recommended. However, an high computing effort has to be considered for the applied fitting routine.

4.6 Influence of dead material in front of the Barrel EMC

The experiments with the Barrel EMC prototypes with tagged photon beams were conducted under idealized conditions. The CMS collaboration observed a significant deterioration of the energy resolution for the ECAL operated within the CMS detector (see Sec. 4.1). Even though the deterioration has been observed at much higher energies compared to \bar{P} ANDA, a certain influence has to be expected for the Barrel EMC as well. Therefore, for example the material budget in front of the Barrel EMC has to be considered for the future operation within the \bar{P} ANDA detector. The interaction of particles in detector material in front of the Barrel EMC affects the reconstruction efficiency of electromagnetic probes and the energy resolution. For the relevant photon energies the dominant interaction process is pair production, while electrons lose their energy via bremsstrahlung. The largest contribution to the material budget in front of the Barrel EMC comes from the Cherenkov detectors. All contributions to the material budget are depicted in Fig. 4.9. Therefore, the photon conversion probability in the Barrel DIRC has been simulated for 1 GeV photons generated homogeneously in a polar angle range between 22° and 145° (see Fig. 4.10). The conversion probability has a minimum of 15% at 90° and increases up to 27% for lower values of the polar angle. The conversion of a photon causes a preshower (see Fig. 4.11a) in the DIRC which can lead to a degradation of the energy resolution if part of the secondary showers are not identified. The reconstructed energy of 1 GeV photons has been simulated with and without DIRC preshowers. Fig. 4.11a illustrates the geometrical arrangement. Fig. 4.11b confirms that the energy distribution for preshower photons becomes significantly worse. In particular, the distribution becomes broad and asymmetric with a strong low energy tail because a fraction of the photon energy is deposited in the DIRC material. The shifted lineshape leads to a wrong reconstruction of the primary photon energy.

A major goal of the beamtime test at ELSA in Bonn was to study the influence of the material budget of the DIRC experimentally. For this reason, a 1.5 cm thick quartz plate, which is the radiator material of the DIRC, was placed in front of PROTO60.

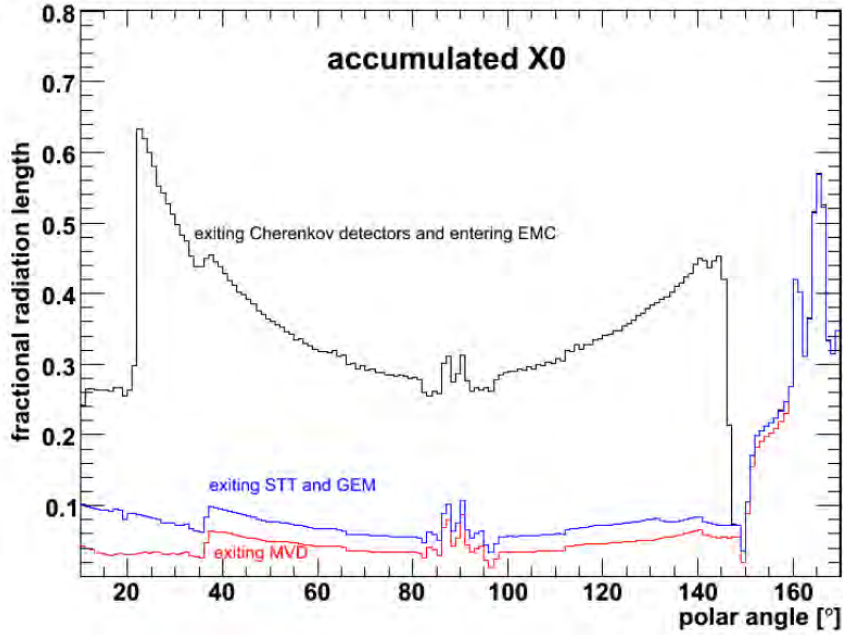


Figure 4.9: Material in front of the EMC in units of X_0 as a function of the polar angle [30].

A plastic paddle in front and behind the quartz plate made it possible to identify and select conversion in air and within the passive material. The relative energy resolution of a 6×6 crystal matrix with the quartz plate in front of the PROTO60 turned out to be comparable to the relative energy resolution without the quartz plate. If the Vetos are used to discriminate photon from electron events, it is evident that the energy resolution of a 6×6 crystal array for exclusively conversion events is significantly better than for exclusively photon events. The same holds true for a 3×3 crystal array, but only for energies above 1 GeV. Below 1 GeV the resolution gets significantly worse. A simulation of the summed lineshapes of a 3 GeV photon and positrons impinging a crystal array could verify a significantly better energy resolution for electrons/positrons.

For \bar{P} ANDA it is proposed to implement a SciTil detector between the DIRC and the EMC as a time of flight detector acting as a trigger for pre-showers in the DIRC. The SciTil based on plastic scintillator of low Z features a low material budget and is therefore insensitive to photons but has a high efficiency to detect charged particles.

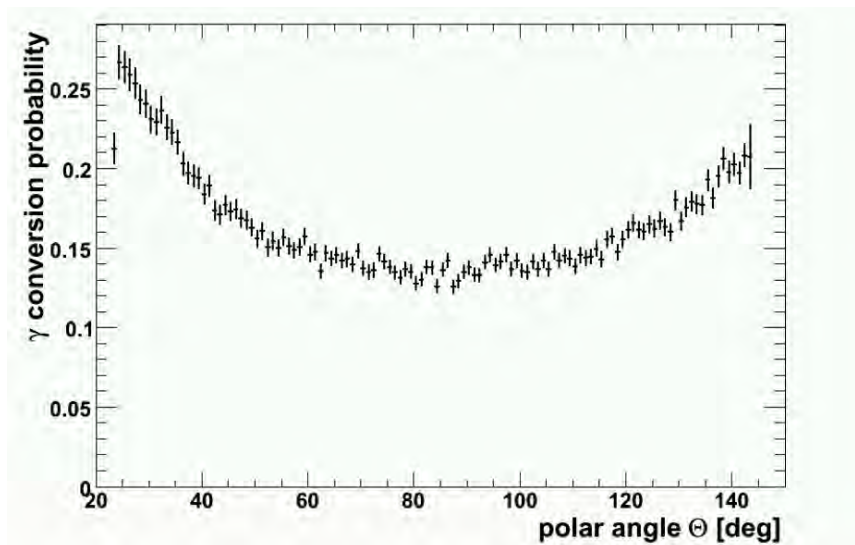


Figure 4.10: Photon conversion probability in the DIRC as a function of the polar angle [30].

In a study for the BaBar experiment, it was shown that, by detecting preshowers in the DIRC detector itself, the resolution for π^0 could be improved by about 5% [66]. Comparing directly samples with and without conversions the resolution is worse by about 50% with conversions. The reason for a rather small conversion detection efficiency in the BaBar case was that the light from conversion electrons had to be detected by the DIRC itself. But a separate detector at \bar{P} ANDA, the SciTil, shall discover conversion with full efficiency and therefore enhance the energy resolution. This conclusion seems to be supported by the results of the beamtime test at ELSA in Bonn but only for energies above 1 GeV. The \bar{P} ANDA physics program requires a sufficient energy resolution for low energetic photons which cannot be assured by the experimental results with the quartz plate at the moment due to too large uncertainties. However, preliminary simulations with the PandaRoot framework of the SciTil group observed that there is no prominent deterioration of photon energy resolution due to preshowers. The SciTil detector seems to be indispensable for the \bar{P} ANDA experiment as a Veto detector.

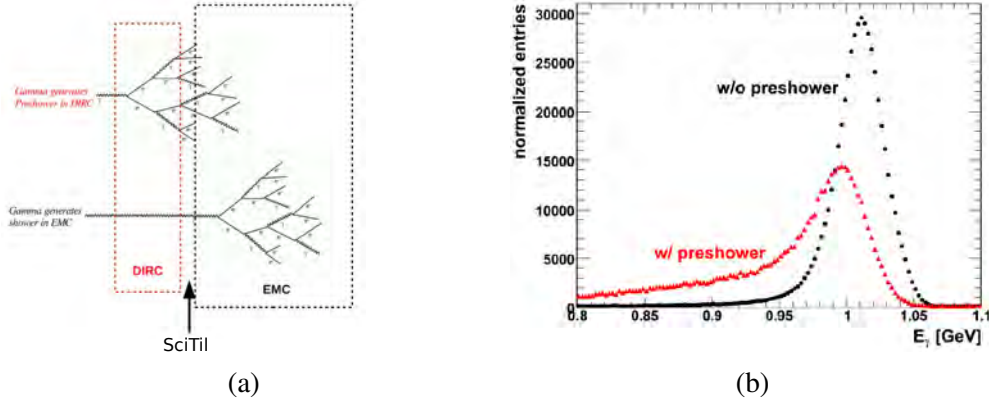


Figure 4.11: Shower development with and without a DIRC preshower (a) and the reconstructed energy for 1 GeV photons with and without DIRC preshower (b). The curve with the preshower is scaled with a factor of 4.87 [30].

4.7 Outlook

The performance of the PROTO120 and in particular the performance of the specially developed preamplifier turned out to be inferior compared to the PROTO60 and its discrete preamplifier. However, recent studies have shown that a depolishing of one crystal surface, like at CMS, provides a comparable resolution at lower energies and an improved resolution for increasing energies [22]. It has been shown that the performance can also be optimized by a different feature extraction and improved calibration.

In order to judge the performance of the PROTO120 even better and to understand and reduce the noise level further, a beamtime test at MAMI with a larger 5×5 crystal array of polished and de-polished crystals, respectively, has been performed in December 2015. The analysis is still ongoing and provides only preliminary results so far. Furthermore, the construction of a first barrel slice will be finished by the end of the year and will be tested at a beamtime test afterwards.

In addition, a measurement with a quartz plate in front of the PROTO120 was performed during the beamtime test in December 2015 in order to confirm the results with the PROTO60 and to provide a better understanding of the possible benefits from a preshower detector.

Bibliography

- [1] **FAIR** Collaboration, “FAIR CDR - An International Accelerator Facility for Beams of Ions and Antiprotons, Conceptual Design Report,” 2001.
http://www.fair-center.de/fileadmin/fair/publications_FAIR/FAIR_CDR.pdf.
- [2] **PANDA** Collaboration, “Technical Progress Report for PANDA: Strong Interaction Studies with Antiprotons.” https://panda.gsi.de/oldwww/archive/public/panda_tpr.pdf.
- [3] **SLAC-SP-017** Collaboration, J. E. Augustin *et al.*, “Discovery of a Narrow Resonance in e^+e^- Annihilation,” *Phys. Rev. Lett.* **33** (1974) 1406–1408. [Adv. Exp. Phys.5,141(1976)].
- [4] U. Wiedner. private communication.
- [5] **PANDA** Collaboration, M. F. M. Lutz *et al.*, “Physics Performance Report for PANDA: Strong Interaction Studies with Antiprotons,” arXiv:0903.3905 [hep-ex].
- [6] **PANDA** Collaboration, E. Prencipe, “Perspectives of open charm physics at PANDA,” *EPJ Web Conf.* **95** (2015) 04052, arXiv:1410.5680 [hep-ex].
- [7] V. Crede and C. A. Meyer, “The Experimental Status of Glueballs,” *Prog. Part. Nucl. Phys.* **63** (2009) 74–116, arXiv:0812.0600 [hep-ex].
- [8] T. H. Randriamalala, *Conceptual Design of the PANDA Luminosity Monitor and Reconstruction Strategy to Measure the Width of the X(3872) State*. PhD thesis, Ruhr-Universität Bochum, 2011.

- [9] **PANDA** Collaboration, K. Schönning, “Baryon Physics with PANDA.”
https://panda-wiki.gsi.de/foswiki/pub/Physics/Baryons/WebHome/schoenning_baryon_panda_v2.pdf.
- [10] M. Zambrana, “Electromagnetic Processes in PANDA,” *PoS (Photon 2013)* (2013) 058.
- [11] **PANDA** Collaboration, E. Tomasi-Gustafsson, “Form factor measurements with bar PANDA at FAIR,” *Chin. Phys.* **C34** (2010) 863–868.
- [12] P. Achenbach, S. Bleser, J. Pochodzalla, A. S. Lorente, and M. Steinen, “Hypernuclear Physics at PANDA,” *Hyperfine Interact.* **209** (2012) 99–104, arXiv:1206.3149 [nucl-ex].
- [13] **PANDA** Collaboration, “Technical Design Report for the PANDA Internal Targets,” 2012. http://www.fair-center.eu/fileadmin/fair/publications_exp/PANDA_Targets_TDR.pdf.
- [14] **PANDA** Collaboration, “Technical Design Report for the PANDA Micro Vertex Detector,” arXiv:1207.6581v2.
- [15] **PANDA** Collaboration, “Technical design report for the panda (antiproton annihilations at darmstadt) straw tube tracker,” *The European Physical Journal A* **49** no. 2, (2013).
<http://dx.doi.org/10.1140/epja/i2013-13025-8>.
- [16] **PANDA** Collaboration, “Gas Electron Multiplier.” http://www-panda.gsi.de/framework/det_iframe.php?section=GEM.
- [17] **PANDA** Collaboration, J. Schwiening, “The Dirc Detectors for the PANDA experiments at FAIR,” 2011. https://indico.cern.ch/event/102998/session/31/contribution/124/attachments/10502/15361Schwiening_TIPP2011.pdf.
- [18] **PANDA TOF Group** Collaboration, L. Gruber, S. E. Brunner, J. Marton, H. Orth, and K. Suzuki, “Barrel time-of-flight detector for the PANDA experiment at FAIR,” arXiv:1507.05845 [physics.ins-det].

-
- [19] **PANDA** Collaboration, “Technical Design Report for the PANDA Solenoid and Dipole Spectrometer Magnets,” 2009. https://panda.gsi.de/oldwww/archive/public/P_magn_TDR.pdf.
- [20] **PANDA** Collaboration, “Technical Design Report for PANDA Muon System,” 2012. http://panda-wiki.gsi.de/pub/Muon/TechnicalDesignReport/panda_tdr_muon_final.pdf.
- [21] **PANDA** Collaboration, “Technical Design Report for PANDA Forward Spectrometer Calorimeter,” 2015.
- [22] S. Diehl, *Optimization of the Influence of Longitudinal and Lateral Non-Uniformity on the Performance of an Electromagnetic Calorimeter*. PhD thesis, Justus-Liebig-Universität Gießen, 2016.
- [23] S. Eidelman and B. Shwartz, “Interactions of particles and radiation with matter,” in *Handbook of Particle Detection and Imaging*, C. Grupen and I. Buvat, eds., pp. 3–23. Springer Berlin Heidelberg, 2012. http://dx.doi.org/10.1007/978-3-642-13271-1_1.
- [24] **Particle Data Group** Collaboration, C. Amsler *et al.*, “Review of particle physics,” *Phys. Lett. B* **667** (July, 2008) 1.
- [25] W. Leo, “Passage of radiation through matter,” in *Techniques for Nuclear and Particle Physics Experiments*, pp. 17–68. Springer Berlin Heidelberg, 1994. http://dx.doi.org/10.1007/978-3-642-57920-2_2.
- [26] T. Eissner, *The new PWO Crystal Generation and Concepts for the Performance Optimisation of the PANDA EMC*. PhD thesis, Justus-Liebig-Universität Gießen, 2013.
- [27] D. Bremer, *Measurements and Simulations on Position Dependencies in the Response of Single PWO Crystals and a Prototype for the PANDA EMC*. PhD thesis, Justus-Liebig-Universität Gießen, 2013.
- [28] C. Leroy and P. Rancoita., *Principles of Radiation Interaction in Matter and Detection*. World Scientific, 2nd ed., 2009.

- [29] E. A. H. Koch, C. Amsler and T. Armstrong, “Proposal : the crystal barrel meson spectroscopy at lear with a 4π neutral and charged detector,” Tech. Rep. CERN-PSCC-85-56 ; PSCC-P-90, CERN, Geneva, 1985.
- [30] **PANDA** Collaboration, “Technical Design Report for PANDA Electromagnetic Calorimeter (EMC),” 2008.
<http://www.citebase.org/abstract?id=oai:arXiv.org:0810.1216>.
- [31] R. McIntyre, “Multiplication noise in uniform avalanche diodes,” *Electron Devices, IEEE Transactions on* **ED-13** no. 1, (Jan, 1966) 164–168.
- [32] http://www.sales.hamamatsu.com/assets/applications/SSD/Characteristics_and_use_of_SI_APD.pdf.
- [33] M. Moritz, *Measurements and improvements of the response of the PANDA-EMC prototype PROTO60 to high energetic particles and photons in accelerator experiments*. PhD thesis, Justus-Liebig-Universität Gießen, 2013.
- [34] H. Flemming and P. Wieczorek, “Low noise preamplifier asic for the panda experiment,” *Journal of Instrumentation* **6** no. 12, (2011) C12055.
<http://stacks.iop.org/1748-0221/6/i=12/a=C12055>.
- [35] W. Erni, “Technical Design Report for discrete Preamplifier for APD Readout, LNP Preamplifier Version SP 883A02,” 2008. <http://panda-wiki.gsi.de/cgi-bin/view/DCS/SupportedHardware>.
- [36] M. Janecek and W. W. Moses, “Optical reflectance measurements for commonly used reflectors,” *Nuclear Science, IEEE Transactions on* **55** no. 4, (Aug, 2008) 2432–2437.
- [37] http://www.hamamatsu.com/resources/pdf/ssd/s8664_series_kapd1012e.pdf.
- [38] <http://www.struck.de/sis3302.htm>.
- [39] M. Kavatsyuk, E. Guliyev, P. Lemmens, H. Lohner, T. Poelman, and G. Tambave, “Feature-extraction algorithms for the panda electromagnetic

- calorimeter,” in *Nuclear Science Symposium Conference Record (NSS/MIC), 2009 IEEE*, pp. 210–213. Oct, 2009.
- [40] M. Kavatsyuk, D. Bremer, V. Dormenev, P. Drexler, T. Eissner, W. Erni, E. Guliyev, T. Hennino, B. Krusche, B. Lewandowski, H. Löhner, M. Moritz, R. Novotny, K. Peters, J. Pouthas, P. Rosier, M. Steinacher, G. Tambave, and A. Wilms, “Performance of the prototype of the electromagnetic calorimeter for {PANDA},” *Nuclear Instruments and Methods in Physics Research Section A: Accelerators, Spectrometers, Detectors and Associated Equipment* **648** no. 1, (2011) 77 – 91. <http://www.sciencedirect.com/science/article/pii/S0168900211011600>.
- [41] <https://root.cern.ch/>.
- [42] <http://www-elsa.physik.uni-bonn.de/index.html>.
- [43] M. Berger and S. Seltzer., *Tables of Energy Losses and Ranges of Electrons and Positrons*. National Aeronautics and Space Administration Report, 1964.
- [44] S. Friedrich, *Experimental constraints on the real part of the ω -nucleus optical potential*. PhD thesis, Justus-Liebig-Universität Gießen, 2014.
- [45] K. Fornet-Ponse, *Die Photonenmarkierungsanlage für das Crystal-Barrel/TAPS-Experiment an ELSA*. PhD thesis, Rheinisch-Friedrich-Wilhelms Universität, 2009.
- [46] P. Bevington, *Data Reduction and Error Analysis for the Physical Sciences*, vol. Third Edition. McGraw-Hill Higher Education, 2003.
- [47] S. Grape, *Studies of PWO Crystals and Simulations of the $\bar{p}p \rightarrow \bar{\Lambda}\Lambda, \bar{\Lambda}\Sigma^0$ Reactions for the PANDA Experiment*. Dissertation, Uppsala University, 2009.
- [48] B. Brabson, R. Crittenden, A. Dzierba, T. Foxford, J. Gunter, *et al.*, “A Study of two prototype lead glass electromagnetic calorimeters,” *Nucl.Instrum.Meth.* **A332** (1993) 419–443.
- [49] M. M. F. Jr., “Matrix method for finding sets of contiguous non-zero elements in a 2-dimensional array.,” *Pattern Recognition* **19** no. 1, (1986) 73.

- <http://dblp.uni-trier.de/db/journals/pr/pr19.html#Ferguson86>.
- [50] <http://www.dowcorning.de/applications/search/products/details.aspx?prod=01190300&type=PROD&dsctry=USA>.
- [51] P. Wiczorek. private communication.
- [52] <http://www.kph.uni-mainz.de/578.php>.
- [53] A. Jankowiak, “The mainz microtron mami –past and future,” *The European Physical Journal A - Hadrons and Nuclei* **28** no. 1, (2006) 149–160.
<http://dx.doi.org/10.1140/epja/i2006-09-016-3>.
- [54] J. McGeorge, J. Kellie, J. Annand, J. Ahrens, I. Anthony, A. Clarkson, D. Hamilton, P. Lumsden, E. McNicoll, R. Owens, G. Rosner, and A. Thomas, “Upgrade of the glasgow photon tagging spectrometer for mainz mami-c,” *The European Physical Journal A* **37** no. 1, (2008) 129–137.
<http://dx.doi.org/10.1140/epja/i2007-10606-0>.
- [55] <http://www.kph.uni-mainz.de/mami.php>.
- [56] F. Cavallari, “Performance of calorimeters at the lhc,” *Journal of Physics: Conference Series* **293** no. 1, (2011) 012001.
<http://stacks.iop.org/1742-6596/293/i=1/a=012001>.
- [57] “Performance of photon reconstruction and identification with the cms detector in proton-proton collisions at $\sqrt{s} = 8$ tev,” *Journal of Instrumentation* **10** no. 08, (2015) P08010.
<http://stacks.iop.org/1748-0221/10/i=08/a=P08010>.
- [58] A. Benaglia, “The cms ecal performance with examples,” *Journal of Instrumentation* **9** no. 02, (2014) C02008.
<http://stacks.iop.org/1748-0221/9/i=02/a=C02008>.
- [59] CMS Collaboration, “2012 ECAL detector performance plots,”.
- [60] E. Auffray, G. Chevenier, M. Freire, P. Lecoq, J. L. Goff, R. Marcos,

- G. Drobychev, O. Missévitch, A. Oskine, R. Zouevsky, J. Peigneux, and M. Schneegans, “Performance of accos, an automatic crystal quality control system for the {PWO} crystals of the {CMS} calorimeter,” *Nuclear Instruments and Methods in Physics Research Section A: Accelerators, Spectrometers, Detectors and Associated Equipment* **456** no. 3, (2001) 325 – 341. <http://www.sciencedirect.com/science/article/pii/S0168900200006653>.
- [61] E. Auffray, F. Cavallari, M. Lebeau, P. Lecoq, M. Schneegans, and P. Sempere Roldan, “Crystal conditioning for high-energy physics detectors,” *Nucl. Instrum. Meth.* **A486** (2002) 22–34.
- [62] D. Britton, M. Ryan, and X. Qu, “Light collection uniformity of lead tungstate crystals for the {CMS} electromagnetic calorimeter,” *Nuclear Instruments and Methods in Physics Research Section A: Accelerators, Spectrometers, Detectors and Associated Equipment* **540** no. 2–3, (2005) 273 – 284. <http://www.sciencedirect.com/science/article/pii/S0168900204024283>.
- [63] E. Auffray *et al.*, “Beam tests of lead tungstate crystal matrices and a silicon strip preshower detector for the CMS electromagnetic calorimeter,” *Nucl. Instrum. Meth.* **A412** (1998) 223–237.
- [64] P. Adzic *et al.*, “Energy resolution of the barrel of the CMS electromagnetic calorimeter,” *JINST* **2** (2007) P04004.
- [65] CMS Collaboration, F. Tarsitano, “Study of the Noise and Thresholds in CMS ECAL,” https://www.researchgate.net/publication/269105856_Study_of_the_Noise_and_Thresholds_in_CMS_ECAL.
- [66] A. Adametz, “Preshower measurement with the cherenkov detector of the babar experiment,” 2005.
- [67] S. Bianco, *Tracking and vertex reconstruction with the PANDA Micro-Vertex-Detector*. PhD thesis, Rheinisch-Friedrich-Wilhelms Universität, 2013.

- [68] L. Gruber, *Studies of SiPM photosensors for time-of-flight detectors within PANDA at FAIR*. PhD thesis, Technische Universität Wien, 2014.
- [69] B. Voss, J. Kunkel, R. Karabowicz, and G. D. Germany, “The gem-discs for the panda experiment*.”.

Glossary

ADC Analogue to Digital Converter. 59, 168

APD Avalanche Photo Diode. 32, 42, 46, 47, 105, 108, 126–130, 139, 152, 155, 168, 175, 178

APFEL ASIC for PANDA Front-end Electronics. 48–51, 103, 104, 106–108, 110, 111, 120, 121, 139, 148, 154, 155, 168, 176, 177

APPA Atomic Plasma Physics and Applications. 2, 168

ASIC Application Specific Integrated Circuit. 48–51, 103, 104, 106–108, 110, 120, 121, 127, 128, 130, 139, 148, 149, 154, 155, 168, 176, 178

BaBar B and B-bar. 20, 86, 159, 168

BEC Backward End Cap. 41, 42, 168

BNL Brookhaven National Laboratory. 5, 168

CAD Computer-Aided Design. 17, 70, 71, 98, 113, 168, 176

CBM Compressed Baryonic Matter. 2, 168

CERN Conseil Européen pour la Recherche Nucléaire (European laboratory for particle physics). 7, 59, 65, 110, 143, 145, 147, 151, 168

CFD Constant Fraction Discriminator. 62, 168

CFT Constant Fraction Timing algorithm. 60, 62, 168

CMOS Complementary Metal-Oxide-Semiconductor. 50, 168

CMS Compact Muon Solenoid. 40, 42, 43, 46, 140, 142–144, 146, 150, 152, 153, 157, 160, 168

CPU Central Processing Unit. 59, 108, 168

CR Collector Ring. 2, 168

DAQ Data Acquisition. 39, 51–53, 56, 57, 65, 104, 107, 108, 112, 168, 176

DIRC Detection of Internally Reflected Cherenkov Light. 18–22, 25, 32, 95, 157–160, 168, 175, 179

DPM Dual Parton Model. 141, 168

ECAL Electromagnetic CALorimeter. 140, 142, 143, 146, 152, 157, 168

ELSA ELEktronen Stretcher Anlage. 65, 67–70, 78, 86, 94, 141, 145, 146, 157, 159, 168, 176

EMC ElectroMagnetic Calorimeter. I–III, 8–11, 13, 20–23, 25, 26, 28, 32, 38–42, 46, 48–54, 59, 65, 84, 87, 89, 95, 98, 103, 104, 110, 120, 139–142, 144, 146, 148, 150, 153, 154, 156–158, 168, 175–177, 181

ENC Equivalent Noise Charge. 50, 56, 121, 168

FAIR Facility for Antiproton and Ion Research. I, III, 1, 2, 168, 175

FEC Forward End Cap. 41, 47, 48, 50, 168

FPGA Field Programmable Gate Array. 51, 59, 168

FS Forward Spectrometer. 13, 168

FT Forward Tracker. 168

FWHM Full Width at Half Maximum. 40, 101, 168

Geant4 GEometry ANd Tracking Version 4. 73, 97, 98, 128, 168

GEM Gas Electron Multiplier. 16–19, 168, 175

- GPD** Generalized Parton Distribution. 10, 11, 168
- GSI** GSI Helmholtzzentrum für Schwerionenforschung GmbH. 1, 2, 50, 105, 121, 148, 149, 168
- HDSM** Harmonic Double Sided Micrtron. 114, 116, 168, 178
- HESR** High Energy Storage Ring. 2, 3, 5, 168, 175
- HV-MAPS** HighVoltage-Monolithic Active Pixel Sensor. 27, 168
- J-FET** Junction Field Effect Transistor. 50, 168
- KVI-CART** Kernfysisch Versneller Instituut-Center for Advanced Radiation Technology. 99, 101, 168
- LAAPD** Large Area Avalanche Photo Diode. 42, 44–47, 49, 50, 53–57, 59, 99, 101, 103, 105–108, 110, 123–125, 137, 139, 146, 150, 168, 181
- LEAR** Low Energy Antiproton Ring. 7, 168
- LHC** Large Hadron Collider. 40, 143, 168
- LINAC** LINear ACcelerator. 67, 114, 116, 168
- LNP-P** Low Noise and Low Power charge Preamplifier. 48, 50, 56, 57, 59, 60, 168
- LY** Light Yield. 41, 42, 168
- MA** Moving Average algorithm. 60–62, 168, 176
- MAMI** MAinzer MIkrotron. 65, 112–114, 116–119, 141, 145–148, 154, 160, 168, 178, 181
- MDT** Mini Drift Tube. 22, 168
- MF** Muon Filter. 23, 168
- MIP** Minimum Ionizing Particle. 30, 32, 41, 79, 168
- MRS** Muon Range System. 19, 22, 23, 26, 168

- MVD** Micro-Vertex-Detector. 16, 17, 148, 168, 175
- MWD** Moving Window Deconvolution algorithm. 59–63, 168, 176
- NCE** Nuclear Counter Effect. 46, 168
- NESR** New Experimental Storage Ring. 2, 168
- NIM** Nuclear Instrumentation Module. 109, 168
- NUF** Non-UniFormity. 79, 84, 98–101, 168, 177
- NuSTAR** Nuclear Structure Astrophysics and Reaction. 2, 168
- p-LINAC** proton-LINear ACcelerator. 2, 168
- \bar{P} ANDA** Antiproton Annihilation at Darmstadt. I–IV, 2–6, 8–13, 15, 16, 18, 20–22, 26–28, 32, 38–43, 46, 48, 51–53, 59, 65, 84, 86, 87, 89, 94, 98, 99, 103, 110, 120, 139–146, 148, 150, 153, 154, 156–159, 168, 175, 176, 181, 183
- PCB** Printed Circuit Board. 106, 107, 168
- PDF** Parton Distribution Function. 11, 168
- PID** Particle IDentification. 10, 18, 19, 23, 168
- PMT** PhotoMultiplier Tube. 20, 25, 42, 47, 65, 70, 113, 118, 139, 168
- PVC** PolyVynil Chlorid. 54, 168
- PWO** lead tungstate (PbWO_4). 39–43, 168
- PWO-II** lead tungstate (PbWO_4). 32, 40–42, 44, 53, 54, 57, 88, 98, 103, 104, 119, 139, 152, 168, 181
- QCD** Quantum ChromoDynamics. V, 2, 3, 5–7, 9, 168
- QDC** Charge(Q)-to-Digital Converter. 71, 168
- QE** Quantum Effeciency. 43, 56, 57, 107, 168
- R&D** Research & Development. 40, 45, 46, 168

- RESR** Recirculation Experimental Storage Ring. 2, 168
- RF** Radio Frequency. 114, 168
- RICH** Ring Imaging CHerenkov Counter. 19, 21, 25, 168
- RMS** Root Mean Square. 39, 61, 84, 121, 123, 124, 168, 178
- RTM** Race Track Microtron. 114–116, 168, 177
- SADC** Sampling Analogue to Digital Converter. 50, 51, 57, 59, 60, 108–110, 119, 121, 154, 155, 168, 176
- SciTiI** Scintillator Tile. 21, 22, 158, 159, 168
- SiPM** Silicion PhotoMultiplier. 22, 168
- SIS100** SchwerIonenSynchrotron 100. 2, 168
- SIS18** SchwerIonen Synchrotron 18. 2, 168
- SLAC** Stanford Linear Acclerator Center. 5, 168
- SPS** Super Proton Synchrotron. 65, 168
- STT** Straw Tube Tracker. 16–18, 24, 168, 175
- TAPS** Two Arms Photon Spectrometer. 65, 168
- TDA** Transition Distribution Amplitude. 11, 168
- TDC** Time-to-Digital Converter. 71, 72, 109, 118, 168
- TDR** Technical Design Report. 39, 65, 98, 103, 141, 146, 148, 149, 156, 168
- TOF** Time Of Flight. 18, 21, 22, 25, 168
- TS** Target Spectrometer. 13, 168
- UNILAC** UNIversal Linear ACcelerator. 2, 168
- VM2000** enhanced specular reflector film. 53, 55, 99, 104, 105, 168

VME Versa Module Eurocard. 59, 108, 168

VPTT Vacuum Photo TeTrode. 42, 47, 48, 50, 168, 176

List of Figures

1.1	Schematic view of the FAIR facility.	1
1.2	Schematic view of the HESR.	3
1.3	Invariant mass range accessible to \bar{P} ANDA.	4
1.4	Schematic of production and formation experiments.	6
1.5	Level scheme of the charmonium system.	7
1.6	Dalitz plot for the glueball candidate $f_0(1500)$	8
1.7	Simulation of a \bar{P} ANDA reconstruction of $X(3872)$ mass.	9
1.8	Layout of the \bar{P} ANDA detector.	13
1.9	Layout of the target spectrometer.	14
1.10	Layout of the MVD.	17
1.11	Layout of the STT.	18
1.12	Layout of the GEM tracker.	19
1.13	Principle of the detection based on Cherenkov light.	20
1.14	Layout of the Barrel DIRC.	21
1.15	Layout of the EMC.	23
1.16	Layout of the forward spectrometer.	24
1.17	Layout of the \bar{P} ANDA shashlyk EMC.	26
1.18	Design of the luminosity detector.	27
1.19	Ionization energy-loss rate in different materials.	29
1.20	Mass attenuation coefficient of lead tungstate.	36
1.21	Shower energy profiles.	38
1.22	Arrangement of the crystals in the Barrel EMC.	42
1.23	Schematic drawing of the crystal geometry.	43
1.24	Method to find the optimal gain for an APD [32].	46
1.25	Layout of the structure of an APD.	47

1.26	Schematic layout of a VPTT.	48
1.27	Schematic layout of the APFEL.	49
1.28	Picture of the APFEL 1.4 ASIC.	51
1.29	Schematic layout of the \bar{P} ANDA EMC DAQ.	52
2.1	Schematic from the Barrel EMC to the PROTO60.	54
2.2	Photographs of the PROTO60.	55
2.3	Schematic of the PROTO60 readout.	58
2.4	SADC traces after feature extraction steps.	60
2.5	Variation of MWD parameter M	61
2.6	Variation of MA parameter L	62
2.7	Signals for different feature extraction values.	63
2.8	Deduction of the energy information.	63
2.9	Noise event.	64
2.10	Threshold scan for different tagger energies.	64
2.11	CBELSA/TAPS experimental area.	66
2.12	Photograph of the PROTO60 setup in Bonn.	66
2.13	Floor plan of the ELSA-facility [42].	68
2.14	Fractional energy loss per radiation length in lead.	69
2.15	CAD model of the tagger.	71
2.16	Energy coverage of the tagger.	72
2.17	Intrinsic tagger energy resolution.	72
2.18	Energy calibration for the tagger.	74
2.19	Tagger configuration during beamtime.	75
2.20	Absolute energy resolution of the tagger.	75
2.21	Schematic crystal map of the PROTO60.	76
2.22	Beampositions within 3×3 matrix.	77
2.23	Deposited energy spectrum of cosmic radiation.	79
2.24	Summed lineshapes for a matrix of 6×6 crystals.	80
2.25	Lineshape for a 6×6 crystal matrix.	81
2.26	Linearity of the response.	82
2.27	Multiplicity for various thresholds.	83
2.28	Fitted lineshapes for the 8 tagger energies.	85

2.29 Energy resolution for a matrix of 6×6 crystals.	86
2.30 Energy resolution for a matrix of 3×3 crystals.	87
2.31 Energy resolution obtained with different shaping parameters.	88
2.32 Energy resolution for different tagger configurations.	89
2.33 Reconstructed impact positions.	90
2.34 Reconstructed beamspot.	91
2.35 Fitted reconstructed impact position.	92
2.36 Position resolution for run1.	92
2.37 Position resolution for run9.	93
2.38 Position resolution for run16.	93
2.39 Position resolution for run20.	93
2.40 Setup to test the influence of dead material in front of the detector.	94
2.41 Energy resolution with a quartz plate.	95
2.42 Position resolution with a quartz plate.	96
2.43 Lineshapes with quartz plate.	96
2.44 Energy resolution photons and electrons for a 6×6 crystal matrix.	97
2.45 Energy resolution photons and electrons for a 3×3 crystal matrix.	98
2.46 Position resolution for electrons.	99
2.47 Position resolution for photons.	99
2.48 Schematic light collection in case of NUF.	100
2.49 Measurement of NUF of a crystal.	101
2.50 Simulated lineshapes for photon and positron beam.	102
3.1 Schematic view of the Barrel EMC.	104
3.2 Vertical and horizontal cross-section through the crystal arrangement.	106
3.3 Schematic of the APD readout with the APFEL.	107
3.4 Schematic of the PROTO120 electronics.	108
3.5 Picture of a PROTO120 test setup.	109
3.6 Schematic of the PROTO120 readout.	110
3.7 Typical trace.	111
3.8 Picture of a PROTO120 test setup.	112
3.9 Pictures of the PROTO120 test setup.	113
3.10 Basic setup of a RTM.	115

List of Figures

3.11	Scheme of the HDSM of MAMI C.	116
3.12	Scheme of the Glasgow Photon Tagging Spectrometer.	117
3.13	Schematic setup of the PROTO120 at MAMI.	118
3.14	Schematic crystal map of the read out matrix of the PROTO120. . .	120
3.15	Schematic design of the charge sensitive preamplifier.	121
3.16	SADC trace without a signal.	122
3.17	Distribution of the RMS of the baseline (high gain).	123
3.18	Distribution of the RMS of the baseline (low gain).	124
3.19	Noise distribution.	125
3.20	Schematic of the calibration procedure.	126
3.21	APD linearity of the central crystal (HG).	127
3.22	APD linearity of the central crystal (LG).	128
3.23	APD linearity of crystal1 (HG).	129
3.24	APD linearity of crystal1 (LG).	129
3.25	Distribution of the slopes of the APD correlation.	130
3.26	Intrinsic ASIC amplification.	130
3.27	Tagged lineshapes for the central crystal 6.	131
3.28	Relative calibration of crystal 2.	132
3.29	Threshold scan.	133
3.30	Comparison of lineshapes.	134
3.31	Summed and tagged lineshapes of the 3×3 matrix.	134
3.32	Energy resolution of the 3×3 matrix.	135
3.33	Multiplicity as a function of the taggerenergy.	136
3.34	Multiplicity for various threshold values.	136
3.35	Energy resolution for added traces.	137
3.36	Comparison summed traces and one APD.	137
4.1	Typical trace.	142
4.2	Electromagnetic shower within the PROTO60.	144
4.3	Electromagnetic shower within the PROTO60.	145
4.4	Position resolution PROTO60.	147
4.5	LY for tapered crystals.	151
4.6	Light collection non-uniformity in tapered crystals.	152

4.7	Electromagnetic shower within the PROTO60.	153
4.8	Performance comparison of PROTO60 and PROTO120.	155
4.9	Material budget in front of the EMC.	158
4.10	Conversion probability in the DIRC.	159
4.11	Reconstructed energy for 1 GeV photons with and without preshower.	160

List of Tables

1.1	Parameters for a longitudinal shower development [28].	37
1.2	Requirements for the \bar{P} ANDA EMC.	39
1.3	Properties of lead tungstate.	41
1.4	Definition of the geometrical parameters of the PWO-II crystals. . .	44
2.1	Properties of LAAPDs used in PROTO60.	56
2.2	Dynamic range and noise of PROTO60.	57
2.3	Electronics modules of the PROTO60 test setup.	58
2.4	Beam positions for the beamtime.	77
2.5	List of obtained position resolutions.	90
2.6	Properties of quartz.	94
3.1	Properties of LAAPDs used in PROTO120.	107
3.2	Electronics modules of the PROTO120 test setup.	111
3.3	General MAMI parameters [53].	114
3.4	Selected Tagger channels at the beamtime.	119
3.5	Noise sources.	122
3.6	Determination of the summation threshold and noise level.	123
4.1	Comparison of PROTO60 results	146

Acknowledgements

Diese Doktorarbeit wäre ohne die Unterstützung von verschiedensten Personen nie zu Stande gekommen. Dafür möchte ich allen ganz herzlich danken!

Als erstes möchte ich meinen beiden Chefs Kai-Thomas Brinkmann und Rainer Novotny für ihre Unterstützung und Anleitung während meiner Zeit als Doktorand danken. Ihre Türen waren stets offen und ich konnte viel von ihrer reichhaltigen wissenschaftlichen Erfahrung lernen. Besonders möchte ich Rainer für seine Kommentare zu dieser Arbeit und seiner Betreuung danken.

Ein großes Dankeschön auch an den gesamten Rest der Arbeitsgruppe. Es war immer eine angenehme Atmosphäre und jeder war immer mit Rat und Tat zur Stelle. Im speziellen möchte ich meiner besseren Hälfte im Büroalltag danken. Till hat immer meine Launen ausgehalten und stets dafür gesorgt, dass ich mittags was leckeres zu essen bekomme habe. Dank für ein angenehmes und unterhaltsames Zusammenleben im Büro geht natürlich auch an Ben, Christopher, Daniel, sowie an Stefan und Stefan aus dem alten Büro. Den ganzen bürokratischen Alltag erträglich machte immer Anita als gute Seele der Arbeitsgruppe. Großen Dank natürlich auch an die Post-docs. Besonderen Dank an Peter für die Arbeit an die Ausleseelektronik. Nicht zu vergessen sind auch der stets die Stimmung aufhellende Valera und die immer hilfsbereiten Hans, Eric, Mariana und Volker. Ohne die Hilfe aus Elektronik und Mechanik wären Messungen am Prototypen nie möglich gewesen. Besten Dank also auch an René, Uli und Marcel! Grazie auch an "La Familia" Tommaso, Alberto und Valentino. Nicht zu kurz kommen sollen natürlich auch die restlichen Doktoranden Robert, Martin, Tobias, Markus und Andreas! Vielen Dank an euch!

Ein weiterer Dank gilt der gesamten PANDA Kollaboration. Es war stets eine konstruktive und freundliche Zusammenarbeit. Besonderer Dank für die Erfahrungen und geknüpften Freundschaften durch den Young Scientist Convent.

Ein großes Dankeschön auch an Milan für das ständige und nervende Nachfragen nach dem Stand der Arbeit.

Außerdem möchte ich den Mitarbeitern von der ELSA und MAMI Beschleunigeranlage für die zuverlässige Bereitstellung des Strahls danken. Dank auch an die Kollegen vom IPN Orsay und IHEP Protvino für die Arbeit an der Mechanik des PROTO120 und an die Kollegen vom KVI-CART Groningen und der GSI Darmstadt für die Arbeit an der Ausleseelektronik.

Mein größter Dank gilt aber meiner Familie! Ich kann mir jederzeit der Unterstützung meiner Eltern und meines Bruders sicher sein. Diese Doktorarbeit ist euch gewidmet!

Erklärung

Ich erkläre: Ich habe die vorgelegte Dissertation selbständig und ohne unerlaubte fremde Hilfe und nur mit den Hilfen angefertigt, die ich in der Dissertation angegeben habe.

Alle Textstellen, die wörtlich oder sinngemäß aus veröffentlichten Schriften entnommen sind, und alle Angaben, die auf mündlichen Auskünften beruhen, sind als solche kenntlich gemacht.

Bei den von mir durchgeführten und in der Dissertation erwähnten Untersuchungen habe ich die Grundsätze guter wissenschaftlicher Praxis, wie sie in der "Satzung der Justus-Liebig-Universität Gießen zur Sicherung guter wissenschaftlicher Praxis" niedergelegt sind, eingehalten.

Christoph Rosenbaum
Gießen, September 2016

